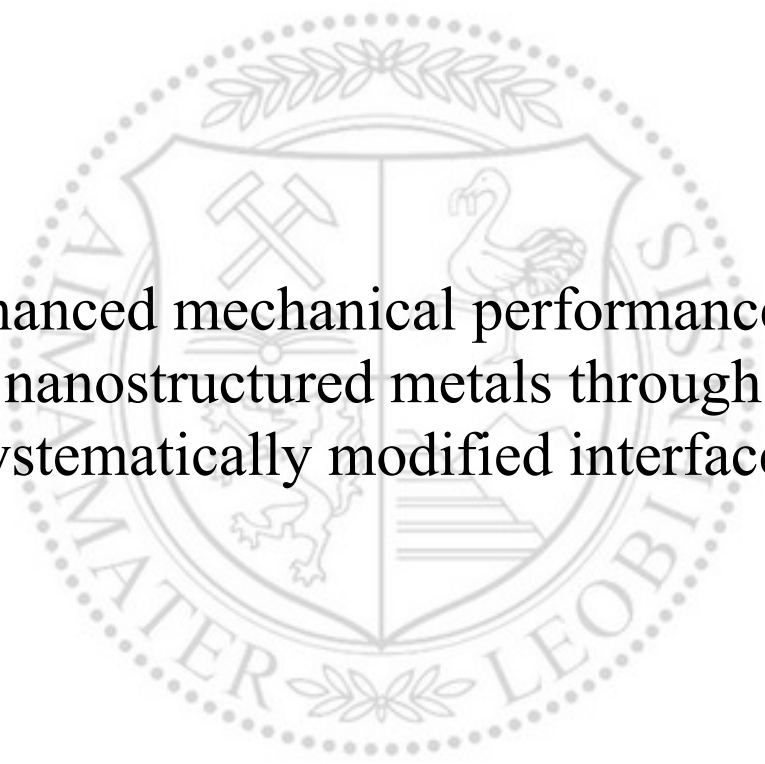




Chair of Materials Physics

Doctoral Thesis



Enhanced mechanical performance of
nanostructured metals through
systematically modified interfaces

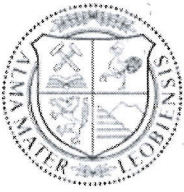
Dipl.-Ing. Michael Wurmshuber, BSc

August 2022

This work has received funding from the European Research Council (ERC) under the European Union's Horizon 2020 research and innovation programme (Grant agreement No. 771146 (TOUGHIT)).

Copyright © 2022 by Michael Wurmshuber. All rights reserved.

Montanuniversität Leoben
Department of Materials Science, Chair of Materials Physics
Jahnstraße 12
8700 Leoben
Austria



AFFIDAVIT

I declare on oath that I wrote this thesis independently, did not use other than the specified sources and aids, and did not otherwise use any unauthorized aids.

I declare that I have read, understood, and complied with the guidelines of the senate of the Montanuniversität Leoben for "Good Scientific Practice".

Furthermore, I declare that the electronic and printed version of the submitted thesis are identical, both, formally and with regard to content.

Date 09.08.2022

Signature Author
Michael Wurmshuber

Acknowledgments

Writing a dissertation represented an especially memorable time and milestone in my life. Given the substantial amount of time and work that has to be invested towards this goal, the help and support from colleagues, collaborators, family and friends over these past years was incredibly valuable and crucial for the successful and sane completion of this thesis. Therefore, some words of thanks are in order.

First and foremost, I would like to express my profound gratitude towards my supervisor Assoc.Prof. Dr. Daniel Kiener. After writing my Bachelor and Master Thesis with him, he entrusted me not only to be the first PhD student working on his ERC grant, but also with several fun and exciting side projects. This deepened my expertise and broadened my scientific horizon substantially. Seeking out his advice and guidance has always been incredibly helpful. I am immensely grateful for his support, constructive criticism and his contribution to my growth as a researcher.

Special thanks go towards Simon Doppermann, whose help with sample fabrication, material testing and data analysis has been exceptionally useful and valuable.

I am highly thankful to Dr. Stefan Wurster and Prof. Reinhard Pippan, who supported this thesis greatly by sharing their experiences and advice on the topics of tungsten, severe plastic deformation and fracture mechanics.

My sincere thanks also go to Prof. Dr. Peter Hosemann and Dr. Mehdi Balooch for the great collaboration that carried over seamlessly from my visit in Berkeley. May the contact stay uninterrupted!

In addition I would like to thank Prof. Dr. Lorenz Romaner and Dr. Rishi Bodlos for their help with DFT simulations.

I would like to express my great appreciation to my colleagues at ESI, who shared many memorable moments, fruitful discussions and fun conference trips with me. Naming them all would immensely prolong this chapter and I would almost certainly forget someone, which is why I will refrain from that and thank you all collectively in this paragraph instead.

A special mention must be given, however, to my office colleagues Dr. Agustina Massone and Dr. Markus Alfreider for their friendship in and outside of work.

Furthermore, I would like to thank my parents for their moral and financial support in all my life decisions and for believing in me. My sister Sandra, as well as my friends in Braunau, Leoben and elsewhere, were always there to celebrate my accomplishments or to distract me when things did not work out as planned. I am immensely grateful for them to balance out the sometimes stressful times at work.

Here a special mention goes to Hannah, greatly missed, who always believed in me.

Last but not least, I would like to express my gratitude towards my life partner, Jess. From the moment we met, you were always there to motivate me, cheer me up or to encourage me. You were understanding and supportive when I had a lot of work on my plate, and you always push me towards my goals, for which I am extremely grateful. I know I can always count on you and your support.

Abstract

In an effort to create structural "supermaterials", combining ultra-high strength, ductility and excellent fracture toughness, nanostructured materials are a promising strategy. Especially nanocrystalline metals, ultrafine-grained metals and metal-metal nanocomposites show great potential to break the mutual exclusivity of these mechanical properties. However, the vast amount of grain boundaries and interfaces within these materials typically act as weak links in the microstructure and limit any further enhancements in ductility and toughness. Thus, this work attempts to increase the strength of these weak links with the help of doping elements that were identified in ab-initio simulations to improve grain boundary- and interface cohesion. The two material systems selected for this approach are ultrafine-grained tungsten and nanocrystalline tungsten-copper composites, two materials with exciting implementation potential in future high-performance applications, such as nuclear fusion reactors.

After introducing the theoretical concepts and state of the art in research, this work presents the developed fabrication and processing routes, involving powder compacting and severe plastic deformation, to create the undoped and doped materials. The influence of the doping elements on microstructure and mechanical properties is assessed using high-resolution characterization methods and small-scale testing techniques. Significant improvements of mechanical properties of either material system could be achieved through certain doping elements, while others had close to no or even a detrimental effect on mechanical performance. The different responses of the nanostructured materials to the various doping elements are discussed in detail. Finally, the effects of helium irradiation, as encountered in nuclear fusion reactors, on swelling and mechanical properties of the investigated material systems was characterized and compared to their conventionally structured counterparts, underlining their application potential in nuclear technology once more.

Altogether, the strength-ductility trade-off could be challenged by applying grain boundary and interface doping to nanostructured metals. The overall mechanical performance of ultrafine-grained W and W-Cu nanocomposite could be enhanced greatly, rendering them viable options for employment in high-performance applications.

Kurzfassung

Nanostrukturierte Materialien sind vielversprechende Kandidaten für die Anstrengungen "Super-Strukturmaterialien", die ultra-hohe Festigkeit, Verformbarkeit und exzellente Bruchzähigkeit vereinigen, zu kreieren. Vor allem nanokristalline Metalle, ultra-feinkörnige Metalle und Metall-Metall Nanokomposite zeigen großes Potential die allgemeine Unvereinbarkeit dieser mechanischen Eigenschaften zu überwinden. Jedoch stellen die Unmengen an Korngrenzen und Grenzflächen innerhalb dieser Materialien Schwachstellen des Gefüges dar und limitieren jegliche weitere Verbesserung von Duktilität und Zähigkeit. Daher zielt diese Arbeit darauf ab, die Festigkeit dieser Schwachstellen mit der Hilfe von Dopinglelementen zu stärken. Ab-initio Simulationen zeigten, dass diese Dopinglelemente die Korngrenz- und Grenzflächenkohäsion verbessern. Die zwei Materialsysteme, welche für diesen Ansatz ausgewählt wurden, sind ultra-feinkörniges Wolfram und nanokristalline Wolfram-Kupfer Verbunde, zwei Werkstoffe mit aufregendem Umsetzungspotential in zukünftigen Hochleistungsanwendungen, wie zum Beispiel in Kernfusionsreaktoren.

Nachdem die theoretischen Konzepte und der Stand der Forschung vorgestellt wurden, präsentiert diese Arbeit die entwickelte Herstellungsrouten, die Pulverkompaktierung und plastische Hochverformung involviert und die verwendet wurde um die ungedopten und gedopten Materialproben zu erzeugen. Der Einfluss von Dopinglelementen auf die Mikrostruktur und die mechanischen Eigenschaften wurde mit Hilfe von hochauflösenden Charakterisierungsmethoden und mikromechanischen Experimenten adressiert. Signifikante Verbesserungen der mechanischen Eigenschaften beider Materialsysteme konnten durch Doping mit bestimmten Elementen erzielt werden, während andere Elemente fast keinen oder sogar einen negativen Effekt auf die mechanische Leistungsfähigkeit zeigten. Die verschiedenen Reaktionen der nanostrukturierten Materialien auf die diversen Dopinglelemente sind in dieser Arbeit ausführlich diskutiert. Schlussendlich wurden die Effekte von Heliumbestrahlung, wie sie in Kernfusionsreaktoren vorkommt, auf das Anschwellen und auf die Veränderung mechanischer Eigenschaften der beiden Werkstoffe untersucht und mit deren konventionell strukturierten Pendanten verglichen, um das Anwendungspotential dieser Materialien in der Kerntechnologie noch einmal zu unterstreichen.

Alles in allem konnte der Festigkeit-Duktilität Kompromiss durch Korngrenz- und Grenzflächendoping von nanostrukturierten Metallen angefochten werden. Die allgemeine mechanische Leistungsfähigkeit von ultra-feinkörnigem W und W-Cu Nanokompositen konnte erheblich verbessert werden, was die beiden Materialien zu plausiblen und praktikablen Optionen für die Verwendung in Hochleistungsanwendungen macht.

Content

| | |
|--|------------|
| Acknowledgments | vii |
| Abstract | ix |
| Kurzfassung | xi |
| List of abbreviations | xv |
| 1 Motivation | 1 |
| 2 Introduction | 3 |
| 2.1 The strength-ductility trade-off | 3 |
| 2.2 Nanostructured metals and composites | 7 |
| 2.3 Grain boundary segregation engineering | 13 |
| 2.4 W-based materials and their potential application in nuclear fusion technology | 15 |
| 3 Summary of results | 21 |
| 3.1 Fabrication of ultrafine-grained W and W-Cu nano-composites | 21 |
| 3.2 Effects of doping elements on mechanical properties of ultrafine- grained W | 27 |
| 3.3 Effects of doping elements on mechanical properties of nanocrystalline W-Cu | 39 |
| 3.4 Helium irradiation of ultrafine-grained W and nano-crystalline W-Cu | 45 |
| 4 Conclusions & Outlook | 51 |
| References | 55 |
| Appendix | 67 |
| A Ultrafine-grained Tungsten by High-Pressure Torsion - Bulk precursor versus powder processing route | 71 |
| B Tuning mechanical properties of ultrafine-grained tungsten by manipu- lating grain boundary chemistry | 83 |

| | | |
|---|---|-----|
| C | Small-scale fracture mechanical investigations of grain boundary doped ufg tungsten | 111 |
| D | Mechanical performance of doped W-Cu nanocomposites | 137 |
| E | Helium-induced swelling and mechanical property degradation in ultrafine-grained W and W-Cu nanocomposites for fusion applications | 165 |

List of abbreviations

| | | |
|------|-----|---|
| AFM | ... | atomic force microscopy/microscope |
| ann. | ... | annealed |
| APT | ... | atom probe tomography |
| ARB | ... | accumulative roll-bonding |
| bcc | ... | body centered cubic |
| cg | ... | coarse grained |
| CSM | ... | continuous stiffness measurement |
| DBTT | ... | ductile-brittle transition temperature |
| DFT | ... | density functional theory |
| EBSD | ... | electron backscatter diffraction |
| ECAP | ... | equal channel angular pressing |
| fcc | ... | face centered cubic |
| FIB | ... | focused ion beam |
| GB | ... | grain boundary |
| GBSE | ... | grain boundary segregation engineering |
| HPT | ... | high pressure torsion |
| nc | ... | nanocrystalline |
| RT | ... | room temperature |
| SE | ... | strength of embrittlement |
| SEM | ... | scanning electron microscope |
| SPD | ... | severe plastic deformation |
| SRS | ... | strain-rate sensitivity |
| SRIM | ... | Stopping Range of Ions in Matter |
| STEM | ... | scanning transmission electron microscopy |
| sxx | ... | single-crystalline |
| TEM | ... | transmission electron microscope |
| TRIP | ... | transformation induced plasticity |
| TWIP | ... | twinning induced plasticity |
| ufg | ... | ultrafine-grained |

1 Motivation

One does not have to be a materials engineer to realize that most materials are either hard and brittle (like glass or diamond) or soft and formable (like plastics or tin). Yet still, overcoming this trade-off of strength (hardness) and ductility (formability) is one of the most researched topics in the field of materials science. Creating a material that combines high strength, ductility and fracture toughness would maximize damage tolerance and render the material practically indestructible. This in turn allows for huge innovations in various fields of engineering, pushing the boundaries of potential application environments to the extreme and ensuring continual technological progress.

When looking at the materials available to us, metals generally exhibit the most favorable combination of strength, ductility and fracture toughness, yet especially ultra-high strength metals and alloys do not show sufficient tolerance to damage and failure from mechanical overloading or pre-existing defects, drastically limiting the application potential due to this reduced accident tolerance.

Reducing the grain size of metals and alloys is a promising approach to enhance the overall mechanical performance, as it generally increases strength and fracture toughness, while having little influence on ductility. Therefore, the highest strengths are achieved for metals in the nanocrystalline (nc) regime, i.e. grain sizes of below 100 nm. However, as the grain size gets this small, a transition from conventional dislocation-controlled plasticity to a grain boundary-controlled plasticity leads to a dramatic decrease in ductility. Moreover, the increased amount of grain boundaries in such nanocrystalline metals and alloys provides a great number of comparably easy crack propagation paths, nullifying the gained strength increase from grain size reduction. Hence, a slightly larger grain size, as shown by ultrafine-grained (ufg) metals (grain sizes of between 100 and 500 nm), often represents a reasonable trade-off and a better overall combination of mechanical properties.

This work aims to take a step towards synergy of strength, ductility and fracture toughness of nanostructured high-strength metals and alloys by strengthening grain boundaries using ab-initio informed doping elements. The material systems used in this work are ultrafine-grained W and nanocrystalline W-Cu composites. W is well

known for its intrinsic strength and for exhibiting the highest melting point among all chemical elements. These, among other beneficial material properties, make it a suitable candidate material for plasma-facing components in nuclear fusion reactors. Naturally, the intrinsic brittleness of W is a major concern and provides a crucial safety-risk in such a harsh and sensitive environment. Therefore, in order to increase ductility and fracture toughness of W and ensure an accident-tolerant mechanical behavior, ultrafine grained W is fabricated and doped with grain boundary cohesion enhancing elements. Extensive microstructural and mechanical characterization are utilized to unveil the effects of selected doping elements, which are outlined and summarized within this thesis.

Similarly, grain boundary doping is applied to nanocrystalline W-Cu composites, in an effort to create high-strength thermal conductors and heat sink materials with increased damage and radiation tolerance. To underline the possible application of the investigated materials in harsh environments, such as a nuclear fusion reactor, investigations regarding the response to helium irradiation are performed on the fabricated ultrafine-grained W and W-Cu nanocomposites.

Altogether, this thesis aims to improve ductility and toughness of ultra-high strength metals and composites through nanostructuring and enhancing of grain boundary cohesion, rendering damage and failure tolerant high-performance materials for application in extreme environments and taking a step towards the dream of creating indestructible structural "supermaterials" with unprecedented mechanical properties.

2 Introduction

To put the significance of the findings presented in this thesis into perspective, this chapter introduces the most important concepts, terminologies and the current state of the relevant research fields.

2.1 The strength-ductility trade-off

The inability of combining high strength and high ductility in conventional materials is one of the most fundamental challenges in materials research [1–11]. While metals generally exhibit a more favorable combination of strength and ductility than ceramics or plastics, the banana-shaped nature of the graph in Figure 2.1 underlines the distinct trade-off between the two properties even in the most advanced alloys.

The origin of this behavior lies within the fascinating crystal lattice defects called dislocations. While the plasticity and deformation carried by these dislocations makes the high achievable combination of strength and ductility in metals possible in the

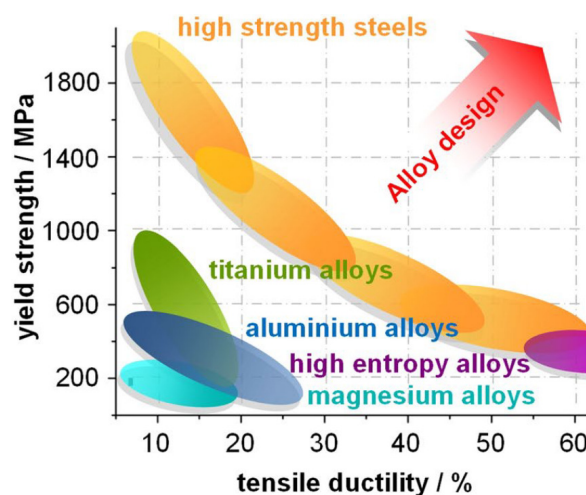


Figure 2.1 Tensile strength and tensile ductility of the most common alloys indicate that complete synergy of the two properties is unachievable [4].

first place, it is at the same time the reason why total synergy of the two properties will never be possible in a material relying exclusively on conventional dislocation-mediated plasticity [3,6].

The existence of dislocations within metals allows the deformation of the material without failure (as opposed to ceramics that break immediately when trying to deform them) while at the same time exhibiting high mechanical strength, which stems from the bonding strength between atoms in the crystal structure (in contrast to the rather weak van der Waals-bonds between the chains of polymers and plastics) [12]. A very common method to increase the strength of metals is to increase the density of dislocations within the material by e.g. cold working. With more dislocations in the material, a higher force, and therefore stress, has to be applied to move them, as they are acting as obstacles to each other. However, this increase in dislocation density also comes with a significant drop in ductility, as dislocations cannot move freely over long distances anymore [3]. As the material is therefore not able anymore to effectively dissipate stress through plastic deformation by dislocation movement, the stress increases until the fracture stress of the material is reached, leading to failure of the component after no or only little deformation. Similarly, other strengthening methods for metals, such as solid solution strengthening and precipitation hardening, result in a reduction of ductility, emphasizing the strength-ductility trade-off once again.

The mutual exclusivity of strength and ductility has a direct influence on fracture toughness as well. Metals generally obtain their excellent fracture toughness from relieving stress around the crack tip through plastic deformation by dislocations. This behavior is called intrinsic toughening [2,13]. One can easily depict that a restricted movement of dislocations through e.g. other dislocations or coherent and incoherent precipitations will result in a less successful dissipation of stress intensity, i.e. crack-driving force, from the crack tip and therefore an easier propagation of cracks through the material, which is generally interpreted as a lower fracture toughness [2,13].

Once again, the existence of dislocation plasticity in metals allows for outstanding strength and toughness, but also provides an inherent mutual exclusivity of the two properties that cannot be enhanced past a certain limit, especially for ultra-high strength materials, as apparent in Figure 2.2.

A special case of failure in metals is fracture along grain boundaries (GBs) or interfaces, which is known as intercrystalline or intergranular failure. This type of failure is on its own very brittle and requires only a low amount of energy for crack propagation, as GBs and interfaces are commonly weak links in the microstructure of metals [14,15]. The toughness of materials breaking via intercrystalline fracture can, however, be improved by e.g. increasing the grain size, which can force crack deflection or even change the failure mode to transgranular failure. Another strategy to increase the

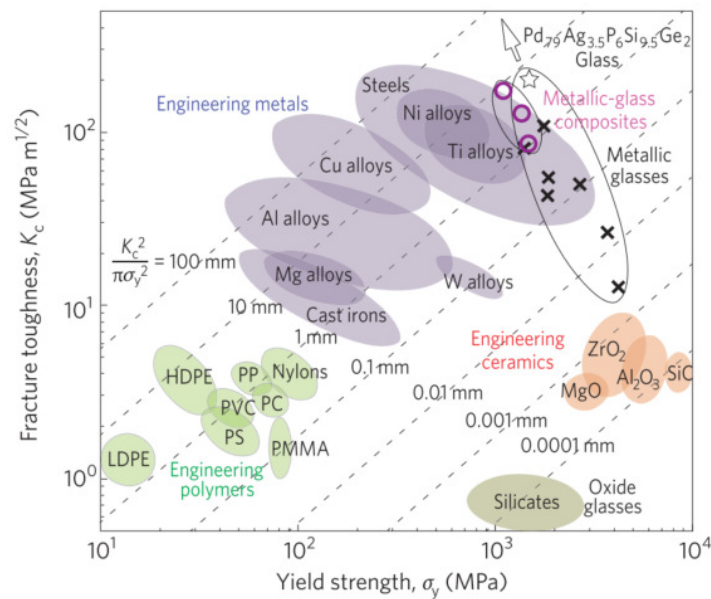


Figure 2.2 Ashby plot of yield strength and fracture toughness for the most common engineering materials [2].

fracture toughness is by strengthening the interface- or GB cohesion [16], as will be discussed in more detail in Section 2.3. Intercrystalline failure is usually seen in very fine grained materials [14, 15], refractory metals [16–18] or in materials exposed to corrosive environments [19].

It is not particularly surprising that overcoming this trade-off of strength, ductility and toughness has been a well researched topic ever since the early days of systematic materials science. After all, a material combining overall excellent mechanical properties would have huge implications on various fields of engineering [1–11]. Materials are frequently the bottleneck to new engineering innovations, as especially high-performance applications in extreme environments often demand impossible to achieve combinations of mechanical, functional and chemical material properties. A famous example for this are the plasma-facing components in novel nuclear fusion reactors, where mechanical and thermal load meet irradiation and contamination with helium [20, 21], as will be explained in more detail in Section 2.4. Especially for mechanically challenging environments the synergy of strength, ductility and toughness is of utmost importance for the safe and damage tolerating employment of structural materials [2].

Various strategies have been utilized to overcome the trade-off, most of them focusing on diverting from a primarily dislocation-based plasticity. Two famous examples in the area of steel design are TRIP and TWIP steels [22]. TRIP steels rely on "trans-

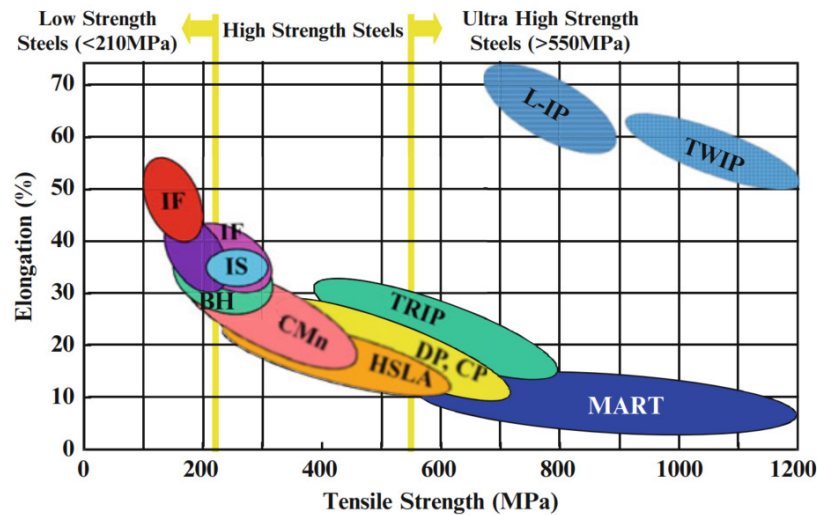


Figure 2.3 TRIP and TWIP steels as examples on how to overcome the strength-ductility trade-off [22].

formation induced plasticity", which describes plastic deformation through a phase transformation. In this case retained austenite in the microstructure transforms to martensite through a critical stress being applied. This transformation leads to a local strengthening of the material, which in turn allows for a high strain-hardening rate and, consequently, a large uniform elongation and ductility [22,23]. As shown in Figure 2.3, the TRIP effect leads to an increase in strength and ductility compared to conventional steels, however, this combination is still far away from ideal synergy of strength and ductility.

A better case can be made for TWIP steels, as they combine ultra-high strength with excellent ductility (see Figure 2.3). The plastic deformation mechanism dominant in TWIP steels is twinning, hence the name "twinning induced plasticity" steels. These materials contain a high amount of Mn, which reduces the stacking fault energy of the austenitic alloy and facilitates twin formation. While named TWIP steels, these alloys also utilize the TRIP effect and conventional dislocation plasticity, which allows for the large tensile strength and ductility values observed [24,25]. Although TWIP steels exhibit a high ultimate tensile strength, the yield strength is relatively low, which is rather impractical for the employment in high-performance and safety-relevant applications [22].

After introducing the strength-ductility trade-off and its implications on materials engineering, as well as some strategies to overcome the trade-off, the next section will describe in detail another way of achieving high strength with great ductility in metals: grain refinement and nanostructuring.

2.2 Nanostructured metals and composites

The use of grain refinement as a method to increase the overall mechanical performance is based on the idea that it is the only strengthening method that does not decrease the ductility of metals. The concept of a strength increase by reducing the grain size is famously known as Hall-Petch relation [26,27], and can be easily followed by visualizing GBs as obstacles to dislocations, much like forest dislocations and precipitations in the examples in Section 2.1.

For materials with coarse grain sizes, a grain size reduction often even results in an increase in ductility. This can be explained by a larger number of grains increasing the probability of grains and their slip planes being oriented in a beneficial way for dislocation movement. Additionally, stress can be transferred to activate slip systems in neighboring grains and GBs themselves can contribute to plastic deformation by GB motion or by changing the shapes of grains [28,29].

Therefore, nanocrystalline (nc) metals, containing grains with diameters smaller than 100 nm, were expected to show extraordinary mechanical properties [29]. However, neither strength nor ductility showed the desired continuous improvement with decreasing grain size in experiments. While the strength of all materials can be increased tremendously by refining the microstructure to the nc regime, at a grain size of about 10-30 nm (depending on the material), the strength can not be improved any further and sometimes even decreases again, a phenomenon commonly referred to as "inverse Hall-Petch relationship" (see Figure 2.4) [28,30]. The reason behind

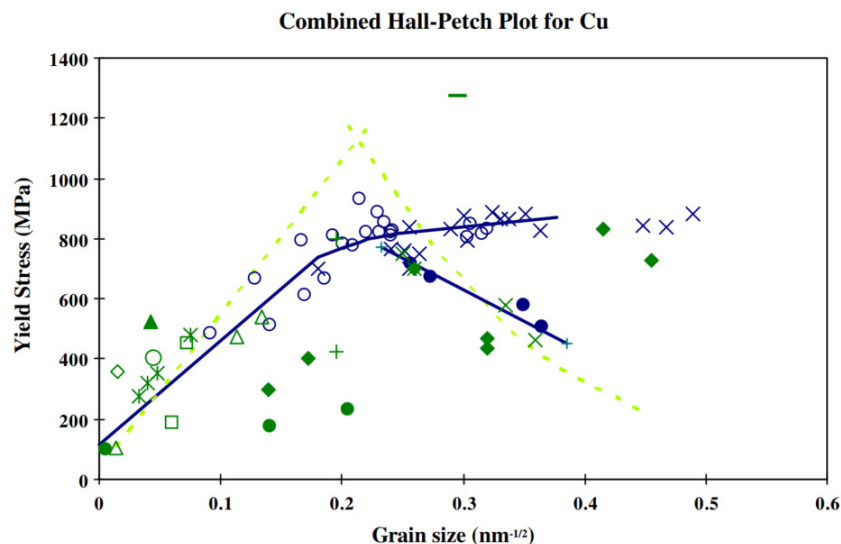


Figure 2.4 Yield strength over grain size for Cu illustrating both the Hall-Petch relationship and the inverse Hall-Petch relationship [28].

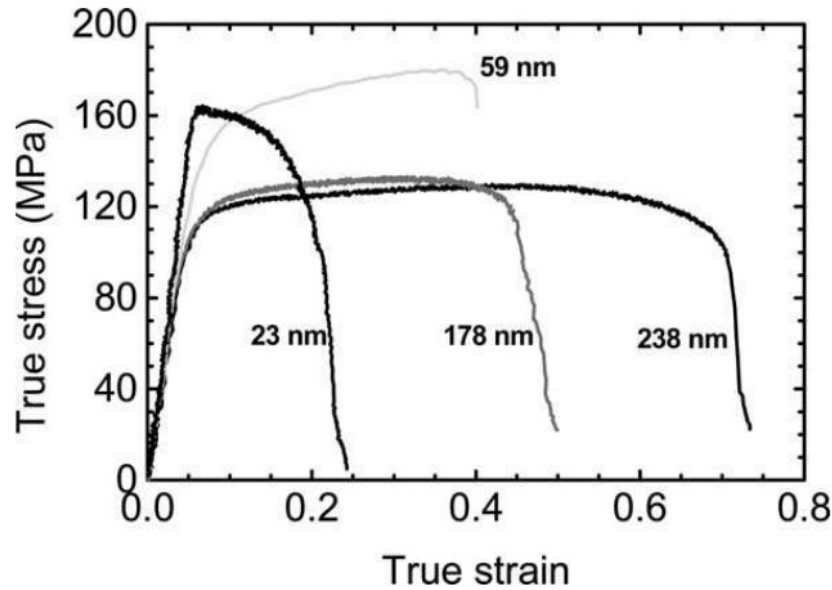


Figure 2.5 Stress-strain curves for nc Zn with different grain sizes [28].

this decrease in strength is to this day still being debated, with the transition to a predominantly GB-controlled plasticity being most likely part of the explanation [28,30].

While the strength of metals can be increased immensely through grain size refinement, their ductility oftentimes deteriorates to atrociously low values when entering the nc regime (see Figure 2.5). This is surprising, as an increase in ductility following grain size reduction was predicted from trends observed in coarse-grained (cg) materials. Koch et al. [7,29] argue that the tensile ductility of metals diminishes upon grain refinement to the nanograined scale because of three reasons: i) artifacts and defects, especially pores, that arise from processing nc materials, ii) the early onset of force instability in tension due to the lack of strain-hardening in nc metals, as described by the Considère criterion [31], and iii) the instability of crack nucleation and propagation, impeding plastic deformation without failure.

The third point indicates that improving the fracture toughness of nc materials can have a positive impact on ductility as well.

Refining the grain size is a common strategy to improve the fracture behavior of conventional (bcc) materials [14,15,32]. However, as with strength and ductility, the fracture toughness also decreases at the very smallest grain sizes. This happens for two reasons: 1) As mentioned earlier, the fracture toughness of metals is closely interlinked with the ability to relieve stress from the crack tip via e.g. plastic deformation through dislocation motion. By reducing the grain size to the nc regime, dislocations

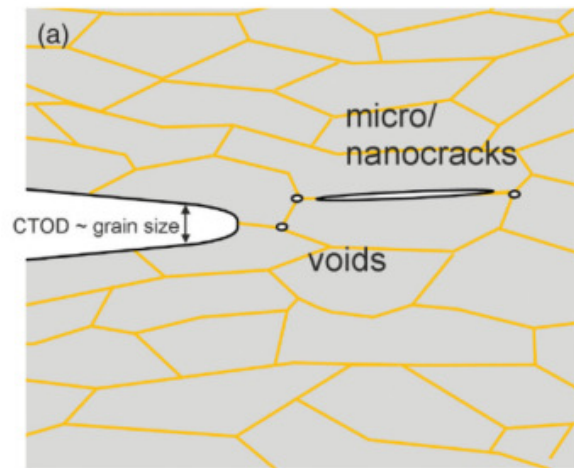


Figure 2.6 Schematic of easy crack propagation along GBs in nanostructured metals [14].

have a harder time nucleating and propagating due to the close spacing of GBs, not allowing stress to dissipate over a large volume from the crack tip and resulting in an unstable and brittle fracture behavior. 2) As introduced in Section 2.1, fine grained materials have a higher tendency to fail via intercrystalline failure. Naturally, for nc metals the probability of cracks propagating along the GBs is extremely high, consequently reducing the fracture toughness (see Figure 2.6) [14].

However, an argument can be made that the product of yield strength and fracture toughness, a measure for the damage tolerance of a material, is still improved remarkably compared to the cg counterparts due to the tremendous strengthening effect of grain refinement [15]. This encourages further research in nc bulk materials as possible candidates for structural "supermaterials".

The majority of research trying to overcome the strength-ductility trade-off in recent years focuses on nanocrystalline and nanostructured metals and alloys, oftentimes in combination with microstructural gradients, nanotwinning or other strategies [4–10]. However, when looking at how the mechanical properties depend on grain size, as summarized in Figure 2.7, a case can be made for settling with a lower strength but higher toughness and ductility as can be found for the smaller grain size regime of the ufg spectrum.

Another possible design of damage tolerant nanostructured materials is the concept of metal-metal composites. Combining a hard and brittle metal with a soft and tough material can lead to extraordinary properties, provided they are immiscible [10,28,33]. Here, the hard metal phase provides the extra strength and hardness, whereas the softer metal allows for easier dislocation plasticity and, hence, ductility. In addition, it was found that the crack driving force can diminish when transitioning from a soft

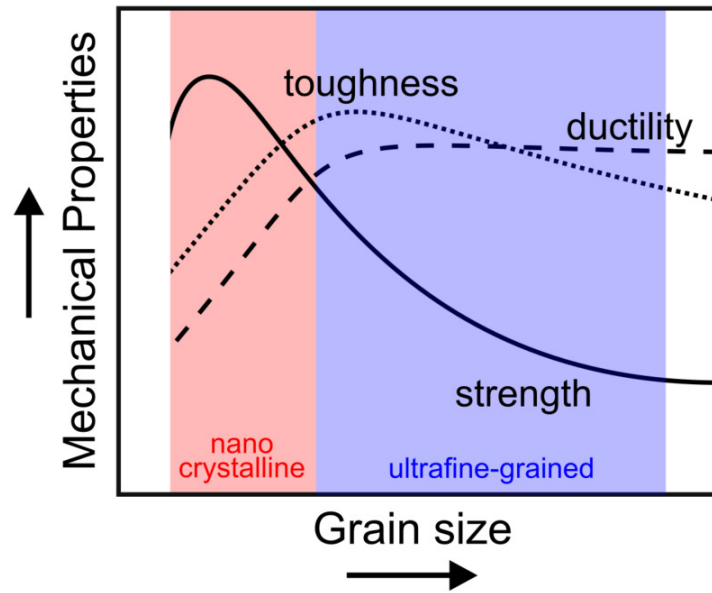


Figure 2.7 Typical dependency of strength, ductility and fracture toughness of metals on grain size in the nc and ufg regimes.

to a hard material phase, leading to crack arrestment and a tremendous increase in fracture toughness. This so-called inhomogeneity effect was identified in deep-sea glass sponges in nature and has since gained great attention in damage tolerant materials design [34,35].

Regarding metal-metal nanocomposites, Cu is a popular choice as soft phase, given its comparably low hardness and elastic modulus as well as high conductivity and immiscibility in harder metals, such as Mo, Nb, or W. Therefore, nanocomposites containing Cu are well researched regarding their mechanical performance, irradiation response and interface stability [36–41].

After establishing the important role that nanostructured metals and composites play in the design of materials that challenge the strength-ductility trade-off, the most common fabrication methods for these materials are presented hereinafter.

Fabrication of nanostructured metals

While conventional fabrication methods, such as rolling, drawing or forging, are commonly used to produce metals with a refined microstructure, this refinement is usually limited to comparatively large grain sizes. Additionally, GBs produced by such cold- or hot-working methods generally consist of dislocations rearranged as low-angle GBs and are not very stable from a mechanical and thermodynamical

standpoint [42–44]. In order to reach grain sizes in the submicrometer range, specialized fabrication processes are required. Here, one can distinguish between bottom-up and top-down methods.

For bottom-up methods, usually deposition-based processes are used, such as chemical or physical vapor deposition. While these fabrication methods can achieve the smallest grain sizes, even below 10 nm, the sample sizes are also limited to films of some 100 nm to tens of μm thickness, which is why they are most important for coatings in e.g. the tool-making industry [29]. Additionally, the common absence of dislocations within nc materials processed by bottom-up methods usually leads to inferior ductility and fracture toughness [42]. Other non deposition-based bottom-up methods rely on the consolidation of nanopowders and usually struggle with porosity issues [28,29].

In contrast, top-down methods are able to produce bulk metals by starting from a conventional material and refining the grain size using special fabrication processes. After their introduction in the 1980s, the methods of severe plastic deformation (SPD) have gained a lot of interest in research and industry, especially since the early 2000s [43–46], as a growing number of publications attests [47–49]. As the name suggests, SPD methods utilize severe plastic deformation, often in combination with confinement and (quasi-)hydrostatic compression to refine the microstructure. The confinement and hydrostatic compression prohibits the sample to change its shape and therefore allows the material to be deformed to extraordinarily high strains without failing [46]. Initially, the grain refinement in SPD-processed materials resembles the mechanisms present in conventional metal-processing methods, such as rolling or forging. Dislocations generated by the plastic deformation of the material rearrange themselves to low-angle GBs and subdivide grains into cell blocks [50]. With the large deformation strains only achievable by SPD processes, the size of these cell blocks decreases and their misorientation increases with continuous deformation, leading to fragmentation of the microstructure and predominantly (about 80%) high-angle GBs [42,51,52].

The most common SPD methods are presented in Figure 2.8.

During equal channel angular pressing (ECAP; Figure 2.8a), a material billet is pushed with a plunger through a die that forms two channels intersecting at a chosen angle. Due to the confinement of the die, the billet cannot change its cross section area, which allows multiple passes through the ECAP device and, hence, an increasing amount of plastic strain applied to the material [43,49].

The big advantage of the method of accumulative roll-bonding (ARB; Figure 2.8b) is that no specialized processing facilities are required. By using the conventional rolling facilities that are readily available in the metal processing industry, metal sheets are rolled to about half their initial thickness. Afterwards, the metal sheets are cut in

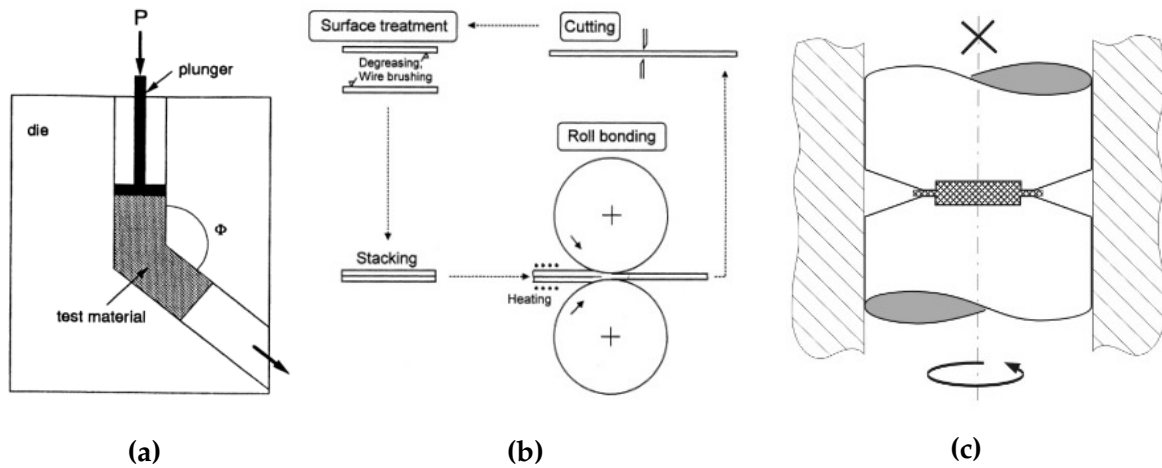


Figure 2.8 Most common SPD methods: (a) ECAP process [43], (b) ARB process [44] and (c) HPT process [52].

half and the resulting two parts are stacked onto each other and rolled again. This procedure is repeated until the material exhibits a nanolayered microstructure [44]. ARB is especially well suited to produce nanolayered metal-metal composites with stable interfaces [37,53].

Particularly the high pressure torsion (HPT; Figure 2.8c) process has been studied extensively [42, 43, 45–48, 51, 52], as it is the only continuous option of the most noteworthy SPD methods [51, 54, 55]. During HPT, a disk-shaped specimen is placed between two anvils made from a high-strength material and compressed under several GPa of pressure. Additionally, one anvil is rotated while the other anvil is held still, applying a torsional plastic deformation to the material disk. Due to this torsional nature of the deformation, a deformation gradient, and consequently a microstructural and property gradient, is present from the center of the sample disk to the edge. As the deformation strain applied to the material is virtually unlimited, one could assume that HPT processed materials can be refined to the smallest possible grain sizes. In reality, grain size fragmentation saturates after deformation to a material-specific saturation strain, where a dynamic equilibrium of dislocation generation and annihilation at GBs sets in and therefore no more subdivision of grains is possible [51].

As HPT can achieve the largest deformation strains out of all SPD methods and due to its straightforward use, it was the method of choice in this thesis.

2.3 Grain boundary segregation engineering

The previous section stresses the importance of GBs in metals with very fine grains and identified them as the major limiting factor for improving fracture and ductility properties in ufg and nc metals. Therefore, most strategies to enhance the mechanical performance of this class of materials revolve around strengthening or restructuring GBs. A popular approach is to control the GB segregation in metallic alloys, a concept known as grain boundary segregation engineering (GBSE) [56].

Although the term has been coined only recently, early examples of GBSE in metals can be traced back to the 16th century, when Georgius Agricola suggested using "bitumen" instead of wood charcoal to refine iron in order to avoid "hot shortness" [57–59]. In metallurgical terms: By using a cleaner reduction agent in the processing of iron and steel, the segregation of embrittling elements like S and P at GBs and, consequently, brittle intergranular failure of the material can be circumvented. Naturally, in medieval times (but also in the larger part of the modern era) such enhancements of materials were found mostly by chance or by trial and error. Only recently the uprising of high-resolution materials characterization techniques, such as high-resolution transmission electron microscopy (TEM) and atom probe tomography (APT), paired with the powerful tool of computer simulations and complemented by novel machine learning methods make a targeted search, prediction and detection of segregation of GB strengthening or weakening elements in materials feasible [16,56,58,60–68].

In general, GBSE can influence the mechanical properties of materials in a variety of ways. While in the example of Agricola the GBs of iron were strengthened indirectly by avoiding embrittling impurity elements, the most direct strategy is to enrich the GBs of a metal with atoms that are known to increase the GB cohesion, i.e. the strength of the GB. A famous application is the addition of B to steels [65], Ni superalloys [66,69] and novel light-weight TiAl alloys [70,71], increasing the ductility and overall mechanical properties of these engineering alloys. As mentioned above, the selective search for GB cohesion enhancing elements in a given host material has been supported by computational materials science in the last decade. Aside from thermodynamical modeling approaches [60,72], especially *ab-initio* simulations, such as density functional theory (DFT), have been used extensively to calculate GB cohesion values of metals doped with various elements [61–63,65–68]. Figure 2.9 shows the results of such a DFT study for impurity and solute elements in a W host material [67,68]. The strength of embrittlement (SE) plotted in this graph is essentially the energy difference between two systems, were (i) the doping element is located at the GB and (ii) the doping element is located at an open surface of the material. It therefore indicates if an element promotes cracking of the GB (element wants to sit on an open surface) or if it suppresses cracking (element prefers to sit at the GB) and

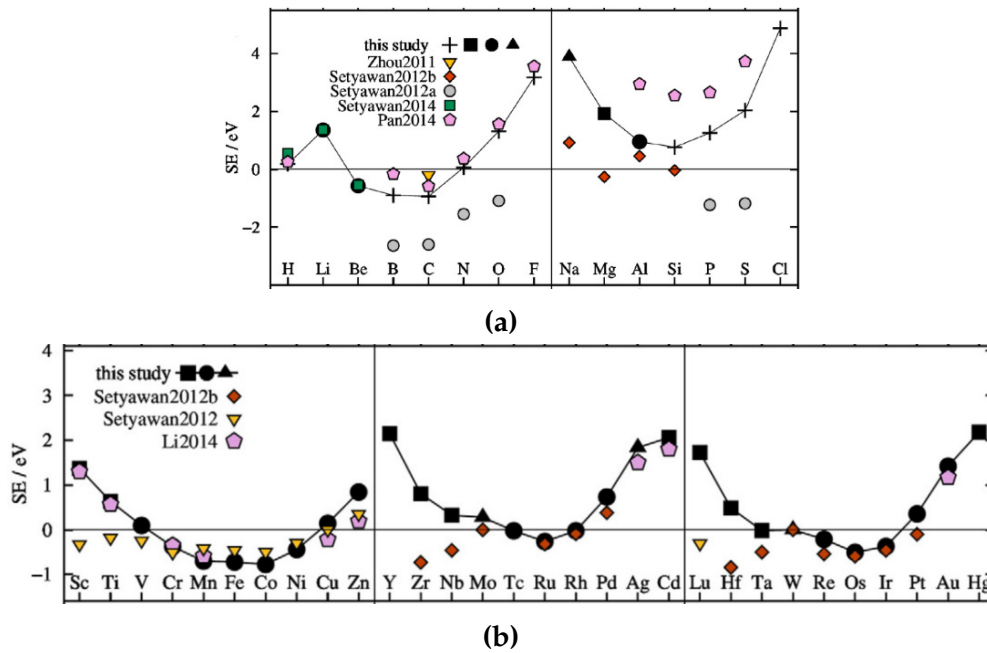


Figure 2.9 DFT calculations showing the effect of various (a) impurity [67] and (b) solute doping elements [68] on strength of embrittlement of GBs in W.

has the physical sense of the change in GB cohesion. If a doping element shows a negative SE in a given host material it strengthens GB cohesion, whereas a positive value indicates an embrittling effect of the dopant on the GB.

Therefore, in theory, every element exhibiting negative SE values in Figure 2.9 should strengthen GBs and improve mechanical properties in W. However, one has to take into account that such calculations are usually made for a representative model GB (in this example a $\Sigma 3[110](-111)$ boundary) and might deviate for GBs that show less (or more) symmetry. Additionally, it is not given that a GB cohesion enhancing element ends up located at GBs in a material. The segregation tendency of each element has to be calculated as well using DFT or thermodynamical models [60,67,68]. Moreover, the phase diagrams of the different element combinations should be examined. For example, Fe and Co would increase the GB cohesion of W, however, rather than going into solution in W, they form very brittle intermetallic μ -phases and can therefore not be used as doping elements to improve the mechanical properties. All these points have to be considered when trying to experimentally validating such DFT predictions.

While strengthening the GB cohesion directly through the segregation of doping elements is straightforward and has proven to be very effective [56,58,60,61], other GBSE techniques have been developed and show promising potential to improve

mechanical properties of nanostructured metals as well. Such other examples involve segregation of elements that induce local stress-induced phase transformations at GBs (similar to the TRIP effect described in Section 2.1) [56,73,74] or segregation of elements that promote formation of amorphous complexions and films along GBs with unique micro-mechanical properties [75–77].

2.4 W-based materials and their potential application in nuclear fusion technology

The model materials investigated within this thesis are W and W-based composites. This section aims to introduce the material systems and the reasons as to why they were selected for this work.

Tungsten is a refractory metal and has the highest melting point among all metals of 3422°C [78]. This high melting point originates in an extraordinarily high bonding strength between the W atoms in the bcc crystal lattice. This bond strength also gives rise to an extremely high mechanical strength and hardness of W and, consequently, poor ductility and fracture toughness, as dislocation propagation is limited. Therefore, the main failure mode for cg W is transcrystalline cleavage failure, yet frequently intercrystalline failure is observed even for conventional grain sizes [17,18]. Naturally, this preference for intercrystalline failure increases substantially when the grain size is reduced. A common phenomenon observed in bcc metals is the existence of a ductile-brittle transition temperature (DBTT), below which a materials toughness is severely reduced. While for common bcc engineering alloys, such as steel, the DBTT lies below the freezing point, for W and W alloys it lies well above RT, with reported values ranging from 300°C to over 1000°C [79–81], depending on chemical composition, grain size and loading conditions.

The research interest in W has inflated in recent years, as the material has several beneficial properties for the employment in nuclear fusion reactors [81–86].

There are two possible application fields for W in first generation (tokamak) fusion reactors, such as e.g. DEMO (DEMONstration fusion power plant) [87]: (i) As a protection layer of the first wall material (a ferritic-martensitic 9% Cr steel) that encloses the magnetically confined fusion plasma (Figure 2.10), where W has mainly shielding purposes from neutron irradiation damage and thermal load [81]. (ii) A more challenging application of W in a fusion reactor is as structural material in the divertor part of the reactor. In order to keep the plasma clean and stable to ensure a continuous nuclear fusion process, impurities such as He ions (a by-product of

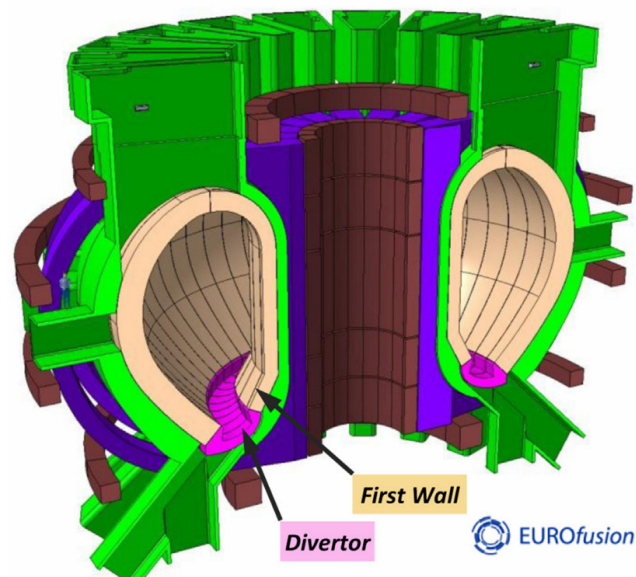


Figure 2.10 Schematic design of DEMO nuclear fusion reactor showing the plasma-facing first wall and divertor components [88].

the fusion reaction) and other particles have to be removed from the plasma. To do so, the particles are redirected using magnetic fields and accelerated towards (helium-)cooled target plates in the bottom part of the reactor (see Figure 2.10). Here the particles collide with these so-called divertor plates and lose their kinetic energy, so they can be easily removed using vacuum pumps. Naturally, this continuous bombardment with impurity particles, in addition to the regular high temperatures (about 800°C - 1700°C) and extreme neutron irradiation experienced by the whole first wall, make the divertor suffer from the highest irradiation damage and thermal loads of all nuclear fusion reactor components [81–83]. While the thermal load on the divertor in regular operation is already extremely high (about 10 - 20 MW/m²), during certain plasma disruptions, such as e.g. edge localized modes, it can escalate to more than 1 GW/m² [89]. Such instabilities occur rather frequently in a fusion plasma and have to be considered when designing the divertor material.

In addition to extreme neutron irradiation and thermal load, a major concern for plasma-facing components is the implantation of He into the material surface [20,21, 83]. As a noble gas, He is insoluble in metals and forms bubbles within the material. This process is largely supported by the accompanying formation of radiation-induced vacancies. This bubble formation and growth can lead to serious destruction of the surface integrity by formation of blisters and fuzz [90–92], but also generally results in swelling of the material and degradation of mechanical properties, as the material is slowly transforming into a metal-gas composite or foam [93,94]. As this deterioration of mechanical properties and thermal conductivity can pose a serious long-term

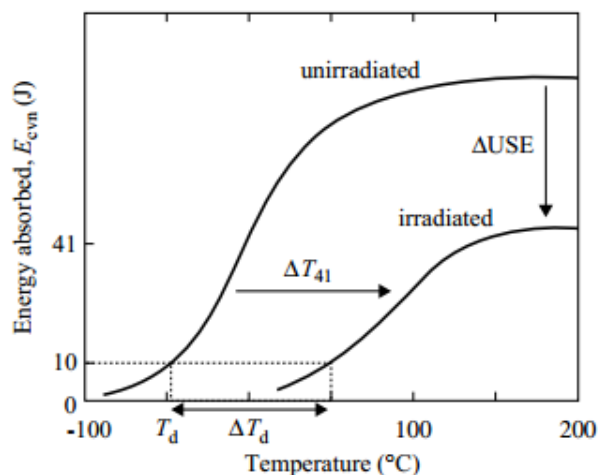


Figure 2.11 Increase of ductile-brittle transition temperature (DBTT) and decrease of upper shelf energy of steel upon neutron irradiation [96].

problem, strategies have to be applied to restrict He bubble formation and growth. A promising pathway is grain refinement, as studies have shown that, even though a reduced bubble formation threshold has been observed, the larger amount and smaller spacing of defect sinks, such as GBs and interfaces, lead to restricted bubble growth within the material [94].

Due to these harsh operating conditions the already mentioned high melting point and mechanical strength, in conjunction with its great thermal conductivity and excellent erosion resistance to ion bombardment make W a promising candidate material for the divertor. Additionally, the tendency of W to transmutation and activation upon neutron irradiation is low, giving it the edge over materials with similar properties, such as Mo or Nb, which activate rather easily [82,95].

The main drawback and major concern for employment of W in fusion reactors is its inherent brittleness at RT, as described above. Cracks and other damage from the harsh plasma-facing environment that occur during operating conditions (generally above the DBTT) can become critical upon cooling down of the reactor (below the DBTT) and lead to failure of structural parts, which is a serious safety risk and unacceptable [83,89]. Hence, the RT ductility and toughness have to be improved, either by decreasing the DBTT or elevating the toughness level in the brittle temperature range. As neutron irradiation is known to generally increase the DBTT of metals (see Figure 2.11) [80,96], the latter option seems to be more feasible.

Due to the promising application of W in fusion reactors, great efforts were undertaken in recent years to identify ways to improve the ductility and toughness [83,85,86]. It is well known that Re alters the core of screw dislocations in W, thereby reducing

2.4. W-based materials and their potential application in nuclear fusion technology

the Peierls stress and activating more slip planes, enhancing the overall mobility of dislocations and increasing ductility [97,98]. Yet Re is rather expensive and not available in large quantities, making a large scale fabrication impractical. An effort has been made to reproduce the effect of Re in W using other alloying elements that show solid solubility in W, such as Ta, V and Ti [82,83,89,99]. However, the addition of these elements resulted either in a similar fracture performance as pure W or even in an increased DBTT and decreased ductility. Therefore, a microstructural design approach seems most promising to enhance ductility and toughness of W. However, the improvement of mechanical properties by grain refinement alone is limited by the low-energy intergranular fracture mode.

Therefore, as introduced in Sections 2.2 and 2.3, this work aims to improve the mechanical properties of W by grain refinement to the ufg regime, which shows a favorable combination of strength, ductility and toughness (Figure 2.7), in conjunction with GBSE to increase the GB cohesion of W and, consequently, further improve the mechanical properties.

Considering the extreme thermal load and temperature fluctuations present in the fusion reactor, fast and efficient heat transport from the plasma-facing components to the cooling units has to be guaranteed.

A potential candidate material for such required high-strength thermal conductors and heat-sink materials are W-Cu composites [100–103]. W and Cu are immiscible, which means they do not form a solid solution [104]. While the Cu phase shows excellent thermal conductivity and ductility, W serves as a strengthening phase with still sufficiently good conductivity. To provide extra strength and tolerance against radiation damage, nanostructuring of the composite would be beneficial.

Moreover, a graded W-Cu interlayer could serve as transition between W divertor material and e.g. CuCrZr pipes, which are currently being proposed for use in a water-based cooling system for fusion reactors [100]. Such an interlayer would facilitate the complicated and difficult joining process of W and Cu and avoid thermal stresses arising from the mismatch in thermal expansion coefficient of the two materials [100–103].

Admittedly, the concept of employment of W-Cu material in a nuclear fusion environment is not as well developed as the usage of W, however, the requirement is given. As mentioned in Section 2.2, a nanostructured composite made out of a hard and a ductile phase is also a promising strategy to overcome the strength-ductility trade-off and create a material with a favorable combination of mechanical properties. Combined with a GBSE approach, the increased GB cohesion might lead to even further enhanced ductility and fracture toughness. Due to this exciting prospect of creating a material with high overall mechanical properties and the potential applica-

tion as high-strength thermal conductors, this work will investigate the fabrication, GB doping and mechanical properties of nanocrystalline W-Cu composites as well.

Finally, due to the attractive application potential in fusion reactors, the fabricated ufg W and nc W-Cu materials will also be characterized regarding their response to helium implantation and potential radiation resistance within the framework of this thesis.

3 Summary of results

This chapter provides an overview of the most important outcomes of this work. For a more detailed exhibition of the performed investigations and their results, the interested reader is referred to Publications A [105], B [106], C [107], D [108] and E [109] in the Appendix.

First the fabrication routes for ufg W and nc W-Cu from powders using HPT are discussed. Subsequently, the effect of the different doping elements on microstructure, deformation and fracture properties of ufg W and nc W-Cu are outlined. Finally, the performance of the investigated materials in extreme environments, such as a nuclear fusion reactor, is examined by presenting and discussing their response to helium irradiation.

3.1 Fabrication of ultrafine-grained W and W-Cu nanocomposites

To allow for an easy and straightforward in-lab production of the doped ufg W and nc W-Cu composites, a powder fabrication route for both materials was developed within this thesis. Starting from material powders yields several advantages, but also multiple challenges:

On the one hand, by using powders a precise control of chemical composition of produced samples is possible, allowing for a meticulous regulation of doping element content. Additionally, the in-house fabrication of material samples enables a quick production of certain material combinations without having to rely on the availability and delivery of commercial suppliers.

On the other hand, metal powders have to be stored and handled with caution, as an oxidation or contamination of the powders will lead to poor compactability and performance of the produced samples. Moreover, successfully compacting powders of extremely hard metals, such as W, is a challenging task, as conventional compacting pressures are not sufficient for interparticular bonding of the powder particles.

These and other challenging points for fabrication of ufg W are identified and discussed in Publication A [105] and summarized within this section.

Fabrication of ufg W from powders

In Section 2.2, the fabrication methods of SPD have been introduced as useful tools in producing bulk nanostructured metals. The high achievable deformation strains and straightforward processing of HPT are especially beneficial to reduce the grain size of metal samples [43,51,52]. Therefore, HPT was the method of choice in this work to produce ufg W.

As identified in Publication A, the four main challenges for fabricating ufg W from powders using HPT are:

- Oxidation and contamination of powders
- Compacting W powder
- Sintering W compacts
- Severe plastic deformation of W

In order to create a feasible and reproducible fabrication route for ufg W, these four challenges haven been tackled and overcome individually using the following strategies:

Oxidation is a major problem for all metal powders, as the small particle size (commonly below 100 μm) results in a large surface area and high risk of oxidation if the powders are handled in air and under humid conditions. Oxide layers formed on the surface of the powder particles will remain inside processed bulk materials and lead to unwanted changes in microstructure and mechanical properties. Additionally, such oxide layers can hinder the successful compacting of powder particles. In the concrete case of W, the formation of WO_3 already happens at RT and gets even more critical at temperatures above 750°C , when WO_3 becomes volatile and consumes the material [78,110].

Therefore, to reduce any risk of oxidation and contamination of the material powders, all powders have been stored and handled within Ar atmosphere in a glovebox. To transport the powder mixture from the glovebox to the compression device (in this work a HPT tool [52]) a sealed mini-chamber (see Figure 3.1) was utilized, which is

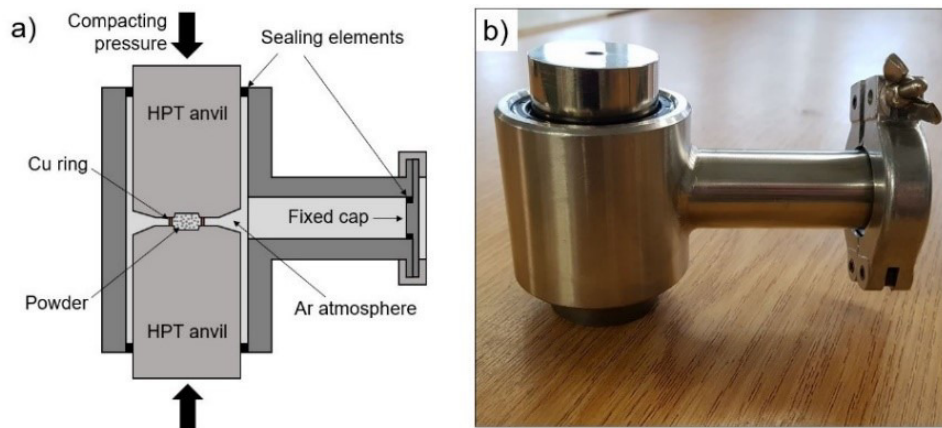


Figure 3.1 (a) Schematic drawing and (b) photograph of sealed mini-chamber for transporting powder in local argon atmosphere from the glovebox to the HPT device [105].

assembled within the glovebox and allows the powder to be transported within local argon atmosphere.

As is often the case with high-performance materials, their extraordinary mechanical properties that prove advantageous for their applications are a big drawback when it comes to fabrication or shaping of the material. Tungsten is no exception to this, as Figure 3.2a shows that the tungsten powder does not compact well, even after compression with a nominal pressure of 12 GPa. The high intrinsic strength of tungsten results in no interparticular connection between the powder particles, which in turn leads to clearly visible micropores and microcracks after HPT processing (shown in Figure 3.2b). Therefore an intermediate annealing or sintering step has to be conducted to allow for better bonding between the powder particles after

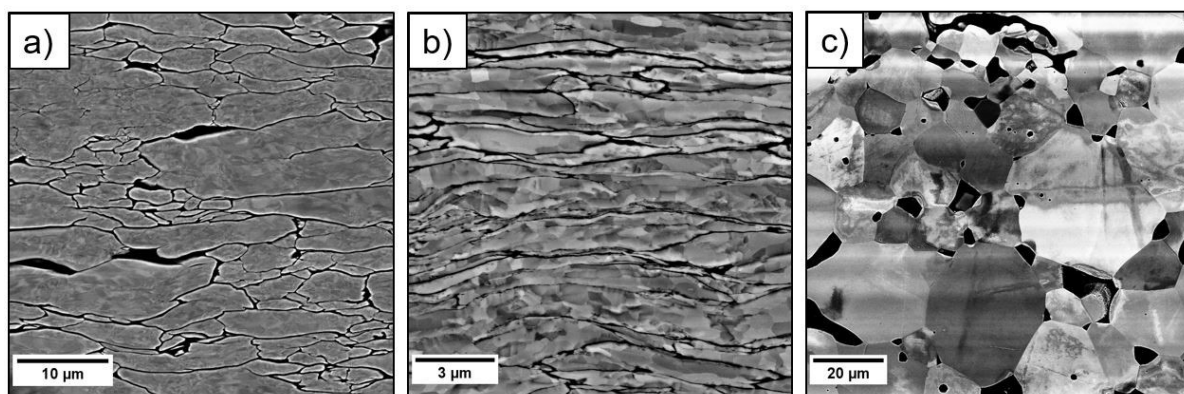


Figure 3.2 Microstructural SEM images of (a) compacted W powder, (b) compacted and deformed W and (c) compacted and sintered W [105].

compression, and consequently a better end product without pores or cracks. Sintering of tungsten is also not a straightforward task, due to the incredibly high melting point of 3422°C [78]. Additionally, the aforementioned oxidation behavior makes it impossible to use a conventional furnace for the heat treatment. Therefore in this work a heat treatment at 1600°C is conducted for 7 hours in a vacuum furnace. As is apparent in Figure 3.2c, significant improvements to the interparticular bonding are made through this sintering step. The occurring grain growth and the residual porosity do not pose a problem, as the subsequent HPT step will close the pores and refine the grains.

When it comes to deforming tungsten using SPD methods, such as HPT, the high intrinsic strength and high melting point provide again fundamental challenges. In general, bcc metals deform easier at higher temperatures, but one also has to take into account the deforming tool. For HPT, the anvils have to be somewhat harder than the material in order to successfully deform it [52]. The tool steel used for the anvils (Böhler S390) can maintain its hardness until approximately 400°C, while tungsten gets softer continuously with increasing temperature. As a consequence, only a small temperature window exists where the anvil material is harder than the tungsten compact and where tungsten can be deformed using HPT. Moreover, since grain refinement occurs through the torsional deformation, the hardness of the material increases during the process until it reaches the hardness of the anvil material. This is the reason why in this work a maximum rotation of only 1-1.5 turns is achievable. This amount of rotations still results in a deformation strain of 1800% and a grain size of about 150 nm.

In Publication A, a fabrication route, taking into account all of the challenges discussed above, was developed and ufg tungsten was fabricated from powders and from bulk, using an HPT deformation temperature of 300°C and 400°C. All fabricated ufg W samples were compared regarding microstructure, hardness and strain-rate sensitive properties. It was found that all investigated specimens showed similar grain sizes of 110 - 160 nm (see scanning electron microscope (SEM) images in Figure 3.3)

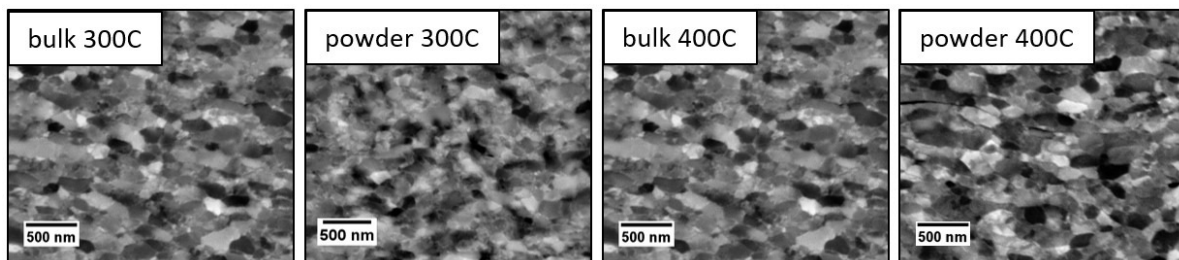


Figure 3.3 SEM micrographs of bulk and powder processed samples after HPT deformation at different temperatures [105].

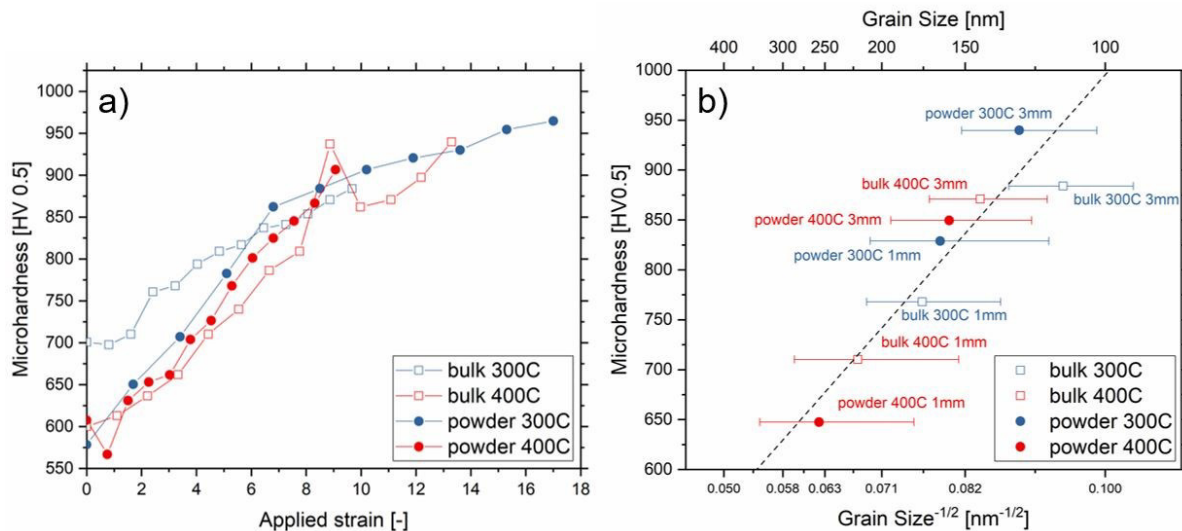


Figure 3.4 (a) Microhardness evolution with applied HPT strain and (b) Hall-Petch plot of processed ufg W samples [105].

and microhardness of 850 - 940 HV0.5 (Figure 3.4a). Moreover, the microstructure-property relationship does not depend on powder or bulk precursor or deformation temperature, as is apparent from the Hall-Petch plot in Figure 3.4b. From dynamic nanoindentation measurements the strain-rate sensitivity (SRS) of all samples were measured to 0.015 - 0.017 and the activation volumes were calculated to 6 - 8 b^3 . Therefore it can be concluded that the established fabrication route for ufg W from powder results in no major differences in microstructure or mechanical properties when compared to ufg W processed from a bulk precursor. With the additional benefit of being able to control the content of possible doping elements, the presented fabrication route provides the basis for processing doped and undoped ufg W samples in Publications B, C and E, which are summarized in Sections 3.2 and 3.4 within this thesis.

Fabrication of W-Cu nanocomposites from powders

Contrary to the rather tedious fabrication route of ufg W, the processing of nc W-Cu composites demands less time and fabrication steps. By adding the rather soft metal copper, most of the aforementioned challenges do not pose a problem anymore. For example, the soft Cu phase allows for easier and more thorough powder compacting, which makes the previously employed intermediate sintering step redundant. Additionally, Cu helps fragmenting big pieces of W during HPT deformation, as was previously observed by Sabirov et al. [111,112], which is why

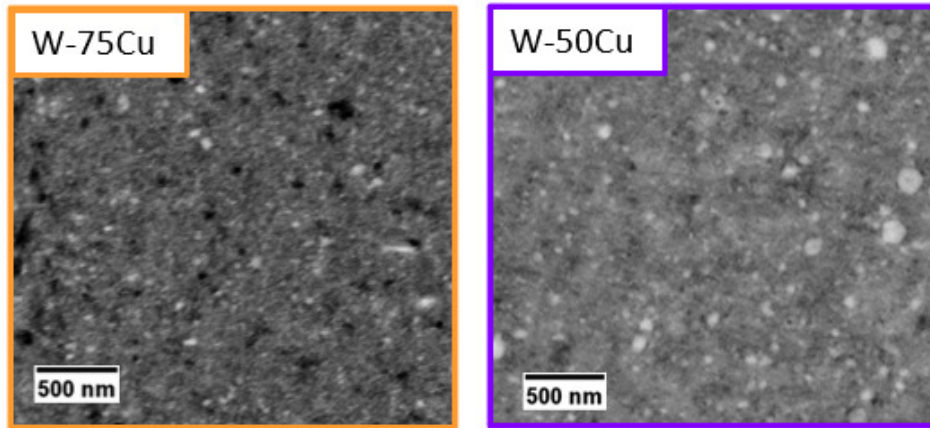


Figure 3.5 SEM micrographs of a W-75at.%Cu composite deformed via HPT to 100 rotations at RT and a W-50at.%Cu composite deformed to 30 turns at 200°C and 100 turns at RT [108,113].

no additional heating during the HPT process is necessary for a homogeneous deformation and grain refinement. Furthermore, because of the overall lower hardness of the material, the sample can not get as hard as the anvils, allowing a deformation to much higher strains and therefore smaller grain sizes [51].

As the work of Doppermann [113] shows, the most satisfying microstructure in terms of refinement and homogeneity for a composite containing 75 at.% Cu and 25 at.% W is achieved by applying HPT deformation for 100 rotations at RT under a pressure of 9 GPa (see Figure 3.5). These W-75Cu nanocomposites show a grain size of around 10-35 nm and are the main composites investigated in Publications D and E as well as in Sections 3.3 and 3.4.

Additionally a composite of 50 at.% W and 50 at.% Cu is also investigated in Publication D. The increased amount of W makes the fabrication of these nanocomposites via HPT more challenging [113]. When processed at RT, W-rich deformation bands are present within the material, indicating a less successful fragmentation of the larger amount of W by the lesser amount of Cu. On the other hand, when the powder compacts are deformed at higher temperatures (200°C), W agglomerates into energetically more favorable large and round particles due to the introduced thermal energy.

A solution on how to achieve a better fragmentation of the higher fraction of W particles and an overall more homogeneous microstructure is also presented in [113]. The W-Cu compact is first deformed at 200°C for 30 rotations to let the tungsten agglomerate and obtain its round form. Subsequently, the material is deformed once more at RT for 100 rotations. This leads to a homogeneous and refined microstructure, as apparent in Figure 3.5, as it is assumed that the rounder W particles are easier to fragment by the Cu phase during HPT deformation.

Thus, the challenges arising from fabricating ufg W and nc W-Cu from powders using HPT are addressed and a suited fabrication route established. The following sections will focus on how the mechanical properties of these fabricated ufg W and W-Cu nanocomposites can be affected by applying GBSE and will summarize the most important findings from this main part of the thesis.

3.2 Effects of doping elements on mechanical properties of ultrafine-grained W

In the case of ufg W a dire need of improving ductility and toughness arises from the brittle nature of W and its preferred intercrystalline failure. While the grain refinement to the ufg regime already improves the fracture toughness tremendously, doping with GB cohesion enhancing elements is expected to push the limits of mechanical performance even further, by strengthening GBs and, consequently, restraining intercrystalline failure.

In Publication B [106], potential doping elements are identified using DFT calculations by Scheiber et al. [67, 68] (see Figure 2.9). Disregarding elements that are toxic, not affordable for commercial use or elements that would form brittle intermetallic phases in W, the interstitial elements C and B were selected alongside the substitutional elements Hf and Re. In the following, the effects of these elements on the microstructural and mechanical properties are summarized.

Effect on microstructure and hardness

Regarding grain size, no noticeable differences were observed, as Figure 3.6 shows that all doped and undoped materials show similar microstructures with grain sizes ranging between 110 - 160 nm. W and W-B samples that were annealed at 500°C for 5h (marked "ann.") also showed no signs of detectable grain growth. Typically, impurities, such as doping elements, result in a smaller saturation grain size of HPT-processed materials compared to their pure counterparts [51, 114], confirming that deformation saturation has not been reached.

APT measurements made from lift-outs of the W, W-B and W-B ann. sample revealed that only a small amount of B is located near or at the GBs in the W-B sample, whereas the W-B ann. sample shows a noticeable GB segregation of B. All investigated APT tips show traces of Ga (from focused ion beam (FIB) processing) and O at and near the GBs.

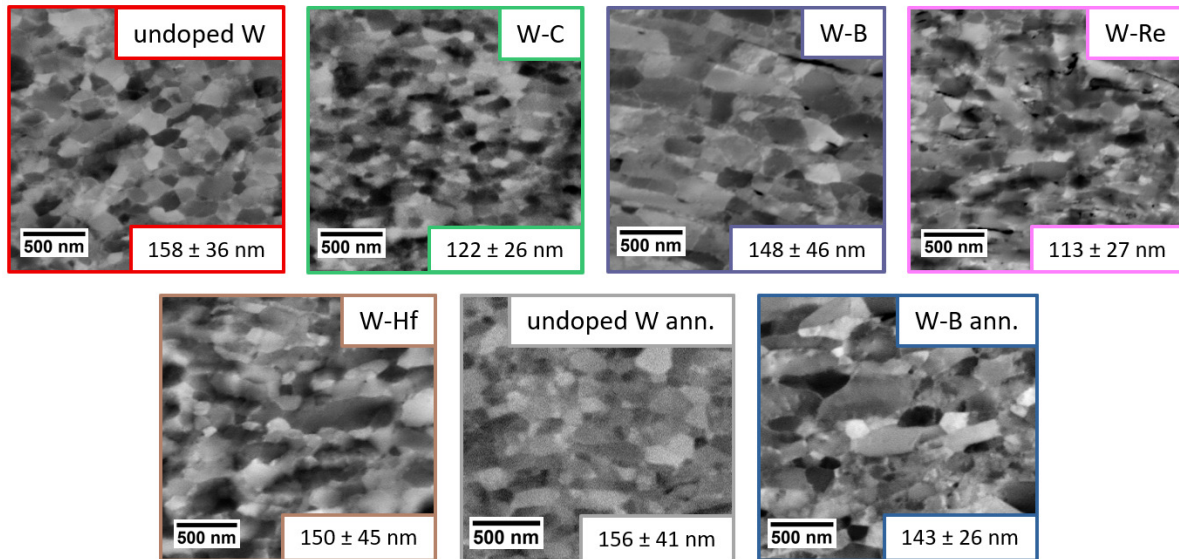


Figure 3.6 SEM micrographs and grain sizes of all investigated ufg W materials [106].

Microhardness measurements performed along the diameter of all fabricated ufg W sample disks are visible in Figure 3.7a and show no significant differences in hardness between the differently doped variants. This indicates that neither the doping elements nor the heat treatment have a pronounced influence on the hardness of the material.

Dynamic nanoindentation strain-rate jump tests utilizing the continuous stiffness measurement (CSM) method allow for measurement of SRS and activation volume of plastic deformation [115, 116]. As apparent from the results in Figure 3.7b and c, no influence of the different doping elements are observed, with the exception of Re which reduces the SRS and increases the activation volume of ufg W. This is in good agreement with literature, as Re is known to alter the core of screw dislocations in W and promote dislocation plasticity as a consequence [98]. Altogether, the values of about 0.015 for SRS and 7-9 b^3 as activation volume are commonly observed for bcc metals and attributed to the kink-pair mechanism [117–119].

Effect on strength and ductility

After unveiling that the doping elements have no detectable influence on microstructure and hardness of ufg W, the effects on the mechanical performance under tensile loading conditions were investigated next in Publication B. As this loading mode represents the most crucial mode for testing W and ufg materials in general, a possible beneficial influence of the doping elements on GB cohesion is expected to be

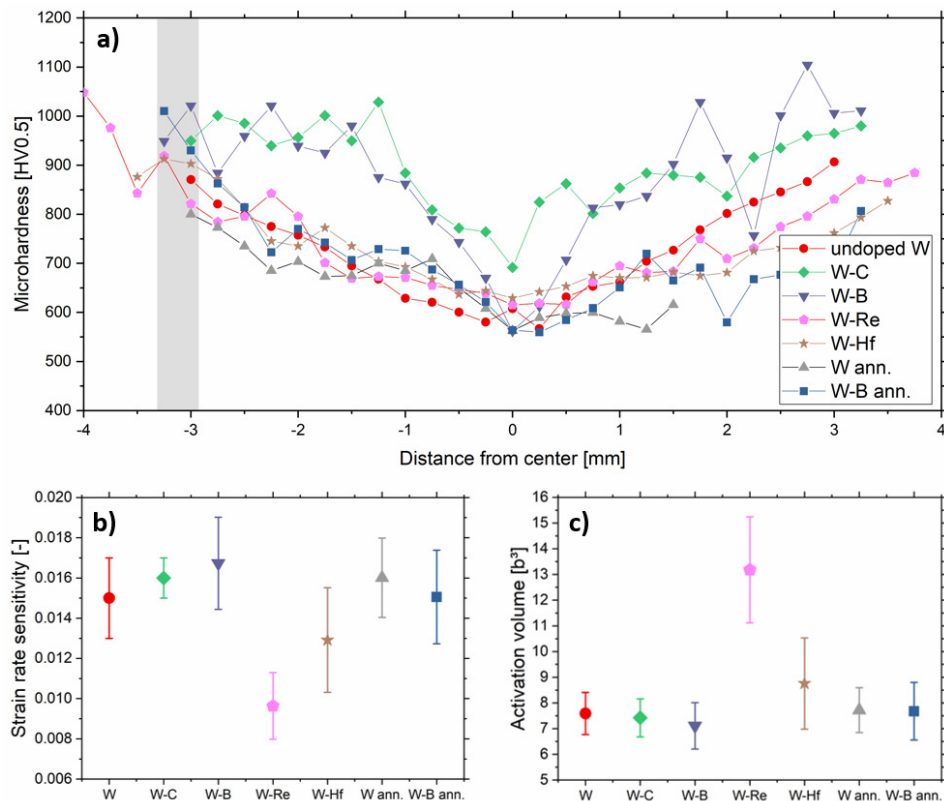


Figure 3.7 Indentation results of all investigated W samples [106]. a) Microhardness across the diameter of the HPT disks. The grey shaded area marks the region on the samples, where all further experiments are performed. b) SRS and c) activation volume results from nanoindentation strain-rate jump tests.

perceptible through these experiments.

Due to the torsional nature of the HPT deformation and the fact that W is not deformable until saturation, a clear microstructural and therefore property gradient is present along the radius of every fabricated HPT sample disk, as is apparent from the microhardness measurements in Figure 3.7a. As a consequence, the desired ufg microstructure and mechanical properties are only found in a small region at the edge of the disk. Due to this limited amount of ufg W material, conventional mechanical testing methods have to be disregarded and small-scale testing is utilized instead. As microtensile tests are demanding in sample preparation and not well suited for testing materials as hard and stiff as ufg W [120], a partial tensile loading can be mimicked through microcantilever bending tests.

For this, cantilevers of sizes $3 \times 3 \times 10 \mu\text{m}$ are fabricated from a pre-ground wedge of the sample using a FIB-SEM. They are tested in-situ inside an SEM using a nanoindentation device equipped with a wedge-shaped tip. From the recorded force-displacement data the (tensile) bending stress and bending strain at the outermost

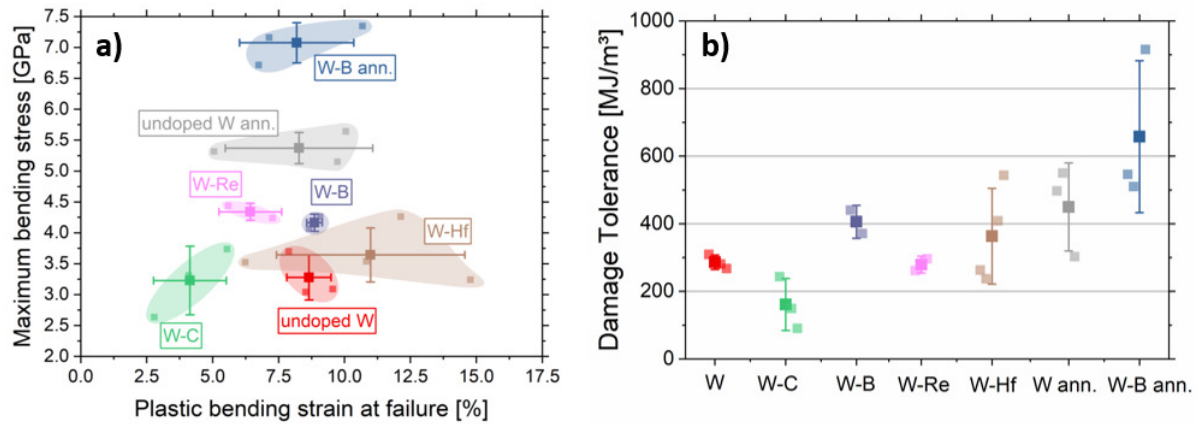


Figure 3.8 a) Maximum bending stress over plastic bending strain at failure representing a strength-ductility map of all fabricated materials. Each small square represents a successful microcantilever bending test, the large squares represent the average values for each respective material. b) Damage tolerance (integrated area below the stress-strain curves until failure) for all fabricated samples [106].

fiber of the cantilever can be calculated. As a measure of strength this work compares the level of the maximum bending stress on each material, while the plastic strain at the failure point (determined from the in-situ images and stress-strain curves) was deemed to represent the ductility of the cantilevers.

A map comparing the strength and ductility as defined above for each fabricated ufg W variant can be seen in Figure 3.8a. From this it is evident that, with the exception of C, all doping elements improve the already extraordinarily high mechanical strength of ufg W. However, only B and Hf seem to also maintain or even increase the ductility, respectively. Furthermore it is obvious that the strength of ufg W can be increased by a heat treatment of 500°C for 5h. This effect is observed even stronger when combining the heat treatment with the doping element B.

When assessing the integrated area under the bending stress - bending strain curve for each variant (Figure 3.8b), which has the physical sense of the amount of plastic work consumed by the material or, in other words, the respective damage tolerance, similar effects can be observed: B and Hf increase this measure, and the heat treated version of the undoped and B-doped ufg W shows even higher values.

From this valuable data the following conclusions can be deduced:

Annealing effect:

For the annealed and undoped W sample a tremendous increase in strength was observed while the plastic strain at failure remained the same at about 8%. This strength increase from 3.3 to 5.4 GPa can be explained by the hardening-by-annealing effect. This effect commonly found in nanostructured metals describes the phe-

nomenon of an increased hardness after annealing below the grain growth threshold temperature [121,122]. Through the excess thermal energy dislocations within the grain interior migrate towards and annihilate at GBs, which relaxes those into an energetically more stable state. This GB relaxation leads to "smoother" GBs without any ledges or other GB defects. By removing mobile dislocations in the grain interior, plastic deformation can only occur through dislocation nucleation at GBs [28,123–125]. But since the GBs annealed GB ledges during the annealing, dislocations have to be nucleated from smooth GBs, which requires a much higher stress, explaining the increase in strength from the heat treatment. Ductility is not influenced by this hardening-by-annealing effect, indicating that dislocation plasticity is still present and that GB cohesion is the limiting factor to ductility. This is also supported by the electron backscatter diffraction (EBSD) orientation maps of tested cantilevers in Figure 3.9a and b, where intercrystalline failure is clearly evident.

Carbon:

Doping with C decreases ductility of ufg W and has no significant influence on strength, therefore reducing the overall damage tolerance. The DFT calculations in [67] determined C as a GB cohesion enhancing element in W, however, no positive influence on the mechanical properties of ufg W could be observed in this work. The definitive reason as to why C does not show GB cohesion enhancement or why it even deteriorates the mechanical performance could not be discovered within the scope of this thesis. Yet possible explanations include the formation of (so far undiscovered) nanosized tungsten carbides at GBs or a restricting influence of C on the dislocation core in W as reported in [126].

Boron:

The addition of B improves the strength of ufg W while maintaining ductility, thereby drastically enhancing the damage tolerance. When applying a heat treatment at 500°C for 5h, the bending strength increases even more to values of over 7 GPa, while still displaying a ductility of about 8%. These exciting results are explained by the combination of several different effects:

- While the unannealed W-B sample showed only small amounts of B at GBs, APT measurements unveiled that the heat treatment leads to a pronounced B segregation at GBs. The more B atoms segregate to the GB, the more their cohesion enhancing properties [67] influence the mechanical performance of ufg W.
- As an interstitial element in W, B cannot only influence the GB cohesion directly but also indirectly, by removing embrittling O from the interstitial GB sites (see Figure 3.9c).
- The aforementioned hardening-by-annealing effect also leads to a tremendous

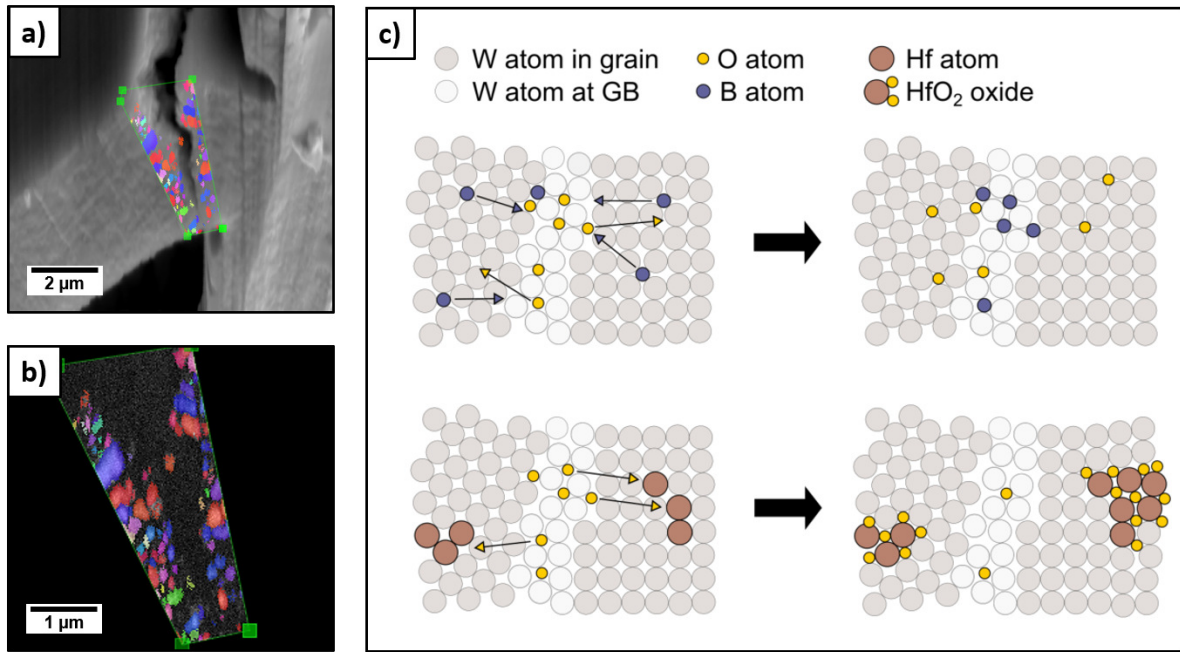


Figure 3.9 a) Post-mortem SEM image with EBSD overlay of an annealed W-B cantilever. b) Zoom-in of EBSD map around the crack. c) Sketch of the effects of B and Hf on GB chemistry in W. Boron diffuses to the GB and replaces O, while Hf attracts O from the GBs and forms HfO₂ oxides [106].

increase in strength in this doped ufg W variant.

Thus, an adaptive immense improvement of mechanical performance can be reported for W-B and W-B ann. material samples through GB cohesion strengthening and hardening-by-annealing.

Rhenium:

Small additions of Re are known to increase ductility and decrease hardness of W [97, 98], yet from the bending experiments conducted in this work the exact opposite was observed for ufg W. Re slightly reduced the ductility of ufg W while improving the strength, resulting in no improvement in overall damage tolerance from the undoped sample. This could once again indicate that dislocation plasticity is not the main factor contributing to ductility in ufg W. As no improvement of mechanical properties could be observed and Re is a rather expensive material, this variant was discarded as a potential property-enhancing doping element.

Hafnium:

The Hf-doped sample showed an increased ductility and strength, but also a large variance among the tested cantilevers. As the only doping element that was able to

improve the ductility of ufg W, Hf actually does not have a strengthening effect on GB cohesion [68]. Instead, Hf forms HfO_2 oxides with the O that is primarily situated at GBs in W. By doing that, an element that reduces GB cohesion in W gets removed from the GB and GB cohesion is therefore improved indirectly (see Figure 3.9c). The large variance between the different cantilevers of this material might be a sign of a varying effectiveness of Hf in binding O throughout the sample.

In conclusion, the strength, ductility and damage tolerance of ufg W could be improved by doping with B and Hf, optionally in combination with a heat treatment below the grain growth threshold temperature. These enhancements in mechanical performance were achieved by:

- Direct strengthening of GB cohesion (W-B, W-B ann.),
- Indirect strengthening of GB cohesion by removing O from the GBs (W-Hf, W-B, W-B ann.) and
- Increased segregation and hardening effect through annealing (W-B ann., W ann.).

Effect on fracture toughness

Moving forward from deformation to failure characteristics, Publication C [107] investigates the effects of GBSE on the fracture toughness of ufg W. As mentioned in Section 2.4, the fracture toughness of W plays an important role in the feasibility of application in e.g. structural divertor components in future nuclear fusion power plants [81–83]. Therefore, these investigations are essential for a prediction of the application potential of W in fusion technology.

At the same time, Publication C also explored the influence of specimen size on the validity and apparent fracture toughness of small-scale fracture mechanical experiments on W. This sensitive topic is highly discussed in literature [127–132] and additional experimental insights will be appreciated by the community. After all, the application of small-scale mechanical testing has found great interest in recent years, for example, for the evaluation of control samples in nuclear fission reactors [133–140]. It is reasonable to assume that such control samples will also find application in future nuclear fusion reactors, requiring the correct assessment of mechanical properties of ufg W. Out of all mechanical experiments on the microscale, fracture mechanical tests provide the biggest challenges with size effects and validity of experiments [127, 130, 131].

Only the most promising doped variants (W-B, W-B ann. and W-Hf) were selected for the fracture mechanical investigations alongside the undoped ufg W reference material. Multiple notched cantilevers with different sample dimensions (approximately $3 \times 3 \times 10 \mu\text{m}$ and $8 \times 8 \times 30 \mu\text{m}$) were fabricated for all samples using FIB. Additionally, a single bigger cantilever ($30 \times 30 \times 110 \mu\text{m}$) was fabricated in the undoped W and W-Hf materials via femtosecond laser cutting and subsequent FIB milling. Considering the semi-brittle nature of the ufg W material, linear elastic fracture mechanics (LEFM) is not applicable, as the samples show too much plasticity for the given sample sizes [127, 131]. Therefore, elastic-plastic fracture mechanics (EPFM) experiments are utilized in this work. The J-Integral is evaluated throughout the in-situ experiments utilizing the commonly used formulae [132, 141]. The crack propagation is monitored via frequently performed partial unloadings. For more details regarding the fracture mechanical experiments, the reader is referred to Publication C.

From the experiments it was found that some cantilever specimen fail in an unstable manner, while others show stable crack growth. To compare the fracture toughness between samples of different crack growth stability, the following measures were defined as fracture toughness: for the unstable failing samples the critical J_c at the failure point was used, while for the samples showing stable failure the initiation toughness J_i is utilized. This initiation toughness can be found at the transition from blunting line to regular crack extension or tearing in the J- Δa curve. The fracture toughness results are given in Figure 3.10. The x-axis in this graph represents the ratio of smallest sample dimension (between sample thickness and ligament length) to plastic zone size and is calculated using the flow stress from bending results in Publication B and the valid fracture toughness $J_{c,true}$ gained from the largest fracture specimen of every material. It is interesting to note that above a value of about 23 on the x-axis (samples marked in regime "C"), all samples show unstable crack growth and similar toughness values of about 1000 J/m^2 or $20 \text{ MPa}\sqrt{m}$ (with the exception of W-Hf). This suggests that above this value the samples show size-independent fracture toughness values and that the instability of crack growth might be an indicator for a valid and geometry-independent fracture experiment in ufg W. The samples with a lower x-value than 23 show very different behavior. While all the small samples (marked in regime "A") show a lower fracture toughness (between $300\text{-}700 \text{ J/m}^2$ or $12\text{-}18 \text{ MPa}\sqrt{m}$) and a linear increase with sample-to-plastic zone size ratio, most medium-sized cantilevers (marked in regime "B") show very high fracture toughness values up to over 2000 J/m^2 or $30 \text{ MPa}\sqrt{m}$.

To explain this curious behavior, we have to take a closer look at how the different sample dimensions influence the apparent fracture toughness of a small-scale experiment. It is widely known that the ratio of ligament length to plastic zone size

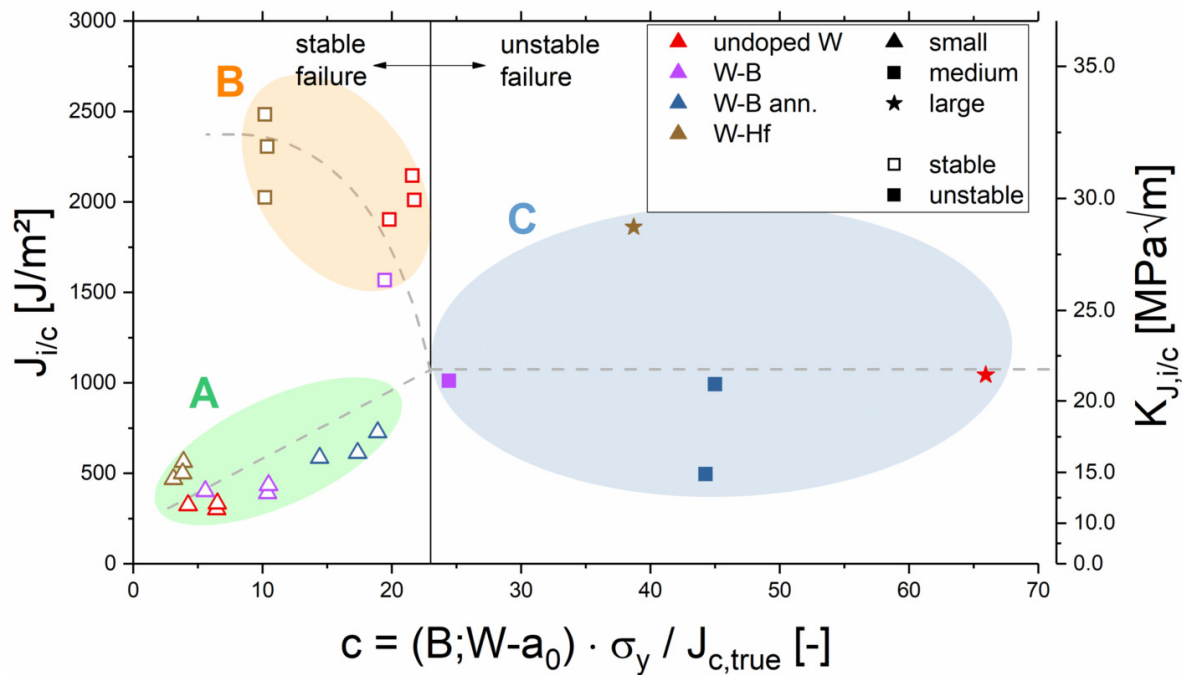


Figure 3.10 J-Integral fracture toughness (J_i or J_c) of all tested cantilever samples [107]. The x-axis is proportional to the ratio of smallest sample dimension to plastic zone size in front of the crack tip.

determines if the specimen exhibits small scale yielding or large scale yielding, or if the sample rather fails through complete plastic collapse of the ligament. The application of EPFM concepts is only valid if small or large scale yielding conditions are present in the specimen [127, 129, 142]. The sample thickness, however, influences the stress state in front of the crack tip of the sample. The stress in z-direction (parallel to the crack front) has to be zero at the edge of the sample, which is why plane stress conditions are encountered there. In the center of the sample, on the other hand, a high stress triaxiality and plane strain conditions are commonly found. Because of this high stress triaxiality, yielding is suppressed and the plastic zone size is smaller. As the sample gets thinner, the influence of the plane stress conditions of the surface near regions increases, which consequently leads to the measurement of a sample thickness dependent fracture toughness. The more the thickness decreases, the higher the apparent fracture toughness gets [127, 142]. It is crucial to note, that such thin samples are still valid fracture test specimen, as long as the sample shows small or large scale yielding conditions. However, the measured fracture toughness is sample size dependent and can not be compared to toughness values from larger specimen. Only when the sample shows predominantly plane strain conditions, the fracture toughness is thickness and sample size independent. Additionally, one has to keep in mind the stress and strain gradient inside a cantilever

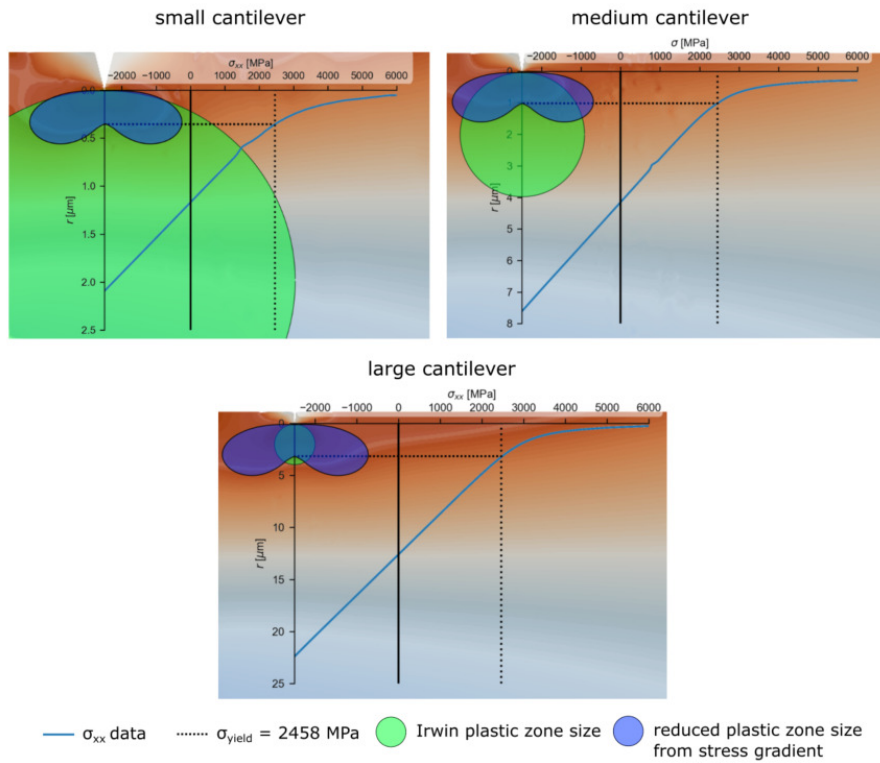


Figure 3.11 FEM simulations showing the bending stress gradient influencing the size of the plastic zone, compared to the classic Irwin model [107].

bending sample and its influence on the stress field in front of the crack tip. As FEM simulations show (Figure 3.11), the size of the plastic zone can be restricted due to this bending stress gradient, especially in very small samples, where the gradient is significantly steeper. Moreover, the size of the fracture process zone is sample size independent. Therefore, as the sample dimensions get reduced, the fracture process zone will extend past the neutral fibre of the bending cantilever. The present compressive strains on this side of the cantilever specimen can also lead to a restriction of the fracture process zone, resulting in a lower measured fracture toughness [127].

The results of fracture mechanical experiments can therefore be explained as follows:

- The smallest samples ("A") show an increased influence of the very steep bending stress gradient on the stresses in front of the crack tip (see Figure 3.11). This leads to an immense restriction of the plastic zone size (blue shape) in comparison with the classic Irwin model [142, 143] (green circle), as well as to a restriction of the fracture process zone. Naturally, the less plastic deformation

can happen inside the sample, the less energy can be dissipated, leading to a lower fracture toughness of the material. Harder and more brittle materials show a less restricted plastic zone size, explaining the slight increase of apparent fracture toughness values of "A" samples in Figure 3.10.

- The samples marked "B" in Figure 3.10 are expected to be less affected by the bending stress gradient due to the larger sample dimensions. However, given the still rather small sample thicknesses of about 8 μm , the influence of the surface near regions on the stress triaxiality is large. Hence, a thickness dependent and higher fracture toughness is measured for these samples.
- Lastly, the samples marked "C" mostly show similar toughness values. This indicates that for these specimen predominantly plane strain conditions and no influence of the bending gradient are present and that the measured fracture toughness represents valid and size-independent values. Increased influence of plane stress conditions is known to promote R-curve behavior and stable crack growth [127], explaining why only the "C" specimen fail in an unstable manner and all other samples show stable crack growth.

After identifying the effects of specimen size on apparent fracture toughness in our tested ufg W samples, we can finally compare the differently doped materials. For this, of course, only the valid and specimen size-independent values are used. Figure 3.12 compares the average bending strength and (size-independent) fracture toughness (converted to more commonly used $K_{J,c}$ values) of all investigated samples. The undoped ufg W material already showcases a remarkable fracture toughness of over $20 \text{ MPa}\sqrt{m}$, clearly outperforming single crystalline and commercially available tungsten and fulfilling the application criteria as structural divertor material in nuclear fusion technology [81–83, 132]. The W-B sample that showed a slight increase in bending strength maintains a similar fracture toughness compared to the undoped sample. Furthermore, we discovered that a heat treatment of this sample can immensely increase the bending strength, while the fracture toughness decreases only slightly. The only improvement of the already high fracture toughness of ufg W was achieved by doping with Hf. A fracture toughness of about $28 \text{ MPa}\sqrt{m}$ is measured for this sample. Given that Hf was also the only element that could improve bending ductility of ufg W, this is additional proof that ductility and fracture toughness are closely related, especially in materials failing in intergranular fashion. The dashed isolines in Figure 3.12 represent the product of strength and toughness (in $(\text{MPa})^2\sqrt{m}$), which can be used for a measure of damage tolerance of the material [15]. It is apparent that all doped and annealed samples investigated improve the damage tolerance of ufg W. Especially high values are reported for the W-Hf ($105\,000 (\text{MPa})^2\sqrt{m}$) and W-B ann. ($125\,000 (\text{MPa})^2\sqrt{m}$) material.

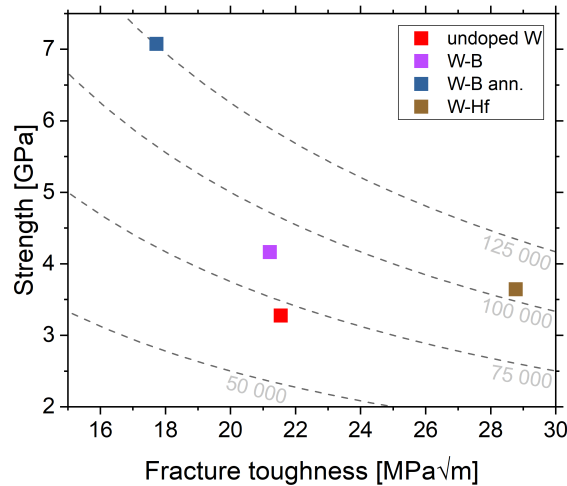


Figure 3.12 Average bending strength against valid fracture toughness ($K_{J,c}$) of all investigated ufg W materials [107]. Dashed isolines represent the product of strength and toughness in $(\text{MPa})^2\sqrt{m}$.

To summarize the findings of Publication C, the fracture toughness of ufg W can be improved by the addition of Hf, removing and binding oxygen from the tungsten GBs. Doping with B in combination with a heat treatment does not improve the fracture toughness of ufg W, but the overall damage tolerance as a consequence of the immense increase in strength.

Furthermore, the effects of sample dimensions on apparent fracture toughness of EPFM experiments have been studied. Depending on the ratio of sample size to plastic zone size, fracture toughness can be both under- and overestimated. It is recommended to only test large enough samples to measure size independent and valid fracture toughness values. Notably, for ufg W this seems to be a x -value (in Figure 3.10) of larger than 23, while the standard recommends a value of 10 [129,144].

3.3 Effects of doping elements on mechanical properties of nanocrystalline W-Cu

After the great success of improving the mechanical properties of ufg W through GBSE, doping of W-Cu nanocomposites using the same elements was investigated in Publication D [108]. As explored in Section 2.2, nanostructured composites made from a hard and soft metal phase are a promising approach for overcoming the strength-ductility trade-off and for improving radiation tolerance [33,36–41]. The effect of the elements C, B, Re and Hf on the work of separation of the W-Cu interface and the segregation energies of the elements were calculated using DFT. The results are seen in Figure 3.13. All elements have a positive effect on the interface cohesion if they are situated on the Cu side of the interface. However, the energetically more favorable segregation to the W side of the interface leaves every element with a negative impact on interface cohesion, with the exception of Re, which has no effect at all. Moreover, a strengthening of Cu GBs can be expected from all doping elements and Scheiber et al. [67,68] report an increase in W GB cohesion for all dopants except Hf. The doped and undoped W-75Cu composites and an undoped W-50Cu composite were fabricated following the routes presented in Section 3.1.

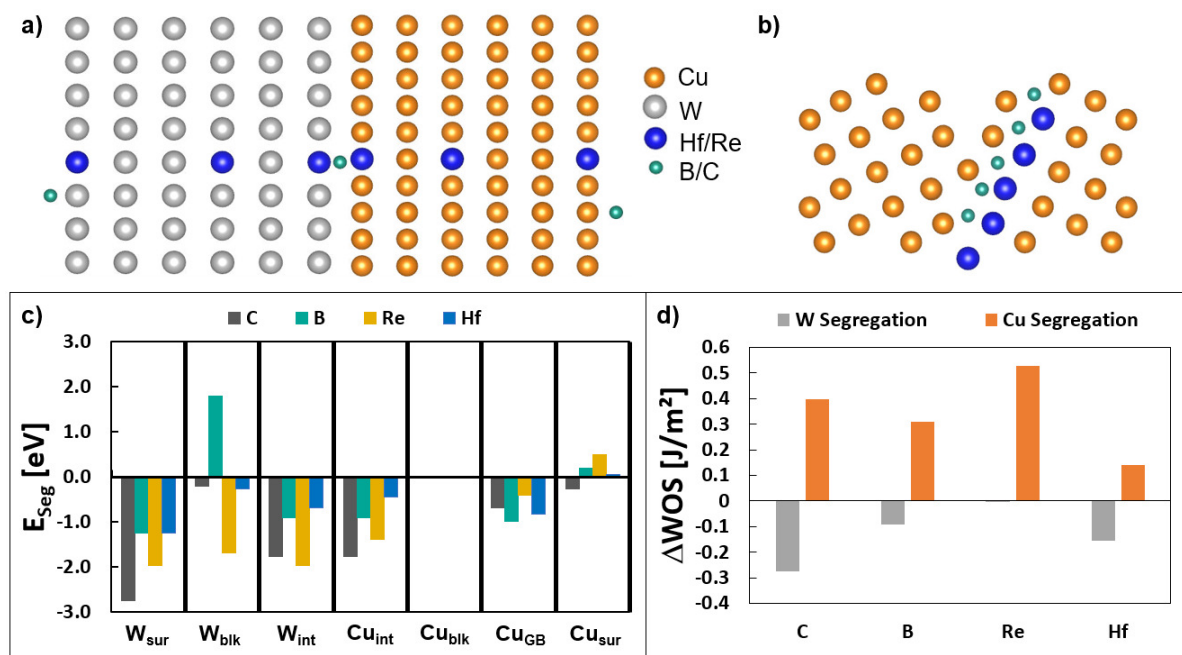


Figure 3.13 DFT calculations of doping elements at W-Cu interface [108]. a) and b) display the simulated cells of W/Cu and Cu GB, respectively. c) shows the calculated segregation energies and d) the calculated work of separation of the W/Cu interface.

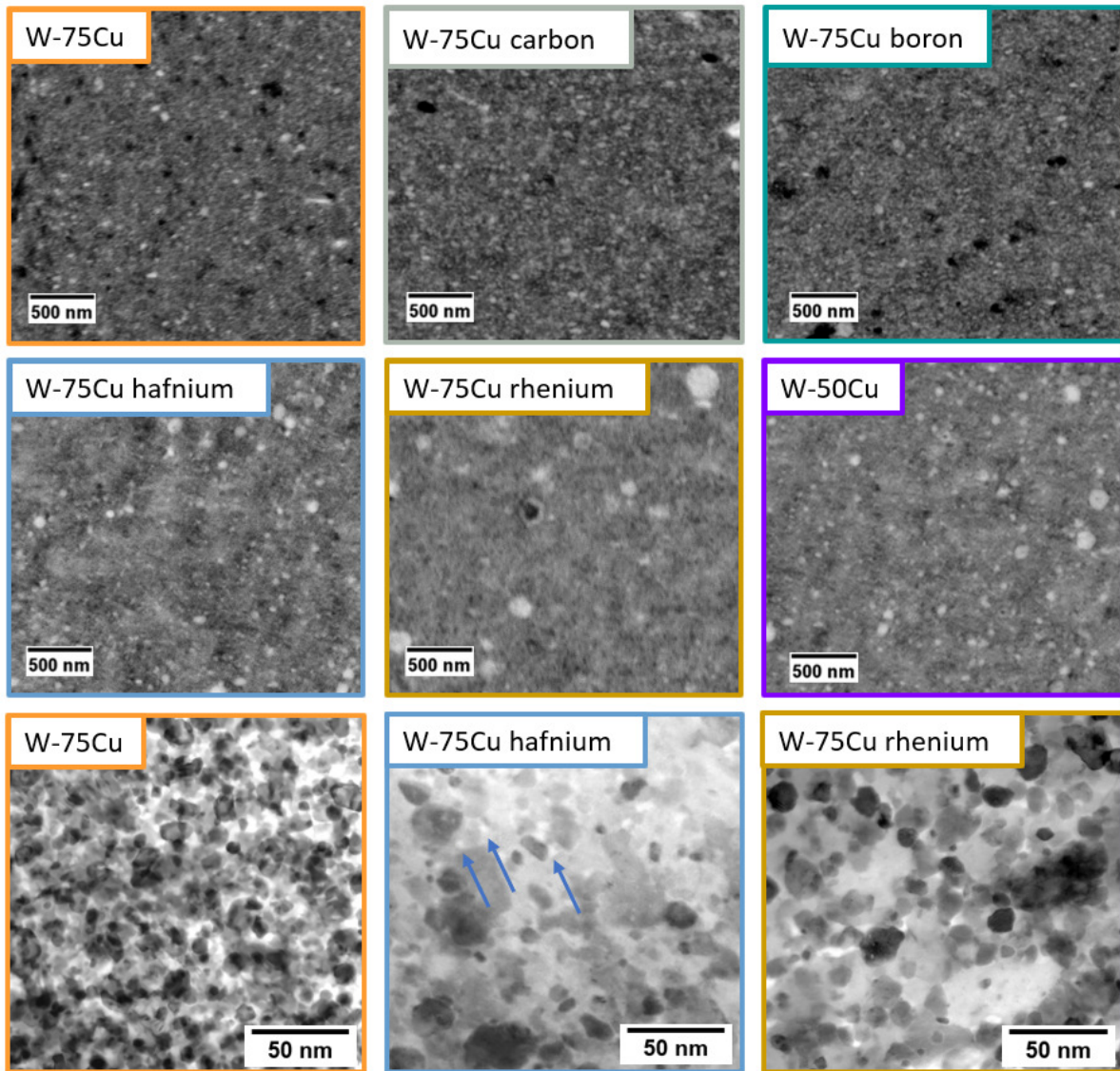


Figure 3.14 SEM images of the nanocrystalline microstructure of all investigated samples and STEM images of selected samples [108].

Effect on microstructure

The microstructures of the fabricated composites were investigated in SEM and STEM and are presented in Figure 3.14. All samples show a homogeneous and nanocrystalline microstructure, with grain sizes around 10 nm (8.5 nm for the undoped, 11 nm for the Hf-doped and 13 nm for the Re-doped W-75Cu composite). Several nm-sized holes are apparent in the Hf-doped material, suggesting the presence of oxides in the material that left the sample during sample preparation.

Effect on strength and ductility

The strength and ductility of all investigated materials was assessed again using microcantilever bending tests. These results are apparent in Figure 3.15. It can be seen that the W-50Cu shows a higher strength and lower ductility than the W-75Cu, which is not surprising. Among the doping elements, C is the only element that leads to mechanical property degradation, while B shows a slight improvement in both strength and ductility. This behavior is the same as the two elements had in ufg W. Doping with Hf seems to substantially increase the strength of the composite, while exhibiting only a minor decrease in ductility. The Re-doped specimen show very unique behavior. While the variance between the different cantilever specimen is pretty large, all of them exhibit higher ductility values than any other doped specimen, while also showing a strength increase compared to the undoped W-Cu composite. Some of the tested specimen did not even fail during the experiment, which means they can be deformed to bending strains of over 40% without breaking or crack formation. An example of such a "super-ductile" sample is shown on the right side of Figure 3.15.

Additional microtensile tests were performed on undoped and Re-doped W-75Cu (see Figure 3.16). It is evident that the "super-ductile" behavior of the composite doped with Re could not be reproduced in these tests. However, a clear improvement of strength and ductility and even some slight necking is observed in the Re-doped

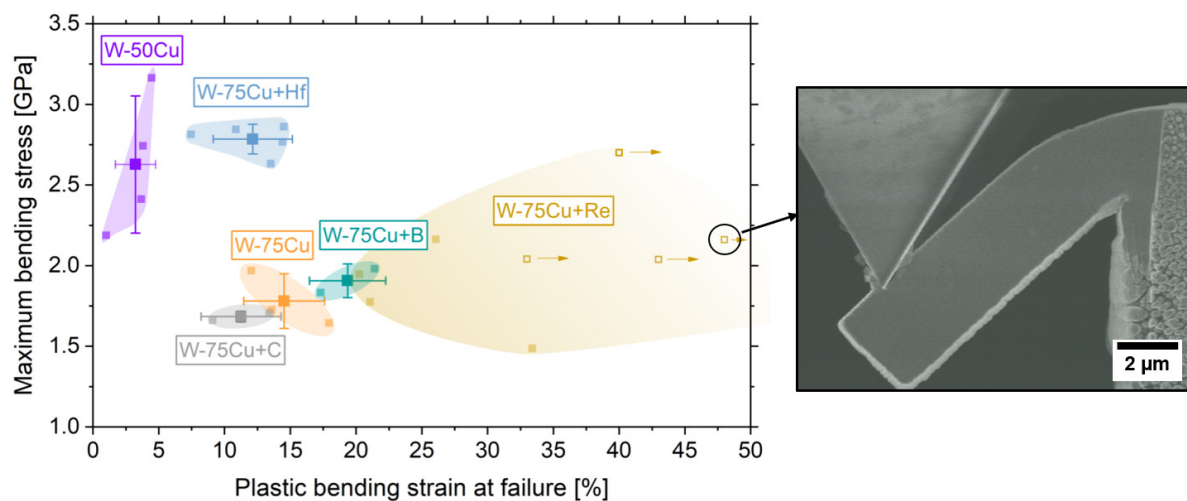


Figure 3.15 Strength-ductility map of all investigated W-Cu composites [108]. Small squares represent single cantilever experiments, large squares represent the average values of one material, respectively. In-situ SEM snapshot shows a representative Re-doped W-75Cu specimen exhibiting "super-ductile" behavior.

3.3. Effects of doping elements on mechanical properties of nanocrystalline W-Cu

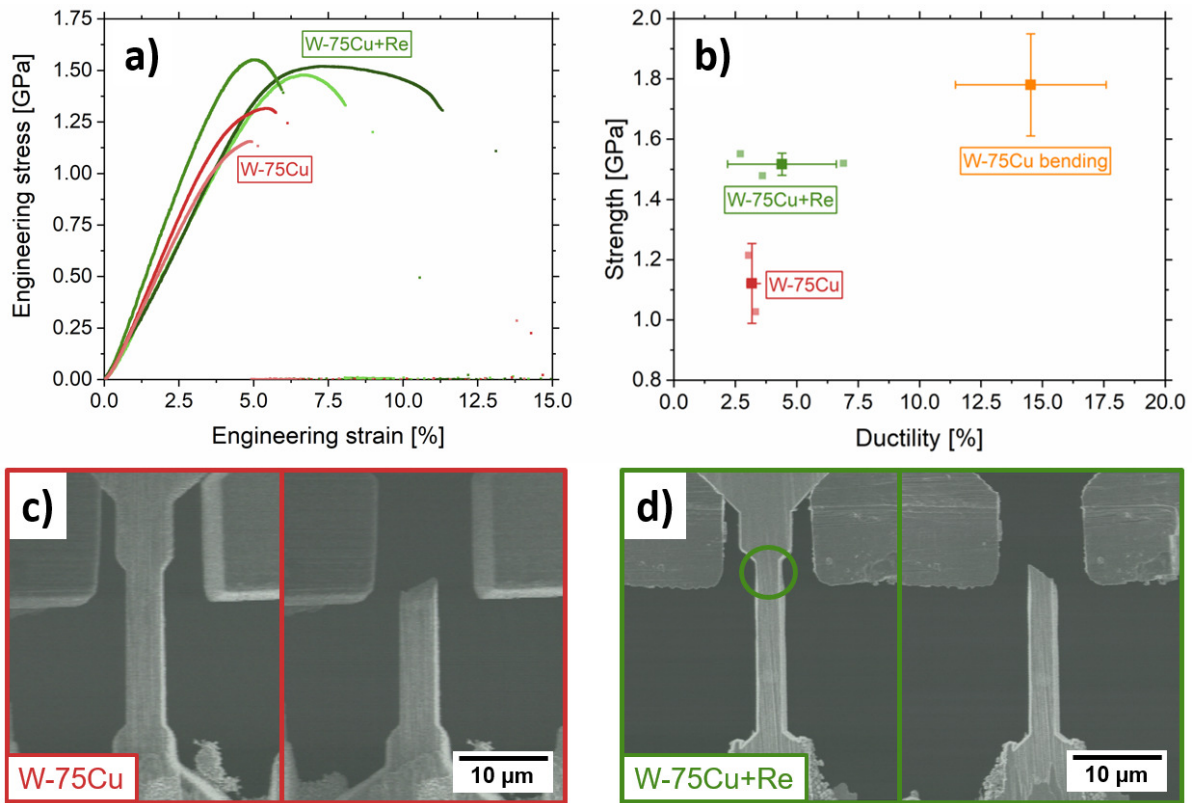


Figure 3.16 Microtensile tests on W-75Cu and W-75Cu+Re [108]. a) Stress-strain curves as well as b) ultimate tensile strength over ductility of all tested specimen. As a reference, the W-75Cu microcantilever bending sample was added to b). Snapshots from in-situ videos of representative c) undoped and d) Re-doped material right before and after failure.

sample. In general, both strength and ductility are overestimated by the bending tests, which is not surprising, given the stress and strain gradient present within a bending cantilever [145] and the fact that only a small part of the sample volume experiences high stresses and strain. In the tensile sample, on the other hand, the volume of the whole gauge length times cross section experiences the same stresses, increasing the probability of finding a critical defect or crack tremendously [146,147].

From the bending and tensile results, the following conclusions can be drawn:

- Bending tests overestimate strength and ductility due to the smaller affected sample volume and the bending stress gradient. However, due to the tedious preparation of tensile samples at the microscale, microcantilever bending tests provide an easier and faster method to qualitatively compare strength and ductility of different materials.

- The addition of C seems to decrease the mechanical properties of W-Cu composites. The reason for this has yet to be unveiled. Doping with B slightly increases the bending strength and ductility, indicating that GB and interface cohesion was improved.
- While Hf improved the ductility and toughness in ufg W, in nc W-Cu it seems to enhance the bending strength tremendously. This is most likely from the formation of nanoscale HfO₂ oxides, leading to precipitation hardening while at the same time removing embrittling O from the GBs and interfaces, diluting the usually accompanying loss of ductility.
- The addition of Re leads to "super-ductile" behavior and immense plastic deformation without failure in some bending samples. In tensile samples, this behavior was not reproducible to the same extent, suggesting it is another consequence of the smaller sample volume being affected by high stresses and strains in bending samples. Post-mortem SEM images (Figure 3.17) show pronounced plastic deformation and necking of the cantilevers. STEM images of the highly deformed region of a super-ductile cantilever did not show any differences from the microstructure after HPT fabrication. Therefore, the reason for this unique deformation behavior could not be discovered.

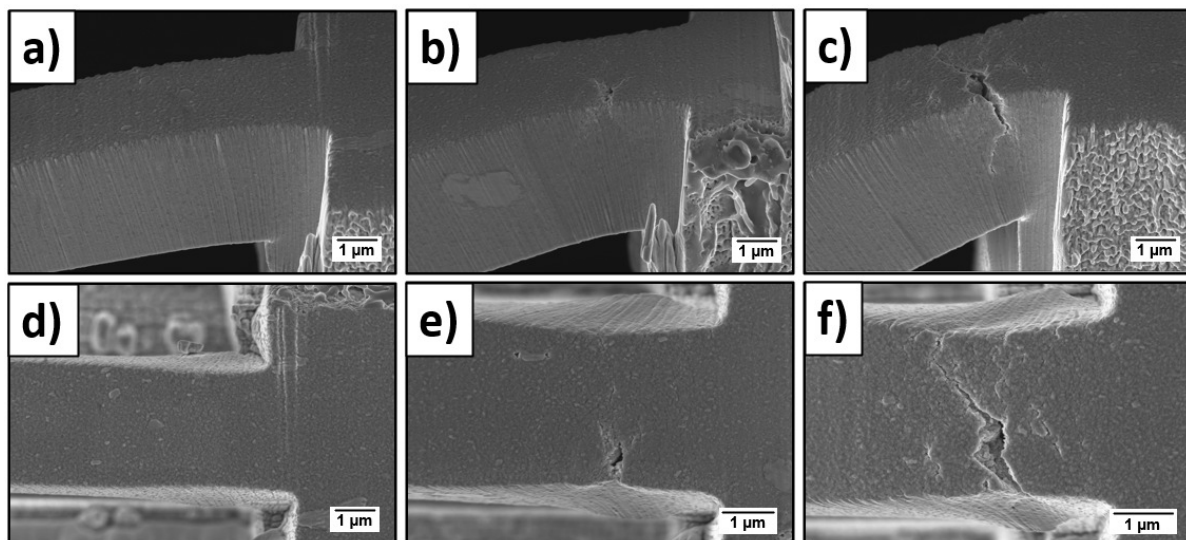


Figure 3.17 SEM images of different W-75Cu+Re cantilevers after bending tests [108]. a,d) Cantilever sample after deformation to about 20% plastic strain, b,e) cantilever sample that failed at high plastic bending strain (35%) and c,f) cantilever sample that was broken forcefully after testing. Bottom row shows top-view.

Effect on fracture toughness

Small-scale fracture mechanical experiments were conducted on selected doped and undoped W-75Cu composites in Publication D in the same manner as for ufg W. The sample dimensions were set to $10 \times 10 \times 35 \mu\text{m}$, to avoid size effects or validity issues [127,129,142]. The gained fracture toughness values are apparent in Figure 3.18. All tested samples show a similar fracture toughness of around 8 to $10 \text{ MPa}\sqrt{\text{m}}$. While the B-doped composite shows a slightly lower toughness of 6 to $8 \text{ MPa}\sqrt{\text{m}}$, this is most likely just a statistical phenomenon, given that one of these tested cantilevers showed a similar fracture toughness compared to the other composites. It is rather surprising that the W-Cu nanocomposite doped with Re shows no improvement in fracture toughness even though it enhanced ductility immensely. For nanocrystalline materials that break in intercrystalline fashion, ductility and fracture toughness are considered to be especially well interlinked [28,29]. These results suggest that Re enhances the resistance against crack initiation and not crack propagation, possibly by strengthening W and Cu GBs but not the interface, as proposed by the DFT calculations in Figure 3.13. This would also further explain why the variance among the measured bending ductility is that high and why no "super-ductile" behavior was observed in tensile tests, as the failure of the material becomes solely reliant on the presence of critical defects within the highly strained region of the test sample and is therefore highly influenced by probability and tested sample volume.

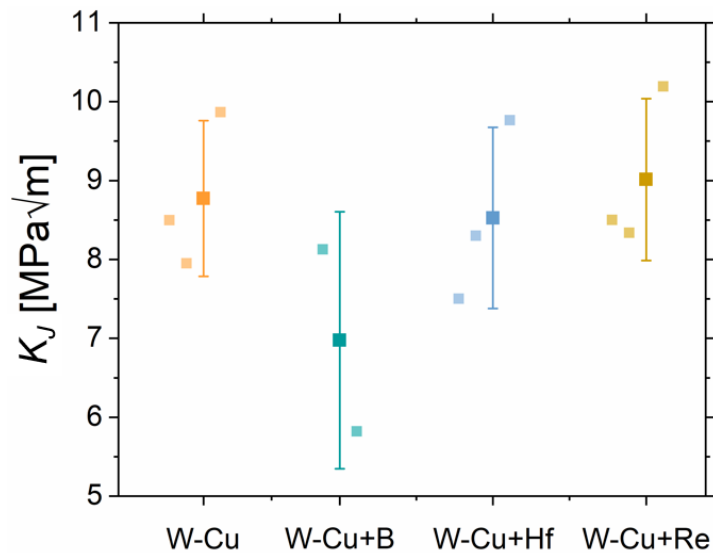


Figure 3.18 J-Integral fracture toughness of undoped and the most promising doped W-75Cu nanocomposites [108].

To summarize, the mechanical performance of W-75Cu nanocomposites can be influenced and improved by the addition of various doping elements. While Hf improves the strength tremendously, Re shows enhancements in strength and particularly bending ductility, where extremely high deformation strains could be achieved without failure. The fracture toughness of the composite could not be improved by interface doping, but also did not suffer any degradation. Nevertheless, the fracture toughness of 8 to 10 MPa \sqrt{m} is still respectable when compared to other nanostructured high-performance materials [15,148–150].

3.4 Helium irradiation of ultrafine-grained W and nanocrystalline W-Cu

Section 2.4 of this thesis introduced the possible application of ufg W and nc W-Cu in nuclear fusion technology as divertor material and high-strength heat sink material, respectively. As was asserted, helium irradiation is a major concern for materials employed in proximity to the fusion plasma. Therefore, the effect of helium implantation on the swelling behavior and mechanical properties of undoped ufg W and W-75at.%Cu nanocomposites was investigated in Publication E [109] within the scope of this thesis.

Helium was implanted in 10 x 10 μm^2 squares at a sample radius of 3 mm on the polished HPT disks of both materials to various different fluences using a helium ion microscope [151] with 25 keV helium ions. This corresponds to a penetration depth of about 180 nm in W and 230 nm in W-Cu, as calculated by the "Stopping Range of Ions in Matter" (SRIM) software [152]. Subsequently, the swelling response was evaluated using atomic force microscopy (AFM) and the change in mechanical properties was determined via nanoindentation.

Swelling response due to helium implantation

AFM has already been utilized to measure the swelling occurring from helium bubble formation and growth in previous works [93,94,151]. A useful measure to evaluate and compare the swelling between materials is the swelling height, i.e. the average height difference between irradiated and unirradiated areas (see Figure 3.19a).

The measured swelling heights of ufg W and nc W-Cu after implantation with the different helium fluences are compared to literature values of single-crystalline (sxx)

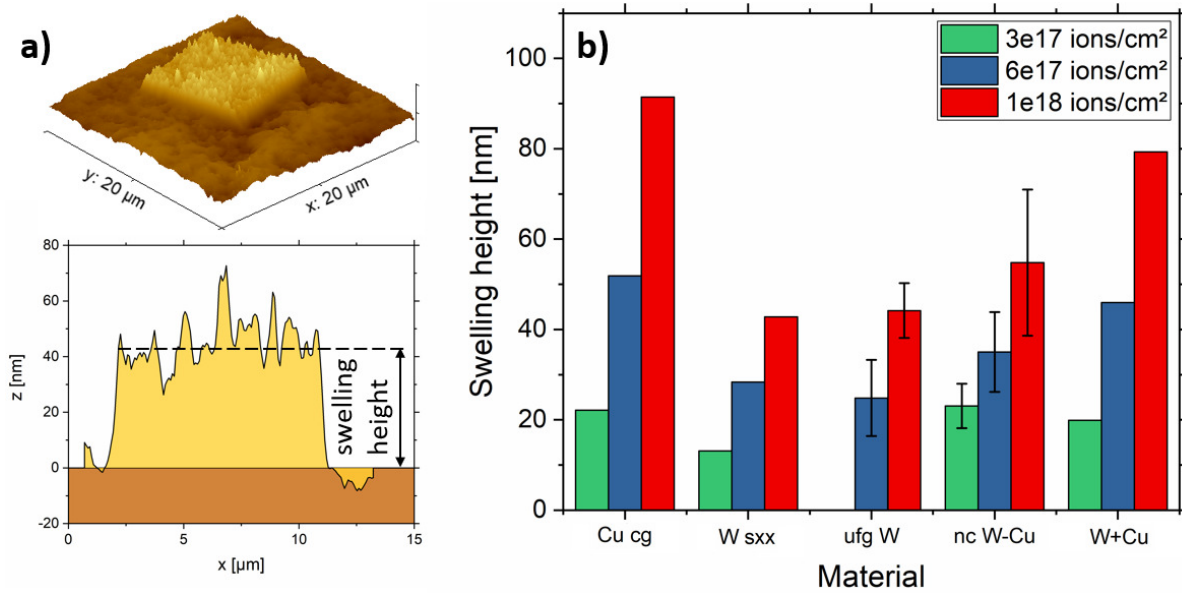


Figure 3.19 a) AFM topology of ufg W implanted with a helium fluence of 10^{18} ions/cm² and sketch on the definition of swelling height [109]. b) Measured average swelling height of ufg W and nc W-Cu compared to literature data for cg Cu [93] and sxx W [90].

W [90] and coarse-grained (cg) Cu [93] in Figure 3.19b. Additionally, an arithmetic combination of 25% sxx W and 75% cg Cu is shown, for a better comparison with the investigated W-75at.%Cu composite.

From this comparison it is evident that Cu and W-Cu composites show much higher swelling heights than the pure W materials. This behavior originates in the fact that fcc metals, such as Cu, are more prone to void and gas bubble swelling due to their densely packed crystal structure [153]. However, the W-Cu nanocomposite investigated in this work showed much less swelling than the cg Cu or the arithmetic combination of sxx W and cg Cu, demonstrating the huge impact that interfaces have at restricting bubble growth. This is in good agreement with previous investigations [94] that observed a linear swelling behavior with increasing helium fluence and a restricted bubble growth through GBs in nc Cu-Fe-Ag.

The swelling heights of ufg W, on the other hand, are comparable to measurements on sxx W. This is surprising, as it was expected that the grain size of about 150 nm in ufg W would also have beneficial effects on bubble formation and growth and thus swelling, albeit less pronounced than for nc grain sizes. In fact, it is presumed that the smaller grain size indeed helps suppressing the formation of big blisters on the implanted area, as seen for sxx W [90] (compare with Figure 3.19a). However, the comparable swelling heights of both materials indicate that the grain size is still too large to effectively remove radiation-induced vacancies before they can agglomerate

with helium atoms to form bubbles. This is in good agreement with the work of El-Atwani et al. [92], who found a grain size threshold of about 35-50 nm for tungsten above which bubble formation can not be effectively suppressed by the absorption of defects at GBs. To further visualize the dramatic impact the grain size has on defect absorption at GBs, one can deduce from the SRIM calculations that in ufg W on average only one GB is located in the helium affected zone of the material in implantation direction. In contrast, the smaller grain size of 10-35 nm and larger penetration depth for the W-Cu composite leads to at least 7 GBs being located in the irradiated zone of the material in implantation direction on average. Using a simple estimation with brick-shaped grains, the GB area of ufg W within the implanted zone amounts to roughly 340 μm^2 , compared to an approximate 1410 μm^2 in nc W-Cu (using the conservative estimate of 35 nm). This explains why the W-Cu nanocomposite is so much more effective in suppressing bubble growth and swelling than the ufg W. However, due to its bcc crystal structure and high displacement threshold energy, ufg W still shows less swelling overall than the nc W-Cu and a generally good swelling behavior without blistering, making both materials viable options for application in helium-irradiative environments based on the swelling measurements.

Mechanical property degradation after helium implantation

Aside from their swelling behavior, the degradation of mechanical properties is another major concern for the employment of materials in the extreme irradiative environment of a nuclear fusion reactor. However, assessing the mechanical properties of only the irradiation-affected zone of a material is challenging, as they tend to be rather small for ion-irradiated materials. Evaluating the mechanical properties using conventional testing methods such as tensile testing or hardness measurements will probe too much unirradiated material to see an effect of the irradiation. Therefore, small-scale testing methods are commonly employed to allow for small sample volumes to be tested and only the irradiation-affected layer of the material to be probed [134, 135]. Nanoindentation is a well established small-scale method that requires no or only little sample preparation and allows for straightforward analysis and interpretation of the results. In this work, 4-5 indents were performed on the helium-implanted areas and then compared to indents on the unirradiated material. The indents were performed to an indentation depth of about 200 nm in ufg W and about 300 nm in W-Cu. Although an indentation experiments probes sample volume up to 5 times deeper than the indentation depth [94, 134, 135, 139, 154, 155], the fraction of probed irradiated layer to probed unirradiated volume is large enough to see clear trends of hardening and softening, especially for smaller indentation depths.

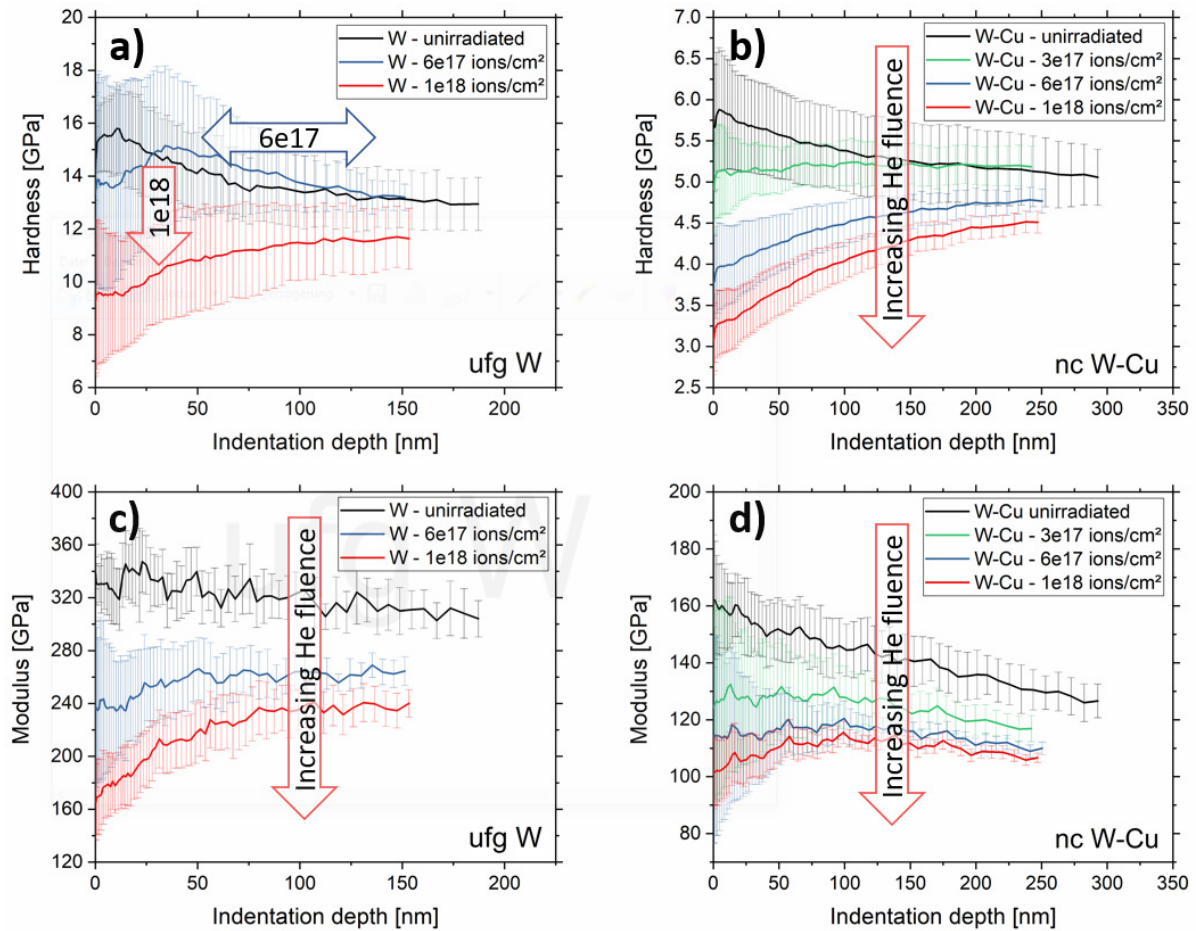


Figure 3.20 Nanoindentation results on helium-implanted materials [109]. Averaged hardness (a,b) and modulus (c,d) curves of ufg W (a,c) and nc W-Cu (b,d).

Figure 3.20 shows the average hardness and modulus curves over indentation depth for each material and helium fluence. It is apparent that the reduced elastic modulus of both materials decreases continuously with increasing helium fluence. This was expected as increasingly more gas is implanted into the material, turning the material eventually into a foam or solid-gas composite. The measured hardness however paints a different picture for each material. While the W-Cu nanocomposite shows a continuously decreasing hardness with increasing helium fluence, the ufg W sample seems to retain its hardness even after implantation with 6×10^{17} helium ions/cm² and exhibits a drop in hardness only after implantation with 10^{18} ions/cm². In reality, this perceived retention of hardness is most likely the product of competing radiation hardening (which is predominant at low fluences of helium) and softening through bubble formation and growth (predominant at high fluences). This assumption is supported by findings in [94], where ufg Cu-Fe-Ag with a grain size of 100 nm showed hardening for doses between 1 and 4×10^{17} ions/cm² and softening

ing for doses higher than 7×10^{17} ions/cm². While this competition of hardening and softening leads to a seemingly unchanged hardness of ufg W implanted with 6×10^{17} helium ions/cm², it would still have dramatic consequences on ductility and fracture toughness that cannot be ignored and should be investigated in future work. As already discussed above, the grain size in nc W-Cu is small enough for the GBs to effectively remove radiation-induced defects before they can cluster. Due to these excellent defect-sinks in the material, no radiation hardening occurs through defect clusters, yet helium bubbles still form and lead to softening of the composite. Thus, the continuous decrease of hardness with increasing helium fluence is explained by softening through gas bubble formation and the absence of a competing radiation hardening effect.

In summary, fabricated ufg W and W-Cu nanocomposites were evaluated regarding their response to helium irradiation. The effect of different fluences of helium on swelling and mechanical properties, the most crucial parameters for a safe employment of materials in a fusion environment, were investigated using AFM and nanoindentation. It was observed that grain refinement to the ufg regime did not further enhance the already excellent swelling behavior of W, but could suppress the formation of blisters on the material surface. The nc W-Cu, however, showed a tremendous improvement in swelling compared to a cg composite, as the very small grain size of 10-35 nm is able to absorb radiation-induced vacancies at GBs before they can agglomerate with helium bubbles. This extraordinary effect also has an impact on the mechanical properties, as the absence of radiation hardening in nc W-Cu leads to a much faster degradation of hardness after implantation with helium. Here, the ufg W exhibits a seemingly unchanged hardness up to high fluences of helium, as radiation hardening competes with softening by gas bubble formation and growth. Eventually, at very high helium fluences, the hardness also drops significantly as the softening effect outweighs the radiation hardening.

The findings of Publication E unveiled the effect of helium irradiation on possible candidate materials for nuclear fusion and are expected to have major implications on the future development and employment of high-performance materials for fusion technology.

4 Conclusions & Outlook

In an attempt to overcome the classic strength-ductility trade-off in materials, this thesis investigated the possibility to improve the mechanical properties of nanostructured metals by modifying grain boundary and interface chemistry. The investigated material systems were ultrafine-grained (ufg) W and nanocrystalline (nc) W-Cu composites. Both materials have exciting application potential in high-performance technology, for example in nuclear fusion reactors as structural divertor (W) or heat sink (W-Cu) material.

The strengthening of interfaces and grain boundaries was attempted by using doping elements that were identified to have an increased segregation tendency and a positive influence on grain boundary or interface cohesion. The processing and doping was realized by developing a powder-based fabrication route involving cold compacting and severe plastic deformation in the form of high pressure torsion. All materials showed high reproducibility and an even distribution of doping elements. Grain sizes of about 150 nm for ufg W and around 10 nm for nc W-Cu were achieved.

Given the small available material volume and microstructural gradients from fabrication, all mechanical properties were assessed using small-scale experiments. The effect of the doping elements on mechanical performance were vastly different between the various elements and the two material systems. For ufg W, the most promising strategies to improve the properties were doping with Hf, which improves ductility and fracture toughness, and doping with B in combination with a low temperature heat treatment, which improves the strength immensely and maintains ductility and fracture toughness. For the W-Cu nanocomposite, the addition of Hf leads to a strength increase while adding Re improves the ductility, especially in bending experiments, where a "super-ductile" behavior was observed. No improvement (but also no deterioration) in fracture toughness could be achieved by doping of nc W-Cu. To highlight the application potential in harsh environments, the response of both materials to helium irradiation was investigated as well. Here, especially the nanocrystalline grain size and the related high interface fraction was effective in improving the otherwise poor swelling behavior of W-Cu composites. Ufg W did not show changes in swelling amount compared to coarse-grained W, but the formation of blisters was impeded and hardness is maintained to high fluences of helium.

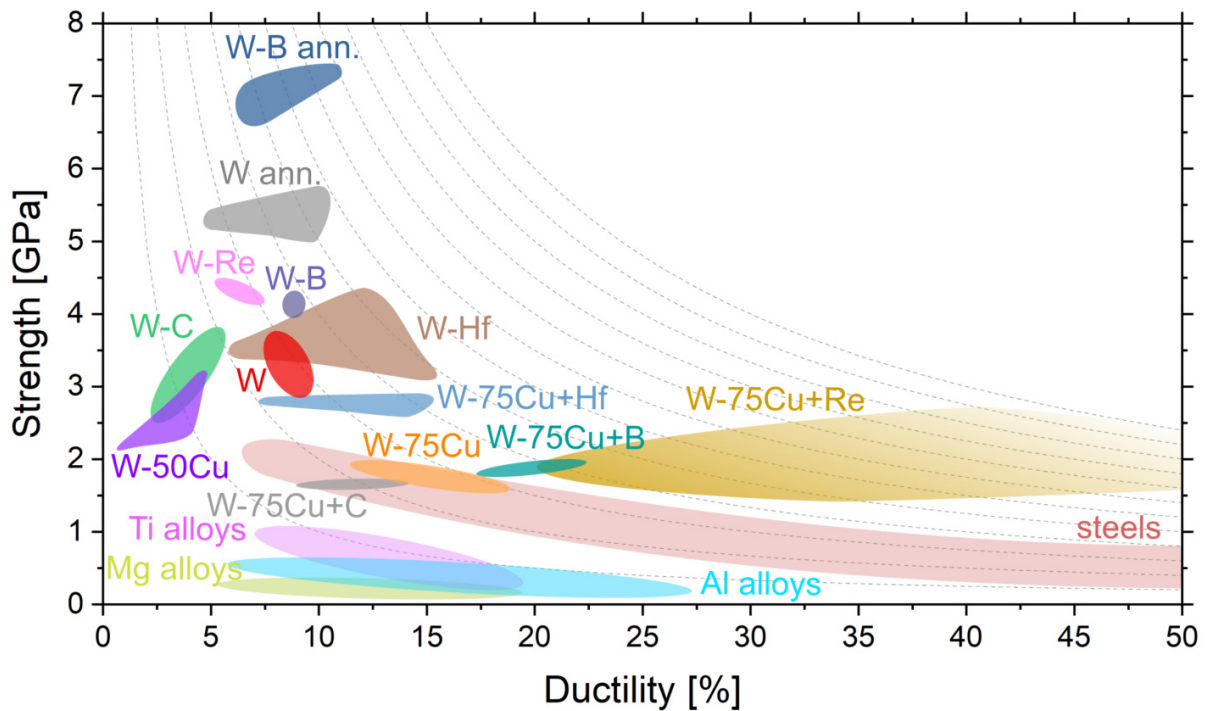


Figure 4.1 Bending strength and ductility of all materials investigated in this thesis in comparison with (tensile) properties of conventional engineering alloys [4]. Isolines represent the product of strength and ductility.

In conclusion, it was shown in this work that the overall mechanical performance of ufg W and nc W-Cu can be improved by doping with cohesion-enhancing elements and that the strength-ductility trade-off can be challenged by applying the concept of grain boundary segregation engineering to nanostructured metals (Figure 4.1). The response to helium irradiation was discovered to be beneficial for these nanostructured materials, compared to their coarse grained counterparts. In addition, remarks regarding the applicability and validity of the used small-scale mechanical experiments were made within the framework of this thesis.

In general, the most promising doping variants found within this thesis can and should be studied in more detail in future, using high-end characterization and computer simulation methods, to unveil the exact mechanisms and effects leading to the presented outstanding mechanical property improvements.

The fracture toughness and ductility of ufg W was found to be sufficiently high for application in nuclear fusion technology, even without grain boundary doping. However, the main problem of fabricating such severely deformed materials in large quantities remains. Until this is realized, doping of W materials with slightly larger grain sizes, such as cold-rolled W sheets, using B and Hf should be pursued to explore how effective the grain boundary doping is in improving the mechanical

properties of such coarser grained materials, which can already be fabricated in large enough quantities.

In case of the W-Cu nanocomposites, future work should be focused on replicating the "super-ductile" behavior of the Re-doped variant in tension and larger samples sizes. To improve the fracture behavior of this composite, an increase in grain size to the ufg regime (to about 100-200 nm) should substantially increase the fracture toughness through crack deflection and possibly even a transition to transcrystalline failure, which would additionally make use of the inhomogeneity effect. However, the fabrication of such a composite with similar grain sizes of both phases will prove challenging, given the large differences in melting point and mechanical strength of W and Cu.

References

- [1] M.F. Ashby, *"Materials Selection in Mechanical Design"*, Butterworth-Heinemann, Oxford, 2011.
- [2] R.O. Ritchie, *"The conflicts between strength and toughness"*, Nature Materials 10: 817-822, 2011.
- [3] B.B. He, B. Hu, H.W. Yen, G.J. Cheng, Z.K. Wang, H.W. Luo, M.X. Huang, *"High dislocation density-induced large ductility in deformed and partitioned steels"*, Science 357: 1029-1032, 2017.
- [4] H. Springer, C. Baron, A. Szczepaniak, V. Uhlenwinkel, D. Raabe, *"Stiff, light, strong and ductile: nano-structured High Modulus Steel"*, Scientific Reports 7: 2757, 2017.
- [5] Y. Wei, Y. Li, L. Zhu, Y. Liu, X. Lei, G. Wang, Y. Wu, Z. Mi, J. Liu, H. Wang, H. Gao, *"Evading the strength-ductility trade-off dilemma in steel through gradient hierarchical nanotwins"*, Nature Communications 5: 3580, 2014.
- [6] K. Lu, L. Lu, S. Suresh, *"Strengthening Materials by Engineering Coherent Internal Boundaries at the Nanoscale"*, Science: 324: 349-352, 2009.
- [7] C.C. Koch, D.G. Morris, K. Lu, A. Inoue, *"Ductility of Nanostructured Materials"*, MRS Bulletin 24: 54-58, 1999.
- [8] K. Lu, *"Making strong nanomaterials ductile with gradients"*, Science 345: 1455-1456, 2014.
- [9] E. Ma, *"Eight routes to improve the tensile ductility of bulk nanostructured metals and alloys"*, JOM 58: 49-53, 2006.
- [10] E. Ma, T. Zhu, *"Towards strength-ductility synergy through the design of heterogeneous nanostructures in metals"*, Materials Today 20: 323-331, 2017.
- [11] Y.F. Gao, W. Zhang, P.J. Shi, W.L. Ren, Y.B. Zhong, *"A mechanistic interpretation of the strength-ductility trade-off and synergy in lamellar microstructures"*, Materials Today Advances 8: 100103, 2020.
- [12] G. Gottstein, *"Physical Foundations of Materials Science"*, Springer, Berlin-Heidelberg, 2004.
- [13] M.E. Launey, R.O. Ritchie, *"On the Fracture Toughness of Advanced Materials"*, Advanced Materials 21: 2103-2110, 2009.

-
- [14] R. Pippan, A. Hohenwarter, *"The importance of fracture toughness in ultrafine and nanocrystalline bulk materials"*, Materials Research Letters 4: 127-136, 2016.
- [15] A. Hohenwarter, R. Pippan, *"Fracture and fracture toughness of nanopolycrystalline metals produced by severe plastic deformation"*, Philosophical Transactions of the Royal Society A 373: 20140366, 2015.
- [16] K. Leitner, D. Scheiber, S. Jakob, S. Primig, H. Clemens, E. Povoden-Karadeniz, L. Romaner, *"How grain boundary chemistry controls the fracture mode of molybdenum"*, Materials & Design 142: 36-43, 2018.
- [17] B. Gludovatz, S. Wurster, A. Hoffmann, R. Pippan, *"Fracture toughness of polycrystalline tungsten alloys"*, International Journal of Refractory Metals and Hard Materials 28: 674-678, 2010.
- [18] B. Gludovatz, S. Wurster, T. Weingärtner, A. Hoffmann, R. Pippan, *"Influence of impurities on the fracture behaviour of tungsten"*, Philosophical Magazine 91: 3006-3020, 2011.
- [19] M.L. Martin, B.P. Somerday, R.O. Ritchie, P. Sofronis, I.M. Robertson, *"Hydrogen-induced intergranular failure in nickel revisited"*, Acta Materialia 60: 2739-2745, 2012.
- [20] S.J. Zinkle, *"Fusion materials science: Overview of challenges and recent progress"*, Physics of Plasmas 12: 058101, 2005.
- [21] S.J. Zinkle, *"Advanced materials for fusion technology"*, Fusion Engineering and Design 74: 31-40, 2005.
- [22] N. Fonstein, *"Advanced High Strength Sheet Steels: Physical Metallurgy, Design, Processing, and Properties"*, Springer International Publishing Switzerland, Cham, 2015.
- [23] V. Zackey, E. Parker, D. Fahr, R. Busch, *"The Enhancement of Ductility in High-Strength Steels"*, Transactions of ASM 60: 252-259, 1967.
- [24] O. Grassel, G. Krieger, G. Frommeyer, L. Meyer, *"High Strength Fe-Mn-(Al,Si) TRIP/TWIP Steel Development - Properties-Application"*, International Journal of Plasticity 16: 1391-1409, 2000.
- [25] G. Frommeyer, U. Brux, P. Neumann, *"Supra-Ductile and High-Strength Manganese - TRIP/TWIP Steels for High Energy Absorption Purposes"*, ISIJ International 43: 438-446, 2003.
- [26] E.O. Hall, *"The Deformation and Ageing of Mild Steel: III Discussion of Results"*, Proceedings of the Physical Society 64: 747-753, 1951.
- [27] N.J. Petch, *"The Cleavage Strength of Polycrystals"*, Journal of the Iron and Steel Institute 174: 25-28, 1953.
- [28] M.A. Meyers, A. Mishra, D.J. Benson, *"Mechanical Properties of nanocrystalline materials"*, Progress in Materials Science 51: 427-556, 2006.

- [29] C.C. Koch, I.A. Ovid'ko, S. Seal, S. Veprek, *"Structural Nanocrystalline Materials - Fundamentals and Applications"*, Cambridge University Press, Cambridge, 2007.
- [30] C.E. Carlton, P.J. Ferreira, *"What is behind the inverse Hall-Petch effect in nanocrystalline materials?"*, *Acta Materialia* 55: 3749-3756, 2007.
- [31] A. Considère, *"Annales des Ponts et Chaussées 9"*, 1885.
- [32] N.J. Petch, *"The ductile-brittle transition in the fracture of α -iron: I"*, *Philosophical Magazine* 3: 1089-1097, 1958.
- [33] A.V. Sergueeva, D.M. Hubert, N.A. Mara, A.K. Mukherjee, *"Mechanical properties of nanocomposite materials"*, Elsevier Ltd, 2009.
- [34] O. Kolednik, J. Predan, F.D. Fischer, P. Fratzl, *"Bioinspired Design Criteria for Damage-Resistant Materials with Periodically Varying Microstructure"*, *Advanced Functional Materials* 21: 3634-3641, 2011.
- [35] O. Kolednik, J. Predan, F.D. Fischer, P. Fratzl, *"Improvements of strength and fracture resistance by spatial material property variations"*, *Acta Materialia* 68: 279-294, 2014.
- [36] N.A. Mara, D. Bhattacharyya, P. Dickerson, R.G. Hoagland, A. Misra, *"Ultrahigh strength and ductility of Cu-Nb nanolayered composites"*, *Materials Science Forum* 633-634: 647-653, 2010.
- [37] W.Z. Han, M.J. Demkowicz, N.A. Mara, E.G. Fu, S. Sinha, A.D. Rollett, Y. Wang, J.S. Carpenter, I.J. Beyerlein, A. Misra, *"Design of radiation tolerant materials via interface engineering"*, *Advanced Materials* 25: 6975-6979, 2013.
- [38] M. Wang, I.J. Beyerlein, J. Zhang, W. Han, *"Defect-interface interactions in irradiated Cu / Ag nanocomposites"*, *Acta Materialia* 160: 211-223, 2018.
- [39] W.Z. Han, N.A. Mara, Y.Q. Wang, A. Misra, M.J. Demkowicz, *"He implantation of bulk Cu - Nb nanocomposites fabricated by accumulated roll bonding"*, *Journal of Nuclear Materials* 452: 57-60, 2014.
- [40] N.A. Mara, D. Bhattacharyya, R.G. Hoagland, A. Misra, *"Tensile behavior of 40 nm Cu/Nb nanoscale multilayers"*, *Scripta Materialia* 58: 874-877, 2008.
- [41] A. Misra, M.J. Demkowicz, X. Zhang, R.G. Hoagland, *"The Radiation Damage Tolerance of Ultra-High Strength Nanolayered Composites"*, *JOM*. 59: 3-6, 2007.
- [42] R. Pippan, F. Wetscher, M. Hafok, A. Vorhauer, I. Sabirov, *"The limits of refinement by severe plastic deformation"*, *Advanced Engineering Materials* 8: 1046-1056, 2006.
- [43] R.Z. Valiev, R.K. Islamgaliev, T.V. Alexandrov, *"Bulk nanostructured materials from severe plastic deformation"*, *Progress in Materials Science* 45: 103-189, 2000.
- [44] N. Tsuji, Y. Saito, S.-H. Lee, Y. Minamino, *"ARB (Accumulative Roll-Bonding) and other new Techniques to Produce Bulk Ultrafine Grained Materials"*, *Advanced Engineering Materials* 5: 338-344, 2003.

-
- [45] R.Z. Valiev, *"Paradoxes of Severe Plastic Deformation"*, Advanced Engineering Materials 5: 296-300, 2003.
- [46] R.Z. Valiev, Y. Estrin, Z. Horita, T.G. Langdon, M.J. Zehetbauer, Y.T. Zhu, *"Producing Bulk Ultrafine-Grained Materials by Severe Plastic Deformation"*, JOM 58: 33-39, 2006.
- [47] R.Z. Valiev, Y. Estrin, Z. Horita, T.G. Langdon, M.J. Zehetbauer, Y.T. Zhu, *"Fundamentals of Superior Properties in Bulk NanoSPD Materials"*, Materials Research Letters 4: 1-21, 2016.
- [48] R.Z. Valiev, Y. Estrin, Z. Horita, T.G. Langdon, M.J. Zehetbauer, Y.T. Zhu, *"Producing Bulk Ultrafine-Grained Materials by Severe Plastic Deformation: Ten Years Later"*, JOM 68: 1216-1226, 2016.
- [49] T.G. Langdon, *"Twenty-five years of ultrafine-grained materials: Achieving exceptional properties through grain refinement"*, Acta Materialia 61: 7035-7059, 2013.
- [50] N. Hansen, F.R. Mehl, *"New discoveries in deformed metals"*, Metallurgical and Materials Transactions A 32: 2917-2935, 2001.
- [51] R. Pippan, S. Scheriau, A. Taylor, M. Hafok, A. Hohenwarter, A. Bachmaier, *"Saturation of Fragmentation During Severe Plastic Deformation"*, Annual Review of Materials Research 40: 319-343, 2010.
- [52] R. Pippan, S. Scheriau, A. Hohenwarter, M. Hafok, *"Advantages and limitations of HPT: a review"*, Materials Science Forum 584-586: 16-21, 2008.
- [53] I.J. Beyerlein, A. Caro, M.J. Demkowicz, N.A. Mara, A. Misra, B.P. Uberuaga, *"Radiation damage tolerant nanomaterials"*, Materials Today 16: 443-449, 2013.
- [54] A. Bachmaier, A. Hohenwarter, R. Pippan, *"New procedure to generate stable nanocrystallites by severe plastic deformation"*, Scripta Materialia 61: 1016-1019, 2009.
- [55] A. Bachmaier, R. Pippan, *"Generation of metallic nanocomposites by severe plastic deformation"*, International Materials Reviews 58: 41-62, 2013.
- [56] D. Raabe, M. Herbig, S. Sandlöbes, Y. Li, D. Tytko, M. Kuzmina, D. Ponge, P.-P. Choi, *"Grain boundary segregation engineering in metallic alloys: A pathway to the design of interfaces"*, Current Opinion in Solid State and Materials Science 18: 253-261, 2014.
- [57] G. Agricola, *"De Re Metallica"*, J. Froben & N. Episcopius, Basel, 1556.
- [58] P. Lejcek, *"Grain Boundary Segregation in Metals"*, Springer Berlin-Heidelberg, Berlin, Heidelberg, 2010.
- [59] P.G. Shewmon, *"Grain boundary cracking"*, Metallurgical and Materials Transactions B 29: 1535, 1998.
- [60] M.A. Gibson, C.A. Schuh, *"Segregation-induced changes in grain boundary cohesion and embrittlement"*, Acta Materialia 95: 145-155, 2015

- [61] H. Lee, V. Tomar, "An examination of nickel doping effect on the mechanical strength of a tungsten grain boundary", *Computational Materials Science* 77: 131-138, 2013.
- [62] P. Lejcek, M. Sob, V. Paidar, "Interfacial segregation and grain boundary embrittlement: An overview and critical assessment of experimental data and calculated results", *Progress in Materials Science* 87: 83-139, 2017.
- [63] X. Wu, Y. You, X. Kong, J. Chen, G. Luo, G. Lu, C.S. Liu, Z. Wang, "First-principles determination of grain boundary strengthening in tungsten: Dependence on grain boundary structure and metallic radius of solute", *Acta Materialia* 120: 315-326, 2016.
- [64] K. Leitner (née Babinsky), P.J. Felfer, D. Holec, J.M. Cairney, W. Knabl, A. Lorich, H. Clemens, S. Primig, "On grain boundary segregation in molybdenum materials", *Materials & Design* 135: 204-212, 2017.
- [65] R. Wu, A.J. Freeman, G.B. Olson, "First Principles Determination of the Effects of Phosphorus and Boron on Iron Grain Boundary Cohesion", *Science* 265: 376-380, 1994.
- [66] V.I. Razumovskiy, A.Y. Lozovoi, I.M. Razumovskii, "First-principles-aided design of a new Ni-base superalloy: Influence of transition metal alloying elements on grain boundary and bulk cohesion", *Acta Materialia* 82: 369-377, 2015.
- [67] D. Scheiber, R. Pippan, P. Puschnig, L. Romaner, "Ab initio search for cohesion-enhancing impurity elements at grain boundaries in molybdenum and tungsten", *Modelling and Simulation in Materials Science and Engineering* 24: 85009, 2016.
- [68] D. Scheiber, R. Pippan, P. Puschnig, A. Ruban, L. Romaner, "Ab-initio search for cohesion-enhancing solute elements at grain boundaries in molybdenum and tungsten", *International Journal of Refractory Metals and Hard Materials* 60: 75-81, 2016.
- [69] C.T. Liu, C.L. White, J.A. Horton, "Effect of boron on grain-boundaries in Ni_3Al ", *Acta Metallurgica* 33: 213-229, 1985.
- [70] H. Clemens, S. Mayer, "Design, Processing, Microstructure, Properties, and Applications of Advanced Intermetallic TiAl Alloys", *Advanced Engineering Materials* 15: 191-215, 2013.
- [71] H. Clemens, S. Mayer, "Intermetallic titanium aluminides in aerospace applications - processing, microstructure and properties", *Materials at High Temperatures* 33: 560-570, 2016.
- [72] A.J. Detor, C.A. Schuh, "Grain boundary segregation, chemical ordering and stability of nanocrystalline alloys: Atomistic computer simulations in the Ni-W system", *Acta Materialia* 55: 4221-4232, 2007.
- [73] D. Raabe, S. Sandlöbes, J. Millán, D. Ponge, H. Assadi, M. Herbig, P.-P. Choi, "Segregation engineering enables nanoscale martensite to austenite phase transformation at grain boundaries: a pathway to ductile martensite", *Acta Materialia* 61: 6132-6152, 2013.

- [74] M. Kuzmina, D. Ponge, D. Raabe, "Grain boundary segregation engineering and austenite reversion turn embrittlement into toughness: Example of a 9 wt.% medium Mn steel", *Acta Materialia* 86: 182-192, 2015.
- [75] Z. Pan, T.J. Rupert, "Amorphous intergranular films as toughening structural features", *Acta Materialia* 89: 205-214, 2015.
- [76] A. Khalajhedayati, Z. Pan, T.J. Rupert, "Manipulating the interfacial structure of nanomaterials to achieve a unique combination of strength and ductility", *Nature Communications* 7: 10802, 2016.
- [77] G.H. Balbus, J. Kappacher, D.J. Sprouster, F. Wang, J. Shin, Y.M. Eggeler, T.J. Rupert, J.R. Trelewicz, D. Kiener, V. Maier-Kiener, D.S. Gianola, "Disordered interfaces enable high temperature thermal stability and strength in a nanocrystalline aluminium alloy", *Acta Materialia* 215: 116973, 2021
- [78] E. Lassner, W.-D. Schubert, "Tungsten - Properties, Chemistry, Technology of the Element, Alloy, and Chemical Compounds", Kluwer Academic / Plenum Publishers, New York, 1999.
- [79] A. Giannattasio, Z. Yao, E. Tarleton, S.G. Roberts, "Brittle-ductile transitions in polycrystalline tungsten", *Philosophical Magazine* 90: 3947-3959, 2010.
- [80] C. Chang, D. Terentyev, A. Zinozev, W. Van Renterghem, C. Yin, P. Verleysen, T. Pardoen, M. Vilemove, J. Matejicek, "Irradiation-induced hardening in fusion relevant tungsten grades with different initial microstructures", *Physica Scripta* 96: 124021, 2021.
- [81] M. Rieth, D.E.J. Armstrong, B. Dafferner, S. Heger, A. Hoffmann, M.-D. Hoffmann, U. Jäntschi, C. Kübel, E. Materna-Morris, J. Reiser, M. Rohde, T. Scherer, V. Widak, H. Zimmermann, "Tungsten as a Structural Divertor Material", *Advances in Science and Technology* 73: 11-21, 2010.
- [82] S. Wurster, N. Baluc, M. Battabyal, T. Crosby, J. Du, C. Garcia-Rosales, A. Hasegawa, A. Hoffmann, A. Kimura, H. Kurishita, R.J. Kurtz, J. Li, S. Noh, J. Reiser, J. Riesch, M. Rieth, W. Setyawan, M. Walter, J.-H. You, R. Pippan, "Recent progress in R&D on tungsten alloys for divertor structural and plasma facing materials", *Journal of Nuclear Materials* 442: 181-189, 2013.
- [83] M. Rieth, S.L. Dudarev, S.M. Gonzalez de Vicente, J. Aktaa, T. Ahlgren, S. Antusch, D.E.J. Armstrong, M. Balden, N. Baluc, M.-F. Barthe, W.W. Basuki, M. Battabyal, C.S. Becquart, D. Blagoeva, H. Boldyryeva, J. Brinkmann, M. Celino, L. Ciupinski, J.B. Correia, A. De Backer, C. Domain, E. Gaganidze, C. Garcia-Rosales, J. Gibson, M.R. Gilbert, S. Giusepponi, B. Gludovatz, H. Greuner, K. Heinola, T. Höschel, A. Hoffmann, N. Holstein, F. Koch, W. Krauss, H. Li, S. Lindig, J. Linke, Ch. Linsmeier, P. Lopez-Ruiz, H. Maier, J. Matejicek, T.P. Mishra, M. Muhammed, A. Munoz, M. Muzyk, K. Nordlund, D. Nguyen-Manh, J. Opschoor, N. Ordas, T. Palacios, G. Pintsuk, R. Pippan, J. Reiser, J. Riesch, S.G. Roberts, L. Romaner, M. Rosinski, M. Sanchez, W. Schulmeyer, H. Traxler,

- A. Urena, J.G. van der Laan, L. Veleva, S. Wahlberg, M. Walter, T. Weber, T. Weitkamp, S. Wurster, M.A. Yar, J.H. You, A. Zivelonghi, "Recent progress in research on tungsten materials for nuclear fusion applications in Europe", *Journal of Nuclear Materials* 432: 482-500, 2013.
- [84] J.W. Davis, V.R. Barabash, A. Makhankov, L. Plöchl, K.T. Slattery, "Assessment of tungsten for use in the ITER plasma facing components", *Journal of Nuclear Materials* 258-263: 308-312, 1998.
- [85] C. Ren, Z. Zak Fang, M. Koopman, B. Butler, J. Paramore, S. Middlemas, "Methods for improving ductility of tungsten - A review", *International Journal of Refractory Metals and Hard Materials* 75: 170-183, 2018.
- [86] J. Reiser, J. Hoffmann, U. Jäntschi, M. Klimenkov, S. Bonk, C. Bonnekoh, A. Hoffmann, T. Mrotzek, M. Rieth, "Ductilisation of tungsten (W): On the increase of strength AND room-temperature tensile ductility through cold-rolling", *International Journal of Refractory Metals and Hard Materials* 64: 261-278, 2017.
- [87] D. Maisonnier, "European DEMO design and maintenance strategy", *Fusion Engineering and Design* 83: 858-864, 2008.
- [88] T.R. Barrett, G. Ellwood, G. Perez, M. Kovari, M. Fursdon, F. Domptail, S. Kirk, S.C. McIntosh, S. Roberts, S. Zheng, L.V. Boccaccini, J.-H. You, C. Bachmann, J. Reiser, M. Rieth, E. Visca, G. Mazzone, F. Arbeiter, P.K. Domalapally, "Progress in the engineering design and assessment of the European DEMO first wall and divertor plasma facing components", *Fusion Engineering and Design* 109-111: 917-924, 2016.
- [89] S. Wurster, "Fracture behavior of tungsten based materials", Montanuniversität Leoben, Leoben, 2011.
- [90] F.I. Allen, P. Hosemann, M. Balooch, "Key mechanistic features of swelling and blistering of helium-ion-irradiated tungsten", *Scripta Materialia* 178: 256-260, 2020.
- [91] O. El-Atwani, S. Gonderman, M. Efe, G. De Temmerman, T. Morgan, K. Bystrov, D. Klenosky, T. Qiu, J.P. Allain, "Ultrafine tungsten as a plasma-facing component in fusion devices: effect of high flux, high fluence low energy helium irradiation", *Nuclear Fusion* 54: 083013, 2014.
- [92] O. El-Atwani, J.A. Hinks, G. Greaves, J.P. Allain, S.A. Maloy, "Grain size threshold for enhanced irradiation resistance in nanocrystalline and ultrafine tungsten", *Materials Research Letters* 5: 343-349, 2017.
- [93] Y. Yang, D. Frazer, M. Balooch, P. Hosemann, "Irradiation damage investigation of helium implanted polycrystalline copper", *Journal of Nuclear Materials* 512: 137-143, 2018.
- [94] M. Wurmshuber, D. Frazer, M. Balooch, I. Issa, A. Bachmaier, P. Hosemann, D. Kiener, "The effect of grain size on bubble formation and evolution in helium-irradiated Cu-Fe-Ag", *Materials Characterization* 171: 110822, 2021.

- [95] S. Cierjacks, "Nuclear data needs for "low-activation" fusion materials development", *Fusion Engineering and Design* 13: 229-238, 1990.
- [96] K.L. Murty, I. Charit, "An Introduction to Nuclear Materials - Fundamentals and Applications", Wiley-VCH, Weinheim, 2013.
- [97] W.D. Klopp, "Review of ductilizing of group VIA elements by rhenium and other solutes", NASA TN D-4955, 1968.
- [98] L. Romaner, C. Ambrosch-Draxl, R. Pippan, "Effect of rhenium on the dislocation core structure in tungsten", *Physical Review Letters* 104: 195503, 2010.
- [99] S. Wurster, B. Gludovatz, A. Hoffmann, R. Pippan, "Fracture behaviour of tungsten-vanadium and tungsten-tantalum alloys and composites", *Journal of Nuclear Materials* 413: 166-176, 2011.
- [100] J.H. You, "Copper matrix composites as heat sink materials for water-cooled divertor target", *Nuclear Materials and Energy* 5: 7-18, 2015.
- [101] E. Tejado, "W-Cu metal matrix composites for next generation fusion devices", *Materials Today* 38: 136-137, 2020.
- [102] E. Tejado, A. v. Müller, J.-H. You, J.Y. Pastor, "The thermo-mechanical behaviour of W-Cu metal matrix composites for fusion heat sink applications: The influence of the Cu content", *Journal of Nuclear Materials* 498: 468-475, 2018.
- [103] G. Pintsuk, S.E. Brünings, J.-E. Döring, J. Linke, I. Smid, L. Xue, "Development of W/Cu-functionally graded materials", *Fusion Engineering and Design* 66-68: 237-240, 2003.
- [104] T.B. Massalski, H. Okamoto, P.R. Subramanian, L. Kacprzak, "Binary Alloy Phase Diagrams", William W. Scott Pub., New York, 1990.
- [105] M. Wurmshuber, S. Doppermann, S. Wurster, D. Kiener, "Ultrafine-grained Tungsten by High-Pressure Torsion - Bulk precursor versus powder processing route", *IOP Conference Series: Materials Science and Engineering* 580: 012051, 2019.
- [106] M. Wurmshuber, S. Jakob, S. Doppermann, S. Wurster, R. Bodlos, L. Romaner, V. Maier-Kiener, D. Kiener, "Tuning mechanical properties of ultrafine-grained tungsten by manipulating grain boundary chemistry", *Acta Materialia* 232: 117939, 2022.
- [107] M. Wurmshuber, M. Alfreider, S. Wurster, R. Pippan, D. Kiener, "Small-scale fracture mechanical investigations of grain boundary doped ufg tungsten", Submitted to *Acta Materialia*.
- [108] M. Wurmshuber, M. Burtscher, R. Bodlos, D. Scheiber, L. Romaner, D. Kiener, "Mechanical performance of doped W-Cu nanocomposites", Submitted to *Materials Science and Engineering: A*.
- [109] M. Wurmshuber, M. Balooch, X. Huang, P. Hosemann, D. Kiener, "Helium-induced swelling and mechanical property degradation in ultrafine-grained W and W-Cu nanocomposites for fusion applications", *Scripta Materialia* 213: 114641, 2022.

- [110] A. Warren, A. Nylund, I. Olefjord, "Oxidation of Tungsten and Tungsten Carbide in Dry and Humid Atmospheres", *International Journal of Refractory Metals & Hard Materials* 14: 345-353, 1996.
- [111] I. Sabirov, R. Pippan, "Formation of a W-25%Cu nanocomposite during high pressure torsion", *Scripta Materialia* 52: 1293-1298, 2005.
- [112] I. Sabirov, R. Pippan, "Characterization of tungsten fragmentation in a W-25%Cu composite after high-pressure torsion", *Materials Characterization* 58: 848-853, 2007.
- [113] S. Doppermann, "Parameters affecting refinement of powder-based W-Cu composites during high pressure torsion", Montanuniversität Leoben, Leoben, 2021.
- [114] G.B. Rathmayr, R. Pippan, "Influence of impurities and deformation temperature on the saturation microstructure and ductility of HPT-deformed nickel", *Acta Materialia* 59: 7228-7240, 2011.
- [115] V. Maier, K. Durst, J. Mueller, B. Backes, H.W. Höppel, M. Göken, "Nanoindentation strain-rate jump tests for determining the local strain-rate sensitivity in nanocrystalline Ni and ultrafine-grained Al", *Journal of Materials Research* 26: 1421-1430, 2011.
- [116] V. Maier-Kiener, K. Durst, "Advanced Nanoindentation Testing for Studying Strain-Rate Sensitivity and Activation Volume", *JOM* 69: 2246-2255, 2017.
- [117] B. Sestak, A. Seeger, "Gleitung und Verfestigung in kubisch-raumzentrierten Metallen", *Zeitschrift für Metallkunde* 69, 1978.
- [118] A. Seeger, "The Temperature and Strain-Rate Dependence of the Flow Stress of Body-Centered Cubic Metals: A Theory Based on Kink-Kink Interactions", *Zeitschrift für Metallkunde* 72: 369-380, 1981.
- [119] D. Kiener, R. Fritz, M. Alfreider, A. Leitner, R. Pippan, V. Maier-Kiener, "Rate Limiting Deformation Mechanisms of bcc Metals in Confined Volumes", *Acta Materialia* 166: 687-701, 2019.
- [120] M. Alfreider, M. Meindlhumer, V. Maier-Kiener, A. Hohenwarter, D. Kiener, "Extracting information from noisy data: strain mapping during dynamic in-situ SEM experiments", *Journal of Materials Research* 36: 2291-2304, 2021.
- [121] X. Huang, N. Hansen, N. Tsuji, "Hardening by Annealing and Softening by Deformation in Nanostructured Metals", *Science* 312: 249-251, 2006.
- [122] O. Renk, A. Hohenwarter, K. Eder, K.S. Kormout, J.M. Cairney, R. Pippan, "Increasing the strength of nanocrystalline steels by annealing: Is segregation necessary?", *Scripta Materialia* 95: 27-30, 2015.
- [123] H. Van Swygenhoven, J.R. Weertman, "Deformation in nanocrystalline metals", *Materials Today* 9: 24-31, 2006.
- [124] H. Van Swygenhoven, "Footprints of plastic deformation in nanocrystalline metals", *Materials Science and Engineering A* 483-484: 33-39, 2008.

- [125] M. Wurmshuber, D. Frazer, A. Bachmaier, Y. Wang, P. Hosemann, D. Kiener, "Impact of interfaces on the radiation response and underlying defect recovery mechanisms in nanostructured Cu-Fe-Ag", *Materials & Design* 160: 1148-1157, 2018.
- [126] B. Lüthi, L. Ventelon, C. Elsässer, D. Rodney, F. Willaime, "First principles investigation of carbon-screw dislocation interactions in body-centered cubic metals", *Modelling and Simulation in Materials Science and Engineering* 25: 84001, 2017.
- [127] R. Pippan, S. Wurster, D. Kiener, "Fracture mechanics of micro samples: Fundamental considerations", *Materials & Design* 159: 252-267, 2018.
- [128] G. Dehm, B.N. Jaya, R. Raghavan, C. Kirchlechner, "Overview on micro- and nanomechanical testing: New insights in interface plasticity and fracture at small length scales", *Acta Materialia* 142: 248-282, 2018.
- [129] J. Ast, M. Ghidelli, K. Durst, M. Göken, M. Sebastiani, A.M. Korsunsky, "A review of experimental approaches to fracture toughness evaluation at the micro-scale", *Materials & Design* 173: 107762, 2019.
- [130] B.N. Jaya, C. Kirchlechner, G. Dehm, "Can microscale fracture tests provide reliable fracture toughness values? A case study in silicon", *Journal of Materials Research* 30: 686-698, 2015.
- [131] A.K. Saxena, S. Brinckmann, B. Völker, G. Dehm, C. Kirchlechner, "Experimental conditions affecting the measured fracture toughness at the microscale: Notch geometry and crack extension measurement", *Materials & Design* 191: 108582, 2020.
- [132] S. Wurster, C. Motz, R. Pippan, "Characterization of the fracture toughness of micro-sized tungsten single crystal notched specimens", *Philosophical Magazine* 92: 1803-1825, 2012.
- [133] P. Hosemann, "Small-scale mechanical testing on nuclear materials: bridging the experimental length-scale gap", *Scripta Materialia* 143: 161-168, 2018.
- [134] D. Kiener, A.M. Minor, O. Anderoglu, Y. Wang, S.A. Maloy, "Application of small-scale testing for investigation of ion-beam-irradiated materials", *Journal of Materials Research* 27: 2724-2736, 2012.
- [135] P. Hosemann, C. Shin, D. Kiener, "Small scale mechanical testing of irradiated materials", *Journal of Materials Research* 30: 1231-1245, 2015.
- [136] J.P. Wharry, K.H. Yano, P.V. Patki, "Intrinsic-extrinsic size effect relationship for micromechanical tests", *Scripta Materialia* 162: 63-67, 2019.
- [137] P. Hosemann, D. Kiener, Y. Wang, S.A. Maloy, "Issues to consider using nano indentation on shallow ion beam irradiated materials", *Journal of Nuclear Materials* 425: 136-139, 2012.
- [138] H.T. Vo, A. Reichardt, D. Frazer, N. Bailey, P. Chou, P. Hosemann, "In situ micro-tensile testing on proton beam-irradiated stainless steel", *Journal of Nuclear Materials* 493: 336-342, 2017.

- [139] C.K. Dolph, D.J. da Silva, M.J. Swenson, J.P. Wharry, "Plastic zone size for nanoindentation of irradiated Fe-9%Cr ODS", *Journal of Nuclear Materials* 481: 33-45, 2016
- [140] K.H. Yano, M.J. Swenson, Y. Wu, J.P. Wharry, "TEM in situ micropillar compression tests of ion irradiated oxide dispersion strengthened alloy", *Journal of Nuclear Materials* 483: 107-120, 2017.
- [141] M. Alfreider, D. Kozic, O. Kolednik, D. Kiener, "In-situ elastic-plastic fracture mechanics on the microscale by means of continuous dynamical testing", *Materials & Design* 148: 177-187, 2018.
- [142] T.L. Anderson, "Fracture Mechanics: Fundamentals and Applications", Taylor & Francis Group, Boca Raton, 2017.
- [143] G.R. Irwin, Fracture dynamics, *Fracturing of Metals*, American Society for Metals, Cleveland, 1948.
- [144] ASTM Standard E 813-89, ASTM International, 1989.
- [145] D. Leguillon, E. Martin, M.C. Lafarie-Frenot, "Flexural vs. tensile strength in brittle materials", *Comptes Rendus Mecanique* 343: 275–281, 2015.
- [146] P. Sudharshan Phani, K.E. Johanns, E.P. George, G.M. Pharr, "A simple stochastic model for yielding in specimens with limited number of dislocations", *Acta Materialia* 61: 2489–2499, 2013.
- [147] P. Sudharsan Phani, K.E. Johanns, E.P. George, G.M. Pharr, "A stochastic model for the size dependence of spherical indentation pop-in", *Journal of Materials Research* 28: 2728–2739, 2013.
- [148] Y. Liu, J. Zhou, L. Wang, S. Zang, Y. Wang, "Grain size dependent fracture toughness of nanocrystalline materials", *Materials Science and Engineering A* 528: 4615-4619, 2011.
- [149] D.E.J. Armstrong, A.S.M.A. Haseeb, S.G. Roberts, A.J. Wilkinson, K. Bade, "Nanoindentation and micro-mechanical fracture toughness of electrodeposited nanocrystalline Ni-W alloy films", *Thin Solid Films* 520: 4369-4372, 2012.
- [150] R. Hahn, M. Bartosik, R. Soler, C. Kirchlechner, G. Dehm, P.H. Mayrhofer, "Superlattice effect for enhanced fracture toughness of hard coatings", *Scripta Materialia* 124: 67-70, 2016.
- [151] F.I. Allen, "A review of defect engineering, ion implantation, and nanofabrication using the helium ion microscope", *Beilstein Journal of Nanotechnology* 12: 633-664, 2021.
- [152] J.F. Ziegler, J.P. Biersack, "SRIM - The Stopping and Range of Ions in Solids", 1985.
- [153] A. Bhattacharya, S.J. Zinkle, "Cavity Swelling in Irradiated Materials", In *Comprehensive Nuclear Materials*, Elsevier, 2020.
- [154] K.L. Johnson, "The correlation of indentation experiments", *Journal of the Mechanics and Physics of Solids* 18: 115-126, 1970.

- [155] M. Mata, O. Casals, J. Alcala, "*The plastic zone size in indentation experiments: The analogy with the expansion of a spherical cavity*", *International Journal of Solids and Structures* 43: 5994-6013, 2006.

Appendix

The following publications are appended to this thesis:

Publication A

M. Wurmshuber, S. Doppermann, S. Wurster, D. Kiener

Ultrafine-grained Tungsten by High-Pressure Torsion - Bulk precursor versus powder processing route

IOP Conference Series: Materials Science and Engineering 580: 012051, 2019. doi:10.1088/1757-899X/580/1/012051

Publication B

M. Wurmshuber, S. Jakob, S. Doppermann, S. Wurster, R. Bodlos, L. Romaner, V. Maier-Kiener, D. Kiener

Tuning mechanical properties of ultrafine-grained tungsten by manipulating grain boundary chemistry

Acta Materialia 232: 117939, 2022. doi:10.1016/j.actamat.2022.117939

Publication C

M. Wurmshuber, M. Alfreider, S. Wurster, R. Pippan, D. Kiener

Small-scale fracture mechanical investigations of grain boundary doped ufg tungsten

Submitted to Acta Materialia

Publication D

M. Wurmshuber, M. Burtscher, S. Doppermann, R. Bodlos, D. Scheiber, L. Romaner, D. Kiener

Mechanical performance of doped W-Cu nanocomposites

Submitted to Materials Science and Engineering: A

Publication E

M. Wurmshuber, M. Balooch, X. Huang, P. Hosemann, D. Kiener

Helium-induced swelling and mechanical property degradation in ultrafine-grained W and W-Cu nanocomposites for fusion applications

Scripta Materialia 213: 114641, 2022. doi:10.1016/j.scriptamat.2022.114641

Remark

In the appended papers, I, Michael Wurmshuber, performed all experiments, data analyses and was the primary author with the following exceptions:

- Simon Dopfermann assisted with sample preparation in all publications.
- Stefan Wurster provided help with sample fabrication and interpretation of results in Publications A, B and C.
- Severin Jakob performed and analyzed the APT measurements in Publication B.
- Rishi Bodlos, Daniel Scheiber and Lorenz Romaner provided DFT calculations and helped interpreting results in Publications B and D.
- Markus Alfreider contributed to Publication C with providing FEM simulations and interpretation of results.
- Reinhard Pippan contributed to Publication C with helpful advice and interpretation of results.
- Michael Burtscher performed all TEM investigations in Publication D.
- Mehdi Balooch and Xi Huang performed helium implantation, AFM measurements and nanoindentation measurements in Publication E.
- Peter Hosemann helped designing the experiments in Publication E.
- Daniel Kiener contributed to all publications with principal ideas from design of experiments to final analysis and interpretation of results.

Further publications

- M. Wurmshuber, D. Frazer, M. Balooch, I. Issa, A. Bachmaier, P. Hosemann, D. Kiener, *The effect of grain size on bubble formation and evolution in helium-irradiated Cu-Fe-Ag*, *Materials Characterization*, 171: 110822, 2021.
- M. Wurmshuber, D. Frazer, A. Bachmaier, Y. Wang, P. Hosemann, D. Kiener, *Impact of interfaces on the radiation response and underlying defect recovery mechanisms in nanostructured Cu-Fe-Ag*, *Materials & Design* 160 : 1148-1157, 2018.
- S.-H. Oh, J.-K. Kim, Y. Liu, M. Wurmshuber, ... , H. Gao, *Limpet teeth microstructure unites auxeticity with extreme strength and high stiffness*, Submitted to *Science Advances*.
- M. Burtscher, M. Zhao, J. Kappacher, A. Leitner, M. Wurmshuber, M. Pfeifenberger, V. Maier-Kiener, D. Kiener, *High-Temperature Nanoindentation of an Advanced Nano-Crystalline W/Cu Composite*, *Nanomaterials* 11:2951, 2021.
- M. Gsellmann, T. Klünsner, C. Mitterer, M. Krobath, M. Wurmshuber, H. Leitner, W. Ecker, S. Marsoner, V. Maier-Kiener, D. Kiener, G. Ressel, *Strength ranking for interfaces between a TiN hard coating and microstructural constituents of high speed steel determined by micromechanical testing*, *Materials & Design* 204:109690, 2021.
- M. Zhao, K. Schlueter, M. Wurmshuber, M. Reitgruber, D. Kiener, *Open-cell tungsten nanofoams: Scaling behavior and structural disorder dependence of Young's modulus and flow strength*, *Materials & Design* 197:109187, 2021.
- M. Zhao, I. Issa, M.J. Pfeifenberger, M. Wurmshuber, D. Kiener, *Tailoring ultra-strong nanocrystalline tungsten nanofoams by reverse phase dissolution*, *Acta Materialia* 182: 215-225, 2020

A Ultrafine-grained Tungsten by High-Pressure Torsion - Bulk precursor versus powder processing route

M. Wurmshuber¹, S. Dopfermann¹, S. Wurster², D. Kiener¹

¹ Department of Materials Science, Montanuniversität Leoben, Jahnstraße 12, 8700 Leoben, Austria

² Erich-Schmid Institute for Materials Science, Austrian Academy of Sciences, Jahnstraße 12, 8700 Leoben, Austria

The continuous enhancements and developments in the field of power engineering, as well as the uprising of nuclear fusion technology, demand novel high performance materials featuring exceptional strength and damage tolerance as well as durability in harsh environments. Ultra-fine grained bulk materials fabricated by high-pressure torsion, exhibiting a grain size less than 500 nm are promising candidates for these applications. Tungsten, the material of choice for plasma-facing materials in fusion reactors, is expected to exhibit even more enhanced properties by precise doping with impurity atoms, strengthening grain boundary cohesion. In order to allow this meticulous control of chemical composition, in-house mixing of the raw material powders is preferable to use of commercially available alloys. Several challenges arise in powder processing of tungsten via high-pressure torsion, originating in the intrinsic strength and high melting point of the material, and in the affinity of the powder to oxygen. Strategies to overcome these problems will be addressed in this work. Furthermore, we compare ultra-fine grained tungsten produced from a bulk precursor to that from the developed powder approach regarding microstructural features, hardness and rate-sensitive properties. The powder route showed promising and widely comparable results to the material processed from bulk tungsten, rendering it an effective way for fabricating ultra-strong tungsten, while keeping the additional ability to accurately control chemical composition and tailor grain boundary segregation states.

A.1 Motivation

When it comes to implementing new ground-breaking technologies or optimizing and improving existing concepts in the sectors of power engineering, nuclear engineering, armored protection or other safety relevant applications, materials fulfilling the

required standards are often the limiting factor. Ultrastrong and damage tolerant materials are of demand in these fields of application: two characteristics that are deemed mutually exclusive in many conventional materials. Nanostructured and ultra-fine grained (ufg) metals are a promising material class to combine high strength with enhanced damage tolerance [1,2], while also featuring additional beneficial properties such as radiation tolerant behavior [3,4]. While tungsten is frequently considered as candidate material for the mentioned high performance applications due to its physical properties [5–7], a rather low fracture toughness and high ductile-brittle transition temperature often impedes the utilization of tungsten-based materials. The grain boundaries are found to be one of the weak links. However, ab-initio simulations revealed that by controlling grain boundary chemistry, the grain boundary cohesion can be increased [8–10]. The consequences are repression of intercrystalline fracture, the preferred fracture mode in nanostructured materials [1,2], based on which an enhanced fracture toughness can be expected [10]. Severe plastic deformation techniques, such as high-pressure torsion (HPT), have gained a lot of interest in recent years, as they introduce a high amount of deformation and microstructural refinement to materials, creating ultra-fine grained or nanocrystalline bulk materials. During HPT, a millimeter-sized, disk-shaped specimen is shear-deformed between two anvils under high confining pressure (several GPa). The applied von Mises-strain during HPT can be calculated using the number of rotations, the distance from the center of the disk and the thickness of the sample. Further details of the HPT process are reported elsewhere [11–13]. In order to control chemical composition precisely, a powder approach is necessary. Yet, before the chemical composition of tungsten can be altered, it must first be proven that it is possible to fabricate pure ufg tungsten with satisfactory properties from a powder starting material. Since several challenges arise with powder processing of tungsten at low temperatures using HPT, this work will address these problems and ways to mediate them. Finally, ufg tungsten samples produced from powder and a bulk precursor are compared regarding their mechanical properties.

A.2 Challenges with powder processing of ufg W via HPT

In order to realize systematic doping of tungsten grain boundaries, the local chemical composition of the material has to be tuned precisely. To investigate the effect of impurity atoms on the material properties thoroughly, a large number of samples with varying doping concentrations must be fabricated and characterized. Therefore, an in-house fabrication method is essential to provide a fast and easy route for processing such doped material samples, as well as to ensure access to crucial processing parameters. A powder metallurgical approach seems to be the best choice

to realize this. When it comes to high-performance materials, their extraordinary properties that are desired for many of their applications often provide the biggest challenges and limitations in terms of fabrication. Tungsten is yet another example of this phenomenon, as its exceptional intrinsic strength and high melting point result in several problems that have to be tackled when processing ufg tungsten from powders on a laboratory scale. The most severe challenges that need to be handled will be addressed in this section:

A.2.1 Oxidation and contamination of powders

Oxidation and contamination is not only a problem for tungsten powder in particular, but for most metal powders in general. The small particle size of the powders (< 100 μm) leads to a high contact area with the surrounding atmosphere. In air and under humid conditions this can result in severe oxidation or contamination of powder particle surfaces. After processing from oxidized powder, the final components exhibit not only an oxidation layer on the surface, which could be removed rather easily, but also within the material, leading to considerable and most likely unwanted changes in material properties. Furthermore, the high hardness of metal oxides can lead to problems with compacting the powder particles or during later sintering, where oxides usually act as diffusion barriers.

In the case of W, oxidation by air already occurs at room temperature (RT). The oxidation rate accelerates significantly with increasing temperature and humidity. The oxide formed is always WO_3 , which becomes volatile at temperatures above 750°C , leading to consumption of the material [6,14].

As powder oxidation has been a well known problem for decades, several solutions exist today. The most convenient one is storing and handling all powders within a so-called glovebox, a sealed container with a desired inert atmosphere (e.g. argon) inside. It is crucial that all powders are opened and manipulated inside the box using the designated gloves and that the oxygen and humidity level is kept to a minimum. For transporting the powder mixture outside of the box to the compacting facility (in this case the HPT tool) a small sealed container was utilized that has to be assembled together with the HPT anvils and the powder inside the glovebox (Figure A.1). This way the powder mixture can be transported from to the HPT tool in a local argon atmosphere and compacted without unwanted oxidation.

A.2.2 Compacting W powder

Due to the easy availability in the lab and the high achievable uniaxial pressures, the HPT tool can also serve as a compacting press for material powders [15,16]. The pressures reached plus a short additional shear straining is sufficient to compact the powders and close pores for most metals. Materials showing high hardness and limited ductility, such as tungsten, typically do not compact well, even under high nominal pressure. Figure A.2a shows a RT compact of W powder by HPT (nominal pressure of 12 GPa). The initial powder particles changed shape due to the high pressure and applied strain, but no connection formed between the particles. The compaction is enough for the samples to be handled, but subsequent deformation by HPT will only lead to the majority of the particles shearing apart without any proper plastic deformation. The result of this deformation is a material containing lots of microcracks and pores along the initial powder particle interfaces (Figure A.2b). A significant improvement in interparticular bonding is expected from annealing the compacted sample, which is discussed in the next subsection.

A.2.3 Sintering W green compacts

Solid state sintering is a popular method to reduce porosity and increase density of powder compacted specimens of high-melting materials, such as refractory metals

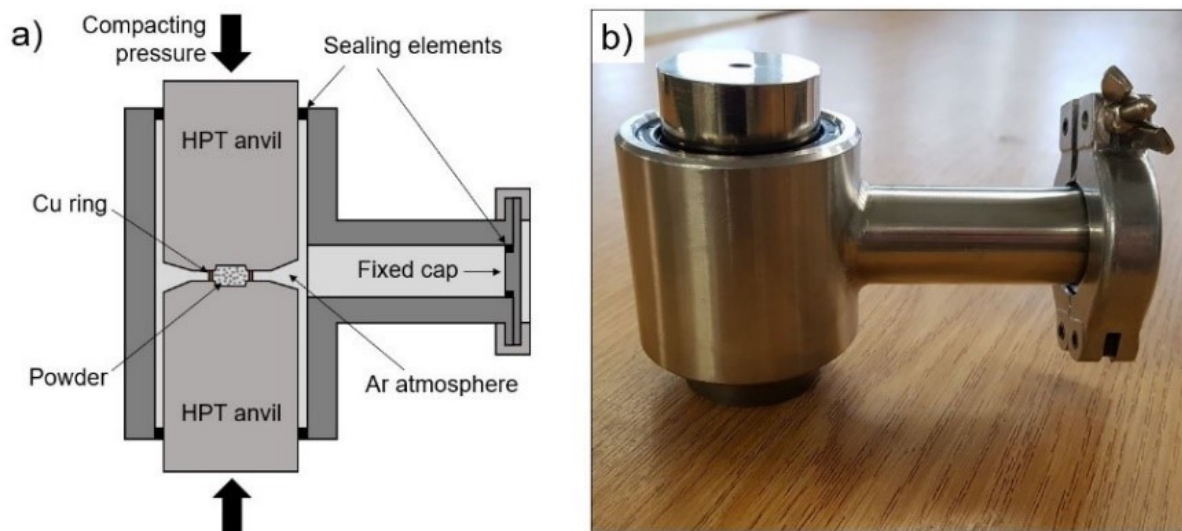


Figure A.1 (a) Sketch and (b) photograph of sealed chamber to allow powder to be transported in local argon atmosphere to the HPT device.

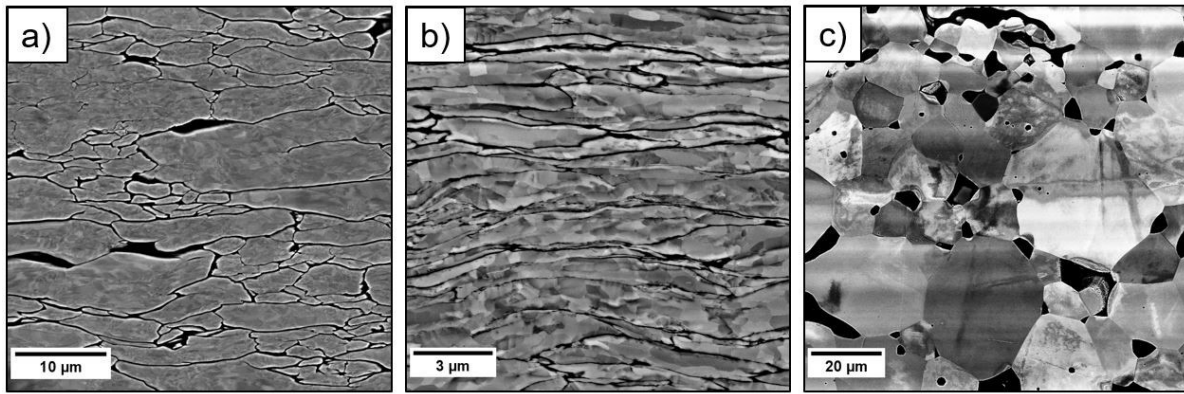


Figure A.2 SEM micrographs (back-scattered mode) of (a) compacted W powder, (b) compacted and deformed W and (c) compacted and sintered W.

and ceramics. The usual temperature range for sintering is $0.6 - 0.8 \cdot T_{\text{melt}} [\text{K}]$ [5,6]. At these elevated temperatures diffusion is enhanced, leading to a redistribution of material and closure of pores. The driving force for this process is the reduction of surface area within the material [5,6]. Conventional sintering temperatures of W are rather high (above 2000°C) due to the high melting point [5,6]. Furthermore, sintering has to be performed either in a reducing gas atmosphere or in vacuum, as oxidation is a serious problem at these temperatures.

In this work, a vacuum furnace with a maximum operating temperature of 1600°C was used for sintering the compacted tungsten samples. The microstructure after sintering is displayed in Figure A.2c. Naturally, the sintering process leads to substantial amount of grain growth, but this should be of no concern, as the subsequent HPT step will re-introduce grain refinement. There is still a large amount of porosity present due to the comparably low sintering temperature and the absence of any pressure applied to the material. However, it is evident that the particles have merged together and formed large grains. Therefore, severe plastic deformation applied during HPT should be able to close the residual pores and deform the material sufficiently to reduce the grain size to the ufg regime. In general, it is beneficial to work with relatively small powders ($< 10 \mu\text{m}$), as they show enhanced surface diffusion, improving the densification by sintering considerably.

A.2.4 Severe plastic deformation of W

While all the limitations from a powder starting material can be handled by adapting the approaches described in the previous subsections, HPT processing of pure W, even from a bulk precursor, is not a straightforward task. High strength, low ductility and the high melting point are again an issue when it comes to severe plastic deformation

of tungsten. The presence of dislocation plasticity is advantageous in order to allow the necessary deformation and grain refinement [13]. For tungsten, a body-centered cubic (BCC) metal, dislocation plasticity is fully thermally activated at 460°C ($0.2 * T_{\text{melt}} [\text{K}]$) [17,18]. On the contrary, in order to deform a material using HPT, the hardness of the anvils (850 HV; tool steel Böhler S390) has to be somewhat higher than the sample [12]. Heating to a temperature above 400°C leads to considerable softening of the anvils. Therefore, a trade-off in deformation temperature is necessary to find the ideal conditions for severe plastic deformation of W. Increasing the applied nominal pressure by decreasing the sample radius also results in better deformability of tungsten.

Even by considering all these aspects, the maximum number of rotations possible by HPT in this work did not exceed 1.5 turns, the equivalent of 1800 % strain, as the material becomes too hard from grain refinement to be further processed by the available anvils.

A.3 Fabrication route for ufg W from powders

The raw tungsten powder (particle size $2\ \mu\text{m}$, purity 99.97%) provided by Plansee SE was opened, stored and handled only in argon atmosphere within a glovebox (M. Braun LABstar Glove Box Workstation). A copper ring is glued around the cavity of the HPT anvil (diameter 6 mm, depth 0.15 mm) to allow more powder to be filled in the cavity without spilling. Subsequently, the sealed mini-chamber is assembled around the powder filled anvil and its counterpart within the glovebox (Figure A.1). The chamber is then inserted in a HPT tool [12] and the powder sample is compacted under a pressure of 12 GPa and deformed for 30-40 seconds at a speed of 0.2 rpm. Afterwards, the mini-chamber is opened and the residual copper around the sample removed. Subsequently, the compacted sample is annealed in a vacuum furnace (Leybold Heraeus PD 1000) at 1600°C for 7 hours at a pressure lower than 10^{-4} mbar. In addition, HPT samples have been manufactured from ultra-high purity tungsten bulk material (99.9999% purity, Plansee SE). The material disks were deformed using the HPT tool with a pressure of 12 GPa at 300°C and 400°C for the maximum amount of turns possible (1 – 1.5 turns).

A.4 Material characterization

After processing, the microstructure of all samples was investigated in the tangential direction using a field-emission scanning electron microscope (SEM; LEO type 1525).

Vickers microhardness was measured along the radius with a load of 500 g (HV0.5) using a Buehler Micromet 5104 machine. Nanoindentation tests were performed with a KLA G200 Nanoindenter using a Berkovich tip and the continuous stiffness measurement (CSM) method [19,20]. Strain rate jump tests [21,22] were conducted with the same nanoindentation setup to investigate strain rate sensitivity and activation volume.

A.5 Results and discussion

A.5.1 Microstructure

Micrographs of all materials at a radius of 3 mm (outer edge of the HPT deformed disk, corresponding to strains of 10-17) were recorded using the SEM in backscattered electron mode and are displayed in Figure A.3. It is apparent from the micrographs that both bulk and powder processed materials exhibit a similar microstructure and grain sizes of 110-160 nm for each deformation temperature, as detailed in Table A.1. No pores or oxide layers are visible in the samples fabricated from powders.

A.5.2 Microhardness

Microhardness testing is a fast method to assess the gradient in mechanical properties in HPT deformed materials to check whether the deformation was high enough to reach the saturation state, i.e. the point where grain size cannot be refined any further due to a dynamic equilibrium of dislocation generation and annihilation [13]. The trend of measured microhardness with applied von Mises-strain for all

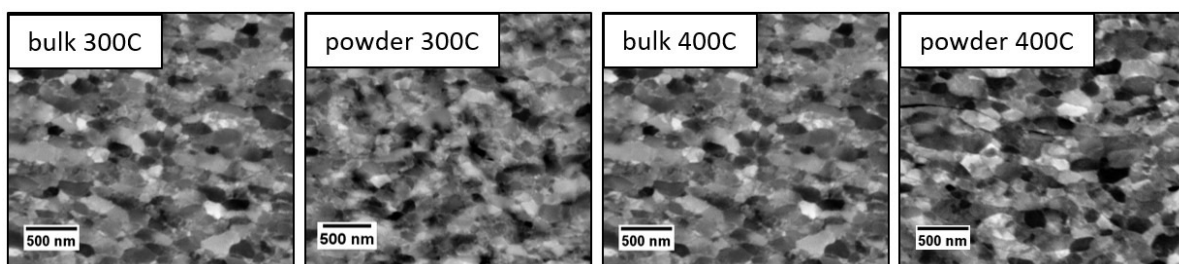


Figure A.3 SEM images (backscattered electron mode, same magnification for all images) of resulting microstructures of bulk and powder processed samples after HPT deformation at different temperatures.

Table A.1 Results from microstructural evaluation, microhardness and nanoindentation tests. If not stated otherwise, the values were measured at a radius of 3 mm on the sample disk.

| Deformation temperature Precursor | 300°C | | 400°C | |
|--------------------------------------|---------------|---------------|---------------|---------------|
| | bulk | powder | bulk | powder |
| Grain size @ 3 mm [nm] | 112 ± 19 | 127 ± 25 | 143 ± 26 | 158 ± 36 |
| Grain size @ 1 mm [nm] | 173 ± 39 | 163 ± 46 | 219 ± 66 | 256 ± 78 |
| Microhardness [HV0.5] | 884 | 940 | 871 | 850 |
| Nanohardness [GPa] | 11.17 ± 0.28 | 11.02 ± 0.16 | 10.27 ± 0.08 | 9.96 ± 0.56 |
| Elastic Modulus [GPa] | 394 ± 8 | 410 ± 4 | 402 ± 4 | 408 ± 16 |
| Strain rate sensitivity [-] | 0.016 ± 0.002 | 0.017 ± 0.002 | 0.016 ± 0.002 | 0.015 ± 0.002 |
| Activation volume [b^3] | 6.78 ± 0.89 | 6.21 ± 0.69 | 7.22 ± 0.99 | 7.59 ± 0.82 |

material samples is displayed in Figure A.4a. All samples could be deformed for between 1 and 1.5 turns, corresponding to strains of 10-17. One can observe that the hardness is still increasing at the highest achieved strains, indicating that the saturation regime was not reached for any material and deformation temperature. The hardness gradient over applied strain for both samples deformed at 400°C and for the powder sample deformed at 300°C are in good agreement. The bulk sample deformed at 300°C shows a higher hardness for low strains, which could be due to possible differences in the initial microstructure. At high strains, this sample shows a similar hardness trend as all other samples.

To allow a better correlation with the mechanical properties gained from microhardness tests, the grain sizes were evaluated at a radius of 1 mm and 3 mm using the grain intercept method (see Table A.1). When plotting the hardness versus the inverse square root of the grain size (Figure A.4b), one can see that all materials follow a clear linear trend in accordance with the Hall-Petch relationship [23,24]. The slope of the Hall-Petch line $k_y = 8.7 \text{ kg/mm}^{-3/2}$ is found to be in good agreement with literature ($10 \text{ kg/mm}^{-3/2}$) [25]. Serious contamination or residual pores in the powder processed material should have led to a pronounced deviation from the Hall-Petch behavior of the bulk samples. This is an important finding, as it proves that by adapting the enhancements to the powder processing route presented in Section A.3, the successful fabrication of ufg W with nanostructured grains and a comparable hardness-microstructure relationship than processed from bulk precursor material is possible.

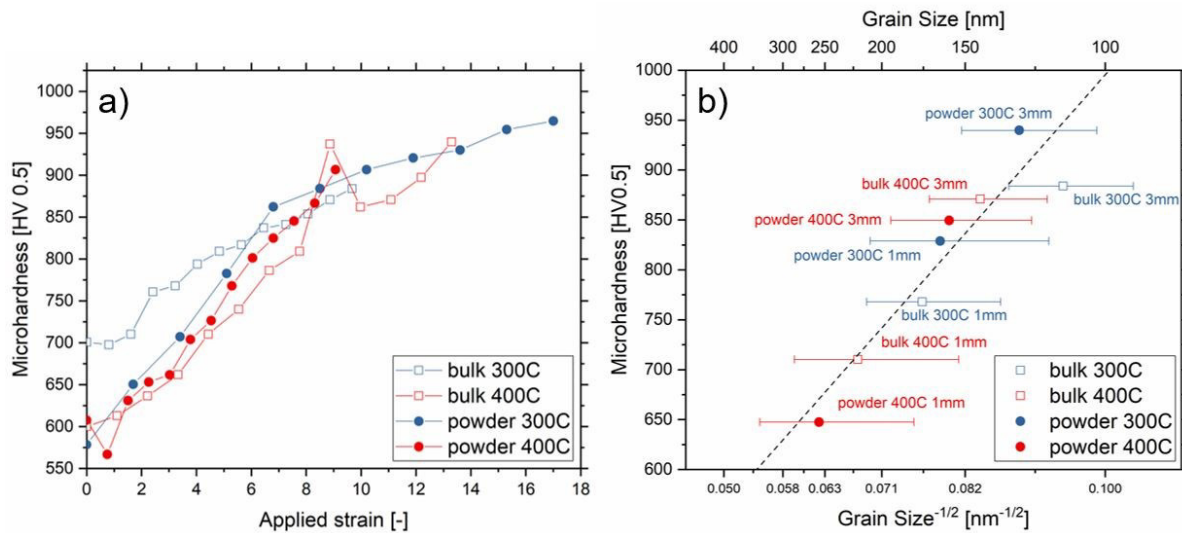


Figure A.4 (a) Microhardness progression with applied HPT strain. (b) Hall-Petch plot of bulk and powder processed samples.

A.5.3 Nanoindentation tests

Nanoindentation provides a locally resolved evaluation of both plastic (hardness) and elastic (modulus) properties of a material. By superimposing a sinusoidal signal on the conventional load signal, a continuous evaluation of hardness and modulus with indentation depth is possible (CSM method) [20]. The results from CSM nanoindentation tests are displayed in Table A.1. All samples were indented at least 6 times at a radius of 3 mm, where the finest grain size and highest hardness values are present. The hardness values from nanoindentation were found to be $\sim 10 - 11$ GPa. The measured elastic moduli lie in the range for the modulus of tungsten reported in literature of 390 – 410 GPa [6,26]. Body-centered cubic and ultra-fine grained metals exhibit different mechanical properties dependent on the strain rate they are loaded with, a phenomenon known as strain-rate sensitivity (SRS) [27]. The origin of this material behavior is believed to lie in the intrinsic deformation behavior of the BCC lattice and the increased amount of dislocation-grain boundary interactions [27]. Dislocation pinning by impurities can also have a significant influence on the SRS. The SRS exponent and the activation volume for plastic deformation can be obtained from nanoindentation strain rate jump tests [21,22].

Calculated values of the SRS and activation volume obtained from strain-rate jump tests for each sample are given in Table A.1. All samples show similar dependence on strain rate, indicating the same deformation mechanisms in all tested materials. Moreover, the similar values of SRS suggest that the powder processed samples do

not exhibit a significantly increased amount of impurities compared to the samples processed from bulk W. The magnitude of the measured activation volume (around $7 b^3$) lies in the regime of grain boundary-dislocation interactions [1,21,27]. However, as previous experiments on single crystalline and ufg W have revealed, this value for activation volume corresponds also to the activation energy for the kink-pair mechanism, which is believed to be the dominant deformation mechanism for this material and testing temperature [18].

A.6 Summary and outlook

In conclusion, we established a powder processing route for ufg W resulting in similar microstructural evolution, mechanical properties, deformation behavior and microstructure-property relationships as ufg W fabricated from a bulk starting material. Although the powder processing route is more time-consuming, the ability to control chemical composition in terms of precise doping with impurity or alloying elements clearly underlines its benefits. The developed fabrication route can now be used to tune grain boundary segregation states and explore the effect of doping of grain boundaries in ufg W on the investigated properties and on fracture behavior and performance in harsh environments, with the goal of fabricating novel high-performance materials for application in future engineering technologies.

Acknowledgements

The authors acknowledge funding by the European Research Council under Grant number: 771146 (TOUGHIT). Financial support under the scope of the COMET program (A2.12) within the K2 Center "IC-MPPE" (Project No 859480) is gratefully acknowledged.

References

- [1] Meyers M A, Mishra A and Benson D J 2006 Prog. Mater. Sci. 51 427–556
- [2] Hohenwarter A and Pippan R 2015 Philos. Trans. R. Soc. A
- [3] Wurster S and Pippan R 2009 Scr. Mater. 60 1083–7
- [4] Wurmshuber M, Frazer D, Bachmaier A, Wang Y, Hosemann P and Kiener D 2018 Mater. Des. 160 1148–57

- [5] Pink E and Bartha L 1989 *The metallurgy of doped/non-sag tungsten* (Essex: Elsevier Science Publishers Ltd)
- [6] Lassner E and Schubert W-D 1999 *Tungsten. Properties, Chemistry, Technology of the Element, Alloys, and Chemical Compounds* (New York: Kluwer Academic / Plenum Publishers)
- [7] Neu R, Dux R, Kallenbach A, Pütterich T, Balden M, Fuchs J C, Herrmann A, Maggi C F et al. 2005 *Nucl. Fusion* 45 209–18
- [8] Scheiber D, Pippan R, Puschnig P and Romaner L 2016 *Model. Simul. Mater. Sci. Eng.* 24 85009
- [9] Scheiber D, Pippan R, Puschnig P, Ruban A and Romaner L 2016 *Int. J. Refract. Met. Hard Mater.* 60 75–81
- [10] Leitner K, Scheiber D, Jakob S, Primig S, Clemens H, Povoden-Karadeniz E and Romaner L 2018 *Mater. Des.* 142 36–43
- [11] Valiev R Z, Islamgaliev R K and Alexandrov I V. 2000 *Prog. Mater. Sci.* 45 103–89
- [12] Pippan R, Scheriau S, Hohenwarter A and Hafok M 2008 *Mater. Sci. Forum* 584–586 16–21
- [13] Pippan R, Scheriau S, Taylor A, Hafok M, Hohenwarter A and Bachmaier A 2010 *Annu. Rev. Mater. Res.* 40 319–43
- [14] Warren A, Nylund A and Olefjord I 1996 *Int. J. Refract. Met. Hard Mater.* 14 345–53
- [15] Zhilyaev A P and Langdon T G 2008 *Prog. Mater. Sci.* 53 893–979
- [16] Bachmaier A and Pippan R 2013 *Int. Mater. Rev.* 58 41–62
- [17] Kraft O and Arzt E 2009 *Phys. Rev. Lett.* 103 105501
- [18] Kiener D, Fritz R, Alfreider M, Leitner A, Pippan R and Maier-Kiener V 2019 *Acta Mater.* 166 687–701
- [19] Pharr G M and Oliver W C 1992 *J. Mater. Res.* 7 1564–83
- [20] Hay J, Agee P and Herbert E 2010 *Exp. Tech.* 34 86–94
- [21] Maier-Kiener V and Durst K 2017 *Jom* 69 2246–55
- [22] Maier V, Durst K, Mueller J, Backes B, Höppel H W and Göken M 2011 *J. Mater. Res.* 26 1421–30
- [23] Hall E O 1951 *Proc. Phys. Soc.* 64 747–53
- [24] Petch N J 1953 *J. Iron Steel Inst.* 174 25–8
- [25] Vashi U K, Armstrong R W and Zima G E 1970 *Powder Met. Trans.* 1 1769–71
- [26] Grünwald E, Nuster R, Treml R, Kiener D, Paltauf G and Brunner R 2015 *Mater. Today Proc.* 2 4289–94
- [27] Caillard D and Martin J L 2003 *Thermally activated mechanisms in crystal plasticity* (Kidlington: Elsevier Ltd.)

B Tuning mechanical properties of ultrafine-grained tungsten by manipulating grain boundary chemistry

M. Wurmshuber¹, S. Jakob², S. Dopfermann¹, S. Wurster³, R. Bodlos⁴,
L. Romaner², V. Maier-Kiener², D. Kiener¹

¹ Department of Materials Science, Chair of Materials Physics, Montanuniversität Leoben, Jahnstraße 12, 8700 Leoben, Austria

² Department Materials Science, Chair of Physical Metallurgy and Metallic Materials, Montanuniversität Leoben, Roseggerstraße 12, 8700 Leoben, Austria

³ Erich-Schmid Institute for Materials Science, Austrian Academy of Sciences, Jahnstraße 12, 8700 Leoben, Austria

⁴ Materials Center Leoben GmbH, Roseggerstraße 12, 8700 Leoben, Austria

Tungsten is, due to a combination of high strength and good physical properties, frequently considered for high-performance applications in the harshest environments. Oftentimes its inherent brittleness and low ductility stand in the way of a successful deployment in these fields. Since tungsten has been proposed as divertor material for nuclear fusion reactors, an improvement of ductility and fracture toughness is essential. An obvious first step to increase these properties is to reduce the grain size to the ultrafine-grained regime. As this still leaves the material with a relatively low-energy intercrystalline fracture mode, this work takes a step further. With the help of doping elements, which are identified from ab-initio simulations, an attempt to increase grain boundary cohesion of ultra-fine grained tungsten to improve ductility is made. After fabrication of the doped samples from powders using severe plastic deformation, thorough microstructural investigations and extensive mechanical characterization, utilizing various small-scale testing techniques, are combined to assess the properties of the materials. We report that the addition of boron and hafnium can significantly increase the bending strength and bending ductility of ultra-fine grained tungsten. An additional heat treatment of the boron doped sample amplifies this effect even further, drastically increasing the strength and overall mechanical properties due to a combination of hardening-by-annealing and increased grain boundary segregation. Thus, an effective way to adaptively improve the mechanical properties of tungsten by manipulating grain boundary chemistry is reported, validating grain boundary segregation engineering as a powerful tool for enhancing damage tolerance in brittle materials.

B.1 Introduction

Since the beginning of systematic materials science, researchers dream of a material that combines the “trinity” of mechanical properties: high strength, high ductility and enhanced fracture toughness. Especially ultra-high strength materials often cannot unleash their full potential, as they lack the ability to absorb damage from overloading or tolerate pre-existing defects within the material. The mutual exclusivity of strength and ductility in homogeneous metals has its roots in dislocation plasticity. As most strengthening mechanisms are based on restricting dislocation movement, this in turn deteriorates plastic deformation and ductility. Similarly, such strengthening mechanisms have a detrimental effect on fracture toughness, as the ability to successfully dissipate stress intensity from the crack tip via nucleation and propagation of dislocations is restricted [1]. The strength-ductility trade-off can, however, be challenged by implementing various strategies explored in recent years [1,2,11–13,3–10]. A reduction in grain size of metals, for example, commonly leads to an increase in strength [14,15] and fracture properties [16–18], while having little influence on the ductility. In fact, for coarse-grained metals sometimes even an increase in ductility can be observed, as the larger amount of grains gives a higher probability of dislocation slip systems being orientated beneficial to mechanical loading [2]. However, when entering the nanocrystalline regime (nc; grain sizes < 100 nm), the transition from a dislocation-controlled plasticity to a grain boundary (GB)-controlled plasticity leads to a strong decrease in ductility [2,3,7,19], with only a few fcc materials being able to retain their ductility through GB sliding and superplasticity [20–22]. Similarly, the vast amount of GBs present in such small grained metals renders a comparably easy path for crack propagation, hindering fracture toughness to improve further [18,23]. Therefore, ultrafine-grained (ufg; grain sizes between 100 and 500 nm) materials seem to represent a favorable tradeoff to achieve ultra-high strength, decent fracture toughness and still acceptable ductility.

Due to the large amount of GBs in ultra-fine grained materials, GB cohesion is of great significance for the mechanical performance. As mentioned above, grain boundaries are usually the weak link in ufg and nc materials. Therefore, in order to reinforce these weak spots, the concept of grain boundary segregation engineering (GBSE) has been introduced [24,25,34,35,26–33]. In GBSE, materials that are known to break in an intercrystalline fashion are doped with elements that are predicted to strengthen GB cohesion. By heat treatments or mechanical mixing, these elements, e.g. boron in steels [36], segregate at the GB for an optimal GB strengthening effect. A related approach, the avoidance or removal of segregation of GB embrittling elements, such as S, P or O, has been practiced ever since medieval times and is an important first step to enhancing GB cohesion [37]. The process of identifying GB strengthening elements in a given host material has been supported in recent years by ab-initio

simulations, such as density-functional theory [26,29,32,33,35,36,38–44].

Tungsten has been considered a promising structural material for the divertor part in nuclear fusion reactors, due to its unique properties such as high strength, high melting point, excellent thermal conductivity, outstanding erosion resistance and its small tendency to become activated or transmuted [45–49]. As a refractory metal, it also shows inherent brittleness and intercrystalline fracture even for conventional grain sizes, which is the major concern for employment of tungsten materials in the harsh environment of nuclear fusion reactors as of today [45–55]. By reducing the grain size of tungsten down to the ufg regime, it could not only gain a valuable increase in strength and fracture toughness [8,10], the large fraction of GBs introduced would also prove themselves beneficial for counteracting and absorbing radiation damage [56–62] and for suppressing the growth of helium bubbles, an unavoidable by-product of the fusion reaction [63–67]. Grain refinement in combination with GBSE is therefore a promising approach to improve the mechanical properties of tungsten and create a material showing an excellent combination of strength, ductility and toughness, even in harsh environments. In this work, several ufg W samples, undoped and doped with various atomic elements, are fabricated using severe plastic deformation. Utilizing extensive microstructural and mechanical characterization, the direct effect of each doping element on the mechanical properties of ufg tungsten is identified and interpreted.

B.2 Experimental Methodology

B.2.1 Material and Fabrication

To enhance the grain boundary cohesion in ufg W, several elements have been chosen as candidate doping elements, based on the ab-initio simulations of Scheiber et al. [38,39]. Disregarding elements that form brittle intermetallic phases in tungsten, are toxic or not affordable for a potential large scale fabrication in the future, the four elements carbon, boron, rhenium and hafnium were selected in this work. It should be noted that, according to [39], Hf does not strengthen the GB cohesion directly. While a different work by Setyawan et al. [40] suggests that Hf could possibly strengthen the grain boundaries in a tungsten host material, in this work it was mainly chosen due to its well-known affinity to oxygen. As oxygen located at GBs is considered as a main contributor to the brittleness of tungsten [38,49,68], it is presumed that Hf as doping element will bind oxygen in the form of hafnium oxide and therefore remove it from the grain boundaries. This strategy has already been applied successfully in previous work on molybdenum [31]. Notably, to ensure their

targeted deployment, all selected doping elements show an increased GB segregation tendency in W [38,39].

A fabrication route for ufg W from elemental powders using high pressure torsion (HPT) has been developed by the authors in a previous work [69]. The advantage of starting from powders is the ability to precisely control chemical composition in terms of doping with impurity and alloying elements. The material powders of W (99.97% purity, 2 μm particle size, Plansee SE, Austria), C (99.95% purity, 2 – 12 μm particle size, Merck KGaA, Germany), B (98% purity, 44 μm particle size, Alfa Aesar, USA), Re (99.99% purity, 10 μm particle size, Mateck GmbH, Germany) and Hf (99.6% purity, 44 μm particle size, Alfa Aesar, USA) are all stored and handled in argon atmosphere within a glovebox. The powders are mixed to adjust the content of the doping element at approximately 3 – 5 at.%. Subsequently, the powder mixtures are compacted in argon atmosphere using a sealed mini-chamber [69] and a high pressure torsion tool [70]. A nominal pressure of 12 GPa and torsional deformation of about 0.1 rotations are applied to the powders. After the powder is compacted, an intermediate annealing step at 1600°C for 7 hours in a vacuum furnace (Leybold Heraeus PD 1000, Leybold GmbH, Germany) is performed to enhance powder particle cohesion. Finally, the samples are deformed using HPT with a nominal pressure of 12 GPa at 400°C for about 1 rotation, resulting in disk shaped specimens with a diameter of 6 mm and a height of 0.6 – 0.8 mm. For more detailed information regarding the fabrication route of the ufg W samples, the interested reader is referred to [69].

Following the results of mechanical property tests presented in Section B.3, an undoped and a boron-doped ufg W sample were heat treated at 500°C for 5 hours in a vacuum furnace (XERION Berlin Laboratories GmbH, Germany) subsequent to the HPT deformation with the intention to increase grain boundary relaxation and doping element segregation. The annealed samples are marked with “ann.” in all Figures in this work.

B.2.2 Microstructural Characterization

The microstructures of the samples were investigated using a field-emission scanning electron microscope (SEM; LEO type 1525, Zeiss GmbH, Germany) equipped with energy dispersive X-ray spectroscopy (EDX; Bruker XFlash 6 | 60, Bruker, Bruker Corp., USA) and electron backscatter diffraction (EBSD; Bruker e-FlashFS, Bruker Corp., USA) detectors. In order to assess the GB chemistry via atom probe tomography (APT), lift-outs of selected samples were fabricated using an Omniprobe 200 manipulator (Oxford Instruments plc, UK) in a dual-beam focused ion beam (FIB)-SEM (Zeiss Auriga, Zeiss GmbH, Germany). From the lift-outs, APT tips containing GBs

were fabricated following the procedure detailed in [71] on an FEI 3D DualBeam workstation (Thermo Fisher Scientific, USA) equipped with an EDAX Hikari XP EBSD-system (AMATEK Inc., USA). The APT experiments were performed on a CAMECA LEAP 3000HR (AMATEK Inc., USA) in laser-pulse mode with a laser energy of 0.6 nJ at 250 kHz, a test temperature of 60 K and a target evaporation set to 0.5%. The software IVAS 3.6.14 was used for the reconstruction and analysis of the measured atom probe tips.

B.2.3 Indentation

In order to get a first assessment of mechanical properties of the produced samples, Vickers microhardness was measured along the sample radius in tangential direction with a load of 500 g using a Buehler Micromet 5104 machine (Buehler ITW Test & Measurement GmbH, Germany). In-depth information about mechanical properties, such as strain-rate sensitivity (SRS) or activation volume, was acquired by performing strain-rate jump tests [72,73] using a G200 Nanoindenter (KLA Corporation, USA) equipped with a diamond Berkovich tip and the continuous stiffness measurement (CSM) option. A minimum of four tests were performed at a sample radius of 3 mm for each material condition.

B.2.4 Microcantilever bending tests

As the HPT process leads to a deformation gradient, and consequently also a microstructural gradient, along the sample radius, the smallest and most desired grain size is usually found in the outer region of the sample disk. To only test this specific microstructure and avoid unintended influences from the coarser grained regions at smaller radii, small-scale testing techniques are necessary to specifically probe the mechanical properties of ufg W.

For the most crucial assessment of the mechanical performance of tungsten, samples should be loaded under tensile stress conditions. However, microtensile tests are demanding in sample preparation and unforgiving in terms of alignment [74–80]. Additionally, it is challenging to find a suitable gripper material stiff and hard enough to test the samples produced in this work. As most available grippers for tensile testing are made of tungsten themselves, it is likely that plastic deformation will also occur in the gripper during the experiment, damaging the gripper and distorting the recorded force-displacement data [80].

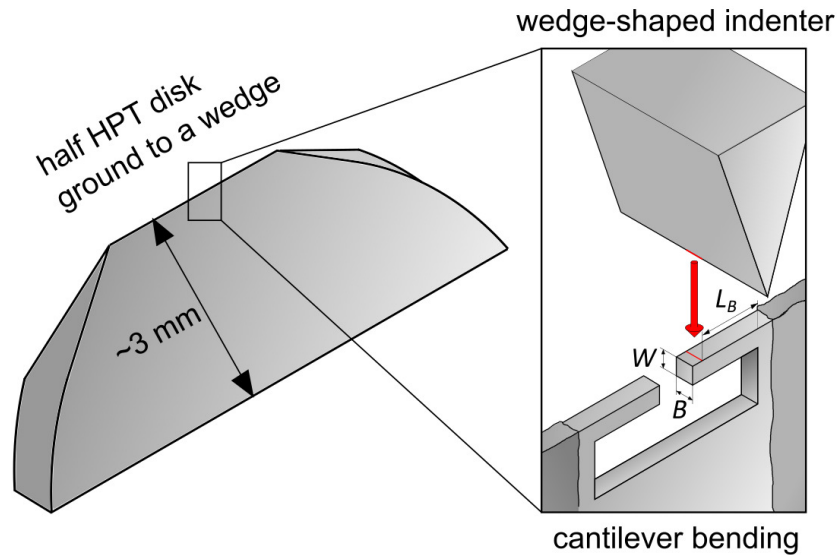


Figure B.1 Micromechanical testing setup for microcantilever bending.

Therefore, in an attempt to combine (partial) tensile testing conditions and practicability in unveiling mechanical properties and deformation behavior of the doped and undoped ufg W samples, microcantilever bending tests were performed. For this, the as-deformed HPT disks are cut in half using a diamond wire saw and then ground to a wedge shape using a special sample holder. From the very top of the wedge, cantilevers with dimensions of about $3 \times 3 \times 10 \mu\text{m}$ are fabricated using a dual-beam FIB-SEM (Zeiss Leo 1540XB, Zeiss GmbH, Germany), as depicted in Figure B.1. The cantilevers are tested in-situ in a field-emission SEM (Zeiss LEO 982, Zeiss GmbH, Germany) using an UNAT-SEM indenter (Zwick GmbH & Co KG, Germany) equipped with a conductive diamond wedge indenter tip (Synton-MDP AG, Switzerland). The recorded force and displacement data, can be converted to bending stress and bending strain, respectively, using the following equations [81–83]:

$$\sigma_{max,tensile} = 4 \cdot \frac{F \cdot L_B}{B \cdot W^2} \quad (\text{B.1})$$

$$\varepsilon_{max,tensile} = \frac{3 \cdot W \cdot u}{2 \cdot L_B^2} \quad (\text{B.2})$$

here $\sigma_{max,tensile}$ and $\varepsilon_{max,tensile}$ are the maximum tensile stress and tensile strain at the outermost fiber of the cantilever, respectively, F is the load, u the displacement, L_B the bending length, B the width and W the thickness of the cantilever (compare with Figure B.1). The displacement rate for these experiments was set to 20 nm/s , which corresponds to a strain rate of about 10^{-3} s^{-1} . In-situ videos of all experiments were

compiled by collecting an image of the SEM screen every second. For each material condition 3-4 cantilevers were fabricated and at least 2 were successfully tested.

B.3 Results

B.3.1 Microstructure and grain boundary chemistry

SEM images of the microstructure of the as-deformed undoped and doped ufg W samples are displayed in Figure B.2. All images were taken at a radius of 3 mm from the disk center in tangential direction. The grain sizes were measured using the grain intercept method. As apparent in Figure B.2, the microstructures for all produced samples are rather similar, the measured grain sizes confirm this assumption with all of them lying in the range of 110 – 160 nm. It should also be noted that – as intended – the heat treatment of an undoped and a boron doped specimen did not lead to any noticeable grain growth. As is apparent in lower magnification overview pictures (Figure B.3), the formation of various up to several micron-sized particles was observed in the final microstructure of the doped materials. The formation of HfO₂ oxides in the hafnium-doped sample was expected and desired and the formation of

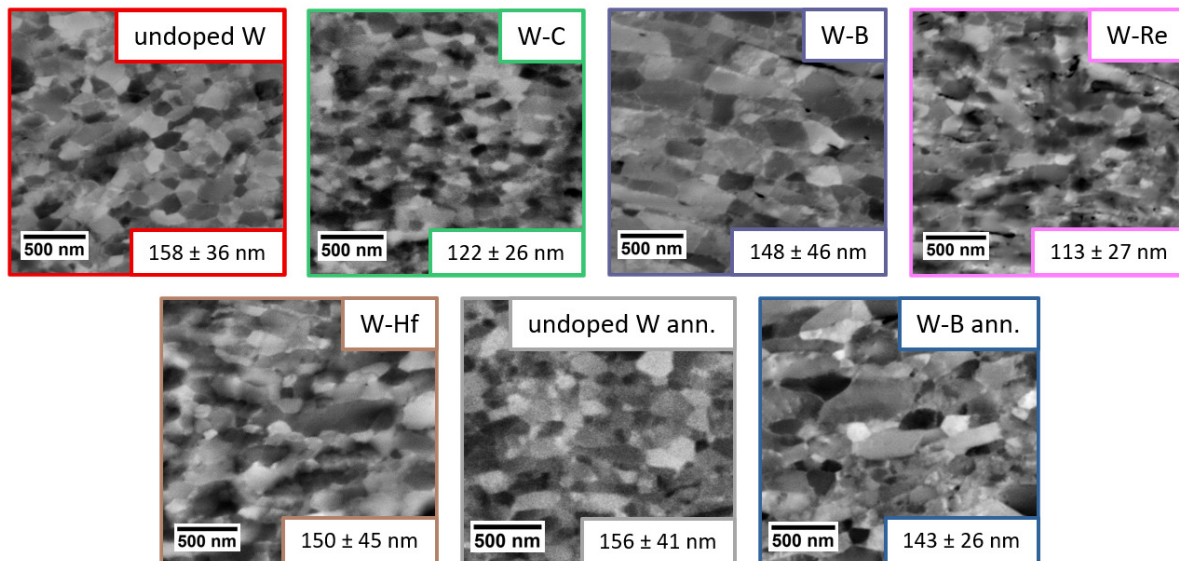


Figure B.2 SEM microstructure images and grain sizes of all investigated W materials. Images were taken using a backscattered electron detector at a sample radius of 3 mm in tangential direction. Samples marked with “ann.” underwent a heat treatment at 500°C for 5h in vacuum after HPT deformation.

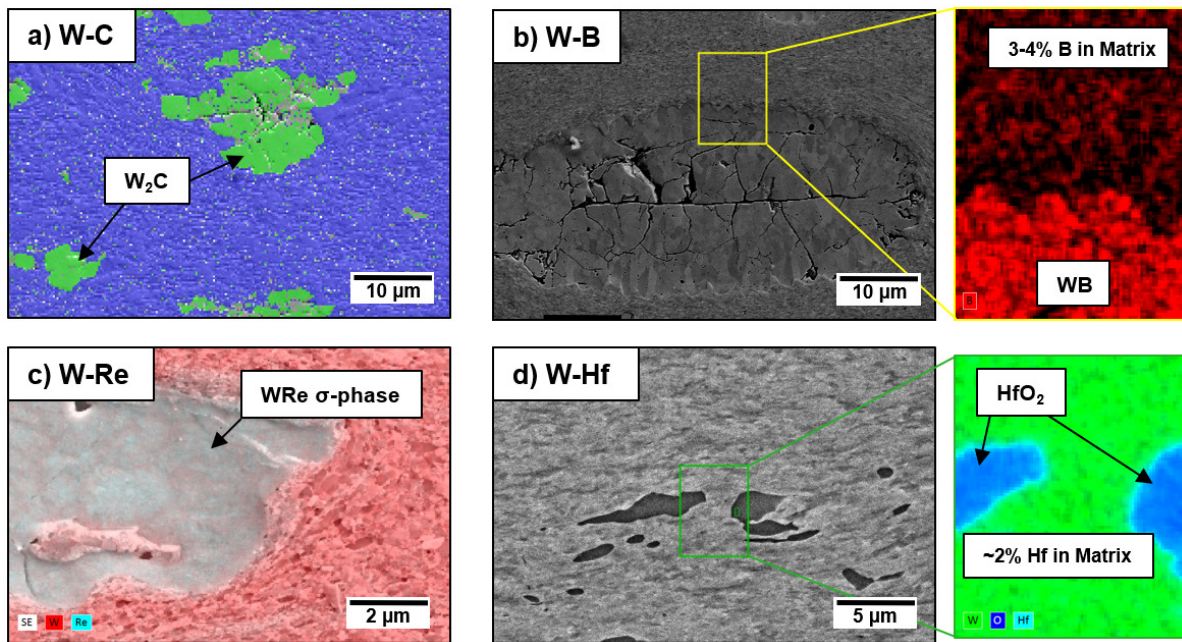


Figure B.3 Lower magnification micrographs revealing various particles formed through HPT. a) EBSD map of carbon doped sample with metastable W_2C carbides. b) SEM image and EDX map of boron doped sample with WB borides. c) EDX map of rhenium doped sample with WRe intermetallic σ -phase. d) SEM image and EDX map of hafnium doped sample with HfO_2 .

WB borides can be easily explained by the large negative mixing enthalpy of B and W [84] in combination with the high shear strain present during HPT processing. The formation of the other large particles, on the contrary, is rather surprising. The W_2C carbide should not be stable below $1200^\circ C$ under equilibrium conditions according to the phase diagram and the formation of WRe intermetallic phase contradicts the well-known high solubility of Re in W [85]. It is assumed that, due to the metastable nature of some of the phases, these particles form through intimate mixing originating from the high pressure and shear strain during the HPT-deformation [86,87], yet their exact origin is not fully clear and will be subject to future work. As EDX measurements revealed that there is still enough concentration (2 – 4 at.%) of the doping elements in the W matrix, and it is relatively easy to avoid them when fabricating micromechanical specimens, the particles do not influence the outcome of the present small-scale testing experiments (with the exception of the HfO_2 oxides, which are supposed to remove and bind pre-existing oxygen from the GBs).

To explore the segregation behavior of B, undoped W, W-B and heat treated W-B samples were additionally investigated regarding their GB chemistry using APT. The samples doped with B were chosen as representative APT samples, due to the difficulties of measuring B with EDX and because of the clear improvement of mechanical

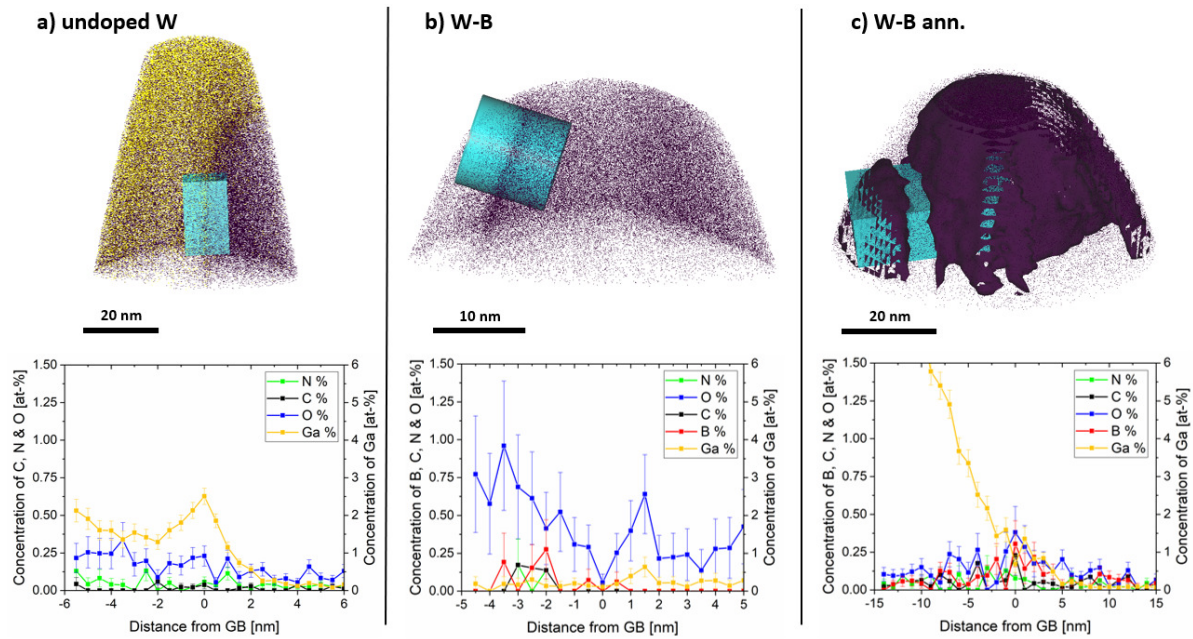


Figure B.4 APT tips and investigations of element segregation at the GB in a) undoped W, b) W-B and c) annealed W B samples.

properties of ufg W by doping with B, as presented in Section B.3.3. The results from these measurements are depicted in Figure B.4. For every material condition, a tip containing a vertical grain boundary was selected for analysis and detailed investigation. The presence of a GB is indicated by the different Ga-content (Figure B.4a), W isosurfaces (Figure B.4c) as well as the respective region of interests for GB analysis. The undoped W sample shows no significant segregation of any elements along the GB, with the exception of Ga, which is unavoidable to be introduced into the material during FIB preparation. The unannealed boron doped specimen also shows signs of Ga and only a small amount of B inside the material. This indicates that the B must be very finely distributed within the sample and not segregated at the GB. After a heat treatment at 500°C for 5 hours, segregation of about 0.3 at% B in the 1D-concentration profile was detected at the GB of the material (see Figure B.4c). The interfacial excess value for B was calculated according to [88,89] and amounts to 0.23 at%/nm². Oxygen was identified to some extent in all investigated APT specimen at and near the GB.

B.3.2 Hardness and strain-rate sensitivity

Figure B.5a shows the hardness along the sample diameter for all samples. A clear gradient in hardness, originating from the deformation gradient of the torsion deformation, is apparent. It seems that the two interstitial doping elements, C and

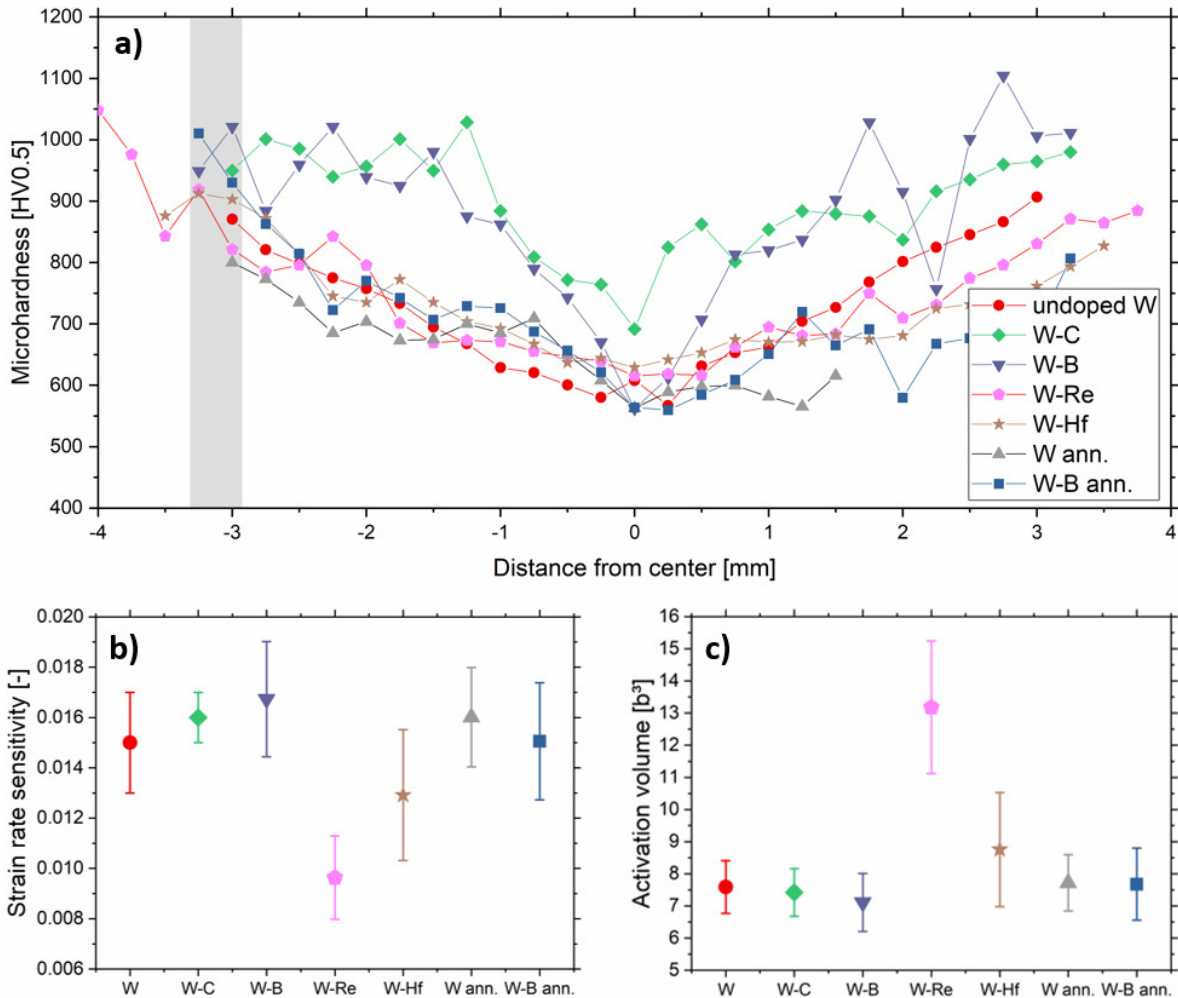


Figure B.5 Indentation results of all investigated W samples. a) Microhardness across the diameter of the HPT disks. The grey shaded area marks the region on the samples, where all further experiments are performed. b) SRS and c) activation volume results from nanoindentation strain-rate jump tests.

B, lead to slightly higher hardness in the inner regions of the disks. However, at a distance of about 3 mm from the disk center, where all further experiments in this work will be performed at, the hardness values all lie in a range of 800 – 1000 HV0.5 (grey shaded area in Figure B.5a). The undoped annealed sample broke during sample preparation, which is the reason for not testing the whole specimen.

Results from strain-rate jump tests are visible in Figures B.5b and B.5c. The SRS coefficient and the activation volume were analyzed following the procedure of Maier-Kiener et al. [72,73]. It is apparent that the values are comparable, around 0.013 - 0.017 for SRS and 7-9 b³ in activation volume, with the exception of W-Re that showed a reduced SRS of 0.010 and increased activation volume of 13 b³.

B.3.3 Microcantilever bending

A representative stress-strain curve ($\sigma_{max,tensile} - \epsilon_{max,tensile}$, see Equations (B.1), (B.2)) for the boron doped sample including snapshots from the in-situ SEM video of the respective cantilever test is depicted in Figure B.6. As there is no standard procedure for extracting material properties out of bending stress - bending strain curves, the following parameters were used in this work to compare the different materials: As a measure of strength, the maximum bending stress recorded in the experiments was used. This serves as an equivalent to a UTS value and was deemed to be the most reasonable quantity to compare. Obtaining a measure of ductility from the bending curves is a more challenging task. As all experiments are performed in-situ in an SEM, one can utilize the available video information for that. The point in the video of each tested cantilever that shows first signs of crack formation was correlated with the stress - strain curve. The plastic strain at this point (i.e. total strain minus elastic strain) is used as a measure to compare ductility of the tested samples. A drawback of this method is, that through the in-situ pictures we only gain information of one side of the tested cantilevers, thereby possibly overlooking crack formation on the backside of the specimen. However, due to the small cantilever dimensions, it is likely that such a crack would be visible on the observed side shortly after, in which case only a minimal error in ductility is made. Moreover, for the presented experiments whenever there was a sudden load drop in the recorded curves, this point was set

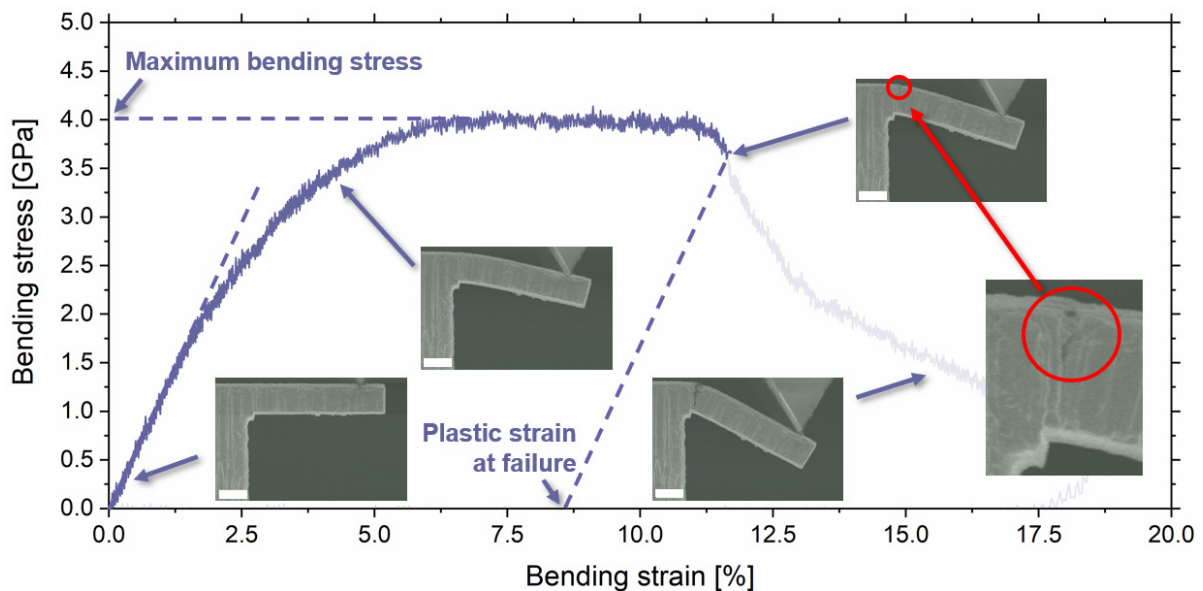


Figure B.6 Representative stress-strain curve of boron doped ufg tungsten and in-situ pictures of the respective bending test. The white scale bars in the lower left of the in-situ pictures represent a length of 2 μm.

as default failure event, and – most importantly – always coincided with visible crack formation. Out of these reasons and in the absence of a better alternative, this measure of ductility was defined. It should, however, be clear that this is not to be regarded as a one-to-one equivalent to tensile ductility.

Cantilevers that have been found to contain visible cracks or pores in or near the bending area have been discarded already before testing.

A compiled “strength - ductility map” of all fabricated material samples is shown in Figure B.7a. It is no surprise that the strength of all tested materials lies well within the ultra-high strength regime, given the immense intrinsic strength of the tungsten base material combined with an ultra-fine grain size. All tested unannealed samples show strengths exceeding 2500 MPa up to 4500 MPa. The ductility ranges from rather small failure strains of 2.5% to strains of 15%, which is very respectable for such a high strength material. It is noteworthy that, with the exception of C, all doping elements increase the strength of ufg W, while only two of them, B and Hf, also maintain or improve ductility. The positive effect of B and Hf is further underlined in Figure B.7b, where the area below the stress-strain curves until failure, i.e. the plastic work of the material or plastic energy density, are shown. Values of $406 \pm 5 \text{ MJ/m}^3$ (boron) and $363 \pm 14 \text{ MJ/m}^3$ (hafnium) are a clear improvement compared to the undoped material ($286 \pm 21 \text{ MJ/m}^3$). In Figure B.7 it is also apparent that doping with C deteriorates the mechanical properties of ufg W, even though Scheiber et al. [38] predicted it to be a GB strengthening element in tungsten, and the beneficial effect was demonstrated in Mo [31].

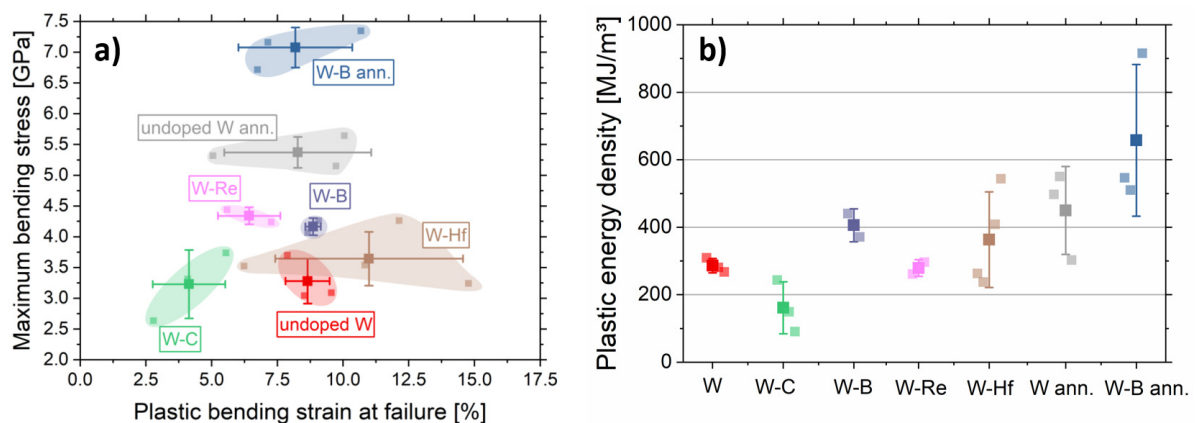


Figure B.7 a) Maximum bending stress (i.e. strength) over plastic bending strain at failure (i.e. ductility) of all fabricated materials. Each small square represents a successful microcantilever bending test, the big squares represent the average strength and ductility of each material. b) The integrated area below the stress-strain curves until failure is taken as a measure for plastic work expended during deformation for all fabricated samples.

Following the great performance of the B doped ufg W sample, this material was additionally heat treated at 500°C to deliberately enhance the GB segregation of the doping element. The undoped ufg W was also annealed at the same conditions to provide a reference sample. As is apparent in Figure B.7a, the annealed samples show an enormous increase in strength compared to all other tested samples. The strength of the undoped and annealed W material is 5.37 ± 0.25 GPa, whereas the annealed W-B material displays an even higher strength of 7.08 ± 0.33 GPa, more than double the strength of the undoped and unannealed W material (3.28 ± 0.37 GPa). Moreover, the ductility of the annealed samples (8.3 ± 2.8 % and 8.2 ± 2.2 %, respectively) is comparable with the unannealed undoped W (8.7 ± 0.8 %) and unannealed W-B samples (8.9 ± 0.3 %). By maintaining ductility while at the same time drastically raising the strength, the overall spent plastic work also increases dramatically to 450 ± 130 MJ/m³ and 658 ± 224 MJ/m³, respectively, as can be observed in Figure B.7b.

B.4 Discussion

The fabrication route presented in [69] and applied in this work was found to be successful in reliably processing tungsten powders to dense bulk samples of ultra-fine grain size in the range of 110-160 nm (Figure B.2). These ufg samples do not only excel on their own in terms of high strength and noticeable ductility, the powder fabrication route also allows for precise doping with GB strengthening elements to enhance these properties even further.

As revealed by APT measurements on the boron-doped sample (Figure B.4), respective doping elements are not primarily situated at the GB, which is not too surprising as their distribution is achieved by mechanical deformation with only little thermal input. Only an additional heat treatment provides the necessary energy for the doping elements to diffuse towards and segregate at the GBs. From the presented APT results, it is safe to assume that before such a heat treatment, the doping elements are randomly distributed within the material, as an enhanced GB segregation tendency is thermodynamically given [38,39], but kinetically limited.

While the hardness results (Figure B.5a) might indicate that the interstitial doping elements C and B lead to higher hardness, a more reasonable explanation for the bulk hardness increase is the formation of μm -sized and extremely hard W_2C carbides and WB borides, as seen in Figure B.3a and B.3b. Remember that carbides and borides were avoided for microcantilever testing. While there are also HfO_2 oxides and WRe intermetallic phases found in the other fabricated samples (Figure B.3c and B.3d), those are smaller in size and amount and assumed to be softer than the borides and carbides. As such, only for the carbides and borides a noticeable increase in

bulk hardness was observed. At the edge of the disk specimen, where all further experiments were conducted, the hardness of all samples lies in the same range of 800 - 1000 HV0.5, so no significant change related to the doping elements is observed here. Furthermore, the annealed samples show a similar hardness distribution as the ufg W variants doped with substitutional elements or the undoped material. This confirms that no significant grain growth occurred during the annealing. It should be mentioned that the annealed W-B sample shows lower hardness than the unannealed W-B material in the inner regions of the sample disks. This can be explained by dislocation recovery phenomena in these coarser grained regions, which are known to onset in cold-worked W at about 400°C [90].

The SRS and activation volumes probed by nanoindentation strain-rate jump tests (Figure B.5c) lie in a range of 0.013 - 0.017 and 7-9 b³, respectively, which is commonly attributed to the kink-pair mechanism regarded in bcc metals at low temperatures [91-97]. Here, the rhenium doped sample shows a slightly higher activation volume and reduced SRS, which is in good agreement with the theory that Re promotes dislocation glide in tungsten by altering the asymmetry of the screw dislocation core [98]. Annealing the W and W-B samples leads to no obvious change in SRS and activation volume, indicating once again that no major microstructural changes are taking place during the heat treatment, except for the intended B diffusion and segregation.

While the doping elements seem to only have a minor influence on GB mobility and thus resulting grain size as well as hardness and activation volume, the results from microcantilever bending tests paint a different picture. Due to the partial tensile nature of the bending test, the most crucial loading mode for tungsten is tested. Therefore, any influence of a modified GB cohesion would show the biggest effect in these tests. Before discussing the results of the microbending tests, it should be mentioned that the cantilevers were examined with the crack growth direction in radial specimen orientation. To demonstrate the influence of this test orientation on the mechanical properties, further microstructural analysis has been performed. Figure B.8a and B.8b show the cumulative grain size distribution in axial and radial direction, respectively. From this data it can be seen that the grain size distribution is relatively slim, indicating a uniform grain size in the respective directions. However, it is also apparent that the average grain size in axial direction is smaller than in radial direction. This grain anisotropy is further visualized in Figure B.8c. The grain aspect ratio of all investigated ufg W samples lies between 1:1 and 1:2, with the majority of samples showing a ratio close to 1:1.5. As demonstrated in previous work [99,100], this slight grain shape anisotropy originating from the torsional deformation leads to an orientation dependence of fracture performance for HPT processed ufg materials. The configuration used in the present work, with the crack growth direction in radial specimen direction, was found to yield the highest fracture toughness values.

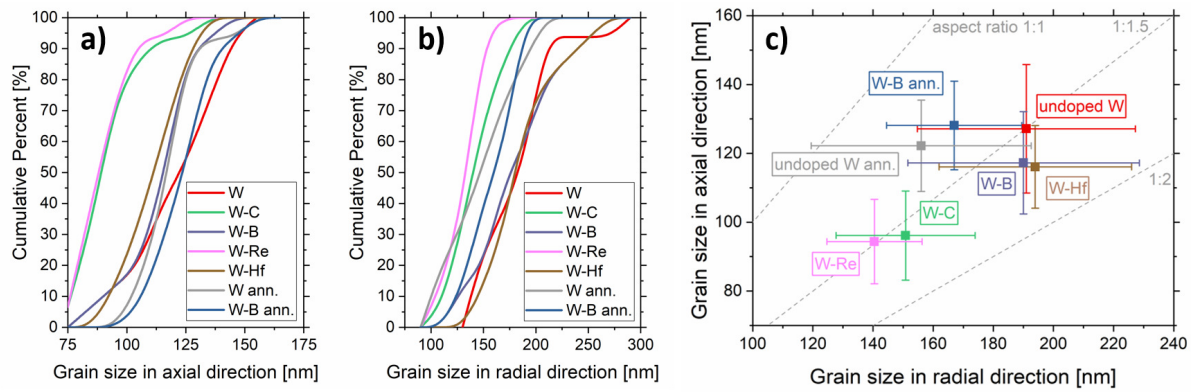


Figure B.8 Cumulative grain size distribution of grains in a) axial and b) radial direction of all investigated samples. c) Grain anisotropy of axial and radial direction show an aspect ratio of 1:1.5 for most ufg W samples.

As intercrystalline fracture is also a major factor controlling ductility in such an ultra-fine grained material, a similar directional dependence is assumed for ductility. However, since grain shape and anisotropy could potentially be tuned by larger scale fabrication methods (e.g. rolling) and aligning the microstructure in a preferred loading direction is usually possible, the authors decided it is best to test the material in this direction to show the potential of the material, rather than testing a potentially weaker direction.

The microcantilever bending results in Figure B.7a underline that ufg W shows very attractive mechanical properties. The undoped material already demonstrates a strength of 3.28 ± 0.37 GPa, higher than cold-rolled tungsten [101], highest-strength steels [102,103] or previous works on ufg W [94,104], while also exhibiting a formidable bending ductility of 8.7 ± 0.8 %, unprecedented in tungsten [49,101]. Notably, as the stress and strain distribution is much more complex for a bending experiment than for a tensile experiment, we do not advise to directly compare the strength and ductility values gained in this work with tensile or compression values in literature. That being said, as the nature of the experiment still yields a valid stress-strain curve, the feasibility to compare the strength and ductility for materials tested in the same bending test conditions, and therefore the ability to correctly assess the effect of each doping element on strength and ductility, prevails.

From the EBSD images in Figure B.9a and B.9b, it is apparent that the undoped W cantilevers fail – as expected – in an intercrystalline fashion, since the grains on either side of the crack have different orientations. This is crucial, as an improvement of mechanical properties by GBSE can only be expected when the failure mode is in fact intergranular. All tested ufg W variants failed intergranularly, as is evident by EBSD images on a representative annealed W-B cantilever shown in Figure B.9c and B.9d. The profiles of the crack onset and fracture surfaces seen in top view

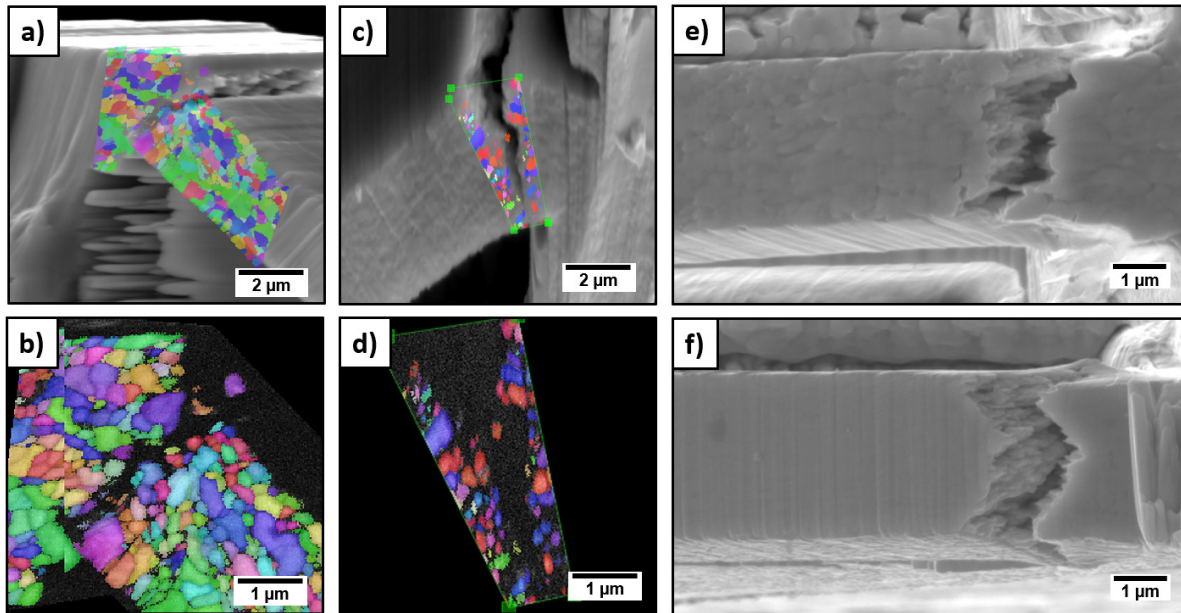


Figure B.9 EBSD overlay on SEM image of a) an undoped W and c) an annealed W-B cantilever after testing. b,d) Zoomed in EBSD maps around the crack, indicating intercrystalline failure. Top view SEM micrographs of annealed undoped W (e) and annealed B doped W (f) cantilever indicating predominantly homogeneous deformation in the gauge area and clear evidence of intercrystalline failure.

SEM micrographs of annealed undoped W (Figure B.9e) and annealed B doped W (Figure B.9f) provide additional evidence for intercrystalline failure in the materials. Figures B.9e and B.9f also show that there is no pronounced necking in the gauge area of the cantilevers, indicating homogenous deformation. In fact, the transverse strain measured in all cantilevers never exceeded 2.3%. When accounting for this strain using a Mohr's strain circle, a maximum relative error of < 3% is made for ductility, which corresponds to a maximum absolute error in failure strain of 0.3% (percentage points) for a worst case scenario. Therefore it is safe to assume that the cantilevers show predominantly homogeneous deformation in the bending area, justifying the chosen testing method for strength and ductility.

By adding the targeted doping elements to ufg W and conducting heat treatments, different effects on strength and ductility can be observed, which are outlined and discussed individually below:

The effect of annealing:

As showcased by the undoped annealed sample, a moderate heat treatment at 500°C for 5 hours enhances the strength of the material, while preserving the microstructure. This adaptive strength increase can be explained by the hardening-by-annealing

effect, a phenomenon commonly found in very fine grained metals [105–109]. By annealing nc and ufg materials below the grain growth threshold temperature, on the one hand mobile dislocations annihilate at GBs, and on the other hand GBs relax into an energetically more favorable state. In the case of severely plastically deformed materials, this relaxed GB state is usually associated with “smoother” GBs that do not contain many GB ledges or other GB defects which could serve as possible sources for easier dislocation nucleation [2,59,106,109–113]. By removing both, mobile dislocations in the grain interior and potential nucleation sites at GBs, plastic deformation could only occur through a limited amount of conventional dislocation sources in the grain interior or nucleation of dislocations at relatively smooth GBs, which requires a higher stress level compared to dislocation nucleation at GB ledges, therefore explaining the increase in strength. It should be noted that this hardening-by-annealing phenomenon does not seem to have an influence on ductility of ufg W, indicating that there is still sufficient dislocation plasticity present in the material and underlining once more that GB cohesion is the limiting factor to ductility. It is interesting to note that the hardening-by-annealing seems to have no influence on the measured microhardness of ufg W, as can be seen in Figure B.5. Considering that both the required stress level for dislocation nucleation from GBs as well as the type of nucleated dislocations are severely different between tensile and compressive loading conditions [114], this might be an indicator that tensile stress conditions are more sensitive to such a GB relaxation effect. Such a presumed scenario would bear critical implications, since most hardening-by-annealing studies are conducted using hardness measurements, but this requires further investigation to proof in detail.

Carbon:

The addition of C decreases ductility and, as a consequence, the overall plastic energy density (see Figure B.7b) of ufg W. Even though it has been identified as a GB cohesion enhancing element [38], such an effect could not be confirmed with the current testing efforts. C is known to change the core of screw dislocations in W and other bcc metals to a less mobile hard core configuration, limiting the ductility in a W-C solid solution [115–117], which would natively deteriorate ductility. Another possible explanation for the reduction of mechanical properties might be the formation of nanosized carbides at the GBs, but within the present investigations we were not able to identify any. However, as doping of ufg W with C seems to not improve the bending stress-strain properties, this work aims its detailed attention at more promising variants instead.

Boron:

Doping with B increases the strength and also slightly the ductility of ufg W. Therefore, also the spent plastic work and overall mechanical properties improve. As deduced

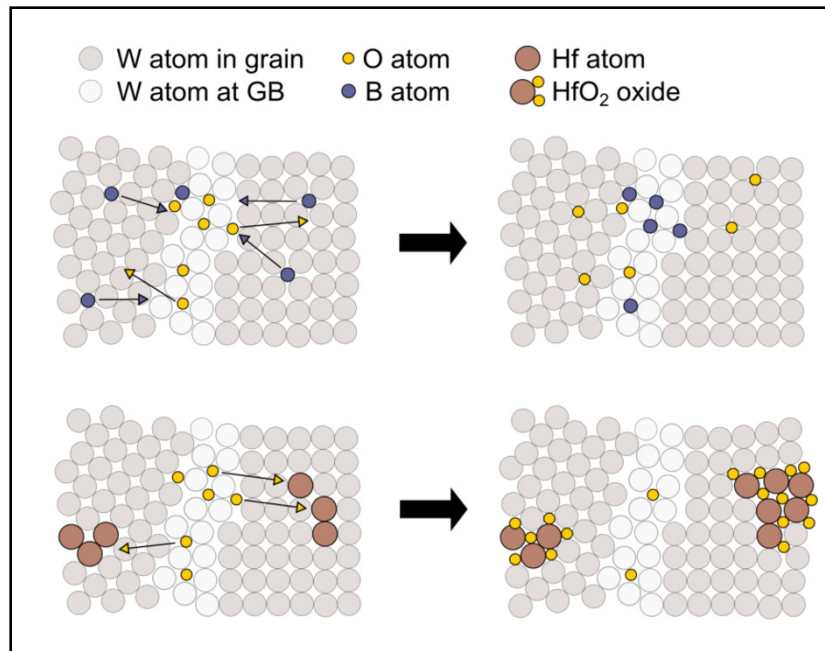


Figure B.10 Schematic of the effects of B and Hf on the GB chemistry. Boron diffuses to the GB and replaces O, while Hf attracts O from the GBs and forms HfO₂ oxides.

from APT measurements and mentioned above, the B in this sample is most likely very finely and randomly distributed within the specimen, indicating that already a very small amount of B at the GB can improve the properties tremendously. Therefore, it is no surprise that an additional heat treatment, which promotes more segregation of B at the GB, amplifies this effect even further. As can be seen in Figure B.7a, the boron doped and annealed samples shows extraordinarily high strength values even exceeding 7 GPa. Furthermore, this incredible increase in strength is achieved while simultaneously maintaining the bending ductility at the same level as for the undoped W or unannealed W-B sample. Naturally, this increase in strength also leads to outstanding values for the plastic energy density of the material (Figure B.7b). This increase in mechanical performance is explained by a combination of three effects: 1) The above mentioned hardening-by-annealing effect leads to a strength increase on its own through GB relaxation and dislocation annihilation. 2) Moreover, out of all predicted elements within the simulations of Scheiber et al. [38,39], B showed one of the highest potentials for GB strengthening, making it a very potent GB cohesion enhancer, and 3) as an interstitial element with a high GB segregation tendency in W [38], boron could potentially remove and replace the weakening oxygen at the interstitial GB sites, thereby strengthening the GB both directly and indirectly (see Figure B.10). These combined positive aspects explain the highly effective property enhancement of B in annealed ufg W. The APT measurements in Figure B.4b are confirming that oxygen is depleted directly at the GB in the W-B sample. However, in

the annealed material (Figure B.4c) a slight segregation of O is found in addition to the B segregation. This indicates that the strengthening effect of the segregated B is enough to completely outweigh the weakening effect that O has on GB cohesion.

Rhenium:

The W-Re material showed an increase in strength but a slight decrease in ductility. This is surprising, as Re usually has the opposite effect in a W host material [85,97,98]. Considering the reduced SRS and increased activation volume values acquired by nanoindentation strain-rate jump tests, it is evident that Re has a positive effect on dislocation mobility [98,118], yet from the bending experiments it does not seem to be very potent in avoiding GB failure. While the ab-initio simulations in [39] predict Re to strengthen the GB cohesion in W, they also show that the effect of Re on the GB would only be about 20% compared to that of e.g. boron. We could rationalize this behavior by considering that higher dislocation mobility might promote pile-up formation at GBs, with the related stress localizations promoting grain boundary failure. However, as no clear improvements of the mechanical properties by doping with Re were observed (Figure B.7b) and Re is a rather expensive material, making it unattractive for future large scale fabrication and application, we do not follow this consideration up with detailed investigations, as this would require e.g. in-situ TEM studies.

Hafnium:

The hafnium doped sample shows improved strength and ductility, but also a large variability among the individual tested microcantilever. The well-known affinity of Hf to O and the observed formation of HfO₂ (Figure B.3d) leads to the conclusion that Hf is very effective in binding oxygen, therefore removing the embrittling element from the GB to indirectly strengthen GB cohesion in ufg W (see Figure B.10). This behavior has already been observed for Mo in the past [31]. While this effect is rather interesting and leads to a clear improvement of the mechanical properties, it is not evident that it can be further improved or utilized for an adaptive material characteristic, e.g. by forced segregation through annealing, since a direct strengthening effect of Hf at the GB is not likely [39,40] and the majority of oxygen is presumably already bound in the hafnium oxides. The large variation among the different W-Hf cantilevers, however, could be a sign of a varying effectivity of Hf in removing oxygen throughout the sample, indicating that more oxygen from the initial powder surfaces could potentially be bound either through diffusion by an annealing step or by initially adding more Hf to the powder mixture. Another possible explanation for the large variation among the cantilever properties could be undetected smaller HfO₂ particles within the cantilevers, reducing the probed ductility.

Finally, as B and Hf show the most promising improvement of mechanical properties

of ufg W and the material is potentially interesting for employment in nuclear fusion reactors, the behavior of the two doping elements under irradiation should be briefly discussed. Both B and Hf are very good radiation absorbers, which is why they can be used as moderator rods in a variety of nuclear fission reactors [119]. This would add a minor radiation-shielding effect to the deployed material. The boron isotope B^{10} can decay into Li and He after neutron irradiation, following: $B^{10} + n^1 \rightarrow Li^7 + He^4$. The insoluble Helium is well known to form bubbles within metals, which leads to degradation of mechanical properties, swelling and structural disintegration [120]. However, considering the application in a nuclear fusion reactor, this rare occasion of B decay is expected to have a minor impact, compared to the continuous bombardment with He ions from the fusion reaction. Nevertheless, one has to take into account that in such a case, the positive effect of B on GB cohesion and mechanical properties is potentially lost over time.

B.5 Conclusion

In this work, ufg W samples doped with various interstitial and solute elements have been successfully fabricated. While the doping elements seem to only have little influence on grain size and hardness of the bulk material, a clear effect on the bending properties has been discovered utilizing microcantilever bending experiments. While the addition of C and Re seems to have a negative or hardly any effect on the mechanical properties of ufg tungsten, B and Hf serve to improve the mechanical performance and expended plastic energy density. It was demonstrated that B strengthens the GBs in tungsten directly (by enhancing GB cohesion) and also potentially indirectly (by replacing oxygen at the GB), which leads to an increase in bending strength, while maintaining the bending ductility level of the undoped ufg W. The strength of the boron doped tungsten can be increased even further by a heat treatment, leading to more segregation of B at GBs as well as an additional hardening-by-annealing effect. Hafnium, on the other hand, is not known to strengthen the GB directly, but it is very effective in binding oxygen from them, leading to an improvement in bending strength and ductility. Due to the clear enhancement in GB cohesion and the close interlink of ductility and fracture toughness, it is assumed that the fracture toughness of ufg W also improves tremendously with the addition of B and Hf. Fracture mechanical tests to assess this expectation are planned and subject of future work.

In conclusion, it was demonstrated that the mechanical properties of ufg tungsten can be enhanced by the addition of suitable GB strengthening doping elements, such as B and Hf. These findings should also relate towards improving properties of

coarser-grained tungsten material. However, once the fracture mode changes from intercrystalline to transcrystalline, no further increase in ductility and toughness through GB doping can be expected, as then the inherent brittleness of the tungsten crystal rather than the grain boundaries is the limiting factor. Therefore, it is recommended to combine the GBSE approach with very small grain sizes first and foremost, to fully tap the strengthening and toughening potential and create a high-performance material suitable to deploy in extreme environments.

Acknowledgements

The authors acknowledge funding by the European Research Council under Grant number 771146 (MW, SD, DK). The authors thank Dr. Wolfram Knabl, Dr. Judith Köstenbauer and Plansee SE for providing tungsten material powder and support with sample annealing.

References

- [1] R.O. Ritchie, The conflicts between strength and toughness, *Nat. Mater.* 10 (2011) 817–822.
- [2] M.A. Meyers, A. Mishra, D.J. Benson, Mechanical properties of nanocrystalline materials, *Prog. Mater. Sci.* 51 (2006) 427–556.
- [3] C.C. Koch, D.G. Morris, K. Lu, A. Inoue, Ductility of nanostructured materials, *MRS Bull.* 24 (1999) 54–58.
- [4] Y. Wang, M. Chen, F. Zhou, E. Ma, High tensile ductility in a nanostructured metal, *Nature.* 419 (2002) 912–915.
- [5] E. Ma, Eight routes to improve the tensile ductility of bulk nanostructured metals and alloys, *Jom.* 58 (2006) 49–53.
- [6] Y. Wei, Y. Li, L. Zhu, Y. Liu, X. Lei, G. Wang, Y. Wu, Z. Mi, J. Liu, H. Wang, H. Gao, Evading the strength-ductility trade-off dilemma in steel through gradient hierarchical nanotwins, *Nat. Commun.* 5 (2014).
- [7] E. Ma, T. Zhu, Towards strength–ductility synergy through the design of heterogeneous nanostructures in metals, *Mater. Today.* 20 (2017) 323–331.
- [8] Q. Wei, K.T. Ramesh, L.J. Kecskes, S.N. Mathaudhu, K.T. Hartwig, Ultrafine and Nanostructured Refractory Metals Processed by SPD : Microstructure and Mechanical Properties, *Mater. Sci. Forum.* 579 (2008) 75–90.
- [9] S. Shahrezaei, Y. Sun, S.N. Mathaudhu, Strength-ductility modulation via surface severe plastic deformation and annealing, *Mater. Sci. Eng. A.* 761 (2019) 138023.
- [10] S.N. Mathaudhu, A. J, K.T. Hartwig, L.J. Kecskes, Microstructures and recrystallization behavior

- of severely hot-deformed tungsten, *Mater. Sci. Eng. A.* 503 (2009) 28–31.
- [11] N.A. Mara, D. Bhattacharyya, P. Dickerson, R.G. Hoagland, A. Misra, Ultrahigh strength and ductility of Cu-Nb nanolayered composites, *Mater. Sci. Forum.* 633–634 (2010) 647–653.
- [12] A. Khalajhedayati, Z. Pan, T.J. Rupert, Manipulating the interfacial structure of nanomaterials to achieve a unique combination of strength and ductility, *Nat. Commun.* 7 (2016).
- [13] Z. Pan, T.J. Rupert, Amorphous intergranular films as toughening structural features, *Acta Mater.* 89 (2015) 205–214.
- [14] E.O. Hall, The Deformation and Ageing of Mild Steel: III Discussion of Results, *Proc. Phys. Soc.* 64 (1951) 747–753.
- [15] N.J. Petch, The Cleavage Strength of Polycrystals, *J. Iron Steel Inst.* 174 (1953) 25–28.
- [16] N.J. Petch, The ductile-brittle transition in the fracture of α -iron: I, *Philos. Mag.* 3 (1958) 1089–1097.
- [17] T. Hanamura, F. Yin, K. Nagai, Ductile-brittle transition temperature of ultrafine ferrite/cementite microstructure in a low carbon steel controlled by effective grain size, *ISIJ Int.* 44 (2004) 610–617.
- [18] A. Hohenwarter, R. Pippan, Fracture and fracture toughness of nanopolycrystalline metals produced by severe plastic deformation, *Philos. Trans. R. Soc. A.* 373 (2015) 20140366.
- [19] A. V Sergueeva, N.A. Mara, A.K. Mukherjee, Plasticity at really diminished length scales, *Mater. Sci. Eng. A.* 463 (2007) 8–13.
- [20] I.A. Ovid'ko, A.G. Sheinerman, Kinetics of grain boundary sliding and rotational deformation in nanocrystalline materials, *Rev. Adv. Mater. Sci.* 35 (2013) 48–58.
- [21] S.V. Bobylev, N.F. Morozov, I.A. Ovid'ko, Cooperative grain boundary sliding and migration process in nanocrystalline solids, *Phys. Rev. Lett.* 105 (2010) 055504.
- [22] H. Van Swygenhoven, P.M. Derlet, Grain-boundary sliding in nanocrystalline fcc metals, *Phys. Rev. B - Condens. Matter Mater. Phys.* 64 (2001) 224105.
- [23] R. Pippan, A. Hohenwarter, The importance of fracture toughness in ultrafine and nanocrystalline bulk materials, *Mater. Res. Lett.* 4 (2016) 127–136.
- [24] D. Raabe, M. Herbig, S. Sandlöbes, Y. Li, D. Tytko, M. Kuzmina, D. Ponge, P. Choi, Grain boundary segregation engineering in metallic alloys : A pathway to the design of interfaces, *Curr. Opin. Solid State Mater. Sci.* 18 (2014) 253–261.
- [25] M.A. Gibson, C.A. Schuh, Segregation-induced changes in grain boundary cohesion and embrittlement in binary alloys, *Acta Mater.* 95 (2015) 145–155.
- [26] P. Lejcek, M. Šob, V. Paidar, Interfacial segregation and grain boundary embrittlement : An overview and critical assessment of experimental data and calculated results, *Prog. Mater. Sci.* 87 (2017) 83–139.
- [27] M. Kuzmina, D. Ponge, D. Raabe, Grain boundary segregation engineering and austenite reversion turn embrittlement into toughness : Example of a 9 wt.% medium Mn steel, *Acta Mater.* 86 (2015) 182–192.
- [28] J. Bok, J. Wung, Z. Li, J. Chan, J. Gi, D. Raabe, H. Seop, Boron doped ultrastrong and ductile high-entropy alloys, *Acta Mater.* 151 (2018) 366–376.
- [29] X. Wu, Y. You, X. Kong, J. Chen, G. Luo, G. Lu, C.S. Liu, Z. Wang, First-principles determination of grain boundary strengthening in tungsten : Dependence on grain boundary structure and metallic radius of solute, *Acta Mater.* 120 (2016) 315–326.

- [30] K. Leitner (née Babinsky), P.J. Felfer, D. Holec, J.M. Cairney, W. Knabl, A. Lorich, H. Clemens, S. Primig, On grain boundary segregation in molybdenum materials, *Mater. Des.* 135 (2017) 204–212.
- [31] K. Leitner, D. Scheiber, S. Jakob, S. Primig, H. Clemens, E. Povoden-Karadeniz, L. Romaner, How grain boundary chemistry controls the fracture mode of molybdenum, *Mater. Des.* 142 (2018) 36–43.
- [32] K. Leitner (née Babinsky), D. Lutz, W. Knabl, M. Eidenberger-Schober, K. Huber, A. Lorich, H. Clemens, V. Maier-Kiener, Grain boundary segregation engineering in as-sintered molybdenum for improved ductility, *Scr. Mater.* 156 (2018) 60–63.
- [33] S. Jakob, A. Hohenwarter, A. Lorich, W. Knabl, R. Pippan, H. Clemens, V. Maier-Kiener, Assessment of grain boundary cohesion of technically pure and boron micro-doped molybdenum via meso-scale three-point-bending experiments, *Mater. Des.* 207 (2021) 109848.
- [34] S.C. Pun, W. Wang, A. Khalajhedayati, J.D. Schuler, J.R. Trelewicz, T.J. Rupert, Nanocrystalline Al-Mg with extreme strength due to grain boundary doping, *Mater. Sci. Eng. A.* 696 (2017) 400–406.
- [35] H. Lee, V. Tomar, An examination of nickel doping effect on the mechanical strength of a tungsten grain boundary, *Comput. Mater. Sci.* 77 (2013) 131–138.
- [36] R. Wu, A.J. Freeman, G.B. Olson, First Principles Determination of the Effects of Phosphorus and Boron on Iron Grain Boundary Cohesion, *Science* (80-.). 265 (2006) 376–380.
- [37] P. Lejcek, *Grain Boundary Segregation in Metals*, Springer, Berlin-Heidelberg, 2010.
- [38] D. Scheiber, R. Pippan, P. Puschnig, L. Romaner, Ab initio search for cohesion-enhancing impurity elements at grain boundaries in molybdenum and tungsten, *Model. Simul. Mater. Sci. Eng.* 24 (2016) 85009.
- [39] D. Scheiber, R. Pippan, P. Puschnig, A. Ruban, L. Romaner, Ab-initio search for cohesion-enhancing solute elements at grain boundaries in molybdenum and tungsten, *Int. J. Refract. Met. Hard Mater.* 60 (2016) 75–81.
- [40] W. Setyawan, R.J. Kurtz, *Grain Boundary Strengthening Properties of Tungsten Alloys*, 2012.
- [41] V.I. Razumovskiy, S. V. Divinski, L. Romaner, Solute segregation in Cu: DFT vs. Experiment, *Acta Mater.* 147 (2018) 122–132.
- [42] V.I. Razumovskiy, A.Y. Lozovoi, I.M. Razumovskii, First-principles-aided design of a new Ni-base superalloy : Influence of transition metal alloying elements on grain boundary and bulk cohesion, *Acta Mater.* 82 (2015) 369–377.
- [43] L. Huber, M. Militzer, Atomistic simulations of the interaction of alloying elements with grain boundaries in Mg, *Acta Mater.* 80 (2014) 194–204.
- [44] A.S. Ebner, S. Jakob, H. Clemens, R. Pippan, V. Maier-Kiener, S. He, W. Ecker, D. Scheiber, V.I. Razumovskiy, Grain boundary segregation in Ni-base alloys: A combined atom probe tomography and first principles study, *Acta Mater.* 221 (2021) 117354.
- [45] M. Rieth, D.E.J. Armstrong, B. Dafferner, S. Heger, A. Hoffmann, M. Hoffmann, U. Jäntschi, M. Rohde, T. Scherer, V. Widak, H. Zimmermann, Tungsten as a Structural Divertor Material, *Adv. Sci. Technol.* 73 (2010) 11–21.
- [46] S. Wurster, N. Baluc, M. Battabyal, T. Crosby, J. Du, C. Garcia-Rosales, A. Hasegawa, A. Hoffmann, A. Kimura, H. Kurishita, R.J. Kurtz, H. Li, S. Noh, J. Reiser, J. Riesch, M. Rieth, W. Setyawan, M. Walter, J.-H. You, R. Pippan, Recent progress in R&D on tungsten alloys for divertor structural and plasma facing materials, *J. Nucl. Mater.* 442 (2013) 181–189.

- [47] M. Rieth, S.L. Dudarev, S.M.G. De Vicente, J. Aktaa, T. Ahlgren, S. Antusch, D.E.J. Armstrong, M. Balden, N. Baluc, M. Barthe, W. W. Basuki, M. Battabyal, C.S. Becquart, D. Blagoeva, H. Boldyryeva, J. Brinkmann, M. Celino, L. Ciupinski, J.B. Correia, A. De Backer, C. Domain, E. Gaganidze, C. Garcia-Rosales, J. Gibson, M.R. Gilbert, S. Giusepponi, B. Gludovatz, H. Greuner, K. Heinola, T. Höschen, A. Hoffmann, N. Holstein, F. Koch, W. Krauss, H. Li, S. Lindig, J. Linke, C. Linsmeier, P. López-ruiz, H. Maier, J. Matejcek, T.P. Mishra, M. Walter, T. Weber, T. Weitkamp, S. Wurster, M.A. Yar, J.H. You, A. Zivelonghi, Recent progress in research on tungsten materials for nuclear fusion applications in Europe, *J. Nucl. Mater.* 432 (2013) 482–500.
- [48] M. Rieth, S.L. Dudarev, S.M.G. De Vicente, J. Aktaa, T. Ahlgren, S. Antusch, D.E.J. Armstrong, M. Balden, N. Baluc, M. Barthe, W.W. Basuki, M. Battabyal, C.S. Becquart, D. Blagoeva, H. Boldyryeva, J. Brinkmann, M. Celino, L. Ciupinski, J.B. Correia, A. De Backer, C. Domain, E. Gaganidze, C. Garcia-Rosales, J. Gibson, M.R. Gilbert, S. Giusepponi, B. Gludovatz, H. Greuner, K. Heinola, T. Höschen, A. Hoffmann, N. Holstein, F. Koch, W. Krauss, H. Li, S. Lindig, J. Linke, C. Linsmeier, P. Lopez-ruiz, H. Maier, J. Matejcek, T.P. Mishra, M. Muhammed, A. Munoz, M. Muzyk, K. Nordlund, D. Nguyen-manh, J. Opschoor, N. Ordas, M. Walter, T. Weber, T. Weitkamp, S. Wurster, M.A. Yar, J.H. You, A. Zivelonghi, A brief summary of the progress on the EFDA tungsten materials program, *J. Nucl. Mater.* 442 (2013) 173–180.
- [49] C. Ren, Z.Z. Fang, M. Koopman, B. Butler, J. Paramore, S. Middlemas, Methods for improving ductility of tungsten - A review, *Int. J. Refract. Metals Hard Mater.* 75 (2018) 170–183.
- [50] D.E.J. Armstrong, X. Yi, E.A. Marquis, S.G. Roberts, Hardening of self ion implanted tungsten and tungsten 5-wt % rhenium, *J. Nucl. Mater.* 432 (2013) 428–436.
- [51] A. Xu, C. Beck, D.E.J. Armstrong, K. Rajan, G.D.W. Smith, P.A.J. Bagot, S.G. Roberts, Ion-irradiation-induced clustering in W – Re and W – Re – Os alloys : A comparative study using atom probe tomography and nanoindentation measurements, *Acta Mater.* 87 (2015) 121–127.
- [52] D.E.J. Armstrong, P.D. Edmondson, S.G. Roberts, Effects of sequential tungsten and helium ion implantation on nano-indentation hardness of tungsten, *Appl. Phys. Lett.* 102 (2013) 251901.
- [53] B. Gludovatz, S. Wurster, A. Hoffmann, R. Pippan, Fracture toughness of polycrystalline tungsten alloys, *Int. J. Refract. Met. Hard Mater.* 28 (2010) 674–678.
- [54] J.S. Weaver, C. Sun, Y. Wang, S.R. Kalidindi, R.P. Doerner, N.A. Mara, S. Pathak, Quantifying the mechanical effects of He, W and He + W ion irradiation on tungsten with spherical nanoindentation, *J. Mater. Sci.* 53 (2018) 5296–5316.
- [55] B. Gludovatz, S. Wurster, A. Hoffmann, R. Pippan, A study into the crack propagation resistance of pure tungsten, *Eng. Fract. Mech.* 100 (2013) 76–85.
- [56] X. Zhang, K. Hattar, Y. Chen, L. Shao, J. Li, C. Sun, K. Yu, N. Li, M.L. Taheri, H. Wang, J. Wang, M. Nastasi, Radiation damage in nanostructured materials, *Prog. Mater. Sci.* 96 (2018) 217–321.
- [57] S. Wurster, R. Pippan, Nanostructured metals under irradiation, *Scr. Mater.* 60 (2009) 1083–1087.
- [58] I.J. Beyerlein, A. Caro, M.J. Demkowicz, N.A. Mara, A. Misra, B.P. Uberuaga, Radiation damage tolerant nanomaterials, *Mater. Today.* 16 (2013) 443–449.
- [59] I.J. Beyerlein, M.J. Demkowicz, A. Misra, B.P. Uberuaga, Defect-interface interactions, *Prog. Mater. Sci.* 74 (2015) 125–210.
- [60] M. Wurmshuber, D. Frazer, A. Bachmaier, Y. Wang, P. Hosemann, D. Kiener, Impact of interfaces

on the radiation response and underlying defect recovery mechanisms in nanostructured Cu-Fe-Ag, *Mater. Des.* 160 (2018) 1148–1157.

[61] W. Han, M.J. Demkowicz, N.A. Mara, E.G. Fu, S. Sinha, A.D. Rollett, Y. Wang, J.S. Carpenter, I.J. Beyerlein, A. Misra, Design of radiation tolerant materials via interface engineering, *Adv. Mater.* 25 (2013) 6975–6979.

[62] W.S. Cunningham, K. Hattar, Y. Zhu, D.J. Edwards, J.R. Trelewicz, Suppressing irradiation induced grain growth and defect accumulation in nanocrystalline tungsten through grain boundary doping, *Acta Mater.* 206 (2021) 116629.

[63] O. El-Atwani, J.A. Hinks, G. Greaves, J.P. Allain, S.A. Maloy, Grain size threshold for enhanced irradiation resistance in nanocrystalline and ultrafine tungsten, *Mater. Res. Lett.* 5 (2017) 343–349.

[64] O. El-Atwani, J.E. Nathaniel, A.C. Leff, B. Muntifering, J.K. Baldwin, K. Hattar, M.L. Taheri, The role of grain size in He bubble formation: Implications for swelling resistance, *J. Nucl. Mater.* 484 (2017) 236–244.

[65] O. El-Atwani, S. Gonderman, M. Efe, G. De Temmerman, T. Morgan, K. Bystrov, D. Klenosky, T. Qiu, J.P. Allain, Ultrafine tungsten as a plasma-facing component in fusion devices: Effect of high flux, high fluence low energy helium irradiation, *Nucl. Fusion.* 54 (2014).

[66] O. El-Atwani, J.A. Hinks, G. Greaves, S. Gonderman, T. Qiu, M. Efe, J.P. Allain, In-situ TEM observation of the response of ultrafine- and nanocrystalline-grained tungsten to extreme irradiation environments, *Sci. Rep.* 4 (2014) 4–10.

[67] M. Wurmshuber, D. Frazer, M. Balooch, I. Issa, A. Bachmaier, P. Hosemann, D. Kiener, The effect of grain size on bubble formation and evolution in helium-irradiated Cu-Fe-Ag, *Mater. Charact.* 171 (2021) 110822.

[68] E. Smiti, P. Jouffrey, A. Kobylanski, The influence of carbon and oxygen in the grain boundary on the brittle-ductile transition temperature of tungsten bi-crystals, *Scr. Metall.* 18 (1984) 673–676.

[69] M. Wurmshuber, S. Doppermann, S. Wurster, D. Kiener, Ultrafine-grained Tungsten by High-Pressure Torsion – Bulk precursor versus powder processing route, *IOP Conf. Ser. Mater. Sci. Eng.* 580 (2019) 012051.

[70] R. Pippan, S. Scheriau, A. Hohenwarter, M. Hafok, Advantages and Limitations of HPT: A Review, *Mater. Sci. Forum.* 584–586 (2008) 16–21.

[71] K. Babinsky, R. De Kloe, H. Clemens, S. Primig, A novel approach for site-specific atom probe specimen preparation by focused ion beam and transmission electron backscatter diffraction, *Ultramicroscopy.* 144 (2014) 9–18.

[72] V. Maier, K. Durst, J. Mueller, B. Backes, H.W. Höppel, M. Göken, Nanoindentation strain-rate jump tests for determining the local strain-rate sensitivity in nanocrystalline Ni and ultrafine-grained Al, *J. Mater. Res.* 26 (2011) 1421–1430.

[73] V. Maier-Kiener, K. Durst, Advanced Nanoindentation Testing for Studying Strain-Rate Sensitivity and Activation Volume, *Jom.* 69 (2017) 2246–2255.

[74] D.S. Gianola, C. Eberl, Micro- and nanoscale tensile testing of materials, *Jom.* 61 (2009) 24–35.

[75] D. Kiener, C. Motz, G. Dehm, R. Pippan, Overview on established and novel FIB based miniaturized mechanical testing using in-situ SEM, *Int. J. Mater. Res.* 100 (2009) 1074–1087.

[76] D. Kiener, W. Grosinger, G. Dehm, R. Pippan, A further step towards an understanding of

size-dependent crystal plasticity: In situ tension experiments of miniaturized single-crystal copper samples, *Acta Mater.* 56 (2008) 580–592.

[77] D. Kiener, A.M. Minor, Source truncation and exhaustion: Insights from quantitative in situ TEM tensile testing, *Nano Lett.* 11 (2011) 3816–3820.

[78] R. Wheeler, P.A. Shade, M.D. Uchic, Insights Gained Through Image Analysis During In Situ Micromechanical Experiments, *JOM.* 64 (2012) 58–65.

[79] H.T. Vo, A. Reichardt, D. Frazer, N. Bailey, P. Chou, P. Hosemann, In situ micro-tensile testing on proton beam-irradiated stainless steel, *J. Nucl. Mater.* 493 (2017) 336–342.

[80] M. Alfreider, M. Meindlhumer, V. Maier-Kiener, A. Hohenwarter, D. Kiener, Extracting information from noisy data: strain mapping during dynamic in situ SEM experiments, *J. Mater. Res.* 36 (2021) 2291–2304.

[81] C. Motz, T. Schöberl, R. Pippan, Mechanical properties of micro-sized copper bending beams machined by the focused ion beam technique, *Acta Mater.* 53 (2005) 4269–4279.

[82] M. Meindlhumer, *Micromechanical Characterization of Self-Organized Ti_{1-x}Al_xN Nanolamellae: The Influence of Interface Coherency and Phase Alteration on Fracture Behaviour*, Montanuniversität Leoben, 2016.

[83] E. Carrera, G. Giunta, M. Petrolo, *Beam Structures: Classical and Advanced Theories*, John Wiley & Sons, 2011.

[84] H. Duschaneck, P. Rogl, Critical Assessment and Thermodynamic Calculation of the Binary System Boron-Tungsten (B-W), *J. Phase Equilibria.* 16 (1995) 150–161.

[85] W.D. Klopp, Review of ductilizing of group VIA elements by rhenium and other solutes, NASA TN D-4955. (1968).

[86] G.M. Song, M. Science, P.O. Box, The microstructure and elevated temperature strength of tungsten-titanium carbide composite, *J. Mater. Sci.* 37 (2002) 3541–3548.

[87] C. Fan, C. Liu, F. Peng, N. Tan, M. Tang, Q. Zhang, Q. Wang, F. Li, J. Wang, Y. Chen, H. Liang, S. Guan, K. Yang, J. Liu, Phase stability and incompressibility of tungsten boride (WB) researched by in-situ high pressure x-ray diffraction, *Phys. B Phys. Condens. Matter.* 521 (2017) 6–12.

[88] M. Thuvander, H.O. Andrén, PFIM studies of grain and phase boundaries: a review, *Mater. Charact.* 44 (2000) 87–100.

[89] B.W. Krakauer, D.N. Seidman, Absolute atomic-scale measurements of the Gibbsian interfacial excess of solute at internal interfaces, *Phys. Rev. B.* 48 (1993) 6724–6727.

[90] R.C. Koo, Recovery in cold-worked tungsten, *J. Less-Common Met.* 3 (1961) 412–428.

[91] B. Sestak, A. Seeger, Gleitung und Verfestigung in kubisch-raumzentrierten Metallen, *Zeitschrift Für Met.* 69 (1978).

[92] A. Seeger, The Temperature and Strain-Rate Dependence of the Flow Stress of Body-Centred Cubic Metals: A Theory Based on Kink-Kink Interactions, *Zeitschrift Für Met.* 72 (1981) 369–380.

[93] A. Argon, *Strengthening mechanisms in crystal plasticity*, Oxford University Press, New York, 2008.

[94] D. Kiener, R. Fritz, M. Alfreider, A. Leitner, R. Pippan, V. Maier-Kiener, Rate Limiting Deformation Mechanisms of bcc Metals in Confined Volumes, *Acta Mater.* 166 (2019) 687–701.

[95] D. Wu, X.L. Wang, T.G. Nieh, Variation of strain rate sensitivity with grain size in Cr and other

- body-centred cubic metals, *J. Phys. D. Appl. Phys.* 47 (2014).
- [96] B.D. Beake, A.J. Harris, J. Moghal, D.E.J. Armstrong, Temperature dependence of strain rate sensitivity, indentation size effects and pile-up in polycrystalline tungsten from 25 to 950°C, *Mater. Des.* 156 (2018) 278–286.
- [97] J. Kappacher, A. Leitner, D. Kiener, H. Clemens, V. Maier-Kiener, Thermally activated deformation mechanisms and solid solution softening in W-Re alloys investigated via high temperature nanoindentation, *Mater. Des.* 189 (2020) 108499.
- [98] L. Romaner, C. Ambrosch-Draxl, R. Pippan, Effect of rhenium on the dislocation core structure in tungsten, *Phys. Rev. Lett.* 104 (2010) 195503.
- [99] A. Hohenwarter, R. Pippan, Anisotropic fracture behavior of ultrafine-grained iron, *Mater. Sci. Eng. A.* 527 (2010) 2649–2656.
- [100] S. Wurster, B. Gludovatz, A. Hoffmann, R. Pippan, Fracture behaviour of tungsten-vanadium and tungsten-tantalum alloys and composites, *J. Nucl. Mater.* 413 (2011) 166–176.
- [101] J. Reiser, J. Hoffmann, U. Jäntschi, M. Klimenkov, S. Bonk, C. Bonnekoh, A. Hoffmann, T. Mrotzek, M. Rieth, Ductilisation of tungsten (W): On the increase of strength AND room-temperature tensile ductility through cold-rolling, *Int. J. Refract. Met. Hard Mater.* 64 (2017) 261–278.
- [102] N. Fonstein, *Advanced High Strength Sheet Steels*, Springer International Publishing, 2015.
- [103] P. Khedkar, R. Motagi, P. Mahajan, G. Makwana, A Review on Advance High Strength Steels, *Int. J. Curr. Eng. Technol.* 6 (2016) 240–243.
- [104] Q. Wei, T. Jiao, K.T. Ramesh, E. Ma, L.J. Kecskes, L. Magness, R. Dowding, V.U. Kazykhanov, R.Z. Valiev, Mechanical behavior and dynamic failure of high-strength ultrafine grained tungsten under uniaxial compression, *Acta M.* 54 (2006) 77–87.
- [105] X. Huang, N. Hansen, N. Tsuji, Hardening by Annealing and Softening by Deformation in Nanostructured Metals, *Science* (80-.). 312 (2006) 249–251.
- [106] O. Renk, A. Hohenwarter, K. Eder, K.S. Kormout, J.M. Cairney, R. Pippan, Increasing the strength of nanocrystalline steels by annealing: Is segregation necessary?, *Scr. Mater.* 95 (2015) 27–30.
- [107] T.J. Rupert, J.R. Trelewicz, C.A. Schuh, Grain boundary relaxation strengthening of nanocrystalline Ni-W alloys, *J. Mater. Res.* 27 (2012) 1285–1294.
- [108] J. Hu, Y.N. Shi, X. Sauvage, G. Sha, K. Lu, Grain boundary stability governs hardening and softening in extremely fine nanograined metals, *Science* (80-.). 355 (2017) 1292–1296.
- [109] M. Alfreider, I. Issa, O. Renk, D. Kiener, Probing defect relaxation in ultra-fine grained Ta using micromechanical spectroscopy, *Acta Mater.* 185 (2020) 309–319.
- [110] H. Van Swygenhoven, J.R. Weertman, Deformation in nanocrystalline metals, *Mater. Today.* 9 (2006) 24–31.
- [111] H. Van Swygenhoven, Footprints of plastic deformation in nanocrystalline metals, *Mater. Sci. Eng. A.* 483–484 (2008) 33–39.
- [112] L.E. Murr, Dislocation Ledge Sources: Dispelling the Myth of Frank–Read Source Importance, *Metall. Mater. Trans. A Phys. Metall. Mater. Sci.* 47 (2016) 5811–5826.
- [113] V. Turlo, T.J. Rupert, Grain boundary complexions and the strength of nanocrystalline metals: Dislocation emission and propagation, *Acta Mater.* 151 (2018) 100–111.
- [114] M.A. Tschopp, G.J. Tucker, D.L. McDowell, Atomistic simulations of tension-compression asym-

- metry in dislocation nucleation for copper grain boundaries, *Comput. Mater. Sci.* 44 (2008) 351–362.
- [115] B. Lüthi, L. Ventelon, C. Elsässer, D. Rodney, F. Willaime, First principles investigation of carbon-screw dislocation interactions in body-centered cubic metals, *Model. Simul. Mater. Sci. Eng.* 25 (2017) 84001.
- [116] B. Lüthi, F. Berthier, L. Ventelon, B. Legrand, D. Rodney, F. Willaime, Ab initio thermodynamics of carbon segregation on dislocation cores in bcc iron, *Model. Simul. Mater. Sci. Eng.* 27 (2019).
- [117] L. Ventelon, B. Lüthi, E. Clouet, L. Proville, B. Legrand, D. Rodney, F. Willaime, Dislocation core reconstruction induced by carbon segregation in bcc iron, *Phys. Rev. B - Condens. Matter Mater. Phys.* 91 (2015) 1–5.
- [118] J. Qian, C.Y. Wu, J.L. Fan, H.R. Gong, Effect of alloying elements on stacking fault energy and ductility of tungsten, *J. Alloys Compd.* 737 (2018) 372–376.
- [119] K.L. Murty, I. Charit, *An Introduction to Nuclear Materials: Fundamentals and Applications*, WILEY-VCH, Weinheim, 2013..
- [120] M. Wurmshuber, M. Balooch, X. Huang, P. Hosemann, D. Kiener, Helium-induced swelling and mechanical property degradation in ultrafine-grained W and W-Cu nanocomposites for fusion applications, *Scr. Mater.* 213 (2022) 114641.

C Small-scale fracture mechanical investigations of grain boundary doped ufg tungsten

M. Wurmshuber¹, M. Alfreider¹, S. Wurster², R. Pippan², D. Kiener¹

¹ Department of Materials Science, Chair of Materials Physics, Montanuniversität Leoben, Jahnstraße 12, 8700 Leoben, Austria

² Erich-Schmid Institute for Materials Science, Austrian Academy of Sciences, Jahnstraße 12, 8700 Leoben, Austria

The inherent brittleness of the refractory metal tungsten represents a major challenge for its application as divertor material in future nuclear fusion reactors. Grain refinement to the ultrafine-grained regime is a promising strategy to increase the fracture toughness of W, but it also promotes intercrystalline crack growth. Therefore, the strengthening of grain boundary cohesion in W is of great importance. In this work, grain boundary doping with B and Hf, two elements that were identified in previous work to increase bending strength and ductility, is applied to ultrafine-grained W. The fracture toughness is measured utilizing small-scale testing techniques. Fracture mechanical experiments on the microscale provide a plethora of challenges to correctly assess size-independent toughness values, which are presented and discussed within this work. It was found that the toughness of W can be under- and overestimated, depending on the sample dimensions and plastic zone size. When assessing the valid and size-independent fracture toughness measured for the differently doped W specimen, doping with the strengthening element B maintained the already remarkably high toughness of the undoped ultrafine-grained W of around $20 \text{ MPa}\sqrt{m}$. The samples doped with Hf even improved the fracture toughness to values of up to $28 \text{ MPa}\sqrt{m}$. Hence, the effects of GB doping on the fracture toughness of ultrafine-grained W are explored, while simultaneously the influence of sample dimensions on measured fracture toughness are discussed. These insights are expected to have a great impact on the development of superior materials for use in harsh environments, as well as the application of small-scale fracture mechanical experiments, as used e.g. in the assessment of control samples in nuclear technology.

C.1 Introduction

Exhibiting the highest melting point of any pure chemical element (3422°C), high intrinsic strength and many more favorable properties [1], tungsten is frequently considered for high-performance applications in the harshest environments, for example as structural material in the divertor part of nuclear fusion reactors [2–7]. However, the limited ductility and inherent brittleness of the refractory metal oftentimes represent critical obstacles for a successful and safe employment of W in such applications. In recent years, many strategies to improve ductility and fracture toughness of W have been investigated [3,4,7–9] and a reduction in grain size by either cold-rolling [10–13], wire-drawing [14–17] or severe plastic deformation (SPD) [18,19] showed promising results in elevating the overall mechanical properties. As the smaller grain size and, consequently, larger amount of grain boundaries within W favor a preferential inter-crystalline fracture mode [20–23], strengthening the grain boundary (GB) cohesion has potential to further enhance the mechanical properties and especially toughness of W. By applying the concept of grain boundary segregation engineering (GBSE) [24–32] and by selecting ab-initio informed doping elements [33,34], it was shown that doping of ultrafine-grained (ufg) W with B and Hf can significantly improve the bending strength and bending ductility [35], respectively.

In this work, the effect of these doping elements on the fracture toughness of ufg W, fabricated by high-pressure torsion (HPT), is investigated. As the sample volume of such SPD-processed materials is limited and a microstructural gradient is present, small-scale fracture mechanical experiments have to be utilized. By far the most popular test configuration on the microscale is the notched cantilever bending test [36–45] (see Figure C.1). For semi-brittle materials, such as ufg W, the application of such experiments is rather challenging, as the decent ductility and extremely small sample dimensions lead to validity issues [38,40,46]. Thus, in this work fracture mechanical experiments are performed for different cantilever dimensions of the various undoped and doped materials. The validity of the experiments and the micromechanical mechanisms behind perceived invalid toughness values are discussed. These insights are not only valuable for the concrete case at hand, but for micromechanical fracture experiments as a whole. Small-scale fracture mechanical tests can also play an important role in the application of W in fusion reactors: In order to evaluate the risk of continued operation, it is common practice in nuclear fission energy to place control samples made out of the structural reactor-material inside the reactor. This way, the control sample experiences the same environmental conditions, such as irradiation and corrosion, as the employed reactor material. Therefore, in order to assess the mechanical property changes over time due to these environmental effects without stopping the fission operation and disassembling the reactor, one can simply test this control sample. These mechanical tests have in

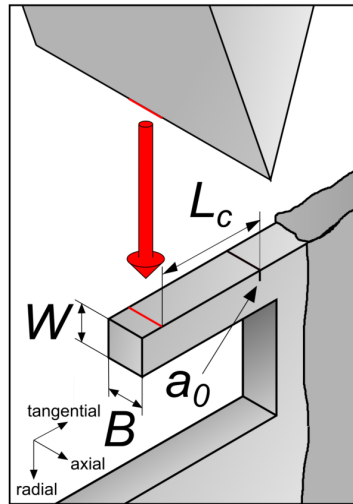


Figure C.1 Micromechanical testing setup for notched cantilever bending fracture experiments.

recent years increasingly been performed in smaller and smaller dimensions, in order not to “waste” any control sample material for the years to come [47–49]. It is reasonable to assume that a similar approach can be employed in novel nuclear fusion reactors. Additionally, irradiation studies on potential reactor materials are frequently performed using ion-irradiation, instead of time-consuming neutron irradiation. Here, the evaluation of mechanical properties using small-scale testing techniques is inevitable, given the shallow penetration depth of ions and therefore limited volume of irradiated material [44,47–56]. Hence, the correct evaluation of fracture toughness on the microscale for a material such as ufg W is crucial.

Therefore, this work investigates the effect of GB doping on the fracture toughness of ufg W , while in addition important remarks on the sensitive topic of sample dimensions for valid small-scale fracture experiments are made.

C.2 Material and Methodology

C.2.1 Material

The materials investigated in this work are ufg W samples as produced in [35]. The undoped, boron-doped and hafnium-doped samples from this work are all fabricated from powders using a combination of cold-compacting, annealing and subsequent HPT deformation at 400°C under a nominal pressure of 12 GPa for about 1 rotation

[35,57]. The amount of B and Hf doping elements was adjusted to between 3-5 at.%. A boron-doped sample underwent an additional low-temperature annealing at 500°C for 5h after the HPT processing, which resulted in a hardening-by-annealing effect and a more pronounced GB segregation of B. This sample is hereinafter marked “W-B ann.”. The result from this fabrication process are specimen disks with a diameter of 6 mm and a thickness of 0.6 mm. These material disks show a microstructural gradient from the disk center to the edge, with the desired microstructure and a grain size of 140 – 160 nm only being present at the outer regions of the sample disks at a radius of 3 mm.

C.2.2 Small-scale fracture mechanical tests

Due to the aforementioned microstructural gradient within the sample disks and limited sample volume containing the studied microstructure, the fracture toughness of the materials was investigated by small-scale fracture mechanical experiments. For this purpose, cantilevers were fabricated at the desired location, i.e. at a radius of 3 mm from the disk center, using a dual-beam FIB-SEM (LEO 1540 XB and Zeiss Auriga, both Zeiss GmbH, Germany) and a small pre-notch was introduced to the cantilevers using a FIB milling current of 30 pA (see Figure C.1). Cantilevers with approximate dimensions of $3 \times 3 \times 10 \mu\text{m}$ as well as $8 \times 8 \times 30 \mu\text{m}$ were fabricated for all investigated materials. Additionally, a combined femtosecond laser (Origami 10 XP, Onefive GmbH, Switzerland) [58] and FIB approach was utilized to prepare one larger cantilever (approximate dimensions of $30 \times 30 \times 110 \mu\text{m}$) in both the undoped W and the hafnium-doped sample. Examples for (already tested) cantilevers with different sample dimensions and their fracture surfaces are shown in Figure C.2. All cantilevers were fabricated with the crack growth direction towards the sample disk center (radial direction). As even the largest cantilever dimensions are still rather small for a semi-brittle material such as ufg W, the small scale yielding criterion [40,46,59,60] (Equation C.1) is not met for any specimen and linear elastic fracture mechanics is not applicable to the cantilever experiments:

$$B, (W - a_0) > 2.5 \left(\frac{K_Q}{\sigma_y} \right)^2 \quad (\text{C.1})$$

With B being the sample thickness, W the sample width and a_0 the initial crack length of the FIB-milled notch (compare with Figure C.1). K_Q represents the conditional critical stress intensity factor of the material measured in the experiment and σ_y the yield strength of the material. According to Equation C.1, the sample thickness and ligament length of the specimens have to be at least $110 \mu\text{m}$ in order to fulfill the

criterion and to be able to apply linear elastic fracture mechanics (LEFM) on undoped ufg W.

As no sample fulfills Equation C.1, elastic-plastic fracture mechanics (EPFM) has to be applied instead in order to derive valid fracture toughness values [46]. As a measure of fracture toughness within EPFM, the experimental J-Integral is a well established option [37,61]:

$$J = \frac{K^2 \cdot (1 - \nu^2)}{E} + \frac{\eta \cdot A_{pl}}{B \cdot (W - a_0)} \quad (C.2)$$

With ν being the Poisson's ratio and E the Young's Modulus of the specimen (for tungsten: $\nu = 0.28$ and $E = 410 \text{ GPa}$ [1]), η is a constant factor equal to 1.9 and A_{pl} is the plastic area under the force-displacement curve of the experiment (i.e. the plastic work). The stress intensity factor K is calculated via [36,37,59]:

$$K = \frac{F \cdot L_C}{B \cdot W^{3/2}} \cdot f\left(\frac{a}{W}\right) \quad (C.3)$$

with L_C being the distance between the point of loading and the notch (see Figure C.1).

The geometry factor $f\left(\frac{a}{W}\right)$ was calculated using FEM simulations [37] to be:

$$f\left(\frac{a}{W}\right) = 4 \cdot \frac{3 \cdot \left(\frac{a}{W}\right)^{0.5} \cdot \left(1.23 - \left(\frac{a}{W}\right) \cdot \left(1 - \frac{a}{W}\right)\right) \cdot \left(-6.09 + 13.96 \cdot \left(\frac{a}{W}\right) - 14.05 \cdot \left(\frac{a}{W}\right)^2\right)}{2 \cdot \left(1 + 2 \cdot \left(\frac{a}{W}\right)\right) \cdot \left(1 - \left(\frac{a}{W}\right)^{1.5}\right)} \quad (C.4)$$

where a represents the current crack length.

As is apparent in Equation C.4, it is essential for EPFM experiments that the crack length is tracked throughout the whole experiment. This can either be done visually from the in-situ videos (manually or automatically with digital image correlation) or by frequent/continuous measurement of the sample stiffness throughout the experiment [62–67]. In this work, the stiffness of the cantilever is measured in regular steps by performing partial unloading segments during the experiment. Using the stiffness gained from the loading/unloading slopes, the current crack length can then be derived using the following FEM-based equation [62]:

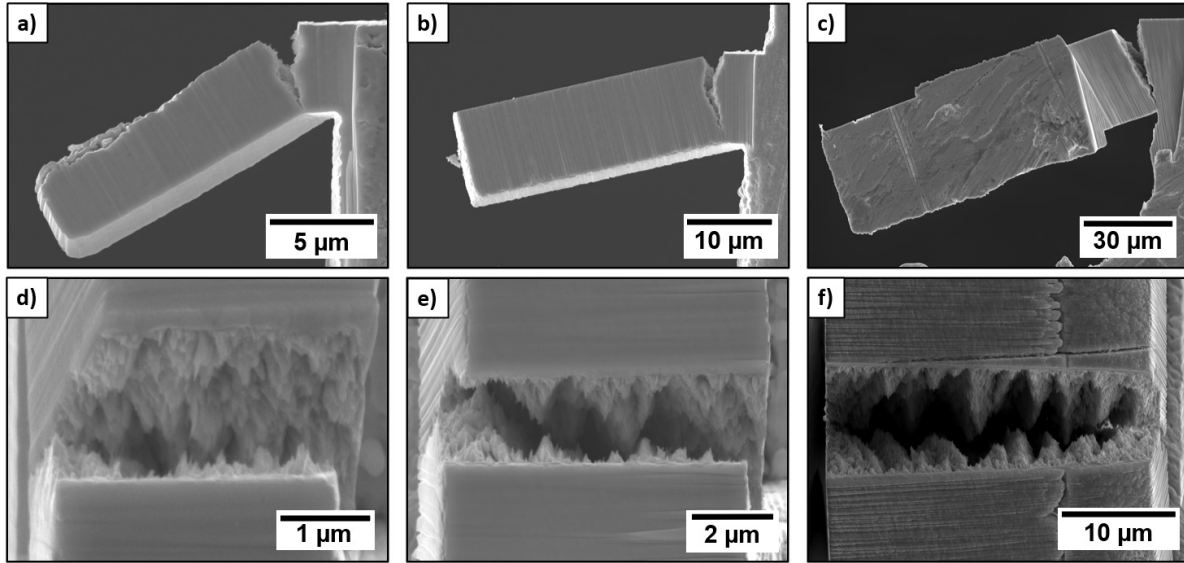


Figure C.2 SEM images of cantilever samples of different sizes and their fracture surfaces after testing. A small W-B cantilever (a,d), a medium sized W-B ann. cantilever (b,e) and a large undoped W cantilever (c,f).

$$\frac{a}{W} = 1 - 2.897\left(\frac{k}{k_0}\right) + 10.618\left(\frac{k}{k_0}\right)^2 - 23.620\left(\frac{k}{k_0}\right)^3 + 24.497\left(\frac{k}{k_0}\right)^4 - 9.600\left(\frac{k}{k_0}\right)^5 \quad (\text{C.5})$$

Where k is the current cantilever stiffness and k_0 is the stiffness the cantilever would have without any crack. k_0 can be calculated from the first sample loading, where both the stiffness and the initial crack length a_0 are known [66,67].

The cantilevers were tested in-situ inside a LEO 982 SEM (Zeiss GmbH, Germany) using an UNAT-SEM indenter (Zwick GmbH & Co KG, Germany) equipped with a conductive diamond wedge indenter tip (Synton-MDP AG, Switzerland). The applied strain rate of the experiments was set to 0.001 s^{-1} at the notched region for all cantilevers.

Post mortem images were taken with an SEM (Tescan Magna, Tescan Orsay Holding, Czech Republic).

C.3 Results

C.3.1 Interpretation of results

The analysis of EPFM experiments is not as straight-forward as for LEFM experiments, where fracture toughness values are determined via a simple equation and by measuring sample dimensions and the critical load. Instead, the J-Integral - crack extension ($J - \Delta a$) curve, also referred to as R-curve, has to be calculated using the recorded force-displacement data in conjunction with Equations C.2-C.5.

A representative example of such a $J - \Delta a$ curve for a medium-sized undoped W cantilever is displayed in Figure C.3a. As apparent, one can fit two straight lines in the R-curve. The first, steeper line is commonly called “blunting line”. Here, crack extension occurs primarily through blunting of the crack tip, hence the name. The second, less steep regime represents actual crack growth or tearing. In the case of Figure C.3a this line increases with ongoing crack extension, indicating stable crack growth and an increasing crack growth resistance throughout the experiment. To receive a fracture toughness value from such a $J - \Delta a$ curve, ASTM recommends to shift the blunting line to a crack extension of 0.2 mm and use the intersection of this parallel shifted line with the R-curve as a critical $J_{c0.2}$ value [59]. Obviously, this is not very helpful for small-scale tests, as the sample dimensions are considerably smaller than 0.2 mm. Therefore, this work relies on the initiation toughness J_i as a measure for fracture toughness, as has been used in microscale experiments before [37,68,69]. J_i represents the plastic energy needed to initiate regular crack growth and can be found at the intersection of the two fitted lines (Figure C.3a). The initiation toughness is especially well suited to characterize microsamples, as it is, contrary to the rest of the R-curve, geometry independent as long as certain specimen size requirements are fulfilled [46]. Another possible approach to make the evaluation of fracture toughness from $J - \Delta a$ curves accessible to both the micro- and macroscale is to shift the blunting line by half of the crack tip opening displacement (CTOD) instead of 0.2 mm [38,62,70]. However, the measurement of CTOD is in many cases impractical. Yet, since CTOD was investigated in this work as well (see Section C.4.2), the fracture toughness deduced from this method was compared to the J_i values for all cantilevers showing stable crack growth. The difference between the values gained by the two methods was negligible for most samples, verifying the application of either method to assess fracture toughness values from $J - \Delta a$ curves.

This kind of analysis can only be performed for stable crack growth and if the material shows R-curve behavior. Some samples presented within this work showed unstable crack growth, meaning the cantilever failed immediately by reaching a

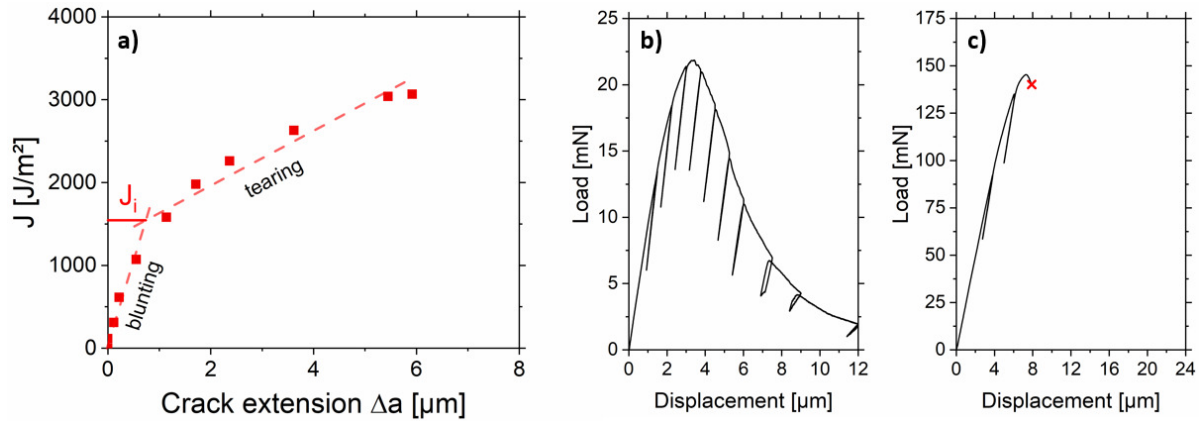


Figure C.3 a) Analysis of fracture toughness from $J - \Delta a$ curves in EPFM experiments for a medium-sized undoped ufg W cantilever. (b, c) Representative load-displacement curves for stable (b, medium-sized cantilever) and unstable (c, large cantilever) crack growth in undoped ufg W.

certain critical load and displacement after the blunting phase. A comparison of the load-displacement data of two experiments showing stable and unstable crack growth is shown in Figure C.3b and C.3c, respectively. As is apparent, even for samples breaking in unstable manner some plastic deformation occurs before total failure. Since a $J - \Delta a$ curve for such a sample would only consist of the blunting line, the J value at the failure point (J_c) is determined and utilized as a measure for fracture toughness for these samples. The comparison of J_i of the stable breaking samples to such critical J-Integral values J_c is in the opinion of the authors reasonable, as J_c is essentially equal to the initiation toughness of a material without increasing crack growth resistance, i.e. without R-curve behavior.

For a better comparability between fracture toughness values of commonly used LEFM experiments and the EPFM experiments utilized in this work, J_i and J_c values can be converted to $K_{J,i}$ and $K_{J,c}$ values, respectively, using the following equation [71]:

$$K_{J,i/c} = \sqrt{\frac{J_{i/c} \cdot E}{1 - \nu^2}} \quad (\text{C.6})$$

within a plane strain assumption.

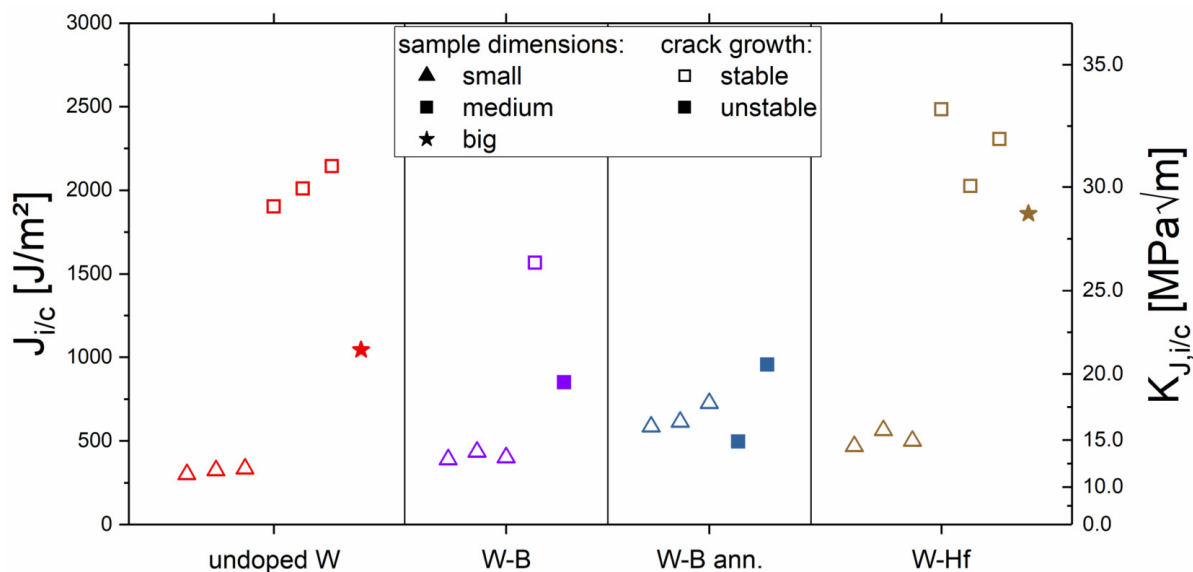


Figure C.4 Fracture toughness (J_i or J_c) of all tested cantilevers gained from EPFM experiments on all investigated ufg W materials. Open symbols represent experiments with stable crack growth, solid symbols display unstable failure.

C.3.2 Fracture toughness

Figure C.4 shows the fracture toughness of all tested samples. J_i is shown for samples that exhibit stable crack growth (open symbols), whereas J_c is shown for samples that fail in an unstable manner (solid symbols). It is immediately apparent that cantilevers of the same material but different sample dimensions can show vastly different toughness values and crack growth behavior, indicating the presence of a size effect and questioning the validity of some experiments, as will be further elaborated in the discussion section. The relative error in J_i and J_c was calculated following the principle of propagation of uncertainty and assuming a possible measurement error of 1 pixel for each sample dimension. It amounts to values between 0.5 and 1% for all tested samples. As this relative error is very small, we refrain from the use of error bars in Figure C.4 and the following figures, as they would not be visible.

The small cantilevers ($3 \times 3 \times 10 \mu\text{m}$, triangle symbols in Figure C.4) of all tested materials show stable crack growth and similar toughness values of around $300\text{--}700 \text{ J/m}^2$ or $12\text{--}18 \text{ MPa}\sqrt{m}$. The medium-sized cantilevers ($8 \times 8 \times 30 \mu\text{m}$, square symbols in Figure C.4) display less uniform behavior. While some samples exhibit stable crack growth and very high toughness values of up to over 2000 J/m^2 ($30 \text{ MPa}\sqrt{m}$), others show unstable failure and toughness values of around 1000 J/m^2 ($20 \text{ MPa}\sqrt{m}$). It is interesting to note, that the materials that show unstable failure (W-B and W-B ann.) were found in microcantilever bending tests to have a higher bending strength

than the undoped W and W-Hf material [35]. For the larger cantilevers (star symbols in Figure C.4), all samples showed unstable crack growth behavior. The fracture toughness was measured to be 1040 J/m^2 ($21.5 \text{ MPa}\sqrt{m}$) for the undoped W sample and 1860 J/m^2 ($28.8 \text{ MPa}\sqrt{m}$) for the W-Hf sample, respectively.

All fractured surfaces show clear signs of intercrystalline failure (delamination) with a share of ductile failure (shearing), regardless of material, cantilever dimensions or stability of crack growth (see also Figure C.2).

C.4 Discussion

C.4.1 Validity of fracture experiments

Following the results of micro- and meso-scale fracture mechanical experiments, some remarks on the validity of the experiments are in order. Given the comparably large sample dimensions, it is safe to assume that the large cantilevers of undoped and Hf-doped ufg W represent valid EPFM experiments. These cantilevers, together with the medium-sized W-B ann. cantilever and one W-B cantilever, show unstable failure and similar toughness values. This raises the question, if the instability of crack growth might be an indicator for a valid EPFM experiment on ufg W.

The validity criterion of EPFM J-Integral experiments is commonly given as:

$$B, (W - a_0) > c \cdot \frac{J_Q}{\sigma_y} \quad (\text{C.7})$$

Where J_Q is the conditional J-Integral fracture toughness gained from the experiment, σ_y is the yield stress of the material and c is a pre-factor. Values ranging from 10 to 50 are reported in literature for this pre-factor [37,38,40] and the official standard by ASTM gives a value of 10 [71].

Figure C.5 shows the fracture toughness of all tested samples, this time displayed against the rearranged validity criterion of Equation C.7 on the x-axis. The smaller dimension among sample thickness B and ligament length $(W - a_0)$ is used for each specimen. The yield strength is taken from bending experiments performed on the same material in [35]. Of course this is not the same value as a yield strength gained from tensile tests, which is why some points might not be placed with highest accuracy, but it serves as a good estimate and provides comparability between the

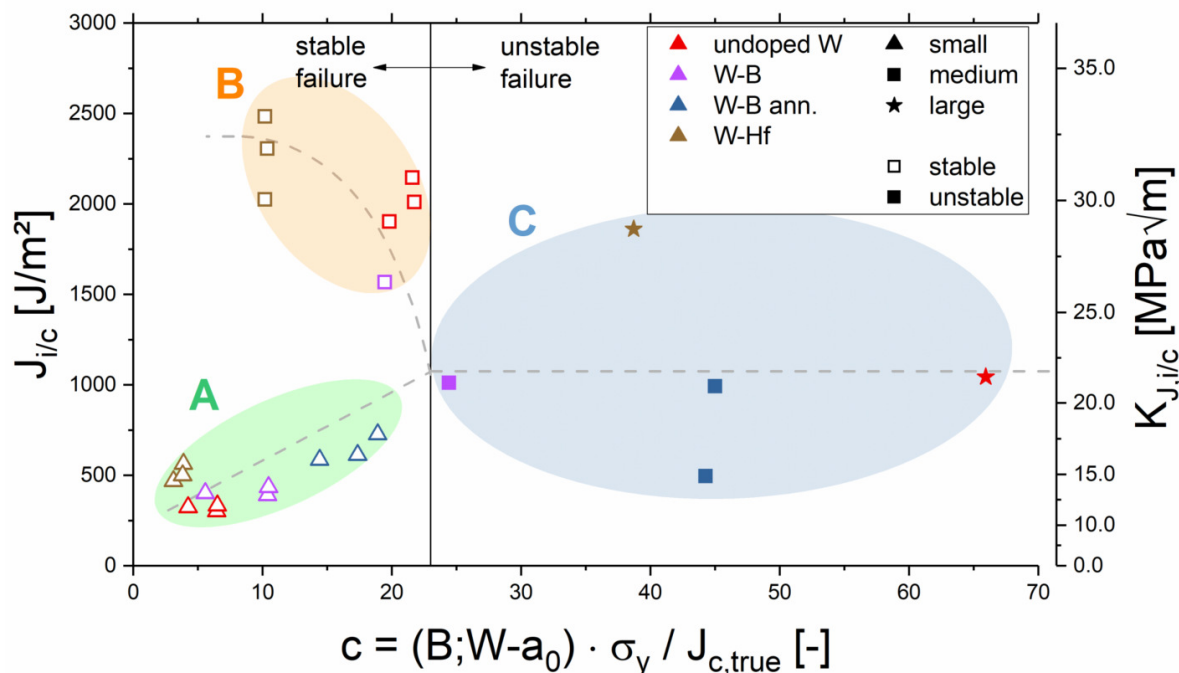


Figure C.5 Fracture toughness (J_i or J_c) of all tested cantilevers over the smallest dimension of the cantilever times yield strength divided by valid fracture toughness of the material. The x-value is proportional to the ratio of sample dimension to plastic zone size in front of the crack tip and resembles c in Equation C.7. For further analysis, the fracture samples are classified in regimes “A”, “B” and “C”.

samples. $J_{c,true}$ represents the valid J-Integral fracture toughness of the material, which is gained from the experiments with the largest sample dimensions for each material (as they are assumed to represent valid EPFM experiments). These experiments all displayed unstable crack growth. The term $\frac{J}{\sigma_y}$ is proportional to CTOD and plastic zone size [46]. Therefore, the x-axis in the graph represents the ratio of sample dimensions to plastic zone size or the pre-factor c in the validity criterion of Equation C.7.

It is apparent in Figure C.5 that above a certain x-value (in this concrete case 23) all samples fail in an unstable manner and show comparable fracture toughness values (regime “C”). This strongly suggests that above this value the experiments are valid and the measured fracture toughness equals the real, size independent fracture toughness of the material. Naturally, the two largest cantilevers fulfill this condition easily. For the medium-sized cantilevers, only the higher strength materials (W-B ann. and one out of two W-B) fulfill this condition, as the higher yield strength leads to a smaller plastic zone within the cantilever. Here it is worth to note that the W-B material has one cantilever on either side of the validity line. This is because the

cantilever sample on the left side had slightly smaller dimensions than the sample on the right side. The medium-sized cantilevers made of softer material and all small cantilevers cannot fulfill the validity criterion ($c > 23$), but they show vastly different fracture toughness values. While the smaller samples underestimate the real fracture toughness (regime “A”), the invalid medium-sized cantilevers overestimate it (regime “B”). Before an explanation for this peculiar behavior can be attempted, a more detailed analysis of the fracture behavior is required and will be performed next.

C.4.2 Analysis of the crack tip opening displacement

To provide further information on fracture behavior and apparent toughness, the second widely used option to measure fracture toughness within EPFM was utilized: the crack tip opening displacement (CTOD). It was proven before that both the J-Integral and CTOD can be used to measure the correct fracture toughness of EPFM samples and are connected via [37,71–73]:

$$CTOD = d_n \cdot \frac{J}{\sigma_y} \quad (C.8)$$

Where d_n is the Shih factor, which is equal to 0.78 for plane strain conditions and a non-hardening material.

Given the in-situ nature of the experiments in this work, the CTOD at crack growth initiation ($CTOD_i$, for stable crack growth) or the critical CTOD before failure ($CTOD_c$, for unstable crack growth) can be measured directly from the videos recorded during the experiments. Due to the fast scanning speed of the SEM during the tests, the resolution of the images is limited, which is why the CTOD was measured multiple times for each sample to provide an accurate average value. The results of the CTOD measurement can be seen in Figure C.6a. The small cantilever samples exhibit a similar trend than in Figure C.5, showing smaller CTOD values with a linear increasing trend. Figure C.6b shows the J-Integral calculated from CTOD results using Equation C.8 and a Shih factor of 0.78. While the J-values of the unstable failing samples are very similar to the J-values gained from Equations C.2-C.5 (with the exception of the annealed W-B sample, see also Figure C.9a), the values of the stable failing samples are rather different and show a dissimilar, more linear trend. It should be mentioned that, in ductile materials, the CTOD at the surface is usually smaller (before crack growth initiation) or larger (after crack growth initiation) than the “valid” CTOD in the midsection of the sample [74]. However, since the values of

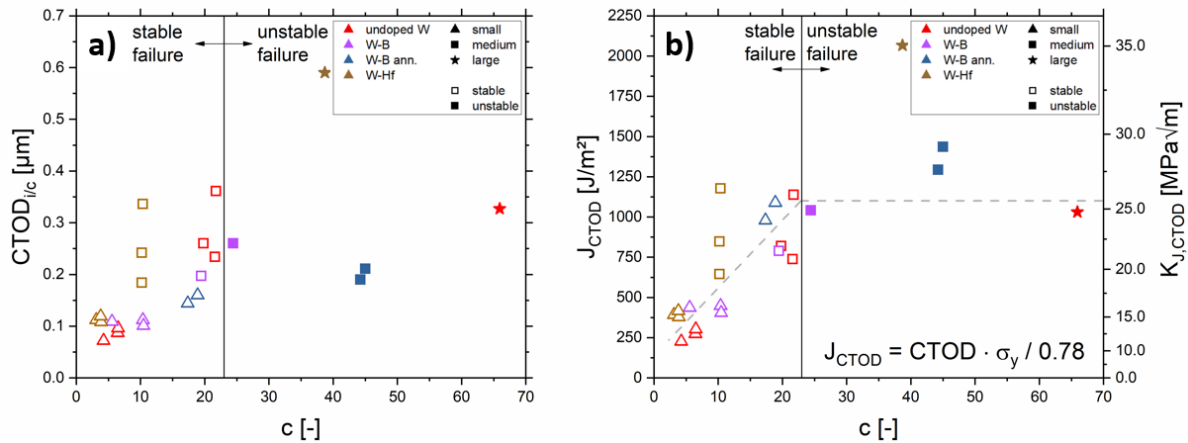


Figure C.6 a) Measured crack tip opening displacement at crack growth initiation ($CTOD_i$) or before failure ($CTOD_c$) for all tested samples. b) J-Integral fracture toughness based on CTOD measurements.

J_{CTOD} and J_c are so similar for the unstable failing samples, it is assumed that for the current failure mode (i.e. a complex mixture of intercrystalline and ductile fracture), the CTOD at the surface and within the sample are comparable.

C.4.3 The role of sample dimensions on perceived fracture toughness

When considering some of the standard validity criteria used in fracture mechanics, e.g. Equations C.1 and C.7, a common misconception can arise that the two critical sample dimensions, i.e. the ligament length $W - a_0$ and the sample thickness B , have a similar effect on the fracture behavior of the material, as the same criterion is applied to either measurement. In reality, the implications of the two dimensions are vastly different. The ligament length (in combination with the plastic zone size) determines if the test specimen exhibits small scale yielding, large scale yielding or failure through plastic collapse, and therefore governs the validity of applying LEFM or EPFM concepts. The sample thickness, on the other hand, influences the stress state in front of the crack tip. A large sample thickness leads to predominantly plane strain conditions and consequently a high stress triaxiality at the crack tip. On the surface of the sample, plane stress conditions prevail. It can be easily deduced that with decreasing sample thickness the influence of this plane-stress dominated region increases, leading to lower overall stress triaxiality in the test specimen [72,75,76]. It has to be mentioned that strictly speaking, a specimen fulfilling the ligament length criterion but not the thickness criterion still represents a valid fracture mechanical experiment. However, as the influence of the plane stress condition increases, the measured fracture toughness becomes thickness dependent. This thickness dependent

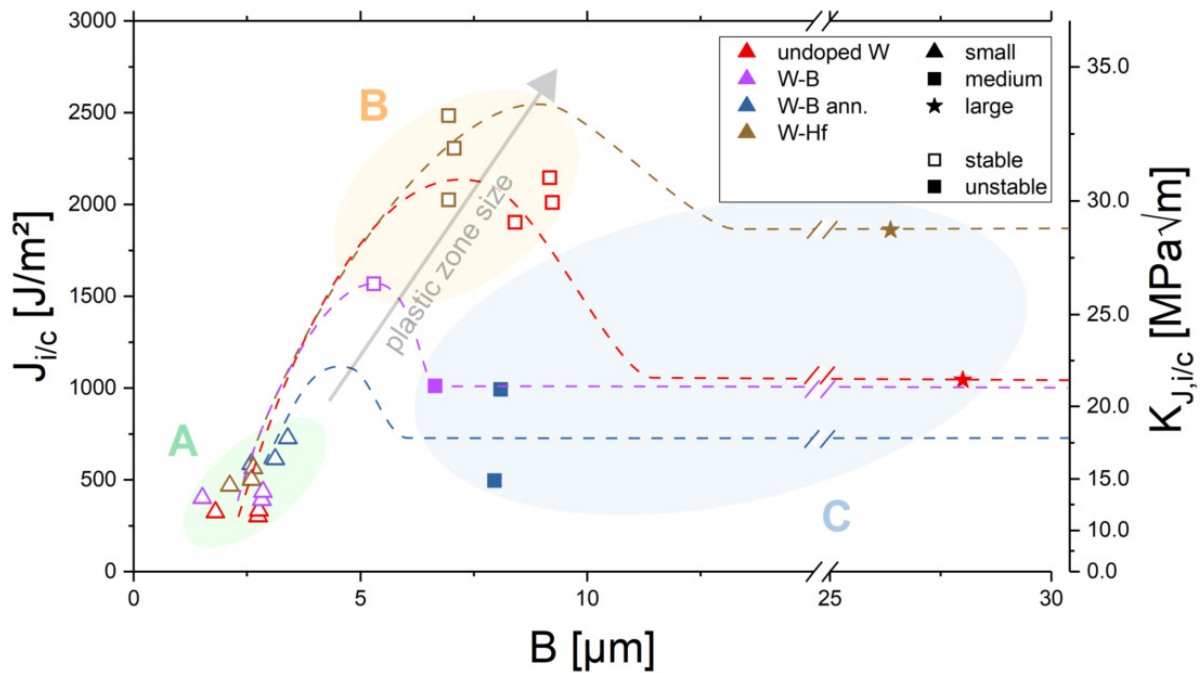


Figure C.7 Fracture toughness (J_i or J_c) of all tested cantilevers over sample thickness B . For each individual material the apparent fracture toughness shows a similar trend with increasing thickness. Dashed lines represent a guide for the eye.

toughness increases with decreasing B , as long as the process zone stays small compared to the sample thickness [46]. Therefore, it is common practice to determine the sample size independent “plane strain fracture toughness”, that can only be measured in samples thick enough to show predominantly plane strain conditions and high stress triaxiality throughout the crack front. In commonly used macro-sized LEFM experiments, one hardly ever measures such a thickness dependent fracture toughness, as the criterion is very strict (Equation C.1) and it is much more likely to run into validity issues regarding the ligament length criterion (assuming ligament length and sample thickness are in the same order of magnitude) [72]. In EPFM experiments, however, where sample dimensions are smaller and/or plastic zone sizes are large, it can become a lot more likely to measure thickness dependent fracture toughness, as the ligament length criterion is way more forgiving and the influence of the sample thickness on stress triaxiality is the same as in LEFM experiments.

When the apparent fracture toughness is plotted against the sample thickness B (Figure C.7), one can visualize a similar trend in all ufg W variants. Small samples show a low fracture toughness, stable failing medium-sized samples display a higher fracture toughness, and unstable breaking samples fall into the regime of a constant, thickness-independent fracture toughness. It is interesting to note that the peak of high toughness values increases with increasing plastic zone size (ratio of $\frac{J}{\sigma_y}$) and

also moves towards larger sample thicknesses. The increase of fracture toughness for the samples in region “B” in Figure C.5 (peak region in Figure C.7) can be explained by a significant influence of plane stress conditions leading to the assessment of a thickness-dependent toughness. The results from CTOD analysis confirm this, as the J_{CTOD} values are significantly lower than the J_c values for regime “B” samples. This is because the Shih factor d_n of 0.78 is only valid for plane strain conditions and has to be adapted if samples show increased plane stress influence and lower triaxiality [73]. As only the unstable failing samples (region “C”) display comparable values of J_{CTOD} and J_c , this suggests that predominantly plane strain conditions are only present in these samples, while the other ones exhibit plane stress influenced conditions, which would require an adaption of the Shih factor for more detailed analysis.

However, the decrease in toughness of the thinnest samples within region “A” cannot be reasoned by such a thickness effect. Since no significant plastic deformation of the sample was observed in the in-situ experiments, plastic collapse of the ligament [60], i.e. the breakdown of large-scale yielding conditions, can be ruled out as well. Given the fact that all these samples are small cantilever specimens and that the ratio of sample dimensions to plastic zone size is comparable to some region “B” samples, it is expected that these specimens are increasingly influenced by sample geometry and less by material properties. It is well known that a (cantilever) bending sample experiences a stress and strain gradient, with tensile stress states on one and compressive stress states on the other side. It can be followed easily that such a gradient will be a lot steeper for a smaller specimen. By introducing a crack/notch to the specimen, the stress field in front of the crack tip as well as the fracture process zone are influenced by both, the crack tip itself and the bending stress gradient field. The fracture process zone is commonly defined as the region where micromechanical processes occur that contribute to crack propagation [46,72]. This rather loose definition ranges from pore formation and coalescence in ductile materials, dislocation emission from the crack tip and their propagation, crack bifurcation and tunneling in semi-brittle materials to the breaking of individual atomic bonds in ideally brittle materials. In ductile materials this fracture process zone is typically in the order of a few CTOD, yet it might be even larger in the case of a mixed ductile and intercrystalline fracture, as is the case in the present study [46]. It seems from the data in Figures C.5 and C.7 (regime “A”) that once the fracture process zone reaches past the neutral fibre of the bending cantilever, the compressive part of the stress and strain gradient influences the fracture process zone and impedes its further expansion. As a consequence, stresses can be dissipated less effective from the crack tip and failure occurs at lower loads and fracture toughness values. This also explains the low CTOD results for the smaller samples in Figure C.6, as a restricted fracture process zone leads to a smaller CTOD. A similar argument can be made for a restriction in plastic zone size (and therefore amount of plastic

deformation), leading to lower fracture toughness through less effective dissipation of crack driving force.

As the accurate assessment of the fracture process zone is near impossible, a closer analysis of the plastic zone size will be attempted next instead. FEM simulations were performed using the free CalculiX 2.17 solver [77], on three representative cantilever sizes: small, medium and large. The 2-dimensional simulations were conducted using 8-node quadrilateral plane strain elements (CPE8) with linear elastic isotropic material assumptions. As the aim was to investigate the opening stress behavior over the whole crack growth direction including the bending gradient the common use of crack tip elements with specific side-node positions (to obtain an element corner singularity) was neglected. The simulated stresses σ_{xx} in front of the crack tip (at the load of crack growth initiation or the transition from blunting to tearing) are displayed in Figure C.8. When considering the yield strength of undoped ufg W known from bending tests [35] (2.46 GPa), one can estimate the size of the plastic zone in these cantilever samples to be the distance from the crack tip to where the simulated stress equals the yield strength (blue shape). This can now be compared to common plastic zone models, such as the Irwin model, which describes the (plane strain) plastic zone size in a semi-infinite body as such [72,78]:

$$r_{pl} = \frac{1}{6\pi} \cdot \left(\frac{K}{\sigma_y}\right)^2 \quad (\text{C.9})$$

The plastic zone calculated after Irwin is about 4.8 μm big for undoped ufg W and is displayed as green circle in Figure C.8. It is immediately apparent that the size of the plastic zone inside the small cantilever, calculated using the stress field provided by FEM, is immensely restricted compared to the plastic zone the material would experience in a semi-infinite tension sample (Irwin model). This restriction is less severe in the medium-sized cantilever and almost non-existent in the large sample. It should be mentioned that, due to the simplicity of both the FEM simulation and the Irwin model, the results in Figure C.8 should not be used for quantitative assessment of the plastic zone size (or the margin of the restriction thereof), but rather as an attempt to qualitatively explain the drop due to the strongly reduced energy dissipation in the small samples with consequently low fracture toughness for very small cantilever specimen. Note that the simulated plastic zones are displayed in the known “butterfly” type shape, yet only the stress in x-direction was actually calculated. The Irwin model plastic zone is displayed in circular shape, representatively. The stress field simulated by FEM is representing plane strain conditions, not taking into account any thickness effects.

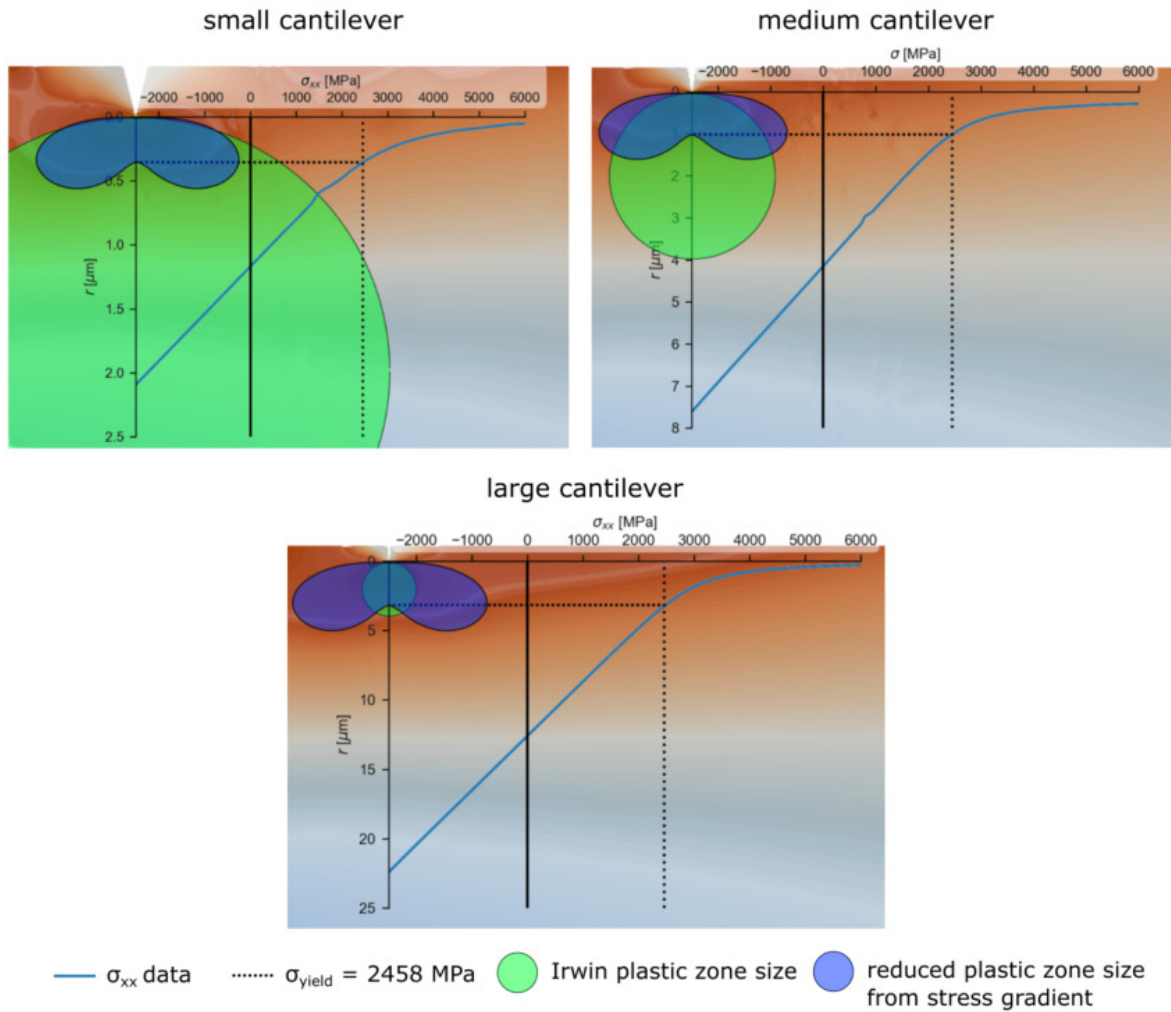


Figure C.8 FEM simulations showing the influence of the bending stress gradient on the size of the plastic zone, compared to the classic Irwin model.

To summarize, the apparent fracture toughness values in Figure C.5 can be explained as such:

- The small cantilever samples marked in region “A” experience a significant influence of the bending strain gradient on the fracture process zone. Additionally, the impact of the bending stress on the stress field in front of the crack tip is shown by FEM simulations to reduce the size of the plastic zone substantially compared to the plastic zone the material would form in a semi-infinite sample (Irwin approximation; see Figure C.8). As both the plastic zone and fracture process zone are being restricted, stresses can be dissipated less effectively from the crack tip, leading to earlier failure and a lower apparent fracture toughness. In these small samples, the plastic zone and fracture process zone get severely

restricted, which clearly outweighs the thickness effect of predominantly plane stress conditions. The larger the sample or harder the material gets, the less the influence of this strain gradient becomes, explaining the slight increase of toughness for the small samples in Figure C.5.

- For the medium-sized cantilever specimens that show stable crack growth and high fracture toughness values (region “B”), this influence of the bending stress gradient on the crack tip stress field is still present, yet widely reduced due to the larger sample dimensions and less steep gradient, but the fracture process zone does likely not extend past the neutral fibre. However, as mentioned above, the influence of the sample thickness cannot be underestimated in EPFM experiments. It is expected that for the specimen marked with “B” in Figure C.5, an increased influence of plane stress conditions and, consequently, a lower overall stress triaxiality within the process zone are present. This results in a thickness dependent and higher perceived fracture toughness compared to predominantly plane strain conditions. For such samples, the crack will most likely start propagating in the center of the specimen when the plane strain fracture toughness value is reached, while the increase in apparent fracture toughness stems from the surface near regions where crack growth lags behind [46].
- Samples that exhibit unstable fracture and more or less constant fracture toughness values (region “C”) are large enough to not be influenced by the bending gradient and also to fulfill the thickness criterion of predominantly plane strain conditions in front of the crack tip. They can be seen as valid “plane strain fracture toughness” values and fully describe the sample size independent fracture behavior of the materials. The fact that all these specimen show unstable crack propagation is further evidence of predominantly plane strain conditions, as it is known that plane stress influenced conditions (such as in region “B”) promote R-curve behavior and stable crack growth [46].

C.4.4 The effect of doping elements on fracture toughness of ufg W

Naturally, only the experiments to the right of the line in Figure C.5 (regime “C”) show the size-independent fracture toughness and can be used to compare the different materials with each other. Figure C.9a displays these values (converted to K_J values using Equation C.6) gained from J-Integral and CTOD analysis for all investigated samples. Overall, the fracture toughness of the ufg W materials show remarkably high values of around $20 \text{ MPa}\sqrt{m}$, clearly outperforming single-crystalline and other ufg W samples, for which values of around $6\text{-}12 \text{ MPa}\sqrt{m}$ are reported in literature

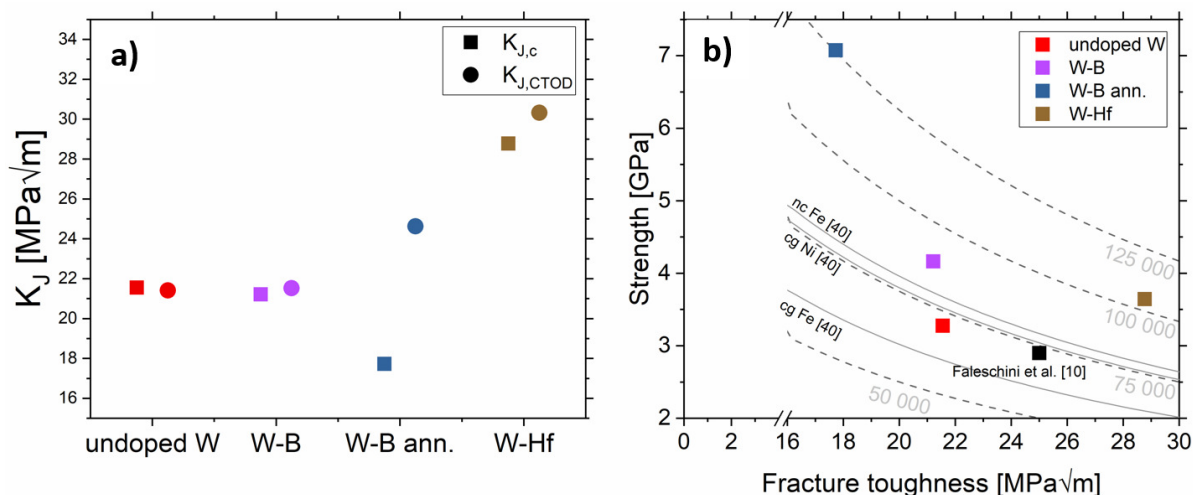


Figure C.9 a) Comparison of fracture toughness values (K_J) gained by J-Integral and CTOD analysis. b) Average bending strength against valid fracture toughness ($K_{J,c}$) of all investigated ufg W materials. Dashed isolines represent the product of strength and toughness in $(\text{MPa})^2\sqrt{\text{m}}$.

[18,37,43,68,79]. Previous work on bulk HPT-processed ufg W by Faleschini et al. reports similar fracture toughness [18,19]. The RT-toughness values measured in this work are even higher than the fracture toughness of cg W above the BDTT [43,79], therefore clearly fulfilling the application requirements in nuclear fusion reactors [2–4], at least for the given testing direction.

The agreement between the fracture toughness gained by the two different methods is given for all materials, except the annealed W-B sample. As the measurement of the CTOD from in-situ images is more prone to errors (a measurement error of 1 pixel (30 nm) would result in a fracture toughness error of about $2 \text{ MPa}\sqrt{\text{m}}$, a measurement error of 3 pixel (90 nm) would misevaluate the fracture toughness by about $5 \text{ MPa}\sqrt{\text{m}}$) and to take a more conservative stance, the lower toughness gained from J-Integral analysis is assumed to be the true fracture toughness for this material. However, given the immense strength increase that was discovered in bending tests on this material [35], this slight decrease in toughness to $17 \text{ MPa}\sqrt{\text{m}}$ is more than being compensated for. While the B—doped and unannealed sample have similar fracture toughness than the undoped material, the fracture toughness of the ufg W material doped with Hf shows a significant improvement to values of 28–30 $\text{MPa}\sqrt{\text{m}}$. This is not particularly surprising, as Hf was the only doping element that was able to improve bending ductility in [35] and, especially for ufg and nanocrystalline materials, ductility and fracture toughness are closely interlinked due to the intercrystalline nature of failure. The extent of improvement of fracture toughness by Hf doping is, however, astounding. As deduced in [35], Hf does not strengthen the GBs in W

directly but indirectly by removing oxygen from the boundaries and binding them in HfO_2 oxides. This seems to be rather effective, given the outstanding improvements in bending ductility and now fracture toughness.

Figure C.9b shows average bending strength (from [35]) and fracture toughness of each investigated material and the ufg W sample fabricated by Faleschini et al. [19] for comparison. Hohenwarter et al. [21] introduced the product of strength and toughness as an easy and accessible measure for damage tolerance of materials. The dashed isolines in Figure C.9b represent this product. It can be seen that all doped and annealed variants show a clear improvement of damage tolerance compared to the undoped ufg W sample, with W-Hf ($105\,000\text{ (MPa)}^2\sqrt{m}$) and W-B ann. ($125\,000\text{ (MPa)}^2\sqrt{m}$) demonstrating the highest values and even outperform coarse grained Ni, coarse grained Fe and nanocrystalline Fe [21] (solid isolines in Figure C.9b), respectively.

C.5 Conclusion

In this work, through the application of small-scale EPFM experiments on doped and undoped ufg W, two major conclusions can be drawn:

- EPFM experiments at the microscales for semi-brittle materials such as ufg W (and for ductile materials) have to be performed with great caution and with the effects of sample dimensions on the apparent fracture toughness in mind. For especially small cantilever samples the effects of the bending strain gradient on the fracture process zone as well as the bending stress gradient on the crack tip stress field and, consequently, the plastic zone size, have to be considered. A severely restricted fracture process zone and plastic zone can lead to lower apparent fracture toughness values. If the sample dimensions are sufficiently large, not being severely affected by the bending gradient, one has to be careful that the sample is thick enough to not experience increasingly plane stress affected conditions, which can lead to a sample size dependent and higher apparent fracture toughness. A safe pre-factor of at least 30 in Equation C.7 (ratio of smallest sample dimension to plastic zone size), thus stricter than in macroscopic standards, is recommended for the correct evaluation of a size-independent fracture toughness.
- The sample size-independent fracture toughness of undoped W can be increased from about $20\text{ MPa}\sqrt{m}$ to almost $30\text{ MPa}\sqrt{m}$ with the addition of Hf as a doping element. The addition of B maintains the toughness, while an additional heat

treatment can lead to a slight decrease in fracture toughness but immensely increases the strength of the material, improving the overall damage tolerance of ufg W.

The insights from this work are expected to be valuable for the application of ufg W in nuclear fusion technology and for the potential future development of a small-scale fracture test routine for control samples in nuclear reactors as well as for material irradiation research centers, such as the *International Fusion Materials Irradiation Facility (IFMIF)*.

Acknowledgements

Funding by the European Research Council (ERC) under grant number 771146 (TOUGHIT) is greatly acknowledged. The authors thank Simon Dopperrmann and Benjamin Seligmann for help with material and sample preparation.

References

- [1] E. Lassner, W.-D. Schubert, Tungsten. Properties, Chemistry, Technology of the Element, Alloys, and Chemical Compounds, Kluwer Academic / Plenum Publishers, New York, 1999.
- [2] M. Rieth, D.E.J. Armstrong, B. Dafferner, S. Heger, A. Hoffmann, M. Hoffmann, U. Jäntschi, M. Rohde, T. Scherer, V. Widak, H. Zimmermann, Tungsten as a Structural Divertor Material, *Adv. Sci. Technol.* 73 (2010) 11–21.
- [3] S. Wurster, N. Baluc, M. Battabyal, T. Crosby, J. Du, C. Garcia-Rosales, A. Hasegawa, A. Hoffmann, A. Kimura, H. Kurishita, R.J. Kurtz, H. Li, S. Noh, J. Reiser, J. Riesch, M. Rieth, W. Setyawan, M. Walter, J.-H. You, R. Pippan, Recent progress in R&D on tungsten alloys for divertor structural and plasma facing materials, *J. Nucl. Mater.* 442 (2013) 181–189.
- [4] M. Rieth, S.L. Dudarev, S.M.G. De Vicente, J. Aktaa, T. Ahlgren, S. Antusch, D.E.J. Armstrong, M. Balden, N. Baluc, M. Barthe, W. Basuki, M. Battabyal, C.S. Becquart, D. Blagoeva, H. Boldyryeva, J. Brinkmann, M. Celino, L. Ciupinski, J.B. Correia, A. De Backer, C. Domain, E. Gaganidze, C. Garcia-Rosales, J. Gibson, M.R. Gilbert, S. Giusepponi, B. Gludovatz, H. Greuner, K. Heinola, T. Höschen, A. Hoffmann, N. Holstein, F. Koch, W. Krauss, H. Li, S. Lindig, J. Linke, C. Linsmeier, P. López-ruiz, H. Maier, J. Matejcek, T.P. Mishra, M. Walter, T. Weber, T. Weitkamp, S. Wurster, M.A. Yar, J.H. You, A. Zivelonghi, Recent progress in research on tungsten materials for nuclear fusion applications in Europe, *J. Nucl. Mater.* 432 (2013) 482–500.
- [5] J.W. Davis, V.R. Barabash, A. Makhankov, L. Plöchl, K.T. Slattery, Assessment of tungsten for use in the ITER plasma facing components, *J. Nucl. Mater.* 263 (1998) 308–312.

- [6] R. Neu, R. Dux, A. Kallenbach, T. Pütterich, M. Balden, J.C. Fuchs, A. Herrmann, C.F. Maggi, M. O'Mullane, R. Pugno, I. Radivojevic, V. Rohde, A.C.C. Sips, W. Suttrop, A. Whiteford, Tungsten : an option for divertor and main chamber plasma facing components, *Nucl. Fusion*. 45 (2005)
- [7] C. Ren, Z.Z. Fang, M. Koopman, B. Butler, J. Paramore, S. Middlemas, Methods for improving ductility of tungsten - A review, *Int. J. Refract. Metals Hard Mater*. 75 (2018) 170–183.
- [8] L. Yang, K. Zhang, M. Wen, Z. Hou, C. Gong, X. Liu, C. Hu, X. Cui, W. Zheng, Highly hard yet toughened bcc-W coating by doping unexpectedly low B content, *Sci. Rep.* 7 (2017) 1–8.
- [9] M.J. Pfeifenberger, V. Nikolic, S. Zak, A. Hohenwarter, R. Pippan, Evaluation of the intergranular crack growth resistance of ultrafine grained tungsten materials, *Acta Mater*. 176 (2019) 330–340.
- [10] J. Reiser, J. Hoffmann, U. Jäntschi, M. Klimenkov, S. Bonk, C. Bonnekoh, A. Hoffmann, T. Mrotzek, M. Rieth, Ductilisation of tungsten (W): On the increase of strength AND room-temperature tensile ductility through cold-rolling, *Int. J. Refract. Met. Hard Mater*. 64 (2017) 261–278.
- [11] C. Bonnekoh, A. Hoffmann, J. Reiser, The brittle-to-ductile transition in cold rolled tungsten: On the decrease of the brittle-to-ductile transition by 600 K to -65°C, *Int. J. Refract. Met. Hard Mater*. 71 (2018) 181–189.
- [12] C. Bonnekoh, J. Reiser, A. Hartmaier, S. Bonk, A. Hoffmann, M. Rieth, The brittle-to-ductile transition in cold-rolled tungsten sheets: the rate-limiting mechanism of plasticity controlling the BDT in ultrafine-grained tungsten, *J. Mater. Sci.* 55 (2020) 12314–12337.
- [13] C. Bonnekoh, U. Jäntschi, J. Hoffmann, H. Leiste, A. Hartmaier, D. Weygand, A. Hoffmann, J. Reiser, The brittle-to-ductile transition in cold rolled tungsten plates: Impact of crystallographic texture, grain size and dislocation density on the transition temperature, *Int. J. Refract. Met. Hard Mater*. 78 (2019) 146–163.
- [14] J. Riesch, J. Almanstötter, J.W. Coenen, M. Fuhr, H. Gietl, Y. Han, T. Höschen, C. Linsmeier, N. Travitzky, P. Zhao, R. Neu, Properties of drawn W wire used as high performance fibre in tungsten fibre-reinforced tungsten composite, *IOP Conf. Ser. Mater. Sci. Eng.* 139 (2016).
- [15] J. Riesch, A. Feichtmayer, M. Fuhr, J. Almanstötter, J.W. Coenen, H. Gietl, T. Höschen, C. Linsmeier, R. Neu, Tensile behaviour of drawn tungsten wire used in tungsten fibre-reinforced tungsten composites, *Phys. Scr.* 2017 (2017).
- [16] V. Nikolić, J. Riesch, R. Pippan, The effect of heat treatments on pure and potassium doped drawn tungsten wires: Part I - Microstructural characterization, *Mater. Sci. Eng. A*. 737 (2018) 422–433.
- [17] V. Nikolić, J. Riesch, M.J. Pfeifenberger, R. Pippan, The effect of heat treatments on pure and potassium doped drawn tungsten wires: Part II – Fracture properties, *Mater. Sci. Eng. A*. 737 (2018) 434–447.
- [18] M. Faleschini, H. Kreuzer, D. Kiener, R. Pippan, Fracture toughness investigations of tungsten alloys and SPD tungsten alloys, *J. Nucl. Mater.* 367–370 (2007) 800–805.
- [19] M. Faleschini, D. Kiener, W. Knabl, R. Pippan, Fracture Toughness Investigations of Tungsten Alloys and Severe Plastic Deformed Tungsten Alloys, *Proc. 16th Int. Plansee Sem.* (2005) 701–711.
- [20] R. Pippan, A. Hohenwarter, The importance of fracture toughness in ultrafine and nanocrystalline bulk materials, *Mater. Res. Lett.* 4 (2016) 127–136.
- [21] A. Hohenwarter, R. Pippan, Fracture and fracture toughness of nanopolycrystalline metals produced by severe plastic deformation, *Philos. Trans. R. Soc. A*. 373 (2015) 20140366.

- [22] A. Pineau, A.A. Benzerga, T. Pardoen, Failure of metals I: Brittle and ductile fracture, *Acta Mater.* 107 (2016) 424–483.
- [23] A. Pineau, A. Amine Benzerga, T. Pardoen, Failure of metals III: Fracture and fatigue of nanostructured metallic materials, *Acta Mater.* 107 (2016) 508–544.
- [24] D. Raabe, M. Herbig, S. Sandlöbes, Y. Li, D. Tytko, M. Kuzmina, D. Ponge, P. Choi, Grain boundary segregation engineering in metallic alloys : A pathway to the design of interfaces, *Curr. Opin. Solid State Mater. Sci.* 18 (2014) 253–261.
- [25] M.A. Gibson, C.A. Schuh, Segregation-induced changes in grain boundary cohesion and embrittlement in binary alloys, *Acta Mater.* 95 (2015) 145–155.
- [26] J.R. Trelewicz, C.A. Schuh, Grain boundary segregation and thermodynamically stable binary nanocrystalline alloys, *Phys. Rev. B - Condens. Matter Mater. Phys.* 79 (2009) 1–13.
- [27] T.J. Rupert, J.R. Trelewicz, C.A. Schuh, Grain boundary relaxation strengthening of nanocrystalline Ni-W alloys, *J. Mater. Res.* 27 (2012) 1285–1294.
- [28] A. Khalajhedayati, Z. Pan, T.J. Rupert, Manipulating the interfacial structure of nanomaterials to achieve a unique combination of strength and ductility, *Nat. Commun.* 7 (2016).
- [29] H. Lee, V. Tomar, An examination of nickel doping effect on the mechanical strength of a tungsten grain boundary, *Comput. Mater. Sci.* 77 (2013) 131–138.
- [30] P. Lejcek, M. Šob, V. Paidar, Interfacial segregation and grain boundary embrittlement : An overview and critical assessment of experimental data and calculated results, *Prog. Mater. Sci.* 87 (2017) 83–139.
- [31] P. Lejcek, *Grain Boundary Segregation in Metals*, Springer, Berlin-Heidelberg, 2010.
- [32] C.A. Schuh, M. Kumar, W.E. King, Analysis of grain boundary networks and their evolution during grain boundary engineering, *Acta Mater.* 51 (2003) 687–700.
- [33] D. Scheiber, R. Pippan, P. Puschnig, L. Romaner, Ab initio search for cohesion-enhancing impurity elements at grain boundaries in molybdenum and tungsten, *Model. Simul. Mater. Sci. Eng.* 24 (2016) 85009.
- [34] D. Scheiber, R. Pippan, P. Puschnig, A. Ruban, L. Romaner, Ab-initio search for cohesion-enhancing solute elements at grain boundaries in molybdenum and tungsten, *Int. J. Refract. Met. Hard Mater.* 60 (2016) 75–81.
- [35] M. Wurmshuber, S. Jakob, S. Dopfermann, S. Wurster, R. Bodlos, L. Romaner, V. Maier-Kiener, D. Kiener, Tuning mechanical properties of ultrafine-grained tungsten by manipulating grain boundary chemistry, *Acta Mater.* 232 (2022) 117939.
- [36] S. Wurster, C. Motz, R. Pippan, Notched-cantilever testing on the micrometer scale-effects of constraints on plasticity and fracture behaviour, *Proc. 18th Eur. Conf. Fract.* (2010). [37] S. Wurster, C. Motz, R. Pippan, Characterization of the fracture toughness of micro-sized tungsten single crystal notched specimens, *Philos. Mag.* 92 (2012) 1803–1825.
- [38] J. Ast, M. Ghidelli, K. Durst, M. Göken, M. Sebastiani, A.M. Korsunsky, A review of experimental approaches to fracture toughness evaluation at the micro-scale, *Mater. Des.* 173 (2019) 107762.
- [39] G. Dehm, B.N. Jaya, R. Raghavan, C. Kirchlechner, Overview on micro- and nanomechanical testing: New insights in interface plasticity and fracture at small length scales, *Acta Mater.* 142 (2018) 248–282.

- [40] A.K. Saxena, S. Brinckmann, B. Völker, G. Dehm, C. Kirchlechner, Experimental conditions affecting the measured fracture toughness at the microscale: Notch geometry and crack extension measurement, *Mater. Des.* 191 (2020) 108582.
- [41] B.N. Jaya, C. Kirchlechner, G. Dehm, Can microscale fracture tests provide reliable fracture toughness values? A case study in silicon, *J. Mater. Res.* 30 (2015) 686–698.
- [42] M. Alfreider, S. Kolitsch, S. Wurster, D. Kiener, An analytical solution for the correct determination of crack lengths via cantilever stiffness, *Mater. Des.* 194 (2020) 108914.
- [43] J. Ast, J.J. Schwiedrzik, J. Wehrs, D. Frey, M.N. Polyakov, J. Michler, X. Maeder, The brittle-ductile transition of tungsten single crystals at the micro-scale, *Mater. Des.* 152 (2018) 168–180.
- [44] D.E.J. Armstrong, C.D. Hardie, J. Gibson, A.J. Bushby, P.D. Edmondson, S.G. Roberts, Small-scale characterisation of irradiated nuclear materials: Part II nanoindentation and micro-cantilever testing of ion irradiated nuclear materials, *J. Nucl. Mater.* 462 (2015) 374–381.
- [45] F. Iqbal, J. Ast, M. Göken, K. Durst, In situ micro-cantilever tests to study fracture properties of NiAl single crystals, *Acta Mater.* 60 (2012) 1193–1200.
- [46] R. Pippan, S. Wurster, D. Kiener, Fracture mechanics of micro samples: Fundamental considerations, *Mater. Des.* 159 (2018) 252–267.
- [47] P. Hosemann, C. Shin, D. Kiener, Small scale mechanical testing of irradiated materials, *J. Mater. Res.* 30 (2015) 1231–1245.
- [48] D. Kiener, A.M. Minor, O. Anderoglu, Y. Wang, S.A. Maloy, P. Hosemann, Application of small-scale testing for investigation of ion-beam-irradiated materials, *J. Mater. Res.* 27 (2012) 2724–2736.
- [49] P. Hosemann, Small-scale mechanical testing on nuclear materials: bridging the experimental length-scale gap, *Scr. Mater.* 143 (2018) 161–168.
- [50] A. Xu, C. Beck, D.E.J. Armstrong, K. Rajan, G.D.W. Smith, P.A.J. Bagot, S.G. Roberts, Ion-irradiation-induced clustering in W – Re and W – Re – Os alloys : A comparative study using atom probe tomography and nanoindentation measurements, *Acta Mater.* 87 (2015) 121–127.
- [51] R. Henry, I. Zacharie-Aubrun, T. Blay, N. Tarisien, S. Chalal, X. Iltis, J.M. Gatt, C. Langlois, S. Meille, Irradiation effects on the fracture properties of UO₂ fuels studied by micro-mechanical testing, *J. Nucl. Mater.* 536 (2020).
- [52] C. Gasparini, A. Xu, K. Short, T. Wei, J. Davis, T. Palmer, D. Bhattacharyya, L. Edwards, M.R. Wenman, Micromechanical testing of unirradiated and helium ion irradiated SA508 reactor pressure vessel steels: Nanoindentation vs in-situ microtensile testing, *Mater. Sci. Eng. A.* 796 (2020).
- [53] J.S. Weaver, S. Pathak, A. Reichardt, H.T. Vo, S.A. Maloy, P. Hosemann, N.A. Mara, Spherical nanoindentation of proton irradiated 304 stainless steel: A comparison of small scale mechanical test techniques for measuring irradiation hardening, *J. Nucl. Mater.* 493 (2017) 368–379.
- [54] F.M. Halliday, D.E.J. Armstrong, J.D. Murphy, S.G. Roberts, Nanoindentation and Micromechanical Testing of Iron-Chromium Alloys Implanted with Iron Ions, *Adv. Mater. Res.* 59 (2008) 304–307.
- [55] D.E.J. Armstrong, X. Yi, E.A. Marquis, S.G. Roberts, Hardening of self ion implanted tungsten and tungsten 5-wt% rhenium, *J. Nucl. Mater.* 432 (2013) 428–436. doi:10.1016/j.jnucmat.2012.07.044.
- [56] D.E.J. Armstrong, P.D. Edmondson, S.G. Roberts, Effects of sequential tungsten and helium ion implantation on nano-indentation hardness of tungsten, *Appl. Phys. Lett.* 102 (2013) 251901.
- [57] M. Wurmshuber, S. Dopfermann, S. Wurster, D. Kiener, Ultrafine-grained Tungsten by High-

- Pressure Torsion – Bulk precursor versus powder processing route, IOP Conf. Ser. Mater. Sci. Eng. 580 (2019) 012051.
- [58] M.J. Pfeifenberger, M. Mangang, S. Wurster, J. Reiser, A. Hohenwarter, W. Pfleging, D. Kiener, R. Pippan, The use of femtosecond laser ablation as a novel tool for rapid micro-mechanical sample preparation, *Mater. Des.* 121 (2017) 109–118.
- [59] ASTM Standard E 399-09, ASTM International, 2009.
- [60] D. Rajpoot, P. Tandaiya, R.L. Narayan, U. Ramamurty, Size effects and failure regimes in notched micro-cantilever beam fracture, *Acta Mater.* 234 (2022) 118041.
- [61] ASTM Standard E 813-89, ASTM International, 1989. [62] M. Alfreider, D. Kozic, O. Kolednik, D. Kiener, In-situ elastic-plastic fracture mechanics on the microscale by means of continuous dynamical testing, *Mater. Des.* 148 (2018) 177–187.
- [63] M. Burtscher, M. Alfreider, K. Schmuck, H. Clemens, S. Mayer, D. Kiener, In situ fracture observations of distinct interface types within a fully lamellar intermetallic TiAl alloy, *J. Mater. Res.* (2020).
- [64] J. Ast, B. Merle, K. Durst, M. Göken, Fracture toughness evaluation of NiAl single crystals by microcantilevers - A new continuous J-integral method, *J. Mater. Res.* 31 (2016) 3786–3794.
- [65] K. Schmuck, M. Alfreider, D. Kiener, Crack length estimations for small scale fracture experiments via image processing techniques, Submitted to JMR. (2022).
- [66] M. Alfreider, J. Zechner, D. Kiener, Addressing Fracture Properties of Individual Constituents Within a Cu-WTi-SiOx-Si Multilayer, *JOM.* 72 (2020) 4551–4558.
- [67] M. Alfreider, R. Bodlos, L. Romaner, D. Kiener, The influence of chemistry on the interface toughness in a WTi-Cu system, *Acta Mater.* (2022) 117813.
- [68] J. Ast, M. Göken, K. Durst, Size-dependent fracture toughness of tungsten, *Acta Mater.* 138 (2017) 198–211.
- [69] I. Issa, A. Hohenwarter, R. Fritz, D. Kiener, Fracture properties of ultrafine grain chromium correlated to single dislocation processes at room temperature, *J. Mater. Res.* 34 (2019) 2370–2383.
- [70] C. Bohnert, N.J. Schmitt, S.M. Weygand, O. Kraft, R. Schwaiger, Fracture toughness characterization of single-crystalline tungsten using notched micro-cantilever specimens, *Int. J. Plast.* 81 (2016) 1–17.
- [71] ASTM Standard E 1820-13, ASTM International, 2013.
- [72] T.L. Anderson, *Fracture Mechanics: Fundamentals and Applications*, Fourth Edition, Taylor & Francis Group, Boca Raton, 2017.
- [73] C.F. Shih, Relationship between the J-integral and the COD for stationary and extending cracks, *J. Mech. Phys. Solids.* 29 (1981) 305–326.
- [74] O. Kolednik, P. Kutleša, On the influence of specimen geometry on the critical crack-tip-opening displacement, *Eng. Fract. Mech.* 33 (1989) 215–223.
- [75] T. Pardoen, F. Hachez, B. Marchioni, P.H. Blyth, A.G. Atkins, Mode I fracture of sheet metal, *J. Mech. Phys. Solids.* 52 (2004) 423–452.
- [76] T. Pardoen, Y. Marchal, F. Delannay, Thickness dependence of cracking resistance in thin aluminium plates, 1999.
- [77] G. Dhondt, *The Finite Element Method for Three-Dimensional Thermomechanical Applications*, John Wiley & Sons, Ltd, Chichester, UK, 2004.

- [78] G.R. Irwin, *Fracture dynamics, Fracturing of Metals*, American Society for Metals, Cleveland, 1948.
- [79] B. Gludovatz, S. Wurster, A. Hoffmann, R. Pippan, Fracture toughness of polycrystalline tungsten alloys, *Int . J. Refract. Met. Hard Mater.* 28 (2010) 674–678.

D Mechanical performance of doped W-Cu nanocomposites

M. Wurmshuber¹, M. Burtscher¹, S. Doppermann¹, R. Bodlos²,
D. Scheiber², L. Romaner³, D. Kiener¹

¹ Department of Materials Science, Chair of Materials Physics, Montanuniversität Leoben, Jahnstraße 12, 8700 Leoben, Austria

² Materials Center Leoben GmbH, Roseggerstraße 12, 8700 Leoben, Austria

³ Department Materials Science, Chair of Physical Metallurgy and Metallic Materials, Montanuniversität Leoben, Roseggerstraße 12, 8700 Leoben, Austria

Nanocomposite materials containing a soft and hard metal phase are a promising strategy to combine ultra-high strength, ductility and fracture toughness. However, given the rather brittle intercrystalline fracture mode, the true potential of these materials is only accessible after strengthening the vast number of interfaces within the composite. In this work, this is realized by doping a W-75Cu nanocomposite with either C, B, Hf or Re, elements that show promising effects on grain boundary cohesion in ab-initio calculations. The samples are fabricated from powders using severe plastic deformation and characterized using electron microscopy. Subsequently, various small-scale mechanical experiments are utilized to investigate the effect of the doping on strength, ductility and fracture toughness. While doping with C and B only leads to slight changes in mechanical properties, it was found that Hf increases the strength of the composite tremendously, most likely via the formation of nanosized oxides. Doping with Re showed an increase in strength and a major improvement in bending ductility, exhibiting “super-ductile” behavior in some cases. In microtensile tests this behavior was reduced, yet an increase in strength and ductility compared to the undoped composite was also apparent in these experiments. Interestingly enough, the fracture toughness of all doped variants did not change compared to the undoped W-Cu composite. This indicates that doping with Re improves resistance against crack initiation but not against crack propagation, making the materials properties highly sensitive to pre-existing defects and probed sample volume.

D.1 Introduction

On the quest to create structural “supermaterials”, combining ultra-high strength, excellent ductility and outstanding fracture toughness, nanostructured metals and composites show a huge potential to escape the bonds of the strength-ductility trade-off commonly present in conventional materials [1–9]. By reducing the grain size to below 100 nm, in the nanocrystalline (nc) regime, even the strength of commonly soft metals, such as Cu, can increase to unprecedented values, outperforming coarse-grained high-strength materials such as steel and Ni alloys [10]. In general, decreasing the grain size of conventional bcc metals and alloys also leads to an increase in fracture toughness and a decrease in ductile brittle transition temperature [11–13]. While a grain size reduction does not significantly deteriorate ductility for conventional grain sizes, as it decreases towards the nc regime, it becomes more challenging to nucleate, move or just fit dislocations in the grain interior. This leads to a transition in deformation mechanisms, from a dislocation-controlled to a predominantly grain boundary (GB)-controlled deformation plasticity [1,2,7,14,15]. The consequence is a serious decrease of ductility, counteracting the aforementioned goal of reaching excellent mechanical performance. Additionally, as the GB area increases tremendously in nc materials, relatively easy crack propagation along GBs and interfaces predominates, leading to a decrease in fracture toughness [11,13,16,17].

In this work, a combined approach of two concepts was utilized to overcome the arising issues with ductility and fracture toughness in nc metals. By a combination of two immiscible metals with large differences in strength and modulus, i.e. W and Cu, one can utilize the strength increase of one phase (W), while still allowing comparably easier dislocation nucleation and motion, and therefore plastic deformation and ductility, in the softer metal (Cu). Nanocomposite systems containing Cu as one phase are especially well researched, particularly regarding their mechanical properties and interface stability [3,9,18–33]. Moreover, cracks can potentially be arrested when they transition from the soft to the hard metal, a phenomenon titled the inhomogeneity effect [34–36]. A more probable crack path along interfaces and GBs, the major reason for poor fracture performance of nc metals [13,16,17], can be combated by applying the concept of grain boundary segregation engineering (GBSE) [37–60]. With GBSE, elements that increase the GB cohesion and show a GB segregation tendency in a given host material are identified, e.g. by implementing density functional theory (DFT) [37,55,60–62] or thermodynamical models [37,38,41,54,55,57] and machine learning approaches [49]. These doping elements are then added to the material and will segregate at GBs after a heat treatment or mechanical mixing process. By increasing GB or interface cohesion, intercrystalline cracks need more energy to propagate, which in turn leads to a higher crack growth resistance and, hence, a promoted fracture toughness of nc materials. Naturally, one has to take into account

the effects of every segregation element on each homo- and heterointerface in a composite material, respectively (e.g. effect of C on W/Cu interface, W GB and Cu GB).

For the present investigations, W-Cu nanocomposites were fabricated from powders using severe plastic deformation and doped with various elements that are expected to enhance GB and interface cohesion. The processed materials were characterized regarding their bending and tensile performance as well as fracture toughness by utilizing various small-scale testing techniques. A significant increase in overall mechanical properties could be achieved by doping with B, Hf or Re, respectively.

D.2 Material and Methods

D.2.1 Material selection and fabrication

Following the impressive application of GBSE in ultrafine-grained W in [63,64], the same doping elements (C, B, Re and Hf) were selected in this work. As information about the effect of these elements on the cohesion of W GBs is already available [61,62,65], DFT was utilized to calculate the effect on cohesion of the W/Cu interface and the Cu GB in the same fashion. DFT calculations were carried out using the Vienna Ab-Initio Simulation Package (VASP) employing the projector augmented wave method and the PBE functional [66–70]. The copper GB segregation calculations used the same GB and methodology as in Razumovskiy et al. [71]. The setup of the simulation cell for the Cu/W interface in the Nishiyama-Wassermann orientation is the same as for the small incoherent cell of Bodlos et al. [72]. To calculate the segregation energy and the influence of the segregant on the cohesion of the Cu/W interface, the following equations are used:

$$E_{Seg}^{X(Y)} = E_{Cu/W}^{X(Y)} - E_{Cu/W}^{X(CuBulk)} + D \quad (D.1)$$

$$D = \epsilon_{Me_B} - \epsilon_{Cu_B}; Me = (Cu, W) \quad (D.2)$$

$$\Delta WOS = E_{Cu/W}^{X(surf)} - E_{Cu/W}^{X(int)} \quad (D.3)$$

with $E_{Seg}^{X(Y)}$ describing the segregation energy within the Cu/W supercell of segregant X from the Cu bulk to position Y (Cu or W bulk, interface, surface) and D being a correction term that accounts for differences in the amount of atoms between the cells used for obtaining $E_{Cu/W}^{X(Y)}$ and $E_{Cu/W}^{X(CuBulk)}$. This correction energy is obtained

from the energy per atom ϵ_{Me_B} , ϵ_{Cu_B} of a pure bulk Cu or Me simulation. In this way, the Cu bulk is the reference energy for all segregation energies. ΔWOS provides the change in the work required to cleave the interface and creating two surfaces. It is given by the difference between surface and interface segregation energy, where a negative ΔWOS indicates a weakening of the interface while a positive ΔWOS would strengthen the interface. Additionally, we consider two possible fracture scenarios which differ in the solute position during fracture: (i) before fracture and after fracture the solute sits on the copper side (orange) of the interface and the copper surface, respectively and (ii) before and after fracture, the solute is found on the tungsten side (grey).

The results of this investigation are depicted in Figure D.1. Figures D.1a and D.1b depict the simulated structures of the W/Cu interface and Cu GB, respectively. Figure D.1c shows the segregation energies to the different interfaces. From all possible positions (i.e. W surface, Cu surface, W bulk, Cu bulk or W/Cu interface) C, B, and Hf prefer the W surface or, in its absence, either side of the interface, while Re prefers the W side of the Cu/W interface where the difference to the W surface is, however, almost negligible. As a result, as shown in Figure D.1d, Re

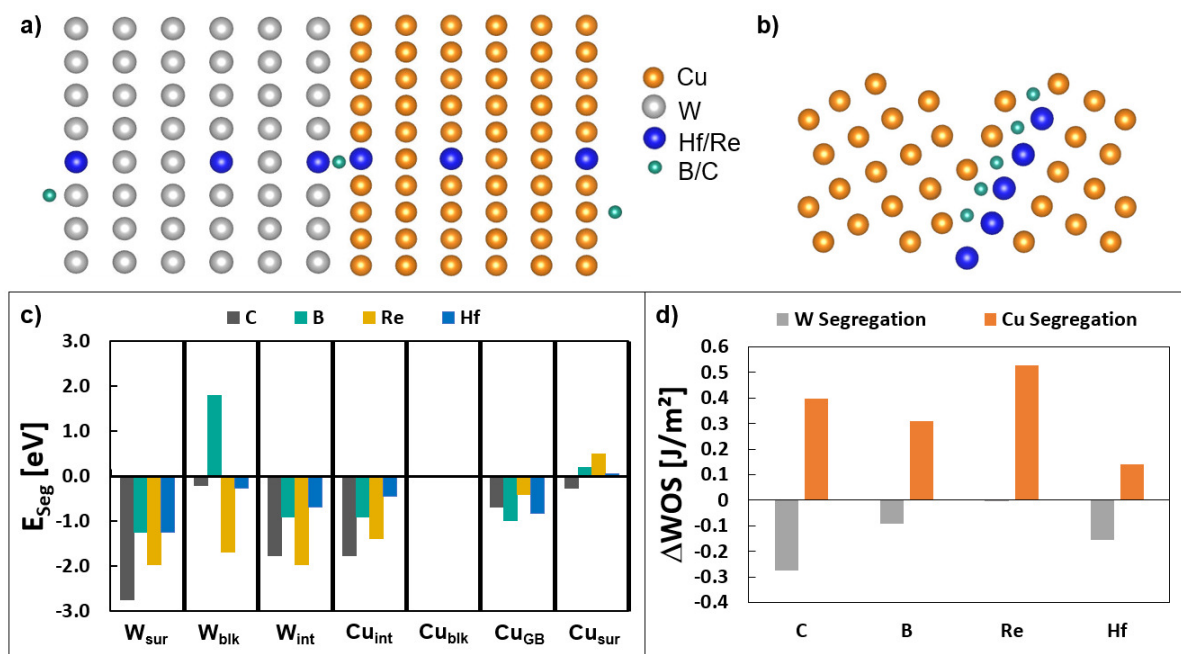


Figure D.1 DFT calculations of interface segregation. a) and b) Structures showing the substitutional (Re, Hf) and interstitial (B, C) segregation positions in the Cu/W cell and the Cu GB, respectively. c) The segregation energies of the selected doping elements at different locations in the W-Cu composite and d) effect of doping elements on the work of separation of the W Cu interface.

shows close to no effect on ΔWOS while C, B and Hf reduce ΔWOS and embrittle the interface. Overall, the ordering of the strengthening propensity that can be derived is $Re > B > Hf > C$. All elements would strengthen the interface if they were found at the copper surface after fracture. However, energetically they prefer to remain attached to the W surface after fracture. Hence, instead of the orange bar, the grey bar should apply and all elements aside from Re show an embrittling effect on the Cu/W interface. The embrittling effect of Hf on the W/Cu interface may be counteracted by the formation of hafnium oxides, as it will bind embrittling oxygen [63,64,73]. Segregation investigations at the Cu GB show that C, B, Re and Hf GB segregation energies are negative and stronger than segregation to the Cu surface. Hence, ΔWOS is positive in this case and segregation to the Cu GB would strengthen the cohesion of the Cu matrix material. The segregation tendency is lower than segregation to the W surface for all segregants. However, as the majority of the material is Cu, the material is mechanically mixed without annealing and large solute contents are added, both the Cu GBs as well as the Cu side of the interface can also be decorated by solute segregants. Furthermore, simulations done on W GBs [61,62,65] show that GB segregation of Re, C and B is stronger than to the Cu/W interface as well as to the W surface. Therefore, despite C, B and Hf weakening the interface cohesion, a strengthening of the Cu and W base material and draining of the Cu/W interface of segregants towards the W GB could potentially mitigate, negate or even reverse this weakening.

For an experimental validation of these theoretical predictions, we will synthesize doped nanocomposites. Fabrication of W-Cu nanocomposites from bulk materials or powders using high pressure torsion (HPT) has been performed before [74–78]. A powder metallurgical approach was selected in this work, as it allows for control and change of doping element content in-lab. The powders of W (99.97% purity, 2 μm particle size, Plansee SE, Austria), Cu (99% purity, 14-25 μm , Merck KGaA), C (99.95% purity, 2-12 μm particle size, Merck KGaA, Germany), B (98% purity, 44 μm particle size, Alfa Aesar, USA), Re (99.99% purity, 10 μm particle size, Mateck GmbH, Germany) and Hf (99.6% purity, 44 μm particle size, Alfa Aesar, USA) were stored and handled only in argon atmosphere within a glovebox. W and Cu powders were mixed in an atomic ratio of 1:3 (W-75Cu) and about 3-5 at.% of doping elements were added. The powder mixture was then compacted still in argon atmosphere using a sealed mini-chamber [79] and the HPT tool [80], applying a pressure of 9 GPa and torsional deformation of 0.1 rotation [77]. Subsequently, the compacted, disk-shaped sample was deformed in the HPT tool under a pressure of 9 GPa for 100 rotations at room temperature. Additionally, an undoped sample with a W:Cu ratio of 1:1 was compacted (W-50Cu). A two-step deformation process was applied, deforming the compacted sample first for 30 rotations at 200°C and afterwards for 100 rotations at room temperature. This was previously identified to result in the most homogeneous

microstructure for this composition when starting from a powder material [77]. Both HPT processes result in disk-shaped specimens with a diameter of 8 mm and a height of about 0.8 mm.

D.2.2 Microstructural characterization and microhardness testing

A field-emission scanning electron microscope (SEM; LEO 1525, Zeiss GmbH, Germany) was used to investigate the microstructure of the fabricated samples. Additionally, TEM samples of the undoped, Re-doped and Hf-doped W-75Cu were prepared by dimpling or FIB cutting and investigated in a JEOL 2200FS TEM (JEOL Ltd., Japan) in bright-field and STEM mode. The same TEM was used to assess the deformed microstructure of selected bending specimens via FIB-processed TEM windows. The grain size distributions were determined via a customized watershed algorithm implemented in Python 3.9 using libraries such as Scikit-Image, Scipy and OpenCV. A proper statistic was achieved by determining more than 3000 single grains for each specimen state from several STEM images.

The microhardness of all samples was tested along the sample diameter using a Buehler Micromet 5104 machine (Buehler ITW Test & Measurement GmbH, Germany) and a load of 500 g.

D.2.3 Microcantilever bending tests

Due to the torsional nature of the deformation, a gradient in microstructure is common for HPT deformed materials [81,82]. Even though the W-Cu matrix in the majority of the produced sample volume should be in saturation after 100 rotations, occasional larger tungsten particles only fragment at a high deformation strain, rendering only the outer regions of the sample disk reliably free from large W particles and with the desired microstructure [77,78].

This restriction makes it challenging to retrieve conventional bulk mechanical properties like strength and ductility from the specimens. Therefore, we rely on small-scale testing to probe only the properties of the confined desired microstructure [78,83]. Micropillar compression tests often overestimate the ductility of nanocrystalline and fine-grained materials [1,2]. Also, it is rather tedious and time-consuming to fabricate samples for microtensile testing [84–87]. Hence, this work utilizes microcantilever bending for sampling of all fabricated material systems. The bending cantilevers were fabricated using a dual-beam FIB-SEM (LEO 1540 XB, Zeiss GmbH, Germany) after

grinding a half HPT disk to a wedge shape (see [63]). The cantilevers were machined to a length L of about $10\ \mu\text{m}$ and a width W and a thickness B of about $3\ \mu\text{m}$ (see Figure D.2a). Testing of the cantilevers was conducted in-situ in a field-emission SEM (LEO 982, Zeiss GmbH, Germany) using an UNAT-SEM indenter (Zwick GmbH & Co KG, Germany) equipped with a conductive diamond wedge indenter tip (Synton-MDP AG, Switzerland). The displacement rate was set to $20\ \text{nm/s}$, which corresponds to a strain rate of about 10^{-3}s^{-1} for the given cantilever dimensions. Bending stresses and strains can be calculated from the force and displacement data recorded by the indenter using well-known equations [63,88–90]:

$$\sigma_{max,tensile} = 4 \cdot \frac{F \cdot L_B}{B \cdot W^2} \quad (\text{D.4})$$

$$\varepsilon_{max,tensile} = \frac{3 \cdot W \cdot u}{2 \cdot L_B^2} \quad (\text{D.5})$$

where $\sigma_{max,tensile}$ is the bending stress at the outermost fiber of the cantilever (i.e. maximum tensile stress in the sample), $\varepsilon_{max,tensile}$ is the bending strain at the same location, F is the recorded force, u the recorded displacement and L_B the bending length of the cantilever (i.e. the horizontal distance between the base of the cantilever and the contact point of the indenter tip with the cantilever, see Figure D.2a). No significant influence of the system compliance on the measured displacement is apparent from in-situ images.

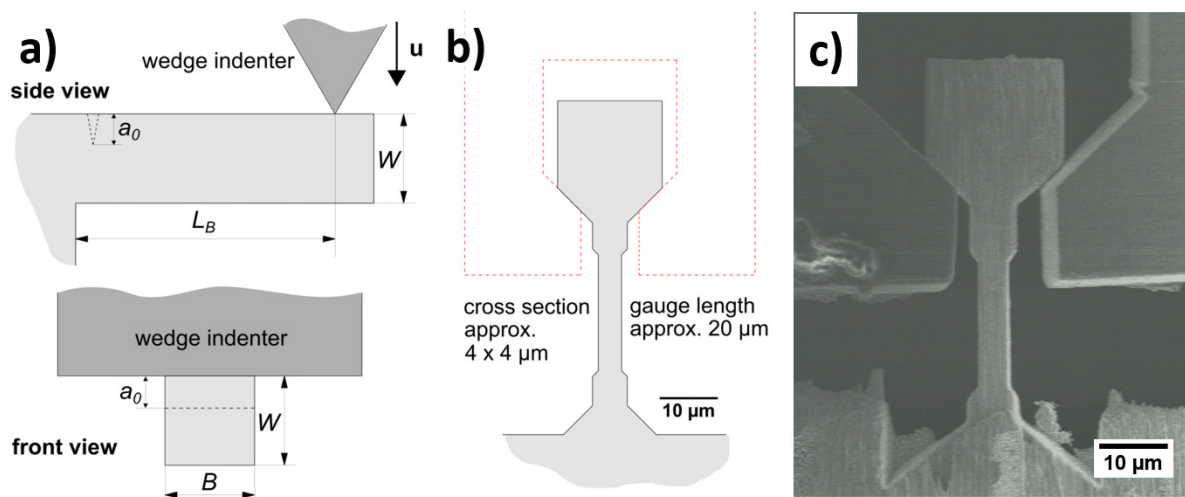


Figure D.2 Test setup for a) microcantilever bending/fracture tests and b) microtensile tests. c) Snapshot from the in-situ video of a microtensile test on W-75Cu material.

D.2.4 Microtensile tests

For selected promising material samples, as detailed later, microtensile specimens were fabricated using the FIB-SEM. To accelerate the time-consuming process of sample fabrication, a femtosecond laser work station (Origami 10 XP, Onefive GmbH, Switzerland) [91] was used for coarse precuts, reducing the necessary fabrication time tremendously. Figures D.2b and D.2c display the test setup and dimensions of the fabricated tensile samples. They were tested using the same equipment as for the bending tests, except that the indenter tip was a gripper made from tungsten (see Figure D.2c). A displacement rate of 20 nm/s was applied, which results in the same strain rate of $10^{-3}s^{-1}$, as for the bending experiments. Recorded force and displacement data were converted to tensile engineering stress and strain curves using the standard equations. The system compliance was accounted for by measuring the real displacement of the indenter from in-situ images and applying a linear correction.

D.2.5 Fracture mechanical tests

Based on their strength and ductility characteristics, the most promising material variants were also investigated regarding their fracture properties. A similar cantilever geometry was fabricated with the FIB-SEM to that for the bending tests (Figure D.2a), however, the dimensions were increased to $10 \times 10 \times 35 \mu\text{m}$ to avoid size effects and invalidity of fracture experiments [64,92]. Moreover, a fine notch ($a_0 = 0.5 \mu\text{m}$) was introduced to the cantilevers using the FIB with a milling current of 30 pA [93]. Because of the given cantilever dimensions, the small-scale yielding criterion is not fulfilled, which makes an analysis using linear elastic fracture mechanics invalid. Therefore, regular partial unloadings were performed on all cantilevers as elastic-plastic fracture mechanics (EPFM) had to be applied for the valid analysis of the fracture toughness [92,94,95]. The experimental J-Integral was used to analyze the fracture toughness of the specimen [94,95]:

$$J = \frac{K^2 \cdot (1 - \nu^2)}{E} + \frac{\eta \cdot A_{pl}}{B \cdot (W - a_0)} \quad (\text{D.6})$$

where ν is the Poisson's ratio and E the Young's Modulus of the material (for W-75Cu: $\nu = 0.34$, based on a simple rule of mixture, and $E = 160\text{GPa}$, according to nanoindentation experiments performed on the same material [77]), $\eta = 1.9$ is a constant pre-factor, A_{pl} is the plastic area under the force-displacement curve [93,95],

B is the sample thickness, W is the width of the cantilever and a_0 is the size of the initial crack length (Figure D.2a). The stress intensity factor K can be calculated using [93,94]:

$$K = \frac{F \cdot L_C}{B \cdot W^{3/2}} \cdot f\left(\frac{a}{W}\right) \quad (\text{D.7})$$

With F being the recorded load on the cantilever and L_C the horizontal distance between the notch and the point of loading. The shape factor $f\left(\frac{a}{W}\right)$ is dependent on current crack length a and sample width and has been calculated in previous work [96,97].

To measure the margin of a throughout the experiment, the slope of the partial unloadings is used to calculate the stiffness change of the cantilever. From this change in stiffness the crack length can be calculated using FEM-based and analytical equations from previous work [93,97].

The notched cantilevers were tested using the same setup and applied strain rates as for the microcantilever bending experiments.

D.3 Results

D.3.1 Microstructure and hardness

Figure D.3 shows the microstructure of all materials investigated by SEM and STEM. All material samples show fairly homogeneous microstructures with very fine nanocrystalline grains and only occasional slightly larger W particles, indicative via their brighter (SEM) or darker (STEM) contrast, respectively. Grain sizes were analyzed for the samples investigated in STEM and yielded approximate average values of 8.5 nm for the undoped, 11 nm for the Hf-doped and 8.5 nm for the Re-doped material. Small holes are visible in the TEM microstructure of the Hf- and Re-doped sample (arrows).

The results from microhardness measurements are displayed in Figure D.4. From these it is evident that the W-50Cu sample shows a much higher hardness (of just below 600 HV0.5) than all W-75Cu samples, which is due to the increased amount of W. All differently doped W-75Cu materials demonstrate a hardness between 400 and 500 HV0.5, with no pronounced influence of the doping elements being obvious. Furthermore, all investigated materials exhibit a relatively flat hardness over radius

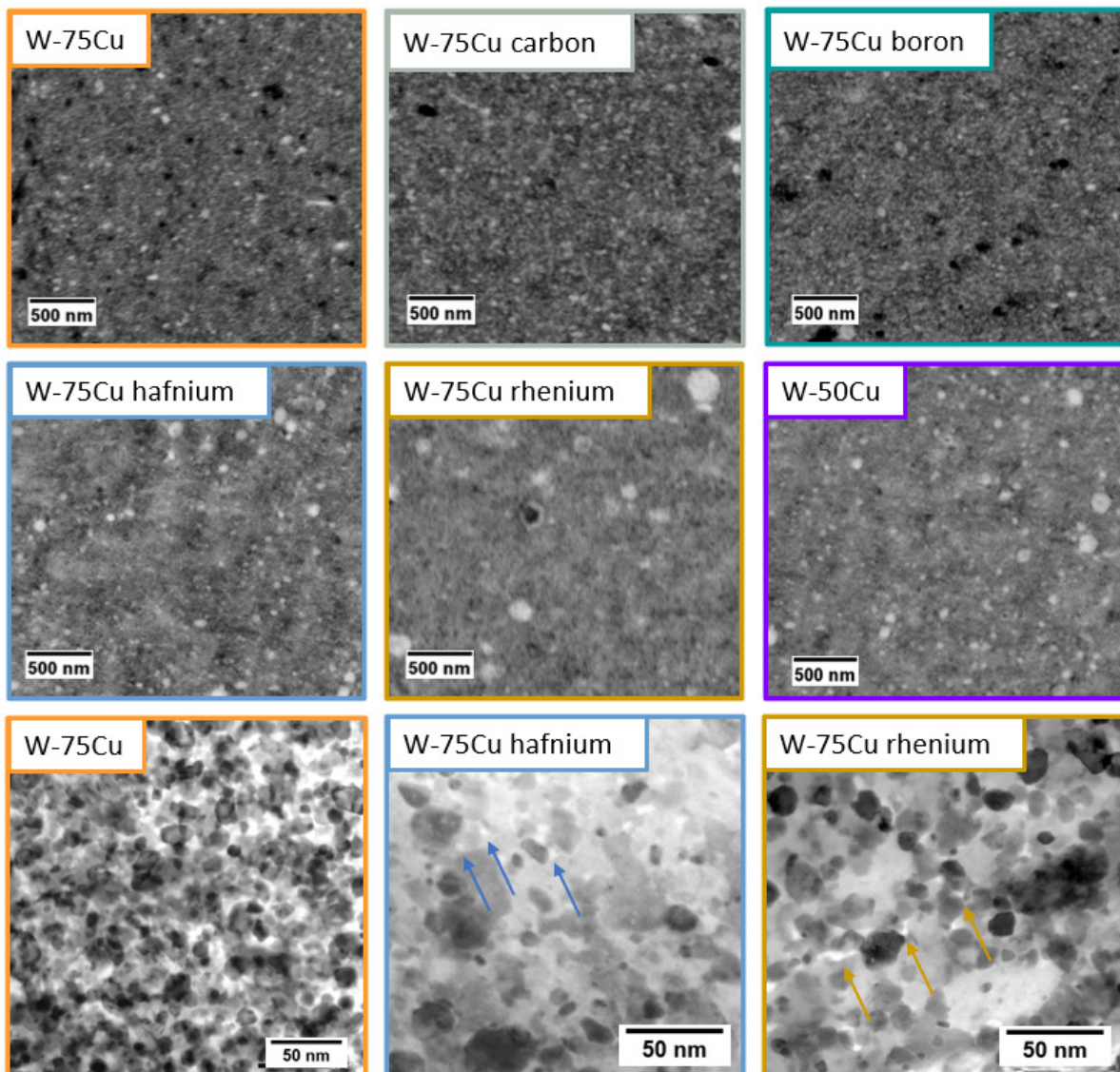


Figure D.3 SEM images of the nanocrystalline microstructure of all investigated samples (top & middle row) and STEM images of selected samples (bottom row).

curve (except the center part of the disks), which indicates that the W-Cu matrix has been successfully deformed to saturation in those regions.

D.3.2 Bending and tensile properties

The results from microcantilever bending tests are shown in Figure D.5. Measures for strength and ductility from bending tests were defined following the procedure of the author's previous work [63]:

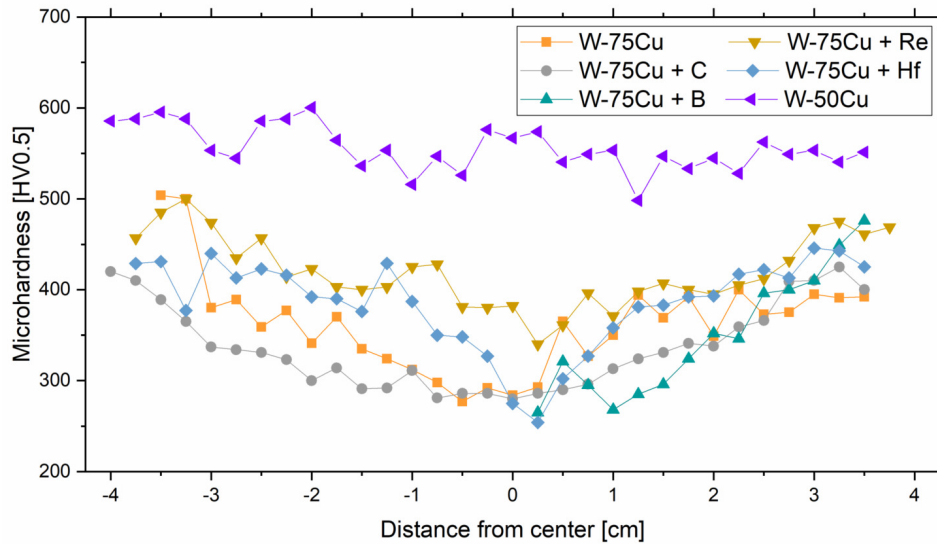


Figure D.4 Microhardness of all investigated materials along the diameter of the HPT disk.

Regarding the strength, the maximum bending stress throughout the experiment, calculated from Equation D.4, is utilized and serves as an equivalent to ultimate tensile strength (UTS). The ductility of the material was defined as the plastic bending strain (Equation D.5 minus the elastic strain gained from the loading slope) at the failure point. This failure point was defined as the point where first crack formation was observed in the in-situ images from the experiments. This point always coincided with a (sudden or continuous) load drop in the load-displacement curve. Naturally, although the bending samples exhibit partial tensile loading conditions, the strength and ductility values gained from this method cannot be compared directly to values gained from tensile tests. However, they can serve as a means to compare the strength and ductility of the different materials amongst each other and assess the qualitative improvement or deterioration of mechanical properties, respectively.

As apparent from Figure D.5, with the exception of C, every doping element improves the strength or ductility of W-75Cu. While C decreases the two properties, B improves both strength and ductility, respectively, which is similar to the effect both doping elements have in ufg W [63]. Doping with Hf leads to an extreme improvement of bending strength, while ductility only decreased slightly. For the Re-doped material, the different cantilevers processed from the same sample showed a large variety in strength and ductility, yet generally higher values than the undoped material. Furthermore, some of the fabricated cantilevers did not exhibit any signs of crack formation or failure throughout the experiment. These cantilevers were deformable to extraordinarily high strains of over 40% without showing signs of failure or a drop in bending stress (see Figure D.5). These specimens showing “super-ductile” behavior

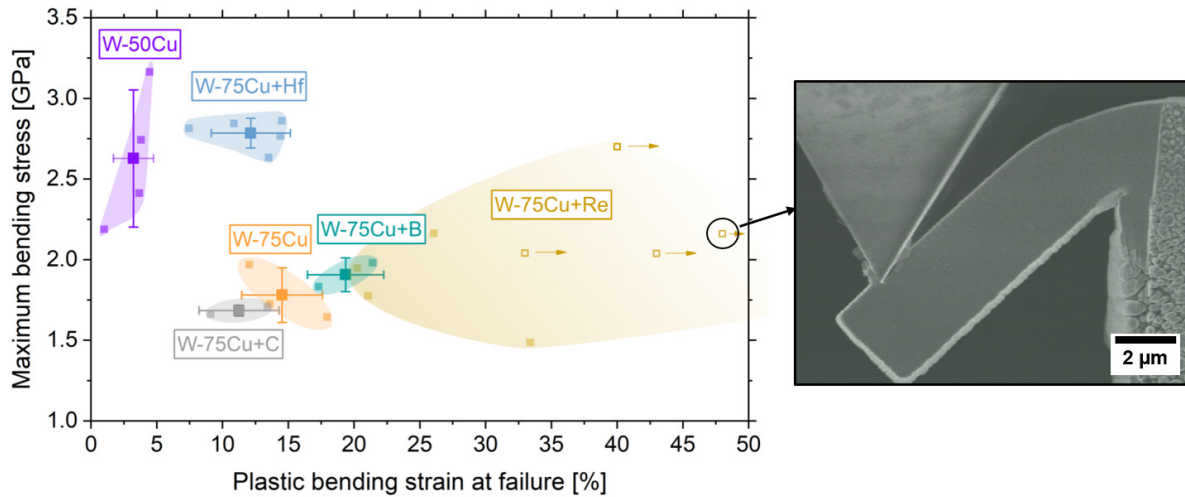


Figure D.5 Maximum bending stress over plastic bending strain at failure for all investigated W-Cu composites. Small squares represent individual cantilever experiments, large squares and error bars represent the average value and standard deviation of a specific material, respectively. The in-situ SEM snapshot shows a representative Re-doped W-75Cu specimen exhibiting “super-ductile” behavior.

are illustrated by open symbols and arrows, indicating that the ductility is even higher than marked in Figure D.5. Since it was not possible to get ductility values for these samples, no average value for ductility or error bars can be provided for the W-75Cu + Re material. However, even the samples that showed signs of failure during the experiment demonstrate higher ductility than the other investigated materials. As expected, the W-50Cu material shows a higher bending strength but an immensely decreased ductility compared to the W 75Cu samples.

For a rigorous assessment of their ductility, microtensile samples of undoped and Re-doped W-75Cu material were fabricated and tested as well, due to the following reasons: (i) to compare strength and ductility gained from bending and tensile tests, for a baseline how to interpret the bending results, (ii) to pinpoint how much the doping with Re increases the strength and ductility of W-75Cu and (iii) to check whether the Re-doped tensile samples also show a “super-ductile” behavior, or whether that solely occurs in bending samples. The results of these tensile tests are visible in Figure D.6. The ultimate tensile strength is plotted against the total plastic elongation to failure in Figure D.6b. It is apparent that, while the tensile samples showed the expected lower strength and ductility values than the bending samples, the addition of Re definitely improves the mechanical properties of W-75Cu. While the UTS increased by 33% from 1.12 GPa to 1.52 GPa, the ductility shows an increase of 38% from 3.2% to 4.4%. All samples failed in a regular fashion, as the stress-strain curves in Figure D.6a confirm. Figure D.6d shows that the Re-doped material exhibits

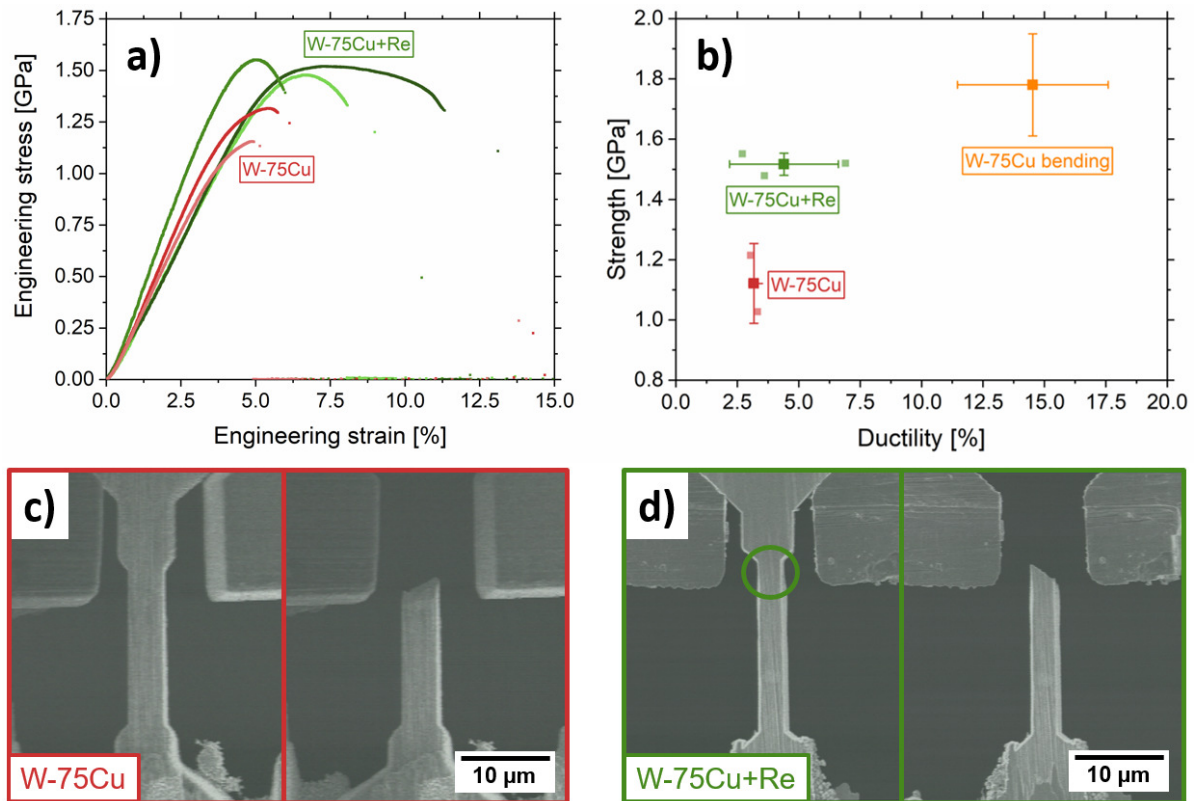


Figure D.6 Microtensile tests on W-75Cu and W-75Cu+Re. a) Stress-strain curves and b) ultimate tensile strength over ductility of all tested specimen. The W-75Cu microcantilever bending sample was added to b) as a reference. Snapshots from in-situ videos of representative c) undoped and d) Re-doped material right before and after fracture, respectively.

some slight necking before fracture, whereas the undoped material (Figure D.6c) does not.

D.3.3 Fracture properties

The fracture toughness of the W-75Cu samples was evaluated in EPFM experiments using the J-Integral method. It should be mentioned that the C-doped W-75Cu and the W-50Cu sample were not tested due to the inferior properties these materials showed in microcantilever bending tests. Considering that all tested notched cantilevers broke in an unstable fashion, one can simply use Equations D.6 and D.7 (in conjunction with tracking of crack length via stiffness measurements) to determine the critical J Integral J_c at failure as a measure of fracture toughness [64]. For reference, the ratio of smallest sample dimension to plastic zone size $\frac{J_c}{\sigma_y}$ (with the yield strength σ_y being

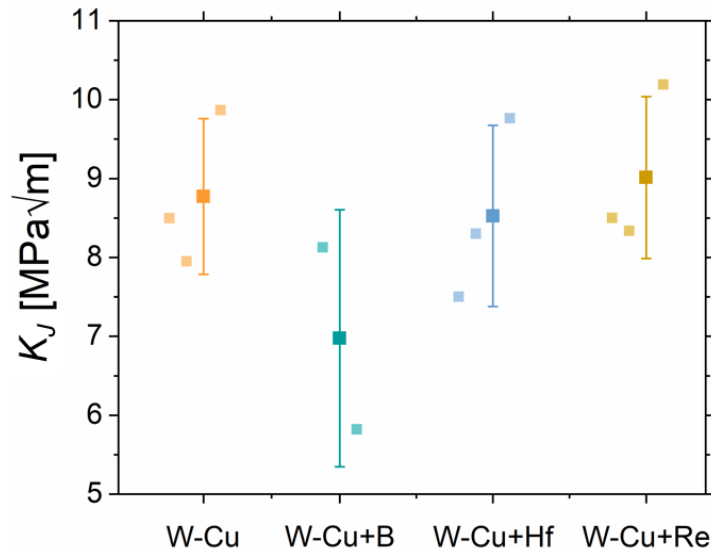


Figure D.7 Results from small-scale fracture mechanical experiments. Small squares represent individual cantilever experiments, large squares and error bars represent the average value and standard deviation of a specific material, respectively.

between 1.5 and 2.0 GPa for all W 75Cu materials in the presented bending tests) amounts to between 40 and 50, thus sufficiently large to gain valid fracture toughness results from EPFM [64,92,98].

Furthermore, the deduced J_c values can be converted to more commonly used $K_{J,c}$ values using the following equation:

$$K_{J,c} = \sqrt{\frac{J_c \cdot E}{1 - \nu^2}} \quad (\text{D.8})$$

As visible from Figure D.7, the doping with B, Hf and Re did not improve the fracture toughness of the undoped W-75Cu. Instead, all samples show roughly the same $K_{J,c}$ values ranging between 8 and 10 $\text{MPa}\sqrt{m}$. The two B-doped cantilevers show marginally lower toughness values between 6 and 8 $\text{MPa}\sqrt{m}$.

D.4 Discussion

The processing route of undoped and doped W-75Cu composites from powders using HPT was successful in reliably fabricating bulk nanocrystalline samples with

comparable grain sizes of about 10 nm. The effects of elemental doping on strength, ductility and fracture toughness were investigated and are discussed hereinafter.

D.4.1 Strength and ductility

The bending strength and ductility for all investigated materials are shown in Figure D.5. Given the unique mechanical behavior of the Re-doped W-75Cu samples, the performance of this material will be discussed separately and in more detail in Section D.4.3.

The W-50Cu composite exhibits a higher strength than the W-75Cu composites, evidently due to the higher amount of W. However, this composition also leads to a serious decrease in bending ductility, rendering the material rather unattractive. Therefore, only the W-75Cu composites were investigated further. Doping with the interstitial elements C and B results in different mechanical responses in the W-75Cu nanocomposite. C leads to a slight decrease in strength and ductility, while B has the exact opposite effect. The DFT calculations presented within this work (Figure D.1) indicate, however, that both elements weaken the W/Cu interface while having a beneficial effect on GB cohesion of copper and according to literature also on W GBs [61,62,65]. Therefore DFT calculations cannot directly explain the qualitatively different effect of C and B. However, a possible reason for this behavior could be that the weakening effect of B on the W/Cu interface is less severe than that of C, while the strengthening effect on Cu GBs is greater for B. Note that the same behavior of C and B was evidenced in ufg W [63]. In this work, it was suggested that the formation of nanosized carbide layers or restricted dislocation mobility could explain the deteriorating properties of C. It is reasonable to assume that similar effects could occur in W-Cu nanocomposites.

Doping with Hf increases the strength tremendously, while showing only a slight decrease in ductility. In fact, this material shows similar strength values than the W-50Cu samples, while exhibiting a substantially improved ductility. A definite reason for this strength increase is not obvious, yet the formation of HfO₂ oxides (as previously observed in W [63] and Mo [60]) may be the explanation. While such oxides were not found directly in TEM investigations on this material, several nanosized holes are evidenced (arrows in Figure D.3), indicating that oxides might have fallen out of the samples during sample preparation via dimpling. The formation of such HfO₂ particles is expected to increase the strength of the composite via precipitation hardening. While this is usually accompanied by a loss of ductility, this effect is severely reduced in the present case due to the simultaneous removal of O from GBs and interfaces. It was shown in previous work on W [63,64] and Mo [60] that the

formation of HfO_2 can lead to improvement of ductility and toughness via binding of detrimental impurity O, which usually embrittles the GBs.

Given the stress gradient, complex stress state and the fact that microcantilever bending tests are not standardized experiments, microtensile tests were performed on undoped W-75Cu to compare strength and ductility gained from either method, as shown in Figure D.6. Both strength and ductility gained from tensile tests are lower than the bending properties. The UTS is about 60% lower than the maximum bending stress, which is in good agreement with macroscopic tests for brittle materials [99]. The bending ductility is significantly higher (about 4-5 times) than the tensile ductility. This is not surprising given the stress and strain gradient inside a bending sample. Additionally, the volume of sample material experiencing high stresses and strains is substantially smaller in a bending cantilever compared to a tensile sample, where the whole cross-section over the total gauge length experiences the same stresses. Therefore, the probability of finding a critical defect leading to failure of the sample is much higher in the tensile sample, explaining the comparably lower ductility. It should be mentioned, however, that the bending results are still valid for qualitative comparison of the differently doped materials [63].

D.4.2 Fracture toughness

The fracture toughness values in Figure D.7 do not show the desired improvement of fracture behavior through GB and interface doping. Instead, the toughness values of about $9 \text{ MPa}\sqrt{\text{m}}$ of the undoped material stay unchanged after the addition of Hf and Re. For B, even a slight decrease in toughness is observed.

As doping with Hf does not increase the ductility of W-Cu nanocomposites, it is not surprising that the toughness is similar as well. However, for the ductility-enhancing elements B and Re an increase in toughness was expected, given how closely interlinked the two properties are, especially for nanocrystalline materials [1,16,64]. The authors assess that a doping element that increases ductility but not fracture toughness is likely to restrict crack initiation but not crack growth. This might be due to both B and Re having a ductilizing effect on the W GBs [61,62] and Cu GBs (DFT results in Figure D.1) and not on the W/Cu interface. Hence, the probability of crack initiation at said GBs is vastly reduced, yet once a defect is present in the material, a relatively easy crack path is provided by the W/Cu interface. It seems that the weakening of the W/Cu interface by B, as deduced from the DFT calculations in Figure D.1, is the reason for the slightly lower fracture toughness. For Re, the W/Cu interface is neither weakened nor strengthened, explaining the retained fracture toughness from the undoped composite, as the crack path of least resistance,

i.e. the W/Cu interface, is equally strong for both materials. However, it should also be mentioned that there is site competition with the O existing in the structure, and even though B is somewhat detrimental at the W/Cu interface, it is certainly less critical than O, thus its presence there has an indirect possible effect [61,63]. Furthermore, as the material is processed via SPD and therefore severe mechanical mixing of the constituent atoms is in place, one cannot rely solely on simulations performed in thermodynamical equilibrium for the prediction of segregation and mechanical performance. It is likely that a large amount of doping elements is present within the Cu material, as even intermixing of W and Cu has been found previously in HPT-processed W-Cu nanocomposites [83]. As deduced from the DFT simulations in Figure D.1, all doping elements would have a positive effect on cohesion when situated on the Cu side of the W/Cu interface. This would counteract the weakening effect the elements have on the interface when situated on the W side, resulting in almost no net-change in fracture toughness as observed here. Moreover the strong segregation tendency of the doping elements to W GBs [61,62], could possibly drain the interface from dopants and strengthen the cohesion of W GBs instead of weakening the W/Cu interface.

As the observed fracture toughness of $8-10 \text{ MPa}\sqrt{m}$ is decent but far from ideal, different strategies to improve the toughness need to be applied. A promising approach would be an increase of grain size to the ultrafine-grained (100 – 500 nm) regime. Relatively high strengths can still be achieved, while the toughness should improve substantially due to crack deflection along interfaces and maybe even incite a transition to transgranular failure, which in turn could make use of the inhomogeneity effect [34,35]. Adjusting the microstructure accordingly, either through annealing or reduced HPT deformation, can prove to be challenging, however, given the large difference in melting point and vastly different intrinsic strength of W and Cu.

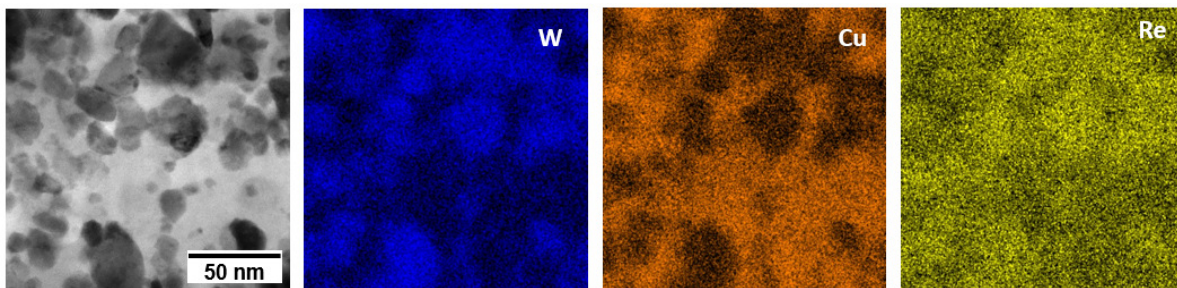


Figure D.8 EDX maps of Re-doped W-75Cu nanocomposite taken in the TEM.

D.4.3 Doping with Re

Doping of W-75Cu nanocomposites with Re resulted in a marked increase of bending strength but especially bending ductility, as apparent in Figure D.5. This “super-ductile” behavior could not be reproduced in a microtensile experiment, but a positive effect of the doping on strength and ductility is still observed (see Figures D.6a and D.6b). Additionally, the Re-doped sample shows slight necking and signs of plastic deformation before failure (Figure D.6d), while the undoped sample did not (Figure D.6c). As mentioned in Section D.4.1, the reasons why the bending experiments show higher ductility than the tensile tests are the bending stress gradient and less volume being exposed to high stresses and strains.

As ductility increases dramatically, but toughness stays unchanged after doping with Re (Figure D.7), a possible explanation is that Re increases the resistance against crack initiation (by strengthening W- and Cu GBs, thereby reducing the probability of crack formation at said GBs) but not against crack propagation (which is commonly defined as fracture toughness and linked to interface cohesion of the weakest interface in nanostructured materials). This would also further explain the discrepancy between bending and tensile ductility, as it is much more likely to find a critical defect in a microtensile sample compared to only the part of a bending cantilever that experiences high tensile stresses. Furthermore, this would also be a reason as to why some of the Re-doped samples break earlier than others and explain the wide variance of measured ductility. Essentially, it becomes just a statistical problem to find a defect that gets critical at certain stresses or strains [100,101].

For a more detailed understanding, EDX measurements were performed in a TEM to investigate the location of Re in the composite. As is apparent in Figure D.8, no pronounced segregation of Re was found at the interfaces. Instead, most Re is located within the W grains or W GBs of the composite. However, one has to be careful with evaluating these EDX measurements, as the peaks of W and Re are very close and mostly overlapping. The segregation energies from DFT calculations in Figure D.1 indicate that Re would be situated either at the W/Cu interface or the W surface, however, the segregation energy for Re in W bulk is also rather low. Other DFT works [62,65] in pure W report a pronounced segregation tendency of Re to the W GBs, stronger than that to the W/Cu interface or W surface. Thus, segregation of Re to W GBs is the more likely case.

To further investigate the unique mechanical behavior of Re-doped W-Cu nanocomposite, a closer look at deformed cantilevers was taken. Figure D.9 shows post-mortem SEM images of three different W 75Cu+Re cantilever samples. It is immediately apparent from the top-view images in the bottom row that there is a pronounced

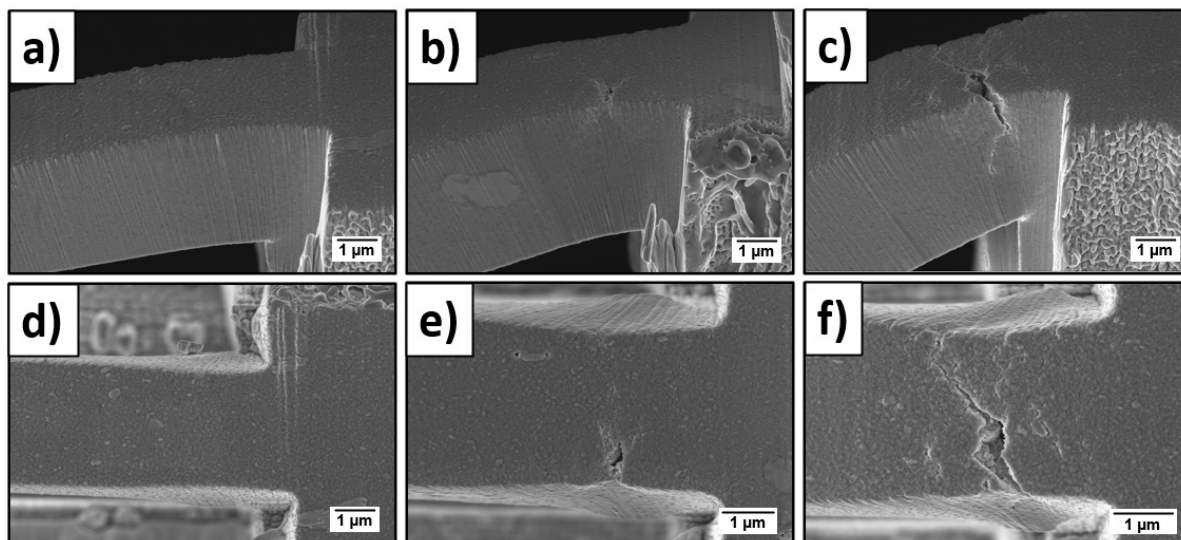


Figure D.9 Post-mortem SEM images of different W-75Cu+Re cantilevers. a,d) Cantilever sample after about 20% plastic strain, b,e) cantilever sample that failed at high strain (35%) and c,f) cantilever sample that was broken forcefully. Bottom row shows top-view.

necking of all samples in the top parts of the cantilevers, where tensile stresses are present. Moreover, the bottom part of the samples each show an increased thickness. Both are signs of pronounced plastic deformation of the cantilever.

The cantilever that was deformed to about 20% plastic strain (Figures D.9a and D.9d) shows smooth deformation without any sign of failure. Compared to the cantilevers that were deformed to higher strains, the necking is less pronounced in these samples. Figures D.9b and D.9e show a cantilever that failed towards the end of the experiment at a plastic surface strain of about 35%. A partial crack that does not seem to have propagated far is visible in this sample. Other than that, no signs of failure but a large amount of deformation is visible. Finally, a cantilever specimen that was broken forcefully after the bending experiment is seen in Figures D.9c and D.9f. A large crack is visible, however, the sample and crack morphology indicate that a high amount of plastic deformation must have happened before failure and further crack propagation.

The SEM images in Figure D.9 confirmed a large amount of plastic deformation that occurred without failure in the tested bending samples, however, no clear explanation for this “super-ductile” behavior was found. Therefore, TEM windows were cut via FIB into the deformed part of a cantilever specimen showing outstanding ductility. The STEM images are depicted in Figure D.10. No signs of severe deformation, dislocation activity or change in grain size or shape are visible in this region of the

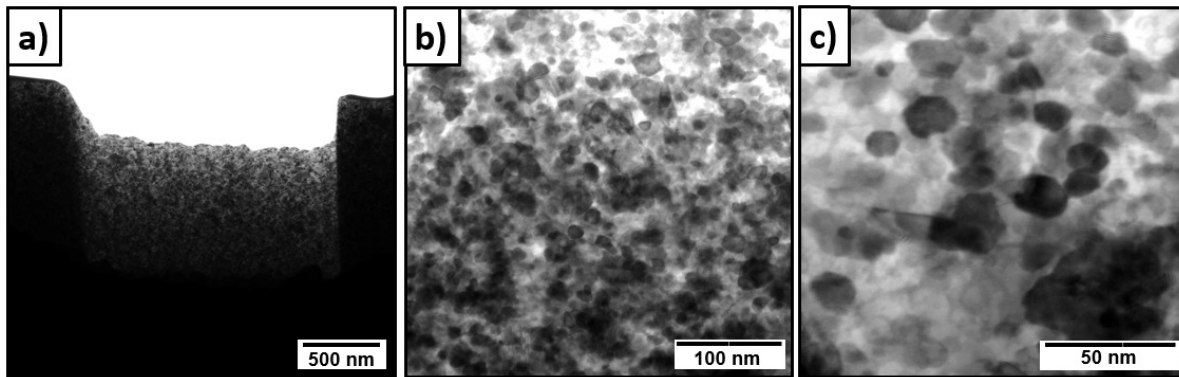


Figure D.10 Post-mortem STEM images of a “super-ductile” W-75Cu+Re cantilever in the deformed region.

cantilever, which experienced more than 30% of tensile bending strain. No formation of micropores or -cracks could be observed either. In fact, the microstructure looks very comparable to the microstructure after processing with HPT in Figures D.3 and D.8, indicating no obvious changes in microstructure occurred in the bending specimen. This is confirmed when looking at the grain size distributions in Figure D.11. The distributions before and after bending deformation are very similar and the mean grain size values for either microstructure are almost identical.

In summary, the definitive reason for the “super-ductile” behavior of Re-doped W-75Cu nanocomposites could not be unveiled within this work. The discrepancies between improved ductility and retained fracture toughness point towards an increase in crack initiation resistance. This would make the material sensitive to pre-existing defects within the material and explains the large variance of measured ductility and the noticeable difference between bending and tensile ductility, respectively. To investigate this highly promising material further, high-resolution characterization, such as atom probe tomography, is needed to clarify if Re is located at the W/Cu interface, W GBs or within the W as a solid solution, where it is known to have a ductilizing effect [102,103]. This information in combination with additional DFT simulation work might provide a clearer picture of the effect that Re has on plastic deformation and fracture processes in W-75Cu nanocomposites.

D.5 Conclusion

This work explored the effects of different interface doping elements on the mechanical properties of W-75Cu nanocomposites with a grain size of about 10 nm. While doping with C decreases the overall mechanical performance, B increases the strength

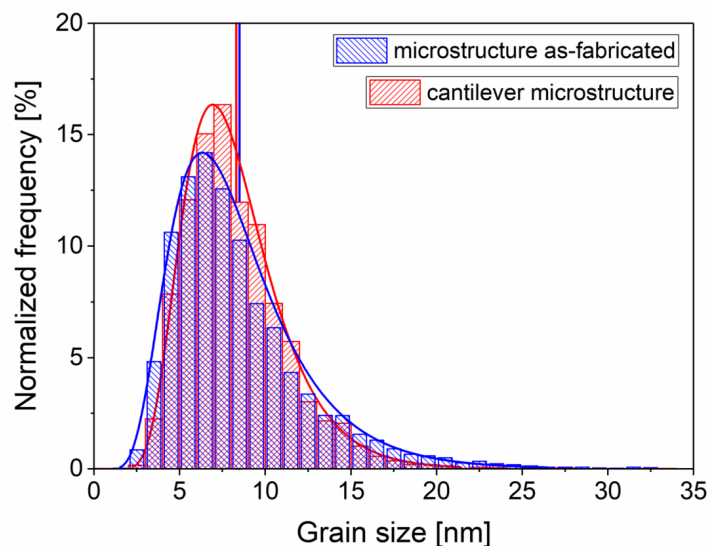


Figure D.11 Histograms of grain size distribution of W-75Cu + Re samples before (blue) and after (red) pronounced plastic bending deformation. Vertical lines represent the mean grain size.

and ductility of the composite slightly. The addition of Hf is expected to lead to the formation of HfO_2 oxides and, consequently, GBs depleted of impurity oxygen, which increases the strength greatly, while maintaining the bending ductility.

Doping with Re had immensely positive effects on the mechanical properties, increasing the strength and showing extraordinarily high bending ductility of up to over 40%. This “super-ductile” behavior could not be observed in related microtensile tests, however, a clear improvement in properties compared to the undoped W-Cu composite is apparent. The deformation microstructure of the “super-ductile” bending samples was investigated in SEM and TEM, yet no obvious explanation for the high achievable plastic deformation without failure was discovered.

Fracture mechanical investigations showed no change in fracture toughness (about $9 \text{ MPa}\sqrt{m}$) through interface doping. This is rather surprising, as ductility and toughness are known to be closely interlinked in nanocrystalline materials. A possible explanation for this unique behavior of B- and especially Re-doped W-75Cu is an increased resistance to crack formation through a strengthening effect in W and Cu GBs, but no improvement in W/Cu interface cohesion and therefore fracture toughness. However, further investigations are necessary to validate this assumption in detail. The unchanged fracture toughness of all investigated doped composites also indicates that the doping elements might not be fully segregated at the interfaces. Here, future annealing studies will unravel how a pronounced segregation of doping elements further affects the mechanical performance of W-Cu nanocomposites.

Overall, it was shown that the strength and ductility of W-75Cu nanocomposites can be improved remarkably by doping with different elements, such as Hf or Re. Therefore, a further step towards a synergy of the two properties in nanostructured materials is taken. The fracture toughness could not be improved via interface doping. Here, increasing the grain size to about 100-200 nm should yield the demanded enhancement of fracture toughness of the composite, but would also decrease strength. However, improving the overall mechanical performance of nanocrystalline alloys and composites by applying the concept of grain boundary segregation engineering proves that the strength-ductility trade-off can be challenged for these materials and paves the way for the creation of structural “supermaterials”, combining high strength, ductility and fracture toughness.

Acknowledgements

This work was funded by the European Research Council (ERC) under grant number 771146 (TOUGHIT). This research was funded in part by the Austrian Science Fund (FWF) [P 34179-N].

Data availability

The datasets generated during the current study are available from the corresponding author on reasonable request.

References

- [1] M.A. Meyers, A. Mishra, D.J. Benson, Mechanical properties of nanocrystalline materials, *Prog. Mater. Sci.* 51 (2006) 427–556.
- [2] C.C. Koch, D.G. Morris, K. Lu, A. Inoue, Ductility of nanostructured materials, *MRS Bull.* 24 (1999) 54–58.
- [3] A. V. Sergueeva, D.M. Hulbert, N.A. Mara, A.K. Mukherjee, *Mechanical properties of nanocomposite materials*, Elsevier Ltd, 2009.
- [4] Y. Wang, M. Chen, F. Zhou, E. Ma, High tensile ductility in a nanostructured metal, *Nature.* 419 (2002) 912–915.
- [5] E. Ma, Eight routes to improve the tensile ductility of bulk nanostructured metals and alloys, *Jom.* 58 (2006) 49–53.

- [6] Y. Wei, Y. Li, L. Zhu, Y. Liu, X. Lei, G. Wang, Y. Wu, Z. Mi, J. Liu, H. Wang, H. Gao, Evading the strength-ductility trade-off dilemma in steel through gradient hierarchical nanotwins, *Nat. Commun.* 5 (2014).
- [7] E. Ma, T. Zhu, Towards strength–ductility synergy through the design of heterogeneous nanostructures in metals, *Mater. Today.* 20 (2017) 323–331.
- [8] Q. Wei, K.T. Ramesh, L.J. Kecskes, S.N. Mathaudhu, K.T. Hartwig, Ultrafine and Nanostructured Refractory Metals Processed by SPD : Microstructure and Mechanical Properties, *Mater. Sci. Forum.* 579 (2008) 75–90.
- [9] N.A. Mara, D. Bhattacharyya, P. Dickerson, R.G. Hoagland, A. Misra, Ultrahigh strength and ductility of Cu-Nb nanolayered composites, *Mater. Sci. Forum.* 633–634 (2010) 647–653.
- [10] J. Schiøtz, K.W. Jacobsen, A maximum in the strength of nanocrystalline copper, *Science* (80-.). 301 (2003) 1357–1359.
- [11] N.J. Petch, The ductile-brittle transition in the fracture of α -iron: I, *Philos. Mag.* 3 (1958) 1089–1097.
- [12] T. Hanamura, F. Yin, K. Nagai, Ductile-brittle transition temperature of ultrafine ferrite/cementite microstructure in a low carbon steel controlled by effective grain size, *ISIJ Int.* 44 (2004) 610–617.
- [13] A. Hohenwarter, R. Pippin, Fracture and fracture toughness of nanopolycrystalline metals produced by severe plastic deformation, *Philos. Trans. R. Soc. A.* 373 (2015) 20140366.
- [14] H. Van Swygenhoven, J.R. Weertman, Deformation in nanocrystalline metals, *Mater. Today.* 9 (2006) 24–31.
- [15] K.S. Kumar, H. Van Swygenhoven, S. Suresh, Mechanical behavior of nanocrystalline metals and alloys, *Acta Mater.* 51 (2003) 5743–5774.
- [16] R. Pippin, A. Hohenwarter, The importance of fracture toughness in ultrafine and nanocrystalline bulk materials, *Mater. Res. Lett.* 4 (2016) 127–136.
- [17] D. Farkas, H. Van Swygenhoven, P.M. Derlet, Intergranular fracture in nanocrystalline metals, *Phys. Rev. B - Condens. Matter Mater. Phys.* 66 (2002) 601011–601014.
- [18] W. Han, M.J. Demkowicz, N.A. Mara, E.G. Fu, S. Sinha, A.D. Rollett, Y. Wang, J.S. Carpenter, I.J. Beyerlein, A. Misra, Design of radiation tolerant materials via interface engineering, *Adv. Mater.* 25 (2013) 6975–6979.
- [19] M. Wang, I.J. Beyerlein, J. Zhang, W. Han, Defect-interface interactions in irradiated Cu / Ag nanocomposites, *Acta Mater.* 160 (2018) 211–223.
- [20] W.Z. Han, E.K. Cerreta, N.A. Mara, I.J. Beyerlein, J.S. Carpenter, S.J. Zheng, C.P. Trujillo, P.O. Dickerson, A. Misra, Deformation and failure of shocked bulk Cu-Nb nanolaminates, *Acta Mater.* 63 (2014) 150–161.
- [21] W.Z. Han, N.A. Mara, Y.Q. Wang, A. Misra, M.J. Demkowicz, He implantation of bulk Cu – Nb nanocomposites fabricated by accumulated roll bonding, *J. Nucl. Mater.* 452 (2014) 57–60.
- [22] N.A. Mara, D. Bhattacharyya, R.G. Hoagland, A. Misra, Tensile behavior of 40 nm Cu/Nb nanoscale multilayers, *Scr. Mater.* 58 (2008) 874–877.
- [23] J.Y. Zhang, S. Lei, Y. Liu, J.J. Niu, Y. Chen, G. Liu, X. Zhang, J. Sun, Length scale-dependent deformation behavior of nanolayered Cu/Zr micropillars, *Acta Mater.* 60 (2012) 1610–1622.
- [24] J.Y. Zhang, S. Lei, J. Niu, Y. Liu, G. Liu, X. Zhang, J. Sun, Intrinsic and extrinsic size effects on deformation in nanolayered Cu/Zr micropillars: From bulk-like to small-volume materials behavior,

Acta Mater. 60 (2012) 4054–4064.

[25] J.Y. Zhang, G. Liu, S.Y. Lei, J.J. Niu, J. Sun, Transition from homogeneous-like to shear-band deformation in nanolayered crystalline Cu/amorphous Cu-Zr micropillars: Intrinsic vs. extrinsic size effect, *Acta Mater.* 60 (2012) 7183–7196.

[26] M.D. Abad, S. Parker, D. Kiener, M.M. Primorac, P. Hosemann, Microstructure and mechanical properties of $\text{Cu}_x\text{Nb}_{1-x}$ alloys prepared by ball milling and high pressure torsion compacting, *J. Alloys Compd.* 630 (2015) 117–125.

[27] M.M. Primorac, M.D. Abad, P. Hosemann, M. Kreuzeder, V. Maier-Kiener, D. Kiener, Elevated temperature mechanical properties of novel ultra-fine grained Cu-Nb composites, *Mater. Sci. Eng. A.* 625 (2015) 296–302.

[28] A. Misra, M.J. Demkowicz, X. Zhang, R.G. Hoagland, The Radiation Damage Tolerance of Ultra-High Strength Nanolayered Composites, *JOM.* 59 (2007) 3–6.

[29] N.A. Mara, D. Bhattacharyya, P. Dickerson, R.G. Hoagland, A. Misra, Deformability of ultrahigh strength 5 nm Cu/Nb nanolayered composites, *Appl. Phys. Lett.* 92 (2008).

[30] A. Misra, R.G. Hoagland, Plastic flow stability of metallic nanolaminate composites, *J. Mater. Sci.* 42 (2007) 1765–1771.

[31] I.J. Beyerlein, A. Caro, M.J. Demkowicz, N.A. Mara, A. Misra, B.P. Uberuaga, Radiation damage tolerant nanomaterials, *Mater. Today.* 16 (2013) 443–449.

[32] A.S. Budiman, S.M. Han, N. Li, Q.M. Wei, P. Dickerson, N. Tamura, M. Kunz, A. Misra, Plasticity in the nanoscale Cu/Nb single-crystal multilayers as revealed by synchrotron Laue x-ray microdiffraction, *J. Mater. Res.* 27 (2012) 599–611.

[33] Y. Kim, A.S. Budiman, J.K. Baldwin, N.A. Mara, A. Misra, S.M. Han, Microcompression study of Al-Nb nanoscale multilayers, *J. Mater. Res.* 27 (2012) 592–598.

[34] O. Kolednik, J. Predan, F.D. Fischer, P. Fratzl, Bioinspired Design Criteria for Damage-Resistant Materials with Periodically Varying Microstructure, *Adv. Funct. Mater.* 21 (2011) 3634–3641.

[35] O. Kolednik, J. Predan, F.D. Fischer, P. Fratzl, Improvements of strength and fracture resistance by spatial material property variations, *Acta Mater.* 68 (2014) 279–294.

[36] A. Tiwari, J. Wiener, F. Arbeiter, G. Pinter, O. Kolednik, Application of the material inhomogeneity effect for the improvement of fracture toughness of a brittle polymer, *Eng. Fract. Mech.* 224 (2020) 106776.

[37] D. Raabe, M. Herbig, S. Sandlöbes, Y. Li, D. Tytko, M. Kuzmina, D. Ponge, P. Choi, Grain boundary segregation engineering in metallic alloys : A pathway to the design of interfaces, *Curr. Opin. Solid State Mater. Sci.* 18 (2014) 253–261.

[38] M.A. Gibson, C.A. Schuh, Segregation-induced changes in grain boundary cohesion and embrittlement in binary alloys, *Acta Mater.* 95 (2015) 145–155.

[39] K. Leitner (née Babinsky), D. Lutz, W. Knabl, M. Eidenberger-Schober, K. Huber, A. Lorich, H. Clemens, V. Maier-Kiener, Grain boundary segregation engineering in as-sintered molybdenum for improved ductility, *Scr. Mater.* 156 (2018) 60–63.

[40] J.R. Trelewicz, C.A. Schuh, Grain boundary segregation and thermodynamically stable binary nanocrystalline alloys, *Phys. Rev. B - Condens. Matter Mater. Phys.* 79 (2009) 1–13.

[41] A.J. Detor, C.A. Schuh, Grain boundary segregation, chemical ordering and stability of nanocryst-

- talline alloys: Atomistic computer simulations in the Ni-W system, *Acta Mater.* 55 (2007) 4221–4232.
- [42] T.J. Rupert, J.C. Trenkle, C.A. Schuh, Enhanced solid solution effects on the strength of nanocrystalline alloys, *Acta Mater.* 59 (2011) 1619–1631.
- [43] T.J. Rupert, J.R. Trelewicz, C.A. Schuh, Grain boundary relaxation strengthening of nanocrystalline Ni-W alloys, *J. Mater. Res.* 27 (2012) 1285–1294.
- [44] S. Jakob, A. Hohenwarter, A. Lorich, W. Knabl, R. Pippan, H. Clemens, V. Maier-Kiener, Assessment of grain boundary cohesion of technically pure and boron micro-doped molybdenum via meso-scale three-point-bending experiments, *Mater. Des.* 207 (2021) 109848.
- [45] A.S. Ebner, S. Jakob, H. Clemens, R. Pippan, V. Maier-Kiener, S. He, W. Ecker, D. Scheiber, V.I. Razumovskiy, Grain boundary segregation in Ni-base alloys: A combined atom probe tomography and first principles study, *Acta Mater.* 221 (2021) 117354.
- [46] J.D. Schuler, T.J. Rupert, Materials selection rules for amorphous complexion formation in binary metallic alloys, *Acta Mater.* 140 (2017) 196–205.
- [47] A. Khalajhedayati, Z. Pan, T.J. Rupert, Manipulating the interfacial structure of nanomaterials to achieve a unique combination of strength and ductility, *Nat. Commun.* 7 (2016).
- [48] Z. Pan, T.J. Rupert, Amorphous intergranular films as toughening structural features, *Acta Mater.* 89 (2015) 205–214.
- [49] M. Wagih, P.M. Larsen, C.A. Schuh, Learning grain boundary segregation energy spectra in polycrystals, *Nat. Commun.* 11 (2020) 6376.
- [50] Z. Pan, T.J. Rupert, Effect of grain boundary character on segregation-induced structural transitions, *Phys. Rev. B.* 93 (2016) 1–15.
- [51] V. Turlo, T.J. Rupert, Grain boundary complexions and the strength of nanocrystalline metals: Dislocation emission and propagation, *Acta Mater.* 151 (2018) 100–111.
- [52] D.S. Gianola, B.G. Mendis, X.M. Cheng, K.J. Hemker, Grain-size stabilization by impurities and effect on stress-coupled grain growth in nanocrystalline Al thin films, *Mater. Sci. Eng. A.* 483–484 (2008) 637–640.
- [53] F. Tang, D.S. Gianola, M.P. Moody, K.J. Hemker, J.M. Cairney, Observations of grain boundary impurities in nanocrystalline Al and their influence on microstructural stability and mechanical behaviour, *Acta Mater.* 60 (2012) 1038–1047.
- [54] H. Lee, V. Tomar, An examination of nickel doping effect on the mechanical strength of a tungsten grain boundary, *Comput. Mater. Sci.* 77 (2013) 131–138.
- [55] P. Lejcek, M. Šob, V. Paidar, Interfacial segregation and grain boundary embrittlement : An overview and critical assessment of experimental data and calculated results, *Prog. Mater. Sci.* 87 (2017) 83–139.
- [56] J. Bok, J. Wung, Z. Li, J. Chan, J. Gi, D. Raabe, H. Seop, Boron doped ultrastrong and ductile high-entropy alloys, *Acta Mater.* 151 (2018) 366–376.
- [57] M. Wagih, C.A. Schuh, Thermodynamics and design of nanocrystalline alloys using grain boundary segregation spectra, *Acta Mater.* 217 (2021) 117177.
- [58] C.A. Schuh, T.G. Nieh, H. Iwasaki, The effect of solid solution W additions on the mechanical properties of nanocrystalline Ni, *Acta Mater.* 51 (2003) 431–443.
- [59] C.A. Schuh, M. Kumar, W.E. King, Analysis of grain boundary networks and their evolution

during grain boundary engineering, *Acta Mater.* 51 (2003) 687–700.

- [60] K. Leitner, D. Scheiber, S. Jakob, S. Primig, H. Clemens, E. Povoden-Karadeniz, L. Romaner, How grain boundary chemistry controls the fracture mode of molybdenum, *Mater. Des.* 142 (2018) 36–43.
- [61] D. Scheiber, R. Pippan, P. Puschnig, L. Romaner, Ab initio search for cohesion-enhancing impurity elements at grain boundaries in molybdenum and tungsten, *Model. Simul. Mater. Sci. Eng.* 24 (2016) 85009.
- [62] D. Scheiber, R. Pippan, P. Puschnig, A. Ruban, L. Romaner, Ab-initio search for cohesion-enhancing solute elements at grain boundaries in molybdenum and tungsten, *Int. J. Refract. Met. Hard Mater.* 60 (2016) 75–81.
- [63] M. Wurmshuber, S. Jakob, S. Doppermann, S. Wurster, R. Bodlos, L. Romaner, V. Maier-Kiener, D. Kiener, Tuning mechanical properties of ultrafine-grained tungsten by manipulating grain boundary chemistry, *Acta Mater.* 232 (2022) 117939.
- [64] M. Wurmshuber, M. Alfreider, S. Wurster, R. Pippan, D. Kiener, Small-scale fracture mechanical investigations on grain boundary doped ultrafine-grained tungsten, Submitted to *Acta Materialia* (2022).
- [65] W. Setyawan, R.J. Kurtz, Grain Boundary Strengthening Properties of Tungsten Alloys, in: *Fusion React. Mater. Progr. Semiannu. Prog. Rep. Period End. June 30, Oak Ridge, 2012*: pp. 82–88.
- [66] G. Kresse, J. Hafner, Ab initio molecular dynamics for liquid metals, *Phys. Rev. B.* 47 (1993) 558–561.
- [67] G. Kresse, J. Hafner, Norm-conserving and ultrasoft pseudopotentials for first-row and transition elements, *J. Phys. Condens. Matter.* 6 (1994) 8245–8257.
- [68] G. Kresse, J. Furthmüller, Efficient iterative schemes for ab initio total-energy calculations using a plane-wave basis set, *Phys. Rev. B.* 54 (1996) 11169–11186.
- [69] G. Kresse, J. Furthmüller, Efficiency of ab-initio total energy calculations for metals and semiconductors using a plane-wave basis set, *Comput. Mater. Sci.* 6 (1996) 15–50.
- [70] B.K. Perdew, J. P. M. Ernzerhof, Generalized Gradient Approximation Made Simple, *Phys. Rev. Lett.* 77 (1996) 3865–3868.
- [71] V.I. Razumovskiy, S. V. Divinski, L. Romaner, Solute segregation in Cu: DFT vs. Experiment, *Acta Mater.* 147 (2018) 122–132.
- [72] R. Bodlos, V. Fotopoulos, J. Spitaler, A.L. Shluger, L. Romaner, Energies and structures of Cu/Nb and Cu/W interfaces from density functional theory and semi-empirical calculations, *Materialia.* 21 (2022) 101362.
- [73] K. Leitner, D. Scheiber, S. Jakob, S. Primig, H. Clemens, E. Povoden-Karadeniz, L. Romaner, How grain boundary chemistry controls the fracture mode of molybdenum, *Mater. Des.* 142 (2018) 36–43.
- [74] I. Sabirov, R. Pippan, Formation of a W-25%Cu nanocomposite during high pressure torsion, *Scr. Mater.* 52 (2005) 1293–1298.
- [75] I. Sabirov, R. Pippan, Characterization of tungsten fragmentation in a W-25%Cu composite after high-pressure torsion, *Mater. Charact.* 58 (2007) 848–853.
- [76] D. Edwards, I. Sabirov, W. Sigle, R. Pippan, Microstructure and thermostability of a W – Cu nanocomposite produced via high-pressure torsion, *Philos. Mag.* 92 (2012) 4151–4166.
- [77] S. Doppermann, Parameters affecting refinement of powder-based W-Cu composites during high

pressure torsion, Montanuniversität Leoben, 2021.

- [78] M. Burtscher, M. Zhao, J. Kappacher, A. Leitner, M. Wurmshuber, M. Pfeifenberger, V. Maier-Kiener, D. Kiener, High-temperature nanoindentation of an advanced nano-crystalline W/Cu composite, *Nanomaterials*. 11 (2021) 1–13.
- [79] M. Wurmshuber, S. Dopperrmann, S. Wurster, D. Kiener, Ultrafine-grained Tungsten by High-Pressure Torsion – Bulk precursor versus powder processing route, *IOP Conf. Ser. Mater. Sci. Eng.* 580 (2019) 012051.
- [80] R. Pippan, S. Scheriau, A. Hohenwarter, M. Hafok, Advantages and Limitations of HPT: A Review, *Mater. Sci. Forum.* 584–586 (2008) 16–21.
- [81] R. Pippan, S. Scheriau, A. Taylor, M. Hafok, A. Hohenwarter, A. Bachmaier, Saturation of Fragmentation During Severe Plastic Deformation, *Annu. Rev. Mater. Res.* 40 (2010) 319–343.
- [82] R.Z. Valiev, Y. Estrin, Z. Horita, T.G. Langdon, M.J. Zehetbauer, Y. Zhu, Producing Bulk Ultrafine-Grained Materials by Severe Plastic Deformation: Ten Years Later, *Jom*. 68 (2016) 1216–1226.
- [83] M. Burtscher, M. Alfreider, C. Kainz, K. Schmuck, D. Kiener, In-situ micromechanical analysis of a nano-crystalline W-Cu, *Mater. Des.* 220 (2022) 110848.
- [84] D. Kiener, W. Grosinger, G. Dehm, R. Pippan, A further step towards an understanding of size-dependent crystal plasticity: In situ tension experiments of miniaturized single-crystal copper samples, *Acta Mater.* 56 (2008) 580–592.
- [85] M. Alfreider, M. Meindlhumer, V. Maier-Kiener, A. Hohenwarter, D. Kiener, Extracting information from noisy data: strain mapping during dynamic in situ SEM experiments, *J. Mater. Res.* 36 (2021) 2291–2304.
- [86] D.S. Gianola, C. Eberl, Micro- and Nanoscale Tensile Testing of Materials, *JOM*. 61 (2009) 24–35.
- [87] G. Dehm, B.N. Jaya, R. Raghavan, C. Kirchlechner, Overview on micro- and nanomechanical testing: New insights in interface plasticity and fracture at small length scales, *Acta Mater.* 142 (2018) 248–282.
- [88] E. Carrera, G. Giunta, M. Petrolo, *Beam Structures: Classical and Advanced Theories*, John Wiley & Sons, 2011.
- [89] C. Motz, T. Schöberl, R. Pippan, Mechanical properties of micro-sized copper bending beams machined by the focused ion beam technique, *Acta Mater.* 53 (2005) 4269–4279.
- [90] M. Meindlhumer, *Micromechanical Characterization of Self-Organized Ti_{1-x}Al_xN Nanolamellae: The Influence of Interface Coherency and Phase Alteration on Fracture Behaviour*, Montanuniversität Leoben, 2016.
- [91] M.J. Pfeifenberger, M. Mangang, S. Wurster, J. Reiser, A. Hohenwarter, W. Pfleging, D. Kiener, R. Pippan, The use of femtosecond laser ablation as a novel tool for rapid micro-mechanical sample preparation, *Mater. Des.* 121 (2017) 109–118.
- [92] R. Pippan, S. Wurster, D. Kiener, Fracture mechanics of micro samples: Fundamental considerations, *Mater. Des.* 159 (2018) 252–267.
- [93] M. Alfreider, D. Kozic, O. Kolednik, D. Kiener, In-situ elastic-plastic fracture mechanics on the microscale by means of continuous dynamical testing, *Mater. Des.* 148 (2018) 177–187.
- [94] S. Wurster, C. Motz, R. Pippan, Characterization of the fracture toughness of micro-sized tungsten single crystal notched specimens, *Philos. Mag.* 92 (2012) 1803–1825.

- [95] ASTM Standard E 1820-13, ASTM International, 2013.
- [96] S. Wurster, C. Motz, R. Pippan, Notched-cantilever testing on the micrometer scale-effects of constraints on plasticity and fracture behaviour, *Proc. 18th Eur. Conf. Fract.* (2010).
- [97] M. Alfreider, S. Kolitsch, S. Wurster, D. Kiener, An analytical solution for the correct determination of crack lengths via cantilever stiffness, *Mater. Des.* 194 (2020) 108914.
- [98] J. Ast, M. Ghidelli, K. Durst, M. Göken, M. Sebastiani, A.M. Korsunsky, A review of experimental approaches to fracture toughness evaluation at the micro-scale, *Mater. Des.* 173 (2019) 107762.
- [99] D. Leguillon, É. Martin, M.C. Lafarie-Frenot, Flexural vs. tensile strength in brittle materials, *Comptes Rendus Mec.* 343 (2015) 275–281.
- [100] P. Sudharshan Phani, K.E. Johanns, E.P. George, G.M. Pharr, A simple stochastic model for yielding in specimens with limited number of dislocations, *Acta Mater.* 61 (2013) 2489–2499.
- [101] P.S. Sudharsan Phani, K.E. Johanns, E.P. George, G.M. Pharr, A stochastic model for the size dependence of spherical indentation pop-in, *J. Mater. Res.* 28 (2013) 2728–2739.
- [102] W.D. Klopp, Review of ductilizing of group VIA elements by rhenium and other solutes, NASA TN D-4955. (1968).
- [103] L. Romaner, C. Ambrosch-Draxl, R. Pippan, Effect of rhenium on the dislocation core structure in tungsten, *Phys. Rev. Lett.* 104 (2010) 195503.

E Helium-induced swelling and mechanical property degradation in ultrafine-grained W and W-Cu nanocomposites for fusion applications

M. Wurmshuber¹, M. Balooch², X. Huang², P. Hosemann^{2,3}, D. Kiener¹

¹ Department of Materials Science, Chair of Materials Physics, Montanuniversität Leoben, Jahnstraße 12, 8700 Leoben, Austria

² Department of Nuclear Engineering, University of California, Berkeley, 4155 Etcheverry Hall, Berkeley, CA 94720, USA

³ Materials Sciences Division, Lawrence Berkeley National Laboratory, 1 Cyclotron Road, Berkeley, CA 94720, USA

Besides high dose radiation and extreme thermal loads, a major concern for materials deployed in novel nuclear fusion reactors is the formation and growth of helium bubbles. This work investigates the swelling and mechanical property degradation after helium implantation of ultrafine-grained W and nanocrystalline W-Cu, possible candidates for divertor and heat-sink materials in fusion reactors, respectively. It is found that ultrafine-grained W and single crystalline W experience similar volumetric swelling after helium implantation but show different blistering behaviour. The W-Cu nanocomposite, however, shows a reduced swelling compared to a coarse-grained composite due to the effective annihilation of radiation-induced vacancies through interfaces. Furthermore, the helium-filled cavity structures lead to considerable softening of the composite.

E.1 Introduction

The effects of helium as a transmutation product in structural nuclear reactor materials have been investigated since the early days of nuclear engineering [1,2]. In-service fission devices, such as currently operating CANDU reactors [3,4], serve as reminders that helium gas in structural materials can lead to materials challenges. Furthermore, the renewed interest in nuclear fusion and the recent efforts in commercializing fusion technology led to an increase in associated research. In addition to radiation effects on materials in fusion environments and transmutation reactions, the fusion reaction itself ${}^2_1D + {}^3_1T \rightarrow {}^4_2He + n + 17.6MeV$ generates helium ions that can interact with the

plasma-facing wall material [5]. Therefore, in addition to well researched radiation effects [1,2,6,7] and extreme thermals loads, one has to account for helium bubble nucleation and growth within the structural materials employed in the vicinity or even facing the fusion plasma. For the divertor, the part of the reactor experiencing the prevalent exposure to the plasma, tungsten is often considered the prime candidate material due to a plethora of advantageous physical properties [8,9]. In particular, ultrafine-grained (ufg) W is an exciting prospect, as the small grain size has beneficial effects on mechanical properties, such as fracture toughness [10,11]. Moreover, to allow for a rapid heat transport away from the divertor and avoid temperature fluctuation-induced failure of the component, high strength heat sinks have to be employed, commonly in the form of W-Cu composite materials [12,13]. Here a nanostructuring of the composite is beneficial for radiation tolerance and mechanical strength [6].

While helium implantation of single-crystalline (sxx) and coarse-grained (cg) W and Cu have been investigated thoroughly in earlier works [14–17], for ufg W most work focuses on bubble evolution and morphology [18–20]. These insights provide a fundamental understanding of the microstructural changes arising from helium implantation, but the concrete implications for swelling and changes in mechanical properties (i.e. elastic modulus and hardness) of the implanted material will define the practical employment of ufg W and W-Cu composites in fusion reactors. In this work, a combined approach of atomic force microscopy (AFM) and nanoindentation was utilized to investigate the swelling and related changes in mechanical properties of ufg W and nanocrystalline (nc) W-Cu as implanted with various fluences of helium.

E.2 Material fabrication and irradiation

Ufg W and nc W-Cu composites are fabricated from powders using severe plastic deformation. W powder (purity 99.97%, particle size $<2\ \mu\text{m}$, Plansee SE, Austria) is stored, handled and compacted within argon atmosphere. An intermediate annealing step after compacting at 1600°C for 7h in a vacuum-furnace (Leybold Heraeus PD 1000, Leybold GmbH, Germany) assures sufficient particle bonding before severe plastic deformation is applied through a high-pressure torsion (HPT) tool [21] for 1 rotation at a nominal pressure of 12 GPa and a temperature of 400°C . More details regarding the fabrication of ufg W can be found in references [11,22]. The grain size of ufg W was measured from micrographs (Figure E.1a) using the line intercept method and is $158 \pm 35\ \text{nm}$ ($125 \pm 10\ \text{nm}$ in implantation direction and $189 \pm 21\ \text{nm}$ in lateral direction). For the W-Cu nanocomposite, 25 at.% of the respective W powder

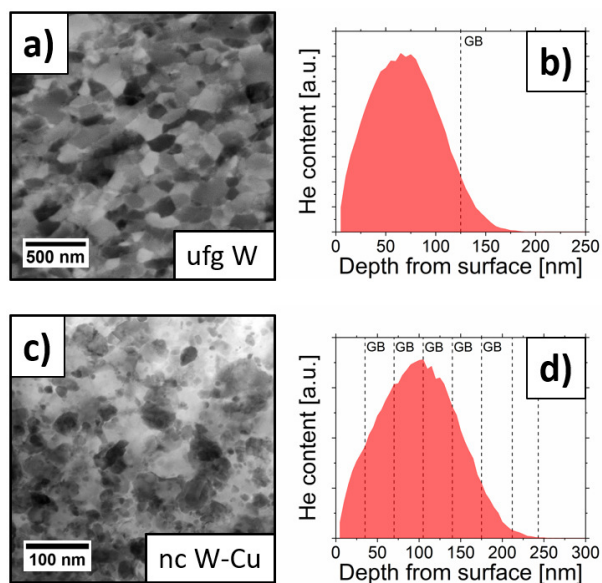


Figure E.1 Microstructures of a) ufg W (SEM) and c) nc W-Cu (TEM). The penetration depths of 25 keV He ions for b) ufg W and d) nc W-Cu were simulated by SRIM. Vertical lines indicate the average location of grain boundaries.

and 75 at.% Cu powder (purity 99%, particle size 14-25 μm , Merck KGaA, Germany) were mixed within argon atmosphere and then compacted using the HPT tool. The powder compact was subsequently deformed using the HPT for 100 revolutions under a pressure of 9 GPa at room temperature. The grains were measured from TEM images (Figure E.1c) to be 35 ± 17 nm in diameter and equiaxed.

A helium-ion microscope (Orion Nanofab, Carl Zeiss GmbH, Germany) [16,23,24] was used to implant 25 keV helium ions to fluences of 6×10^{17} and 10^{18} ions/ cm^2 in ufg W and 3×10^{17} , 6×10^{17} and 10^{18} ions/ cm^2 in nc W-Cu. The helium was implanted on $10 \times 10 \mu\text{m}^2$ squares on the polished surfaces with a dose rate of about 1 dpa/min. The implantations of both materials have been simulated using the software “Stopping Range of Ions in Matter” (SRIM) [25] using the Kinchin-Pease model and displacement energies of 85 eV for W [26,27] and 30 eV for Cu [26,28]. The calculated helium ion profiles are depicted in Figures E.1b and E.1d. For the W-Cu composite, a hypothetical solid solution was chosen as model material for the simulations. This represents a satisfying average of the irradiation response, even though W is expected to exert a higher stopping effect than Cu. This behavior leads to local deviations from the averaged profile in Figure E.1d, depending on the distribution of W and Cu grains inside the material hit by the He beam, but will not influence the average penetration depth significantly.

E.3 Swelling

Subsequent to implantation, the surface topology of and around the implanted areas on both materials was scanned using an atomic force microscope (AFM; Nanoscope III, Digital Instruments, USA) in tapping mode. This way, the amount of surface swelling due to helium bubble formation can be measured by comparing the average height difference of the implanted regions to the unimplanted surface, a quantity commonly referred to as swelling height [14,16,24] (see Figure E.2a). Figure E.2b displays the compiled results of the swelling measurements of ufg W and nc W-Cu, as well as extrapolated values for swelling of sxx W [14] and cg (“quasi-sxx”) Cu [16]. Additionally, a simple arithmetic combination of cg Cu and sxx W values in the same ratio as the investigated composite (25 at.% W + 75 at.% Cu) is shown. Naturally, for all materials the swelling increases with increasing helium fluence. No swelling data could be acquired for the fluence of 3×10^{17} ions/cm² in ufg W, as this implantation unfortunately failed.

From Figure E.2b it is apparent that Cu and the W-Cu composite exhibit a higher swelling than the pure W samples. This is rationalized by the fact that Cu has an fcc crystal structure, which is more densely packed and known to be more sensitive to void and gas bubble swelling than bcc metals [29,30]. The nc W-Cu investigated in

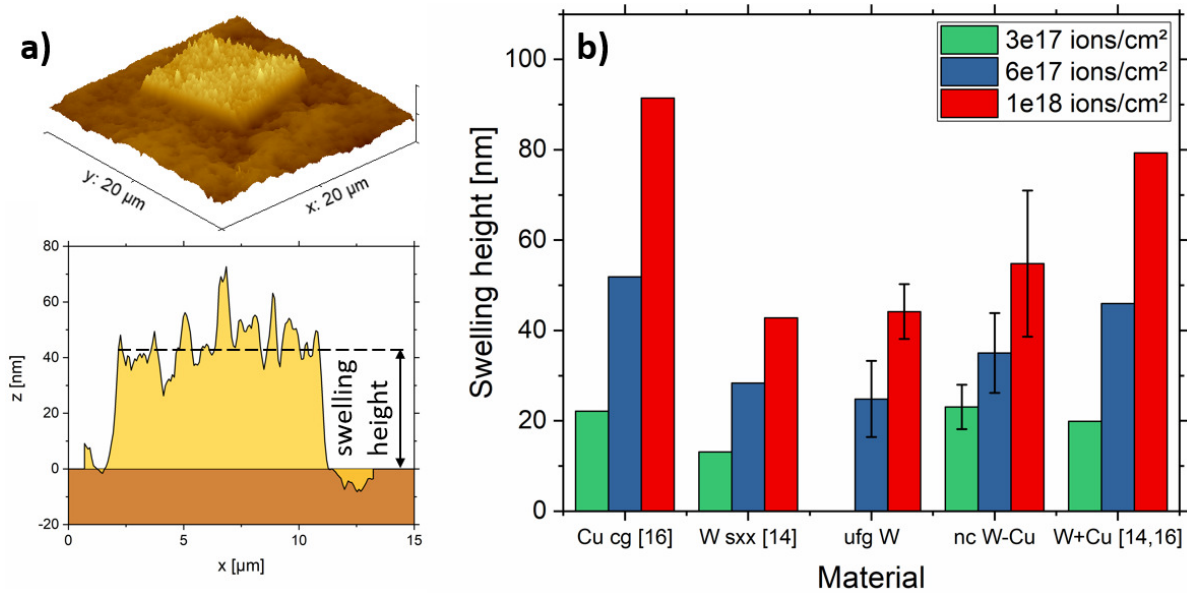


Figure E.2 a) Representative AFM image of ufg W implanted with a helium fluence of 10^{18} ions/cm² and schematic on the definition of swelling height. b) Swelling height of ufg W and nc W-Cu compared to literature data for cg Cu and sxx W. Error bars represent the RMS roughness on the implanted squares.

this work displays far less swelling than the arithmetic combination of c_g Cu and s_{xx} W values. This proves that the vast amount of grain boundaries and interfaces within the nc W-Cu has a significant influence on bubble formation and growth and, therefore, the resulting swelling. Swelling of the ufg W material, however, is comparable to the s_{xx} W investigated by Allen et al. [14]. It appears that the still large amount of grain boundaries within the ufg W does not have any noticeable effect on the measured swelling height, which is supported by the findings of El-Atwani et al. [20], reporting a grain size threshold of 35-50 nm in W. Above this threshold helium bubble size and density, and thus swelling, are not influenced significantly by the grain boundaries at room temperature, as the ability to effectively remove radiation-induced vacancies is not given. Furthermore, as visualized in Figure E.1b, on average only a single grain boundary, located far beyond the peak of helium content, lies within the helium implanted region in implantation direction. In comparison, in the W-Cu nanocomposite the smaller grain size and larger penetration depth result in up to seven grain boundaries being located in the helium-affected zone on average (Figure E.1d). There are of course more grain boundaries in the lateral direction of the implanted area, which could lead to a more pronounced swelling in the horizontal direction. When assuming simple brick-shaped grains, the grain boundary area within the affected zone accumulates to roughly $340 \mu\text{m}^2$ in ufg W and $1410 \mu\text{m}^2$ in nc W-Cu. This significant difference provides an additional explanation as to why the grain size of 35 nm is so much more effective in reducing swelling than a grain size of 150 nm. It should be noted, however, that blisters as observed for s_{xx} W in [14] are not present in the ufg W sample implanted with similar helium fluences (see Figure E.2a), indicating that bubble growth and coalescence are restricted, and bubble nucleation is the main reason for the comparable swelling heights of the two materials. All things considered, the nc W-Cu shows still a higher swelling than either W material, which confirms that W, and bcc materials in general, demonstrate a high resistance to helium bubble swelling. While this resistance could potentially be amplified by reducing the grain size further, following the idea of [20], this would in turn deteriorate the excellent ductility and fracture toughness that ufg W showcases [10,11].

E.4 Mechanical property degradation

Turning from swelling to related changes in mechanical properties, the small penetration depth of the helium ions in W and W-Cu makes it challenging to assess irradiation-induced changes. A number of various small-scale testing methods have been applied in the past to assess irradiation induced property changes of ion-irradiated materials [16,24,31–33]. Nanoindentation offers several advantages, such as

absence of additional sample preparation as well as easy and straightforward testing. By applying dynamic continuous stiffness measurements (CSM) [34–37], hardness and modulus can be probed along the indentation depth. In this work, a TI 950 Triboindenter (Hysitron Inc., USA) with a CSM and a Scanning Probe Microscopy (SPM) option was used to indent the implanted and unimplanted areas. After the Berkovich tip was calibrated on fused silica following Oliver & Pharr [34], the implanted area was scanned using the SPM option. Indents were placed inside and outside of the implanted squares to an indentation depth of about 200 nm in the ufg W material and 300 nm in the W-Cu nanocomposite. For every material condition, 4-5 nanoindentation tests were conducted. Considering the small penetration depth of the helium ions of about 180 nm (W) to 230 nm (W-Cu) (Figures E.1b and E.1d), the indentation tests will always probe additional unaffected material below the implanted helium layer, thus not reflecting only the hardness of the implanted layer. However, the trend of hardening and softening through helium implantation should still be apparent in the results, albeit less pronounced for larger indentation depths [31,32].

The averaged nanoindentation curves plus standard deviation for every condition are presented in Figure E.3. It is obvious that the reduced elastic modulus of both ufg W and nc W-Cu decreases continuously with increasing helium fluence (Figure E.3c and E.3d). This is explained by the continued formation and growth of helium bubbles within the materials with more helium being implanted. Regarding hardness, the two materials show a slightly different behavior. While the hardness of the nanocomposite decreases continuously with increasing fluence (see Figure E.3b), the ufg W seems to retain its hardness after implantation with a fluence of 6×10^{17} ions/cm² and only deteriorate after implantation with a higher fluence of 10^{18} ions/cm² (see Figure E.3a). This is most likely deceiving, as earlier work by the authors unveiled for Cu-Fe-Ag with similar grain size that for such ufg materials, a combination of conventional radiation hardening (dominant at lower fluences) and softening through gas bubble nucleation and growth (dominant at higher fluences) is the reason for a perceived sustained hardness from the unirradiated state at fluences around $4 - 6 \times 10^{17}$ ions/cm² [24]. It is crucial to note that, while the hardness is seemingly unchanged, a critical reduction in ductility and toughness can be expected from these competing hardening and softening mechanisms. For the nc W-Cu composite this effect is not observed, as the much smaller grain size of about 35 nm leads to the efficient annihilation of radiation-induced point defects, thereby suppressing the radiation hardening effect [6,7]. Without such a hardening effect, the size and amount of helium gas bubbles are the major factors influencing the mechanical properties, leading to softening throughout all fluences of helium implantation [24]. Commonly, in single-crystalline metals or metals with grain sizes above 1 μ m, such a softening effect is not observed, especially for low fluences. Here, the formed helium bubbles

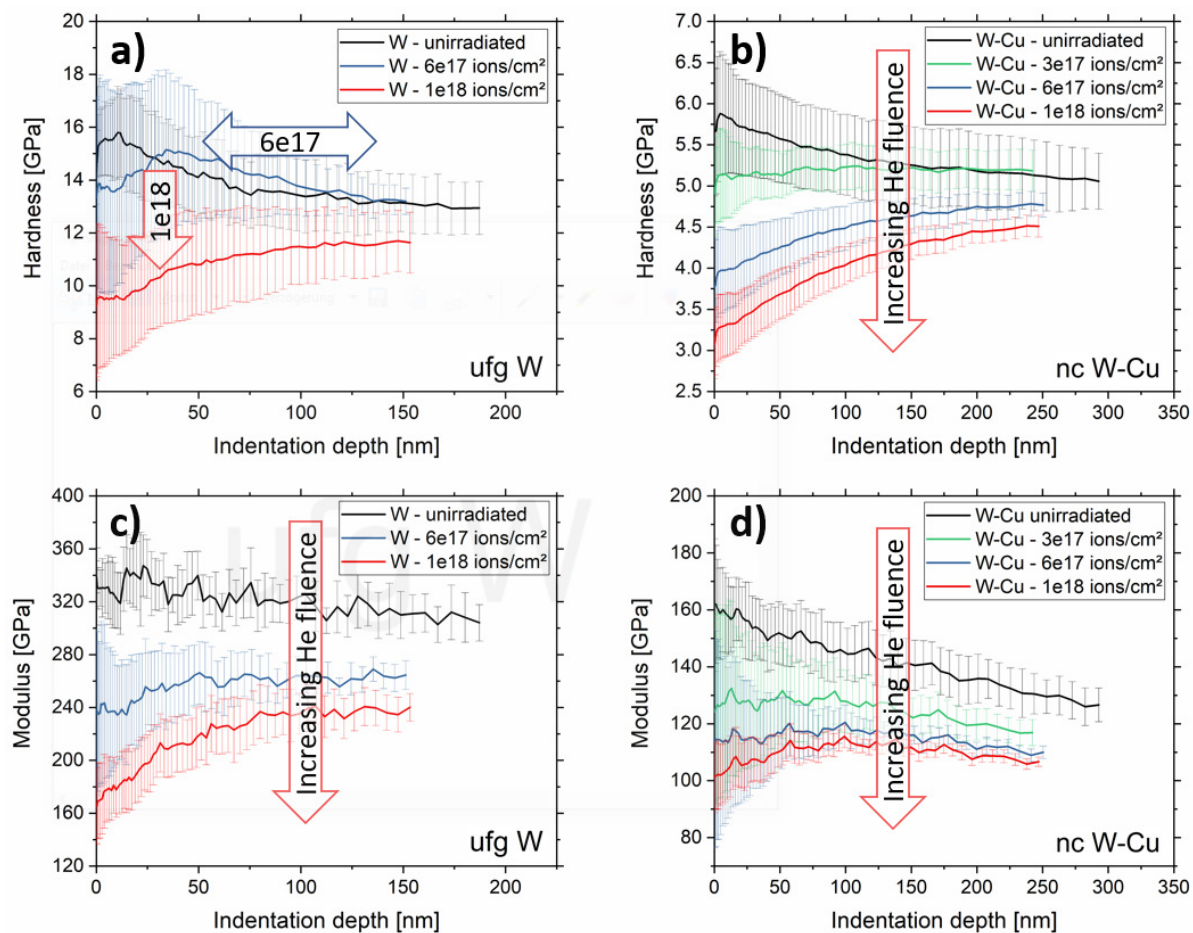


Figure E.3 Averaged nanoindentation curves for hardness (a,b) and reduced modulus (c,d) of ufg W (a,c) and nc W-Cu (b,d). Both moduli and the hardness of nc W-Cu decrease with increasing He fluence. The hardness of ufg W stays preserved after implanting with a fluence of 6×10^{17} ions/cm² and decreases only at a higher fluence of 10^{18} ions/cm².

act as obstacles to dislocation movement within the grains and lead to a pronounced hardening effect [38–40]. In contrast, in nc and ufg metals bubbles nucleate preferably at GBs, where they do not interfere with dislocation propagation. The softening effect can therefore be explained by the slow transformation of the material into a metal foam and a facilitated dislocation nucleation from bubble-decorated GBs, in agreement with other works [7,24,41,42].

E.5 Conclusion

In summary, swelling and mechanical property changes of ufg W and nc W-Cu were assessed after implantation with helium ions. While the W-Cu nanocomposite experiences more swelling than the ufg W due to the contained fcc Cu phase, a reduction of swelling compared to cg Cu and a cg W-Cu composite could be achieved via the small grain size of 35 nm. In contrast, aside from the lack of blister formation, the grain size of 158 nm in ufg W led to no significant changes in measured swelling compared to sxx W. This is explained by the much lower grain boundary area density of ufg W and by the inability to remove vacancies before they nucleate bubbles at a grain size above 50 nm. Similarly, this inability results in a combined radiation-induced hardening and bubble-induced softening effect when probing the mechanical properties of helium-implanted W. As the hardening effect is absent in nc W-Cu, the hardness deteriorates much faster due to the suppressed but still present bubble formation and growth. In conclusion, while the ufg grain size improves the overall mechanical properties of W, the implications for swelling resistance are minor. The nc grain size of W-Cu, however, results in significantly reduced bubble-induced swelling, but also quick degradation of hardness and modulus due to the absence of radiation hardening. The findings presented in this work are expected to contribute to an improved understanding on how promising ultrafine- and nano-grained materials perform in the harsh environment of a nuclear fusion reactor.

Acknowledgements

The authors acknowledge funding by the European Research Council under grant number 771146 (TOUGHIT). Additional financial support was provided by the Austrian Marshall Plan Foundation. The authors acknowledge further support from NSF DMR Award No. 1807822. The authors thank Dr. Michael Burtscher for providing TEM images of the W-Cu nanocomposite and Simon Doppermann for help with sample fabrication.

References

- [1] D.R. Olander, *Fundamental Aspects of Nuclear Reactor Fuel Elements*, Technical Information Center, Office of Public Affairs, Energy Research and Development Administration, Springfield, USA., 1977.
- [2] G.S. Was, *Fundamentals of Radiation Materials Science*, 2007.

- [3] M. Griffiths, *AECL Nucl. Rev.* 2 (2013).
- [4] C. Howard, V. Bhakhri, C. Dixon, H. Rajakumar, C. Mayhew, C.D. Judge, *J. Nucl. Mater.* 517 (2019) 17–34.
- [5] E. Rebhan, D. Reiter, R. Weynants, U. Samm, W.J. Hogan, J. Raeder, T. Hamacher, in: K. Heinloth (Ed.), *Landolt-Börnstein Numer. Data Funct. Relationships Sci. Technol. Gr. VIII Adv. Mater. Technol.*, Springer, 2005, pp. 304–368.
- [6] X. Zhang, K. Hattar, Y. Chen, L. Shao, J. Li, C. Sun, K. Yu, N. Li, M.L. Taheri, H. Wang, J. Wang, M. Nastasi, *Prog. Mater. Sci.* 96 (2018) 217–321.
- [7] M. Wurmshuber, D. Frazer, A. Bachmaier, Y. Wang, P. Hosemann, D. Kiener, *Mater. Des.* 160 (2018).
- [8] M. Rieth, D.E.J. Armstrong, B. Dafferner, S. Heger, A. Hoffmann, M. Hoffmann, U. Jäntschi, M. Rohde, T. Scherer, V. Widak, H. Zimmermann, *Adv. Sci. Technol.* 73 (2010) 11–21.
- [9] M. Rieth, S.L. Dudarev, S.M.G. De Vicente, J. Aktaa, T. Ahlgren, S. Antusch, D.E.J. Armstrong, M. Balden, N. Baluc, M. Barthe, W. Basuki, M. Battabyal, C.S. Becquart, D. Blagoeva, H. Boldyryeva, J. Brinkmann, M. Celino, L. Ciupinski, J.B. Correia, A. De Backer, C. Domain, E. Gaganidze, C. Garcia-Rosales, J. Gibson, M.R. Gilbert, S. Giusepponi, B. Gludovatz, H. Greuner, K. Heinola, T. Höschen, A. Hoffmann, N. Holstein, F. Koch, W. Krauss, H. Li, S. Lindig, J. Linke, C. Linsmeier, P. López-ruiz, H. Maier, J. Matejcek, T.P. Mishra, M. Walter, T. Weber, T. Weitkamp, S. Wurster, M.A. Yar, J.H. You, A. Zivelonghi, *J. Nucl. Mater.* 432 (2013) 482–500.
- [10] M. Faleschini, H. Kreuzer, D. Kiener, R. Phipps, *J. Nucl. Mater.* 367–370 (2007) 800–805.
- [11] M. Wurmshuber, S. Jakob, S. Dopfermann, S. Wurster, R. Bodlos, L. Romaner, V. Maier-Kiener, D. Kiener, *Submitt. to Acta Mater.*
- [12] O.A. Waseem, H.J. Ryu, in: R. Rahman (Ed.), *Nucl. Mater. Perform., IntechOpen*, 2016, pp. 139–161.
- [13] E. Tejado, *Mater. Today* 38 (2020) 136–137.
- [14] F.I. Allen, P. Hosemann, M. Balooch, *Scr. Mater.* 178 (2020) 256–260.
- [15] Z. Chen, L.L. Niu, Z. Wang, L. Tian, L. Kecskes, K. Zhu, Q. Wei, *Acta Mater.* 147 (2018) 100–112.
- [16] Y. Yang, D. Frazer, M. Balooch, P. Hosemann, *J. Nucl. Mater.* 512 (2018) 137–143.
- [17] W. Han, E.G. Fu, M.J. Demkowicz, Y. Wang, A. Misra, *J. Mater. Res.* 28 (2013) 2763–2770.
- [18] O. El-Atwani, J.A. Hinks, G. Greaves, S. Gonderman, T. Qiu, M. Efe, J.P. Allain, *Sci. Rep.* 4 (2014) 4–10.
- [19] O. El-Atwani, K. Hattar, J.A. Hinks, G. Greaves, S.S. Harilal, A. Hassanein, *J. Nucl. Mater.* 458 (2015) 216–223.
- [20] O. El-Atwani, J.A. Hinks, G. Greaves, J.P. Allain, S.A. Maloy, *Mater. Res. Lett.* 5 (2017) 343–349.
- [21] R. Phipps, S. Scheriau, A. Hohenwarter, M. Hafok, *Mater. Sci. Forum* 584–586 (2008) 16–21.
- [22] M. Wurmshuber, S. Dopfermann, S. Wurster, D. Kiener, *IOP Conf. Ser. Mater. Sci. Eng.* 580 (2019) 012051.
- [23] F.I. Allen, *Beilstein J. Nanotechnol.* 12 (2021) 633–664.
- [24] M. Wurmshuber, D. Frazer, M. Balooch, I. Issa, A. Bachmaier, P. Hosemann, D. Kiener, *Mater. Charact.* 171 (2021) 110822.
- [25] J.F. Ziegler, J.P. Biersack, (1985).
- [26] A.Y. Konobeyev, U. Fischer, Y.A. Korovin, S.P. Simakov, *Nucl. Energy Technol.* 3 (2017) 169–175.

-
- [27] M.J. Banisalman, S. Park, T. Oda, *J. Nucl. Mater.* 495 (2017) 277–284.
- [28] E.A. Kenik, T.E. Mitchell, *Philos. Mag.* 32 (1975) 815–831.
- [29] F.A. Garner, M.B. Toloczko, B.H. Sencer, *J. Nucl. Mater.* 276 (2000) 123–142.
- [30] A. Bhattacharya, S.J. Zinkle, *Cavity Swelling in Irradiated Materials*, 2020.
- [31] D. Kiener, A.M. Minor, O. Anderoglu, Y. Wang, S.A. Maloy, P. Hosemann, *J. Mater. Res.* 27 (2012) 2724–2736.
- [32] P. Hosemann, C. Shin, D. Kiener, *J. Mater. Res.* 30 (2015) 1231–1245.
- [33] P. Hosemann, *Scr. Mater.* 143 (2018) 161–168.
- [34] W.C. Oliver, G.M. Pharr, *J. Mater. Res.* 7 (1992) 1564–1583.
- [35] W.C. Oliver, G.M. Pharr, *J. Mater. Res.* 19 (2004).
- [36] G.M. Pharr, J.H. Strader, W.C. Oliver, *J. Mater. Res.* 24 (2009) 653–666.
- [37] A. Leitner, V. Maier-Kiener, D. Kiener, *Mater. Res. Lett.* 5 (2017) 486–493.
- [38] F. Kong, M. Qu, S. Yan, A. Zhang, S. Peng, J. Xue, Y. Wang, *Nucl. Instruments Methods Phys. Res. Sect. B Beam Interact. with Mater. Atoms* 406 (2017) 643–647.
- [39] J.T. Li, I.J. Beyerlein, W.Z. Han, *Acta Mater.* 226 (2022) 117656.
- [40] W. Qin, Y. Wang, M. Tang, F. Ren, Q. Fu, G. Cai, L. Dong, L. Hu, G. Wei, C. Jiang, *J. Nucl. Mater.* 502 (2018) 132.
- [41] W.S. Cunningham, J.M. Gentile, O. El-atwani, C.N. Taylor, M. Efe, S.A. Maloy, J.R. Trelewicz, *Sci. Rep.* 8 (2018) 1–10.
- [42] H. Wang, F. Ren, J. Tang, W. Qin, L. Hu, L. Dong, B. Yang, G. Cai, C. Jiang, *Acta Mater.* 144 (2018) 691.